Modeling asteroid binary systems with the full two-body problem using surface integrals

Alex Ho

UiA University of Agder

Doctoral Dissertations at
the University of Agder 432

Alex Ho

Modeling asteroid binary systems with the full two-body problem using surface integrals

Dissertation for the degree philosophiae doctor (ph.d.)
at the Faculty of Engineering and Science, Specialisation in Engineering Sciences,
scientific field Physics and Applied Mathematics

University of Agder
Faculty of Engineering and Science
2023

Doctoral dissertations at the University of Agder 432

ISSN: 1504-9272

ISBN: 978-82-8427-149-1

Printed by Make!Graphics
Kristiansand

Acknowledgments

I would first like to thank my supervisors Margrethe Wold, John Thomas Conway, and Mohammad 'Ali' Poursina. I am grateful for your guidance throughout the work of my thesis. Margrethe, I am grateful for your helpful input on my work and your valuable advice for both research and teaching. Ali, thank you for your input on different topics I have not experienced and for presenting them in an easy way for me to understand. Finally, to John, I am grateful for both the helpful guidance and also our long conversations.

I would also like to give a special thanks to Thomas Gjesteland for his input related to teaching. Your advice has helped me improve my teaching skills, something that I developed a great passion for over time.

During my PhD, I had the opportunity to visit the University of Helsinki to attend a class taught by Mikael Granvik and also hold a small seminar. I would like to thank Mikael for arranging a pleasant trip to Helsinki, and also for his useful input related to asteroid research.

My time at UiA has been very enjoyable thanks to the friends I have made among my fellow PhD students. Special thanks to Nils, Gulshan, Martin, Josè, Jayant, Shashank, Sveinung, Arild, Siri, Hareesh, Bilal, Dipendra, Wei, Sarang, Alfredo, Emil, Ronny, Teodor, Emilio, Wahiba. You have all made my stay at UiA an incredible and pleasant experience.

Finally, I would like to show my gratitude to my family for their continuous love and support.

Alex Ho
Nesodden, Norway
June 2023

Abstract

An asteroid binary system, where two asteroids are in mutual orbit, is important to study as it can provide knowledge of the history of the asteroid population. The most important mechanism to form asteroid binaries in the near-Earth population, and for asteroids with diameters less than 10 km, is rotational fission. Rotational fission occurs when a rubble pile asteroid, which can be thought of as a collection of rocks held together by gravity, reaches a critical spin rate and the rubble pile starts to shed mass.

Studying the dynamics of asteroid binaries allows one to better understand how they have evolved. However, due to their non-spherical shapes, one has to take into account both the translational and rotational motion of asteroids, which is known as the full two-body problem. The study of the full two-body problem is a challenge as the mutual gravitational potential between two non-spherical bodies cannot be expressed analytically. Previous studies have used approximations to model the mutual potential between two asteroids. However, these approximations often suffer from inaccuracies when the bodies are close to each other, and also from truncation errors. In this thesis, we make use of a new method to determine the mutual potential, between two asteroids, with the use of surface integrals. We apply this method to study the dynamics of the 1999 KW4 binary system, where both bodies are modeled as ellipsoids. With the use of an order nine Runge-Kutta method, the system energy and angular momentum are conserved to the 11th decimal digit.

One of the advantages of the surface integration method is that the results are valid even if the bodies are close to each other. We make use of this advantage to study the dynamics of asteroid systems formed by rotational fission, as the two bodies are very close to each other in the initial formation stages. We consider ellipsoidal bodies for the simulations. Six models are considered, three where the secondary takes different densities and three where we change the shape of the secondary. The simulations show that more than 80% of the simulations result in the two bodies colliding. The secondary is more likely to escape the gravitational pull of the primary, forming an asteroid pair, and experience secondary fission, if the secondary has a higher density than the primary, or has a more elongated shape. We also compare the rotation periods of the bodies from the simulations with the ones from observations of asteroid binaries and pairs. The rotation periods from the simulations match very well with the rotation periods of observed asteroid pairs.

The surface integration scheme can yield exact values to the mutual gravitational potential between two ellipsoidal bodies. This method can therefore be used to determine the accuracy of methods that approximates the mutual potential between two ellipsoids. We compare the surface integration scheme with an approach that expands the mutual potential with the use of inertia integrals. The differences in the gravitational force and torque, between the two methods, are less than 1% if the bodies are separated by $2 - 3$ times the radius of the primary. If the bodies are almost touching, however, the differences can exceed 100% if the shape of the primary becomes elongated. The discrepancies in the torques are typically an order magnitude larger than the difference in the forces.

Sammendrag

Et dobbeltasteroide system, hvor to asteroider går i bane rundt et felles massesenter, er viktig å studere fordi slike systemer kan gi oss kunnskap om historien til asteroider. Den viktigste mekanismen for å danne dobbeltasteroider blant jordnære objekter, og for asteroider med diameter mindre enn 10 km, er rotasjonsfisjon. Rotasjonsfisjon oppstår dersom en "rubble-pile" asteroide, som er en samling av steiner som henger sammen på grunn av gravitasjon, oppnår en kritisk spinnhastighet slik at asteroiden begynner å kaste fra seg masse.

Å studere dynamikken til dobbeltasteroide systemer kan gi oss bedre forståelse på hvordan de har utviklet seg. Siden formen til asteroider ikke er sfæriske, må en ta hensyn til både translasjons- og rotasjonsbevegelsen til disse legemene. Dette er kjent som det fulle to-legeme problemet. Å studere det fulle to-legeme problemet er en utfordring siden det ikke finnes en analytisk løsning for gravitasjonspotensialet mellom to ikke-sfæriske legemer. Tidligere studier har brukt tilnærminger for å beregne potensialet mellom to asteroider, men slike metoder er ofte unøyaktige når legemene er nær hverandre. I tillegg kan slike metoder gi trunkeringsfeil. I denne avhandlingen bruker vi en ny metode for å beregne potensialet mellom to asteroider ved bruk av overflateintegraler. Denne metoden er anvendt for å studere det binære systemet 1999 KW4, hvor begge asteroider er modellert som ellipsoider. Med bruk av en niende ordens Runge-Kutta metode, blir energien og angulærmomentet i systemet bevart til 11. desimalsiffer.

En fordel med overflateintegrasjonsmetoden er at resultatene er gyldige selv om legemene er nær hverandre. Vi tar i bruk denne fordelen for å studere dynamikken til asteroide systemer dannet fra rotasjonsfisjon, siden legemene er veldig nær hverandre i den tidlige formasjonsfasen. Legemene er modellert som ellipsoider i simulasjonene. Seks modeller er studert, tre modeller hvor den sekundære har forskjellige tettheter og tre modeller der vi varierer formen til den sekundære. Mer enn 80% av simulasjonene fører til kollisjon mellom legemene. Det er større sannsynlighet for den sekundære å unnslippe den primære, og dermed danne et asteroide par, dersom den sekundære har høyere tetthet enn den primære eller hvis den sekundære har en avlang form. Vi sammenligner også rotasjonsperioden fra simulasjonene med det som er observert fra dobbeltasteroider og asteroide par. Rotasjonsperiodene fra våre simulasjoner samsvarer godt med rotasjonsperiodene fra observerte asteroide par.

Overflateintegrasjonsmetoden kan gi eksakte verdier av gravitasjonspotensialet mellom to ellipsoider. Denne fremgangsmåten kan derfor brukes for å studere nøyaktigheten til metoder som tilnærmer potensialet mellom to ellipsoider. Vi sammenligner overflateintegrasjonsmetoden med en metode som rekkeutvikler potensialet ved bruk av treghets integraler. Forskjellen på gravitasjonskraften og kraftmomentet, blant metodene, er mindre enn 1% dersom legemene er adskilt med $2-3$ ganger radiusen til den primære. Hvis legemene er nesten i kontakt, kan forskjellene overskride 100% hvis den primære har en avlang form. Forskjellene i kraftmomentene er typisk en størrelsesorden større enn forskjellen i kreftene.

Publications

Journal papers

Paper 1 Alex Ho, Margrethe Wold, John T. Conway, and Mohammad Poursina, Extended two-body problem for rotating rigid bodies. *Celestial Mechanics and Dynamical Astronomy*, 133(8):35, August 2021. doi: 10.1007/s10569-021-10034-8.

Paper 2 Alex Ho, Margrethe Wold, Mohammad Poursina and John T. Conway, Dynamics of asteroid systems post-rotational fission. *Astronomy & Astrophysics*, 665:A43, September 2022. doi: 10.1051/0004-6361/202243706.

Paper 3 Alex Ho, Margrethe Wold, Mohammad Poursina and John T. Conway, The accuracy of mutual potential approximations in simulations of binary asteroids, *Astronomy & Astrophysics*, 671:A38, March 2023. doi: 10.1051/0004-6361/202245552.

Conference proceedings

My thesis work was presented at the following conferences. The proceedings are not included in the thesis.

Margrethe Wold, Alex Ho, Mohammad Poursina, John T. Conway, Two-body integractions with surface integraps, In *europlanet Science Congress 2022, Granada, Spain*, 18-23 September 2022 EPSC2022-711, https://doi.org/10.5194/epsc2022-711.

Alex Ho, Margrethe Wold, John T. Conway, Mohammad Poursina, Dynamics of Asteroid Binary Systems through the Use of Surface Integrals. In *AAS/Division for Planetary Sciences Meeting Abstracts*, volume 53 of *AAS/Division for Planetary Sciences Meeting Abstracts*, page 107.06, October 2021

Margrethe Wold, John T. Conway, and Alex Ho, The Planar rigid two-body problem. In *AAS/Division of Dynamical Astronomy Meeting*, volume 51 of *AAS/Division of Dynamical Astronomy Meeting*, page P11, June 2019

Contents

List of Figures

List of Tables

Symbols and Acronyms

Acronyms

F2BP	Full Two-Body Problem
NEA	Near-Earth Asteroid
TNO	Trans-Neptunian Object

Symbols

G	Gravitational constant
m	Mass
q	Mass ratio
ρ	Density
V	Volume
Φ	Gravitational potential
$\mathbf{g}$	Gravitational field
$\mathbf{F}$	Force
$\mathbf{M}$	Torque
U	Mutual potential
$\mathcal{R}$	Rotation matrix
$\mathcal{I}$	Inertia tensor
a	Ellipsoid semi-major axis
b	Ellipsoid semi-intermediate axis
c	Ellipsoid semi-minor axis

Vector notation

$\mathbf{v}$	A vector in the inertial frame
$\hat{\mathbf{v}}$	A vector in the body-fixed frame

Chapter 1

Introduction

1.1 Motivation

In the solar system, along with the major planets, there are many small objects that orbit the Sun such as asteroids, comets, and dwarf planets. These small objects are sometimes referred to as minor solar system bodies. The majority of the asteroids reside in the main belt, which is located between the orbits of Mars and Jupiter. Due to resonances with Jupiter, some asteroids may leave the main belt and obtain Earth-crossing orbits (Morbidelli et al., 2002). Asteroids with Earth-crossing orbits are also known as near-Earth asteroids (NEA). Figure 1.1 shows an illustration of some observed NEAs and main belt asteroids. The expected lifetime of the near-Earth objects (asteroids and comets with Earth-crossing orbits) is estimated to be roughly 10 Myrs, before they impact with a planet or the Sun, or are ejected from the solar system (Gladman et al., 2000).

Asteroids are also found in the Kuiper belt, located $30-50$ astronomical units from the Sun (Jewitt and Luu, 1993; Stern and Colwell, 1997). Objects residing beyond the orbit of Neptune are also known as trans-Neptunian objects (TNO). TNOs may also obtain Earth-crossing orbits, and it is believed that roughly 6% of the near-Earth objects have originated from the TNOs (Michel et al., 2005). Unlike the planets, asteroids have very low masses, and their shapes are irregular and non-spherical because their gravitational forces are very weak. Asteroids may also have obtained their irregular shapes due to collisions (Sugiura et al., 2018).

Because asteroids are part of the solar system population, understanding their dynamics and relating them to different dynamical events may provide insight into the formation and evolution processes of the solar system. In addition to their dynamics, the knowledge of the density of asteroids can yield valuable information about the composition and the internal structure of an asteroid (Consolmagno et al., 2008; Scheeres et al., 2015). Determining the structural compositions of asteroids in different parts of the solar system may give information on the environment of the solar nebula in the early days of the solar system (Consolmagno et al., 2008). Furthermore, asteroids (and also comets) are believed to be the building blocks of the terrestrial planets, such as Earth, and also the cores of the gas planets (A'Hearn, 2011; Johansen et al., 2015). The knowledge of how these objects are formed, their internal structures, and how they have evolved, is therefore important to understand the history of the solar system.

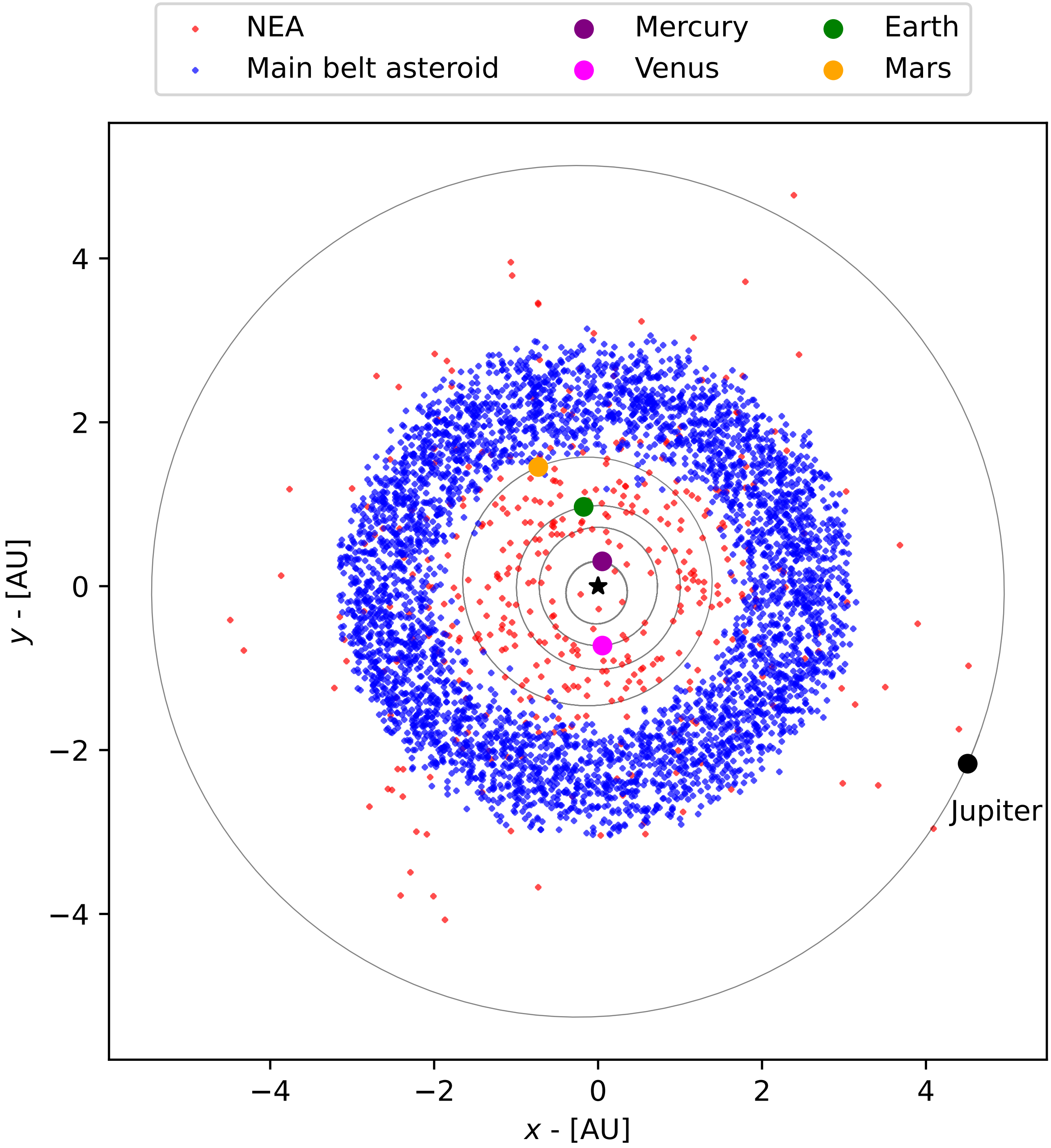

Figure 1.1: Illustration of some NEAs and main belt asteroids. The black star represents the Sun, while the gray lines correspond to the orbits of the planets. The data are obtained from the Python package "astroquery" (Ginsburg et al., 2019). Asteroid data are from the Minor Planet Center database, while planet data are from the JPL Horizons System. The positions of the planets and asteroids in the figure correspond to their positions as of January 1st 2010.

One approach to better understand the asteroid population is to study asteroid binary systems. An asteroid binary system consists of two asteroids in mutual orbit, where a smaller asteroid is in orbit around a larger one. The larger asteroid is often referred to as the "primary", while the smaller one is referred to as the "secondary". Studying asteroid binaries is important because they can provide information to the dynamical processes, e.g. collisions, of asteroids. Furthermore, binary asteroids can also be used to determine the density of asteroids (Merline et al., 2002), which is otherwise obtained through spacecraft missions.

Asteroid binaries can come in different sizes. Known binaries in the NEA population have primaries with diameters between 350 m and 10 km, and the diameters of the corresponding secondaries are usually between 4% and 58% of the primary (Pravec et al., 2012; Walsh and Jacobson, 2015; Pravec et al., 2016). Observations of binaries among NEAs and small main belt binaries (with primary diameter < 15 km) indicate that the primary generally spins faster than the secondary, where the primaries have rotation periods between 2.2 and 4.4 hours, and the secondaries have rotation periods between 13 and 42 hours (Pravec et al., 2016). Furthermore, asteroid binaries are quite common in the NEA population where it is estimated that 15% are binaries (Margot et al., 2002; Pravec et al., 2006). As of 17 February 2023, 485 asteroids and TNOs (including Pluto) in the solar system have been confirmed to have at least one satellite in orbit[1].

Observations of NEAs and binary NEAs, with primary diameters smaller than 10 km, show a lack of asteroids with rotation periods shorter than 2.2 hours (Pravec and Harris, 2000; Warner et al., 2021). This is illustrated in Fig. 1.2, which shows the rotation periods of the primaries as functions of their diameters. These observations indicate that there exists a "spin barrier" for the primaries and small asteroids (with diameters < 10 km) in the NEA and main belt population. This spin barrier can be modeled by a rotating strengthless sphere, which breaks up when its spin period reaches 2.2 hours (black dashed line in Fig. 1.2). Here, it is assumed that the density of the sphere is 2.2 g cm^{-3}, a value close to the estimated density of some observed asteroids (Carry, 2012). This therefore indicates that asteroid binaries in the NEA population, or small asteroids, must have little to no cohesive strength holding the structure of the asteroids together. A strengthless asteroid is also known as a "rubble pile" and can be thought of as a collection of rocks held together by gravity (illustrated in Fig. 1.3).

If a rubble pile spins fast enough, it will start to shed mass as the rapid spin rate allows the centrifugal force to overcome forces holding the asteroid together. The process of mass shedding of asteroids is known as "rotational fission" and is the most established theory that describes the formation of asteroid binaries in the NEA population and small asteroids with diameters < 10 km (Weidenschilling, 1980; Margot et al., 2002; Pravec and Harris, 2007). When a rubble pile experiences rotational fission, the shedded mass may start to accumulate to a new body that orbits the parent asteroid (Walsh and Richardson, 2006; Walsh et al., 2008), thus forming an asteroid binary system.

To achieve rotational fission, the spin rate of a rubble pile asteroid must increase. Early theories suggested that binaries among the NEAs were formed due to rotational fission induced by tidal disruptions (Richardson et al., 1998; Pravec and Harris, 2000; Margot et al., 2002). During close encounters with a planet, tidal forces induce a torque on the asteroid which may increase its spin rate. However, this type of spin-up process is not very efficient for binary formation, as Walsh and Richardson (2008) estimated that tidal disruption could only account for the existence of $1 - 2\%$ of the NEA binaries.

---

[1] Data from Johnston Archives: `https://www.johnstonsarchive.net/astro/asteroidmoons.html`, accessed on 17 February 2023.

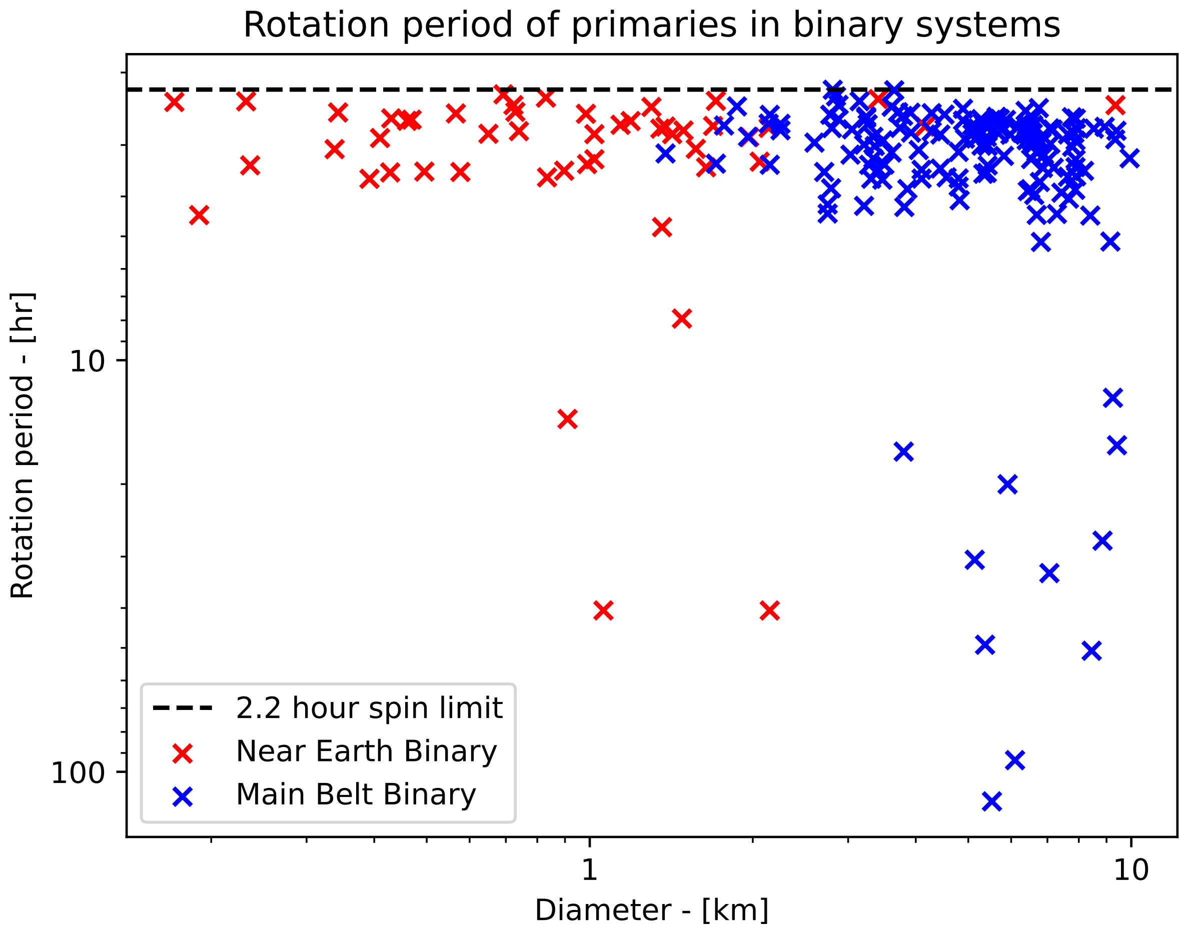

Figure 1.2: Rotation periods of the primaries, in binary systems found among NEAs and the main belt population, as functions of their diameters. Data obtained from the Asteroid Light Curve Database (Warner et al., 2021), and only data with quality code $U = 3$ are included in the figure. The figure only shows primaries with diameters smaller than 10 km. The black dashed line shows the 2.2-hour spin limit.

Moreover, NEA binaries formed by tidal disruptions generally result in more elongated primaries, while observed primaries among the NEAs have more spherical shapes (Walsh and Richardson, 2006).

The most important mechanism that spins up an asteroid, among the NEA population, is the Yarkovsky – O'Keefe – Radzievskii – Paddack effect (YORP effect) (Rubincam, 2000). When photons from the Sun reach the asteroid, the asteroid will absorb the photons and heat up on one of the sides. As the asteroid is rotating in space, different parts of the surface will experience day and night cycles. During the night cycle, the surface will emit heat which will give rise to a torque on the asteroid. Furthermore, photons carry momentum, and when they are scattered off the surface, the momentum will also be carried onto a torque on the asteroid (see Fig. 1.4). The torque induced by the YORP effect is very small, and can take a long time to build up (typically $> 10^5$ years). Moreover, the YORP effect depends on the shape of the body and is only effective for irregularly shaped bodies and bodies with low masses (Vokrouhlický et al., 2015).

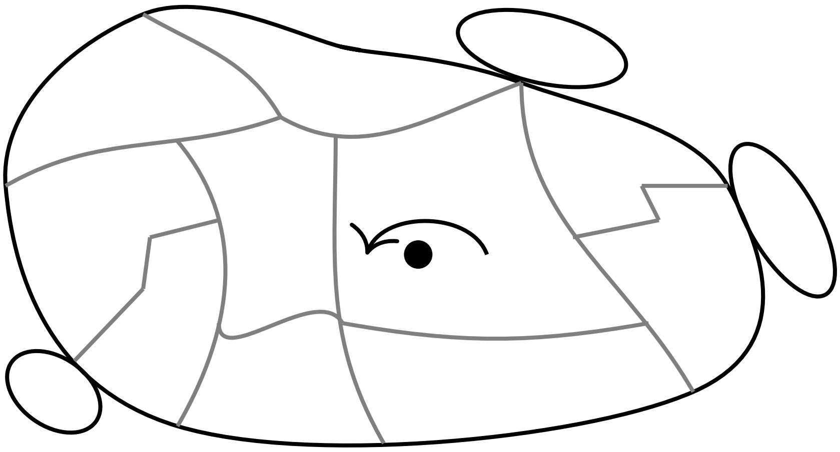

Figure 1.3: Example of a rubble pile asteroid rotating about a point (black dot). A rubble pile consists of a collection of rocks held together by gravity, and some parts may be connected loosely to the surface.

The strength of the YORP effect also depends on the distance between the sun and the asteroid. The greater the separation, the weaker the YORP effect, hence being mainly effective for asteroids in the NEA population.

An asteroid binary system may be in an energetically excited state. If the total energy of the system (sometimes called free energy) is positive, the secondary will eventually escape the gravitational pull of the primary (Scheeres, 2002, 2009), provided that energy is not lost from the system. When the secondary escapes the primary, an asteroid pair is formed. Asteroid pairs, unlike asteroid binaries, no longer orbit around each other. Instead, an asteroid pair move around the sun with similar orbits but the bodies are located in different regions of the solar system. It is believed that rotational fission, caused by YORP spin-up, is the main mechanism to form asteroid pairs among the NEAs and main belt population (Vokrouhlický and Nesvorný, 2008; Pravec et al., 2010, 2019). This is because backward integration of the orbits of observed asteroid pairs in the main belt (Pravec et al., 2010) and among the NEAs (Moskovitz et al., 2019; Fatka et al., 2022) indicate that the respective pairs have common origins.

To better understand the dynamical evolution of binary asteroids, numerical simulations are used. Jacobson and Scheeres (2011) performed a numerical study of the dynamical evolution of asteroid binaries in the NEA population. They modeled a rubble pile asteroid as a "contact binary" (see Fig. 1.5), where two asteroids are resting on each other and separate due to rotational fission (Scheeres, 2007). In addition to the gravitational force, they also included tidal forces which can contribute to energy dissipation of the system. Jacobson and Scheeres (2011) limited their study to planar dynamics for asteroids of ellipsoidal shapes, where the motion of both ellipsoids happens in the same equatorial plane. Despite restricting the study to planar dynamics, their study aided in building a complete theory on how NEA binaries evolve.

Jacobson and Scheeres (2011) used the mass ratio, defined by the mass of the secondary divided by the mass of the primary, to separate the simulations into two categories: The

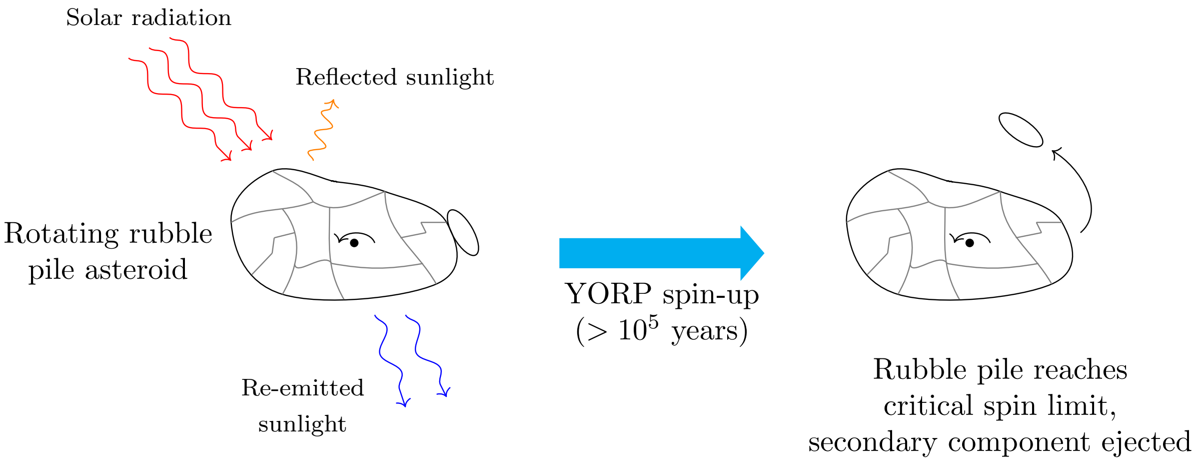

Figure 1.4: Illustration of the YORP spin-up process (following Pravec et al., 2010). The rubble pile asteroid spins up due to the YORP effect. When the rubble pile reaches a critical spin limit, the newly formed satellite is ejected, forming an asteroid binary system or an asteroid pair.

low mass ratio and high mass ratio regimes, corresponding to systems where the total energy is positive and negative, respectively. In the high mass ratio regime, the secondary remained in orbit around the primary. For low mass ratio systems, on the other hand, the additional free energy would result in the secondary escaping the primary, forming an asteroid pair. They found that the mass ratio that separated the systems with positive and negative total energies occured at approximately 0.2, but can change depending on the shapes of the bodies.

Observed binaries in the NEA population have mass ratios that are lower than 0.125 (Pravec et al., 2012, 2016). Due to their low mass ratios, these binary systems should, according to theory, result in the secondary escaping, forming an asteroid pair (Pravec et al., 2010; Jacobson and Scheeres, 2011). However, many of the observed low mass ratio binaries are in an energetically relaxed state, where the secondary cannot escape the primary. In order for a binary system to reach an energetically relaxed state, there must be a form of energy dissipation from the system. Jacobson and Scheeres (2011) found that tidal dissipation, as a form of system energy reduction, was not sufficient to prevent the secondary from escaping. They therefore introduced the concept of “secondary fission” as a mechanism to dissipate energy. Secondary fission, as the name suggests, occurs when the secondary experiences rotational fission due to its rapid spin rate. Energy is then removed from the system if this newly formed component is ejected from the binary system, or if it collides with one of the other two bodies. Jacobson and Scheeres (2011) found that secondary fission was more common as the mass ratio decreased, and never took place for binaries in the high mass ratio regime. They also showed that secondary fission can be used to explain how asteroid triples are formed, where an asteroid has two orbiting satellites. This is achieved when the newly formed component, due to secondary fission, remains in orbit around the primary.

Observations by Pravec et al. (2019) discovered some main belt asteroid pairs where one of the components is a binary. They suggest that the pair could have formed by

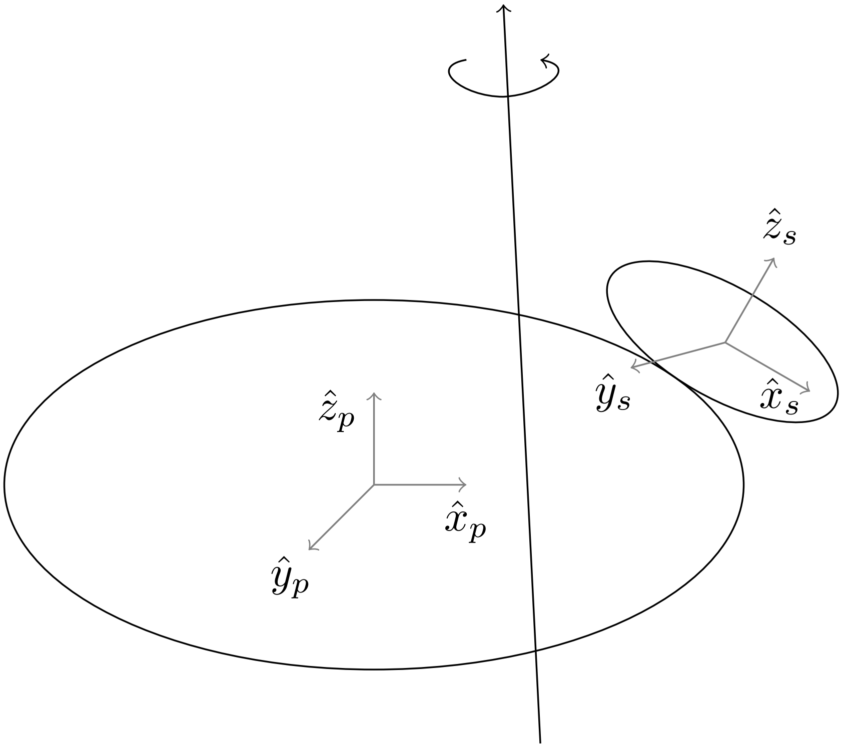

Figure 1.5: Schematic of a contact binary, which consists of two asteroids resting on each other. The contact binary rotates about the center of mass of the combined body. If the contact binary spins fast enough, the smaller component will separate from the larger one. The variables with hats correspond to the principal axes of the respective bodies.

secondary fission process as introduced by Jacobson and Scheeres (2011), where the newly formed body escapes the binary system. Pravec et al. (2019) proposed a second hypothesis for the formation of an asteroid pair with a binary component, which is through a cascade fission of the primary. This idea is similar to the one of secondary fission, but instead of a fission event on the secondary, the primary experiences rotational fission a second time. One of the satellites may then be ejected from the system, while the other satellite remains in a stable orbit around the primary. The escaped component can thus be a contributing factor in dissipating energy of the binary component.

Boldrin et al. (2016) extended on the work of Jacobson and Scheeres (2011) by including non-planar motion. They found that non-planar configurations allow escaped secondaries to obtain non-principal axis rotations (known as tumbling), which may explain how some observed NEAs have tumbling motion (Pravec et al., 2005, 2007). The non-planar configurations also allow a binary system to be in a higher energetic state, which results in the secondary escaping, and form an asteroid pair, for systems with mass ratios as high as 0.3.

Asteroid binaries and pairs, formed by rotational fission, may experience re-impact events between the two bodies (Jacobson and Scheeres, 2011; Boldrin et al., 2016; Davis and Scheeres, 2020a; Ho et al., 2022). A collision even may help dissipate energy from the binary system if the impact velocity is high enough (Walsh et al., 2008), which can prevent the secondary from escaping. However, modeling the impact physics of asteroids is a complicated task, which also restricts the knowledge of the dynamics of binary systems after the impact. Some have modeled impacts as inelastic collisions (Jacobson and Scheeres, 2011) while others terminate the simulations if the bodies intersect (Boldrin et al., 2016; Davis and Scheeres, 2020a; Ho et al., 2022). Jacobson and Scheeres (2011) found that the impact velocities are very low for collisions that occur in high mass ratio systems. The low impact velocities can allow the two components in the binary to merge and form a contact binary.

Modeling the dynamics of asteroid binaries requires one to investigate how the asteroids interact in a common mutual gravitational potential. Studying this kind of interaction between two bodies of arbitrary shapes and mass distributions is known as the full two-body problem, as both the translational and rotational motion of the bodies must be taken into account.

Solving the full two-body problem requires one to model the equations of motion of the rigid bodies, which depend on the gravitational force that act between the bodies. Mathematically, obtaining the gravitational force, **F**, is achieved by taking the gradient of the mutual gravitational potential, U, between the bodies

$$\mathbf{F} = -\nabla U. \tag{1.1}$$

The mutual potential depends on the shape of the bodies. The simplest scenario is the gravitational interaction between two spheres or two point masses. Here, the mutual potential takes the well known form

$$U = -\frac{GMm}{r}, \tag{1.2}$$

where M and m are the masses of the two bodies, r the separation between the center of masses of the bodies and G the gravitational constant.

For asteroids, however, obtaining the mutual gravitational potential is not trivial. Determining the mutual potential between two non-spherical bodies requires one to integrate over the volume of both bodies. For two extended rigid bodies, A and B, the mutual potential is determined by

$$U = -G \int\limits_A \int\limits_B \frac{1}{r} dm_A dm_B, \tag{1.3}$$

where dm_A and dm_B are mass elements of body A and B, and r the distance between them (see Fig. 1.6). The challenge with two non-spherical bodies is that there exist no analytical solution to Eq. (1.3). It is therefore common to use approximations to model the mutual potential between two asteroids. The most common approach is to expand the integrand with, e.g., spherical harmonics but the resulting mutual potential becomes inaccurate when the two bodies are close to each other.

Previous dynamical studies of asteroid binary systems, formed from rotational fission, have used approximations to model the mutual gravitational potential (Jacobson and Scheeres, 2011; Boldrin et al., 2016; Davis and Scheeres, 2020a). As the bodies are very close to each other in the early formation stages, the mutual potential obtained from approximations becomes inaccurate. This is often circumvented by ensuring that the

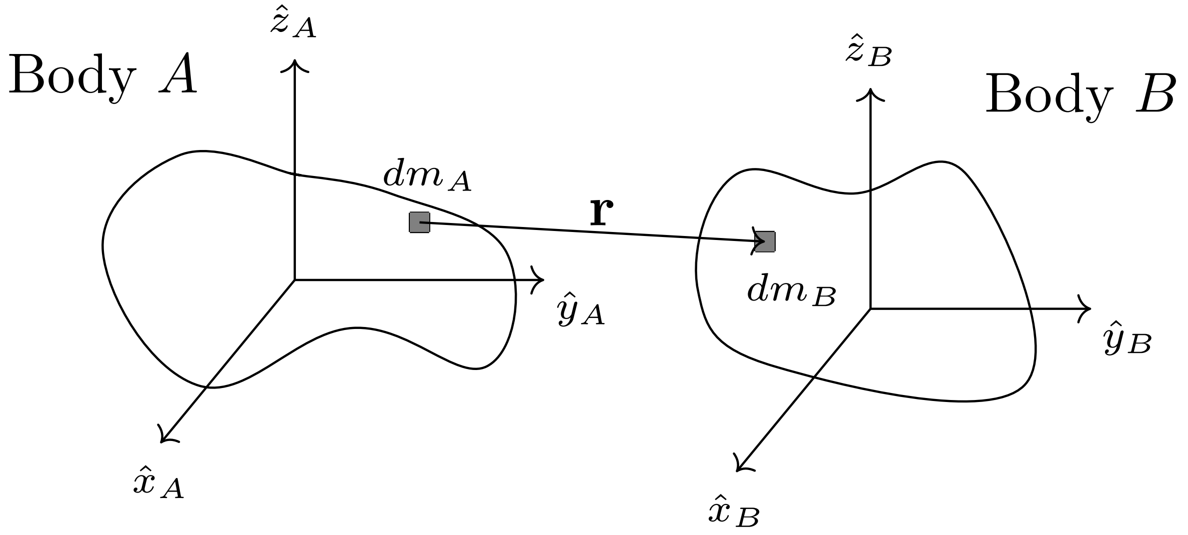

Figure 1.6: The mutual potential between two extended bodies A and B is calculated by integrating over each mass element of the respective bodies. The variables with hats correspond to the principal axes of the respective bodies.

initial separation between the bodies is large enough. However, by doing so, the initial conditions may no longer accurately represent the moment after rotational fission has occurred.

In this thesis, we determine the mutual gravitational potential with the use of surface integral as outlined by Conway (2016). One of the advantages with this method is that the resulting mutual potential is still valid even if the bodies are close to each other. This property is particularly important for binary asteroids formed from rotational fission, as it allows us to start bodies even closer compared to what has been considered in previous studies. The surface integration scheme will therefore allow us to study newly formed binary systems with more realistic initial conditions.

1.2 Objectives

The thesis aims to study the following points:

- As the surface integration method has not previously been used to study asteroid dynamics, we aim to demonstrate its viability by applying the method to study the 1999 KW4 binary system. This binary asteroid is commonly used to test methods that determine the mutual gravitational potential of asteroids, and we can therefore make comparisons in the results between the surface integration scheme and other approaches.

- Study the dynamics of asteroid binaries and pairs that are formed from rotational fission. This allows us to take full advantage of the property from the surface integration scheme, in which the resulting mutual gravitational potential is still valid even when the bodies are close to each other. This objective is aimed to expand on previous dynamical studies of asteroid binaries formed by rotational fission.

- Determine the accuracy of methods that expand the mutual gravitational potential by comparing them with the surface integration method. The goal is to study how the resulting mutual potential, gravitational force, and torque, differ between the methods when two asteroids are in close proximity and when they are far apart. We also study how these differences may affect the dynamical outcome of asteroid binaries over long time periods.

1.3 Structure of the thesis

The remaining chapters of the thesis is divided into three categories, each aimed to address the research objectives.

- **Chapter 2 - The full-two body problem**

  This chapter gives a brief overview methods that solve the full two-body problem, introduces the surface integration method and presents a demonstration of this approach.

- **Chapter 3 - Dynamics of rotationally fissioned asteroid binaries**

  In this chapter, we make full use of the advantage of the surface integration method to study the dynamics of asteroid binaries formed by rotational fission. The simulations are also compared with observations.

- **Chapter 4 - Significance of a more accurate method**

  The accuracy of a method that expands the mutual potential with inertia integrals is compared with the surface integration scheme. The significance of the choice in the mutual potential to determine the dynamics of binary asteroids is also discussed.

- **Chapter 5 - Concluding remarks**

  This chapter presents a summary of the research and potential future research directions.

Following are two appendices that briefly discuss the numerical methods used in this thesis and mathematical proofs. Finally, the research papers published in journals are appended at the end of the thesis.

1.4 Published software

The code developed in this thesis, called Surface Integral Asteroid N-Body Simulator (SIANS), is made publicly available as an open-source project in the following GitHub repository: `https://github.com/alexhosians/SIANS`. The code is mainly written in Python. However, the surface integrals are computationally demanding, and parts of the code are therefore written in C to gain a significant performance boost. The surface integrals are calculated using the QAG[2] adaptive integration algorithm from the QUADPACK implementation in the GNU Scientific Library (Galassi et al., 2002). The Runge-Kutta solvers are written in Cython for increased performance and for the convenience of calling functions written in C.

The software has been generalized as an N-body code and allows for bodies of general ellipsoidal and polyhedral shapes. However, highly detailed polyhedron shapes may require long computation times, due to the nature of the surface integrals and polyhedron potential. Furthermore, several embedded Runge-Kutta solvers have been included from the classical order four Runge-Kutta method to an order 12 method (see Appendix. A.1).

1.5 Description of the publications

The research papers produced from this thesis are described below.

Paper 1 - Extended two-body problem for rotating rigid bodies

In the first paper, the surface integration scheme outlined by Conway (2016) is implemented and tested on spheroidal and ellipsoidal bodies. The simulations involving spheroidal bodies are given in dimensionless quantities, and both bodies have equal shapes and sizes. The ellipsoidal simulation is applied to the 1999 KW4 asteroid binary system. The results are compared to other works that simulate the 1999 KW4 binary system, using different approaches to determine the mutual potential.

Published as:

A. Ho, M. Wold, J. T. Conway, M. Poursina, Extended two-body problem for rotating rigid bodies, *Celestial Mechanics and Dynamical Astronomy*, 133(8):35, August 2021. doi: 10.1007/s10569-021-10034-8

Paper 2 - Dynamics of asteroid systems post-rotational fission

The second paper studies the dynamics of asteroid binaries formed from rotational fission. We consider the dynamics of the asteroid systems the moment after a contact binary has separated due to rotational fission, similar to the work of Boldrin et al. (2016). In this work, we make use of the advantage of the surface integration method, in which the resulting mutual gravitational potential is valid even if the bodies are close to each other.

Published as:

A. Ho, M. Wold, M. Poursina, J. T. Conway, Dynamics of asteroid systems post-rotational fission. *Astronomy & Astrophysics*, 665:A43, September 2022. doi: 10.1051/0004-6361/202243706.

---

[2] QAG is the “simple adaptive integrator” in the QUADPACK library

Paper 3 - On the accuracy of mutual potential approximations in simulations of binary asteroids

Previous studies of the full two-body problem have used approximations to determine the mutual gravitational potential between two extended bodies. In the third paper, we study the accuracy of a method that expands the mutual with the use of inertia integrals. We compare the computed forces and torques between the surface integration method and the mutual potential approach by Hou et al. (2017). Different configurations are considered, including when the bodies are far apart and when the bodies are touching. The long-term effects of these differences are also studied.

Published as:

A. Ho, M. Wold, M. Poursina, J. T. Conway, The accuracy of mutual potential approximations in simulations of binary asteroids. *Astronomy & Astrophysics*, 671:A38, March 2023. doi: 10.1051/0004-6361/202245552

Chapter 2

The full two-body problem

Solving the full two-body problem (F2BP) for non-spherical bodies is often a challenge as there are no known analytical solutions to the mutual gravitational potential. In this chapter, we present a brief overview of the methods that have previously been used to model the mutual potential in order to study the F2BP. The surface integration scheme is then introduced along with a demonstration applied to the 1999 KW4 binary system, where the asteroids are modeled as triaxial ellipsoids.

2.1 The mutual gravitational potential

In the F2BP, the translational and rotational motion of the bodies are fully coupled (Maciejewski, 1995). For non-spherical bodies, the mutual gravitational potential is obtained by integrating G/r over the volume of both bodies, as given by Eq. (1.3). This volume integral cannot be solved analytically, and approximations are therefore used.

A common method to compute the mutual potential in Eq. (1.3) is to expand the scalar potential with the use of spherical harmonics. The aim is to use Legendre polynomials to perform a series expansion so that the mutual potential can be solved analytically. This eliminates the need to solve a six-dimensional integral and allows the method to become very efficient to study the F2BP (Scheeres et al., 1996; Hu and Scheeres, 2002, 2004; Tricarico and Sykes, 2010; Boldrin et al., 2016; Boué, 2017; Feng and Hou, 2017). However, one drawback of this approach is that the solution is only valid for points outside the bounding sphere around the body, which is the smallest sphere that covers the circumference of the body, also known as the Brillouin sphere (Moritz, 1980). Furthermore, as the mutual potential is expressed as a power series, higher-order terms are often excluded, which gives rise to truncation errors in the mutual potential.

Paul (1988) presents a different approach to determine the mutual potential, where the six-dimensional volume integral in Eq. (1.3) is converted to six open summations. This is extended by Tricarico (2008) to apply to bodies of arbitrary shapes and mass distribution. The mass distribution, using this scheme, is described with inertia integrals. This method is further improved by Hou et al. (2017), who, through the use of recursive relations, reduce the six summations down to a single summation, making the method more computationally efficient. However, the inertia integrals are analogous to spherical harmonics, where the former expresses the potential with cartesian coordinates and the latter is expressed in spherical coordinates. As a consequence, the mutual potential determined by expanding inertia integrals suffers from divergences when the bodies are close. Tricarico (2008) shows that the mutual potential, using this approach, is only valid for points outside the bounding spheres of the two bodies, provided that the two bounding spheres do not intersect.

The mutual potential of an arbitrarily shaped asteroid can also be modeled with high precision with the use of a polyhedron (Werner and Scheeres, 2005; Fahnestock and Scheeres, 2006; Scheeres et al., 2006; Fahnestock and Scheeres, 2008; Hirabayashi and Scheeres, 2013). This approach can generate more realistic simulations if the shape models are accurate. However, determining the mutual potential of asteroids with polyhedral shapes is computationally expensive, and increasing the number of faces of the polyhedrons significantly increases the computation time.

Other methods are also used to determine the mutual potential of bodies of arbitrary shapes. Compère and Lemaître (2014) make use of the symmetric and trace-free tensor formalism to determine the coupling between spherical harmonics, which allows for the mutual potential to be expressed in a compact way. Yu et al. (2019) use the finite element method to determine the mutual potential, which can be applied to complex body shapes, such as concave shapes. This approach is also capable of modeling bodies with varying bulk densities. However, this method is computationally demanding. Gao et al. (2022) develop a new approach to increase the efficiency of the mutual potential formulation of Yu et al. (2019).

Detailed shape models for asteroids are often not available due to observational constraints. It is therefore common to approximate asteroids as triaxial ellipsoids to study their dynamics (Scheeres, 2004, 2007; Bellerose and Scheeres, 2008; Scheeres, 2009; Boldrin et al., 2016; Ho et al., 2022). However, because elliptic integrals are involved, determining an ellipsoid potential can be computationally expensive for long dynamical simulations. Furthermore, asteroids in nature are not perfect ellipsoids, and simulations with ellipsoidal shapes may be less accurate compared to methods that model the body shapes with higher precision, such as a polyhedron.

2.2 Surface integration method

With the use of vector potentials, Conway (2016) introduced a new approach to compute the mutual potential of two extended non-spherical bodies with the use of surface integrals. For bodies of ellipsoidal shapes, this method is exact as no series expansions are utilized, and therefore the results do not suffer from truncation errors. The surface integration approach was first demonstrated by Wold and Conway (2021), who studied the co-planar motion of two spheroids and two thin disks. This was later extended by Ho et al. (2021) to include non-planar effects for spheroids and ellipsoids. This is, to our knowledge, the first solution of the F2BP for two ellipsoids without using approximations.

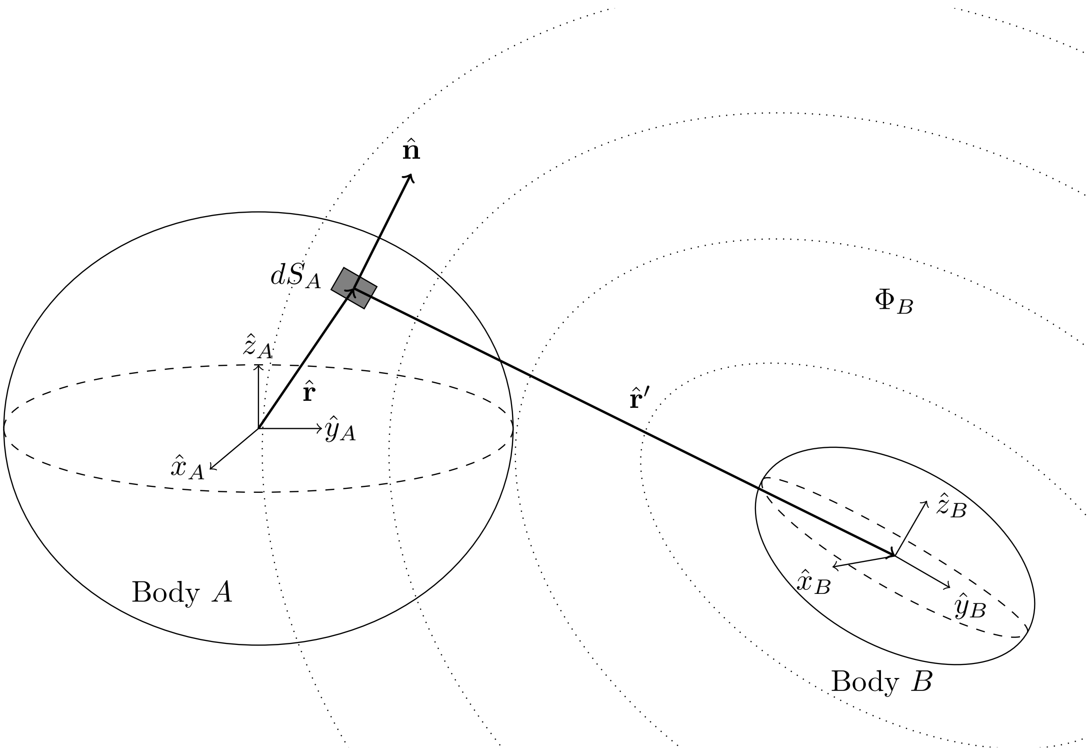

Figure 2.1: Illustration of the surface integration scheme. The left body is being integrated over its surface element dS_A in the potential field Φ_B (dotted lines) of the body to the right.

2.2.1 Surface integrals

Throughout the rest of the thesis, all vector variables with a hat represent the vector in the body-fixed frame, while vectors without a hat correspond to the (global) inertial frame.

The force on an extended body A with constant density ρ_A due to an external gravitational field $\mathbf{g}_B$ can be expressed by integrating over the volume of body A

$$\hat{\mathbf{F}}_A = \rho_A \iiint\limits_{V_A} \mathbf{g}_B(\hat{\mathbf{r}}')dV_A, \tag{2.1}$$

where dV_A is the volume element of body A. The vector $\hat{\mathbf{r}}'$ is the vector from the surface of body A to the mass center of body B (see Fig. 2.1).

Because the gravitational field is given by the gradient of a scalar potential Φ_B, i.e. $\mathbf{g}_B = \nabla\Phi_B$, we can apply the divergence theorem (also known as Gauss' theorem), converting the volume integral to the following surface integral

$$\hat{\mathbf{F}}_A = \rho_A \iint\limits_{S_A} \Phi_B(\hat{\mathbf{r}}')\hat{\mathbf{n}}dS_A, \tag{2.2}$$

where dS_A the surface element, and $\hat{\mathbf{n}}$ is a unit normal to the surface of body A. These parameters are illustrated in Fig. 2.1.

The torque acting on body A can also be expressed with a volume integral

$$\hat{\mathbf{M}}_A = \rho_A \iiint\limits_{V_A} \hat{\mathbf{r}} \times \mathbf{g}_B(\hat{\mathbf{r}}')dV_A. \tag{2.3}$$

To convert this volume integral to a surface integral with the divergence theorem, a vector potential $\mathbf{V}$ is required that satisfies $\nabla \times \mathbf{V} = \mathbf{r} \times \mathbf{g}$. Conway (2016) introduced two vector potentials that satisfy this constraint:

$$\mathbf{V}_1 = -\hat{\mathbf{r}}\Phi_B \tag{2.4}$$

$$\mathbf{V}_2 = \frac{1}{2}|\hat{\mathbf{r}}|^2\mathbf{g}_B. \tag{2.5}$$

Substituting these expressions into Eq. (2.3) and applying the divergence theorem results in two equivalent surface integrals for the torque

$$\hat{\mathbf{M}}_A = -\rho_A \iint\limits_{S_A} \Phi_B(\hat{\mathbf{r}}')\hat{\mathbf{n}} \times \hat{\mathbf{r}}dS_A \tag{2.6}$$

$$\hat{\mathbf{M}}_A = \frac{\rho_A}{2} \iint\limits_{S_A} |\hat{\mathbf{r}}|^2\hat{\mathbf{n}} \times \mathbf{g}_B(\hat{\mathbf{r}}')dS_A. \tag{2.7}$$

The mutual potential from Eq. (1.3) can also be expressed as a volume integral. By integrating over the volume of one of the bodies, such as body B, the six-dimensional integral is reduced to the following volume integral

$$U = \rho_A \iiint\limits_{V_A} \Phi_B(\hat{\mathbf{r}}')dV_A, \tag{2.8}$$

Conway (2016) showed that a combination of $\mathbf{V}_1$ and $\mathbf{V}_2$ gives rise to a third vector potential that also satisfy the constraint $\nabla \times \mathbf{V} = \mathbf{r} \times \mathbf{g}$:

$$\mathbf{V}_3 = \frac{1}{2}(\mathbf{V}_1 + \mathbf{V}_2). \tag{2.9}$$

Using the expression of $\mathbf{V}_3$ and applying the divergence theorem on Eq. (2.8) results in

$$U = \frac{\rho_A}{3} \iint\limits_{S_A} \left(\hat{\mathbf{r}}\Phi_B(\hat{\mathbf{r}}') - \frac{1}{2}\left|\hat{\mathbf{r}}\right|^2 \mathbf{g}_B\left(\hat{\mathbf{r}}'\right)\right) \cdot \hat{\mathbf{n}}dS_A. \tag{2.10}$$

The above surface integrals given by Eqs. (2.2), (2.6), and (2.10) are thus alternative expressions for the force, torque, and mutual potential energy between two non-spherical bodies.

One advantage of the surface integration method, unlike methods that model the mutual potential with series expansions (e.g. with inertia integrals), is that the mutual potential is valid even when the bounding spheres around each body overlap. Furthermore, for ellipsoids, the gravitational potential can be expressed analytically. The resulting forces, torques, and mutual potential energy are therefore mathematically exact for ellipsoids using this scheme. Moreover, an M-dimensional integral scales as K^M, where K is the number of evaluations required for the integral to reach a desired accuracy. Reducing the three-dimensional volume integrals down to two-dimensional surface integrals therefore reduces the computation time required to calculate the force, torque, and mutual potential energy.

A drawback with this method is the computational efficiency. Compared to other methods, e.g. expanding the mutual potential with spherical harmonics or inertia integrals, the surface integration scheme is time-consuming as multiple surface integrals are evaluated at every time step when the equations of motions are solved. Despite this, the surface integration method is still less computationally demanding compared to the corresponding volume integrals.

2.2.2 Coordinate transformation

The forces, torques, and the mutual potential energy computed with the surface integrals are most conveniently performed in the body-fixed frames of each respective body. However, the equations of the gravitational potential Φ are often derived assuming that the body exerting the potential is located at the origin of the coordinate system. It is therefore necessary to transform the gravitational potential in the frame of reference of the integrated body. If the surface integration method is performed over body A, the coordinate transformation is given by

$$\hat{\mathbf{r}}' = \mathcal{R}_B^T \left(\mathcal{R}_A \hat{\mathbf{r}} - \mathbf{r}_c \right), \tag{2.11}$$

where $\mathcal{R}_A$ and $\mathcal{R}_B$ are the rotation matrices of body A and B respectively, the superscript T denotes the transpose, $\mathbf{r}_c$ is the separation vector between the two centroids, and $\hat{\mathbf{r}}$ is the vector from the mass center of the integrated body to its surface. The vector $\hat{\mathbf{r}}'$ is then the input vector used as arguments in the gravitational potential and gravitational fields during the surface integration. Figure 2.2 shows an illustration of the vectors used.

Similarly for the gravitational field, which is required to compute the mutual potential energy given by Eq. (2.10), it can be expressed in the body-fixed frame of the integrated body as (Ho et al., 2021)

$$\hat{\mathbf{g}}_B^{(A)}(\hat{\mathbf{r}}') = \mathcal{R}_A^T \mathcal{R}_B \hat{\mathbf{g}}_B(\hat{\mathbf{r}}'), \tag{2.12}$$

where the superscript (A) denotes the vector expressed in the body-fixed frame of body A.

2.2.3 Demonstration with ellipsoids

An ellipsoid is commonly used to represent the shape of an asteroid. We therefore consider ellipsoidal shapes for our asteroids to demonstrate the surface integration method.

2.2.4 Ellipsoid surface integration

The parametrization required to determine the surface normal vector $\hat{\mathbf{n}}$ and integration limits for Eqs. (2.2), (2.6), and (2.10) can take different forms depending on the shape of

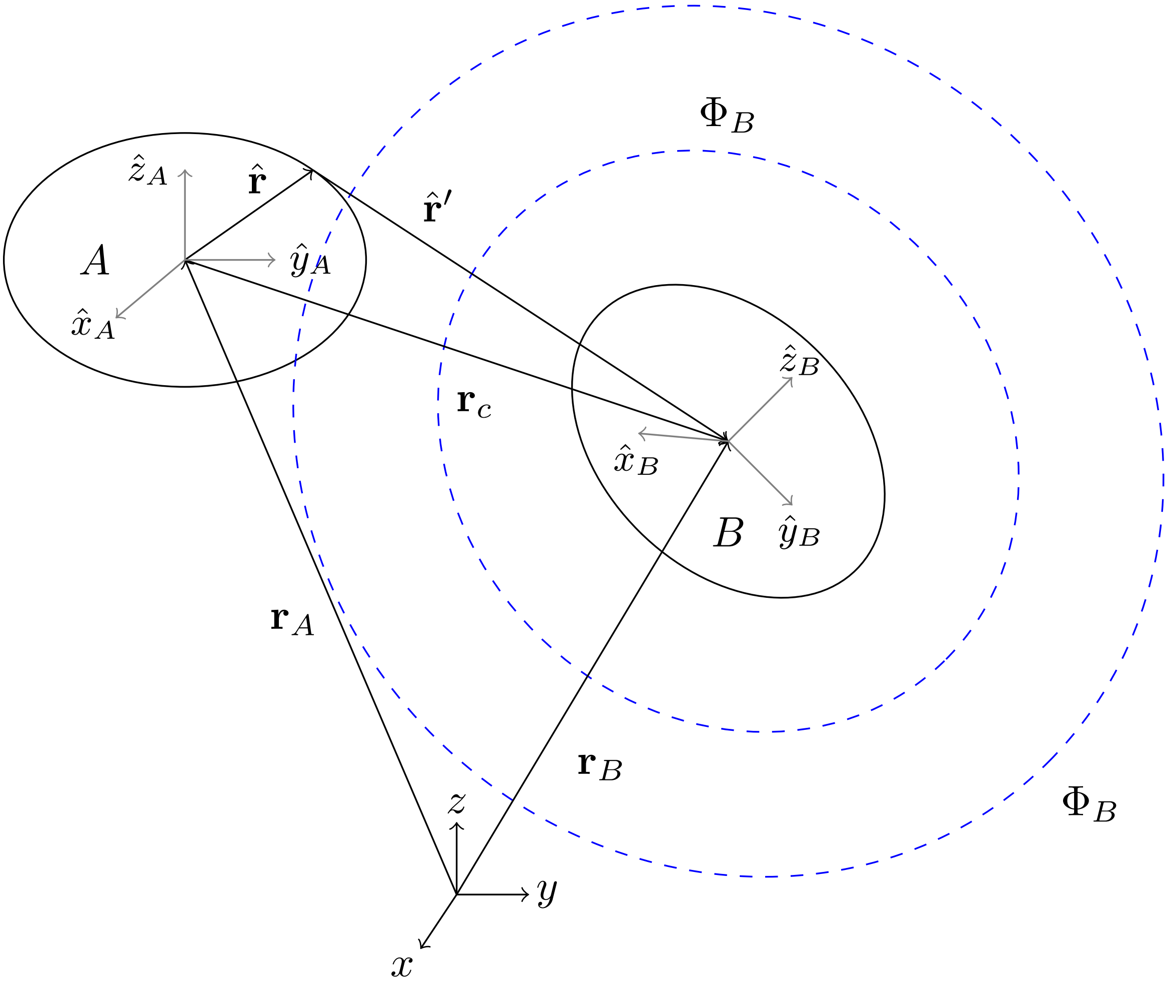

Figure 2.2: Illustration of the vectors used to calculate the gravitational potential Φ_B of body B in the reference frame of the body that the surface integration is performed on (body A). The blue dashed lines correspond to gravitational potential Φ_B. The hat notation of the vectors corresponds to the vectors expressed in the body-fixed frame.

the body. For a general ellipsoid with semiaxes where a, b, c (corresponding to the long, intermediate, and short semiaxes), the surface parametrization take simple expressions (Wold and Conway, 2021; Ho et al., 2021).

To integrate over the surface of ellipsoid A in Fig. 2.1, we utilize the equation for an ellipse

$$\left(\frac{x}{a}\right)^2 + \left(\frac{y}{b}\right)^2 + \left(\frac{z}{c}\right)^2 = 1. \tag{2.13}$$

By introducing the following quantities (Wold and Conway, 2021)

$$a' = \frac{a}{c}\sqrt{c^2 - z^2} \tag{2.14}$$

$$b' = \frac{b}{c}\sqrt{c^2 - z^2}, \tag{2.15}$$

$$\tag{2.16}$$

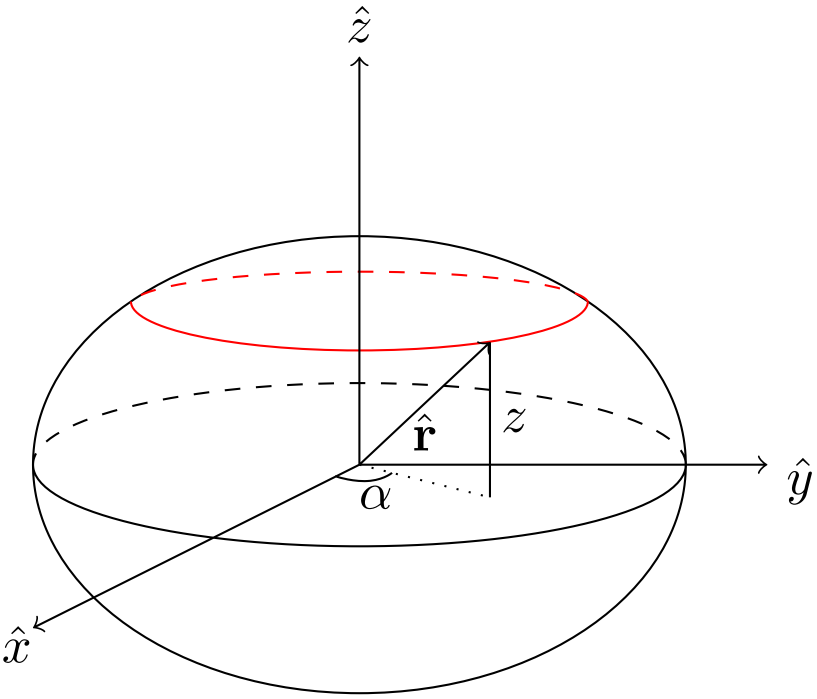

Figure 2.3: Illustration of how the ellipsoid surface is parametrized through ellipses (marked in red).

we can rewrite Eq. (2.13) to

$$\left(\frac{x}{a'}\right)^2 + \left(\frac{y}{b'}\right)^2 = 1. \tag{2.17}$$

This equation parametrizes the surface of the ellipsoid through many ellipses for each constant value of z, each resulting in an ellipse in terms of the azimuthal angle α (see Fig. 2.3)

$$x = a' \cos(\alpha) \tag{2.18}$$

$$y = b' \sin(\alpha) \tag{2.19}$$

so that

$$\hat{\mathbf{r}} = \begin{bmatrix} a' \cos(\alpha) \\ b' \sin(\alpha) \\ z \end{bmatrix}. \tag{2.20}$$

To determine the surface element and surface normal $\hat{\mathbf{n}}dS$, we need to find infinitesimal displacements along the ellipsoid surface along a constant z and α. It can be shown that (Wold and Conway, 2021)

$$\hat{\mathbf{n}}dS = \begin{bmatrix} b' \cos(\alpha) \\ a' \sin(\alpha) \\ \frac{ab}{c^2} z \end{bmatrix} d\alpha dz. \tag{2.21}$$

2.2.4.1 Ellipsoid potential

For a general ellipsoid with semiaxes $a > b > c$, and constant density ρ, the gravitational potential at an exterior position $\mathbf{r} = [x, y, z]$ is expressed as (MacMillan, 1930)

$$\begin{aligned}\Phi(\mathbf{r}) = \frac{2\pi G\rho abc}{\sqrt{a^2-c^2}}\Bigg(&\left[1 - \frac{x^2}{a^2-b^2} + \frac{y^2}{a^2-b^2}\right] F(\omega_\kappa, k) \\ &+ \left[\frac{x^2}{a^2-b^2} - \frac{(a^2-c^2)y^2}{(a^2-b^2)(b^2-c^2)} + \frac{z^2}{b^2-c^2}\right] E(\omega_\kappa, k) \\ &+ \left[\frac{c^2+\kappa}{b^2-c^2}y^2 - \frac{b^2+\kappa}{b^2-c^2}z^2\right] \frac{\sqrt{a^2-c^2}}{\sqrt{(a^2+\kappa)(b^2+\kappa)(c^2+\kappa)}}\Bigg).\end{aligned} \tag{2.22}$$

The gravitational potential of a spheroid can be determined by setting $a = b$, in which Φ takes a simpler form (see MacMillan, 1930, for details).

In Eq. (2.22), $F(\omega_\kappa, k)$ and $E(\omega_\kappa, k)$ are the incomplete elliptic integrals of the first and second kind, respectively

$$F(\omega_\kappa, k) = \int_0^{\omega_\kappa} \frac{d\alpha}{\sqrt{a - k^2 \sin^2(\alpha)}} \tag{2.23}$$

$$E(\omega_\kappa, k) = \int_0^{\omega_\kappa} \sqrt{1 - k^2 \sin^2(\alpha)} d\alpha, \tag{2.24}$$

where

$$\omega_\kappa = \sin^{-1}\sqrt{\frac{a^2-c^2}{a^2+\kappa}} \tag{2.25}$$

$$k = \sqrt{\frac{a^2-b^2}{a^2-c^2}}, \tag{2.26}$$

and κ is the largest real root of the equation

$$\frac{x^2}{a^2+\kappa} + \frac{y^2}{b^2+\kappa} + \frac{z^2}{c^2+\kappa} = 1. \tag{2.27}$$

The components of the gravitational field $\mathbf{g} = \nabla\Phi$ become

$$g_x = \frac{4x\pi G\rho abc}{\sqrt{a^2-c^2}} \frac{E(\omega_\kappa, k) - F(\omega_\kappa, k)}{a^2-b^2} \tag{2.28}$$

$$\begin{aligned}g_y = \frac{4y\pi G\rho abc}{\sqrt{a^2-c^2}}\Bigg[&\frac{F(\omega_\kappa, k)}{a^2-b^2} - \frac{(a^2-c^2)E(\omega_\kappa, k)}{(a^2-b^2)(b^2-c^2)} \\ &+ \frac{(c^2+\kappa)}{b^2-c^2}\frac{\sqrt{a^2-c^2}}{\sqrt{(a^2+\kappa)(b^2+\kappa)(c^2+\kappa)}}\Bigg]\end{aligned} \tag{2.29}$$

$$g_z = \frac{4z\pi G\rho abc}{\sqrt{a^2-c^2}}\left[\frac{E(\omega_\kappa, k)}{b^2-c^2} - \frac{(b^2+\kappa)}{b^2-c^2}\frac{\sqrt{a^2-c^2}}{\sqrt{(a^2+\kappa)(b^2+\kappa)(c^2+\kappa)}}\right]. \tag{2.30}$$

Despite being a function of x, y and z, the variable κ is treated as constant when the partial derivatives are taken. This is because the terms involving the derivative of κ cancel out (MacMillan, 1930).

2.3 Equations of motion

We solve the equations of motion in an inertial frame. For a two-body problem, when the gravitational force is computed on body A, the corresponding force on the other body B can be determined by Newton's third law

$$\mathbf{F}_A = -\mathbf{F}_B. \tag{2.31}$$

However, the forces computed using the surface integration scheme are given in the body-fixed frame of the body whose surface is integrated over. Projecting the force back to the inertial frame, assuming that the surface integration scheme is performed on body A, is achieved by

$$\mathbf{F}_A = \mathcal{R}_A \hat{\mathbf{F}}_A \tag{2.32}$$

where $\mathcal{R}_A$ is the rotation matrix of body A. The velocities $\mathbf{v}$ and positions $\mathbf{r}$ are integrated as

$$\frac{d\mathbf{v}}{dt} = \frac{\mathbf{F}}{m} \tag{2.33}$$

$$\frac{d\mathbf{r}}{dt} = \mathbf{v} \tag{2.34}$$

where m is the mass of the body.

For two non-spherical bodies, the gravitational force will induce torques on both bodies. The torques computed in the inertial frame are equal and opposite, i.e. $\mathbf{M}_A = -\mathbf{M}_B$, which is a consequence of angular momentum conservation. However, this may not necessarily be the case for the torques calculated in the body-fixed frames. As a result, the torques must be computed for each body separately. Furthermore, because the torques are computed in the body-fixed frames, it is convenient to also work with the angular velocities in the body-fixed frames. The angular velocities are integrated as

$$\mathcal{I}\frac{d\hat{\boldsymbol{\omega}}}{dt} + (\hat{\boldsymbol{\omega}} \times \mathcal{I}\hat{\boldsymbol{\omega}}) = \hat{\mathbf{M}} \tag{2.35}$$

where $\mathcal{I}$ is the inertia tensor and $\hat{\boldsymbol{\omega}}$ the body-fixed angular velocity of the body. For an ellipsoid, the inertia tensor can be expressed analytically, and only the diagonal components are non-zero, and given by

$$\mathcal{I}_{xx} = \frac{4\pi\rho abc}{15}(b^2 + c^2) \tag{2.36}$$

$$\mathcal{I}_{yy} = \frac{4\pi\rho abc}{15}(a^2 + c^2) \tag{2.37}$$

$$\mathcal{I}_{zz} = \frac{4\pi\rho abc}{15}(a^2 + b^2). \tag{2.38}$$

The equations of motions in Eqs. (2.33), (2.34), and (2.35) are solved as a standard initial value problem with the use of a Runge-Kutta method.

2.3.1 Tait-Bryan angles

Solving the rotational equations of motion for the bodies can be conveniently performed through the use of Tait-Bryan angles, ϕ, θ, ψ, which describe rotations about x, y, z- axes respectively. The rotation matrix, using this convention, is

$$\mathcal{R} = \mathcal{R}_z \mathcal{R}_y \mathcal{R}_x, \tag{2.39}$$

where

$$\mathcal{R}_x = \begin{bmatrix} 1 & 0 & 0 \\ 0 & \cos\phi & -\sin\phi \\ 0 & \sin\phi & \cos\phi \end{bmatrix} \tag{2.40}$$

$$\mathcal{R}_y = \begin{bmatrix} \cos\theta & 0 & \sin\theta \\ 0 & 1 & 0 \\ -\sin\theta & 0 & \cos\theta \end{bmatrix} \tag{2.41}$$

$$\mathcal{R}_z = \begin{bmatrix} \cos\psi & -\sin\psi & 0 \\ \sin\psi & \cos\psi & 0 \\ 0 & 0 & 1 \end{bmatrix}. \tag{2.42}$$

Figure 2.4 shows an example of the rotation ordering using the Tait-Bryan convention.

The equations of motion that describe the change of the angles over time, using the Tait-Bryan convention, are given as

$$\frac{d\phi}{dt} = \hat{\omega}_x + (\hat{\omega}_y \sin\phi + \hat{\omega}_z \cos\phi)\tan\theta \tag{2.43}$$

$$\frac{d\theta}{dt} = \hat{\omega}_y \cos\phi - \hat{\omega}_z \sin\phi \tag{2.44}$$

$$\frac{d\psi}{dt} = (\hat{\omega}_y \sin\phi + \hat{\omega}_z \cos\phi)\sec\theta \tag{2.45}$$

(Fossen, 2011).

An issue that may arise when Tait-Bryan angles are used is that singularities may occur in the equations of motion. Equations (2.43) and (2.45) contain singularities when $\theta = n\pi/2$ for any non-zero integer n. Near these singularities, the simulations may show non-physical behavior in the rotational motion. It may therefore be more beneficial to use other conventions to determine the rotational motion, such as Euler parameters.

One of the demonstrations, of the surface integration method, by Ho et al. (2021) showed that the rotation angle θ of one of the bodies approached 90 degrees. This was initially a concern, as the singularity may result in odd physical behaviors to the body. However, upon closer inspection, the particular body did not show any non-physical motion (e.g. sudden turns in the rotational state).

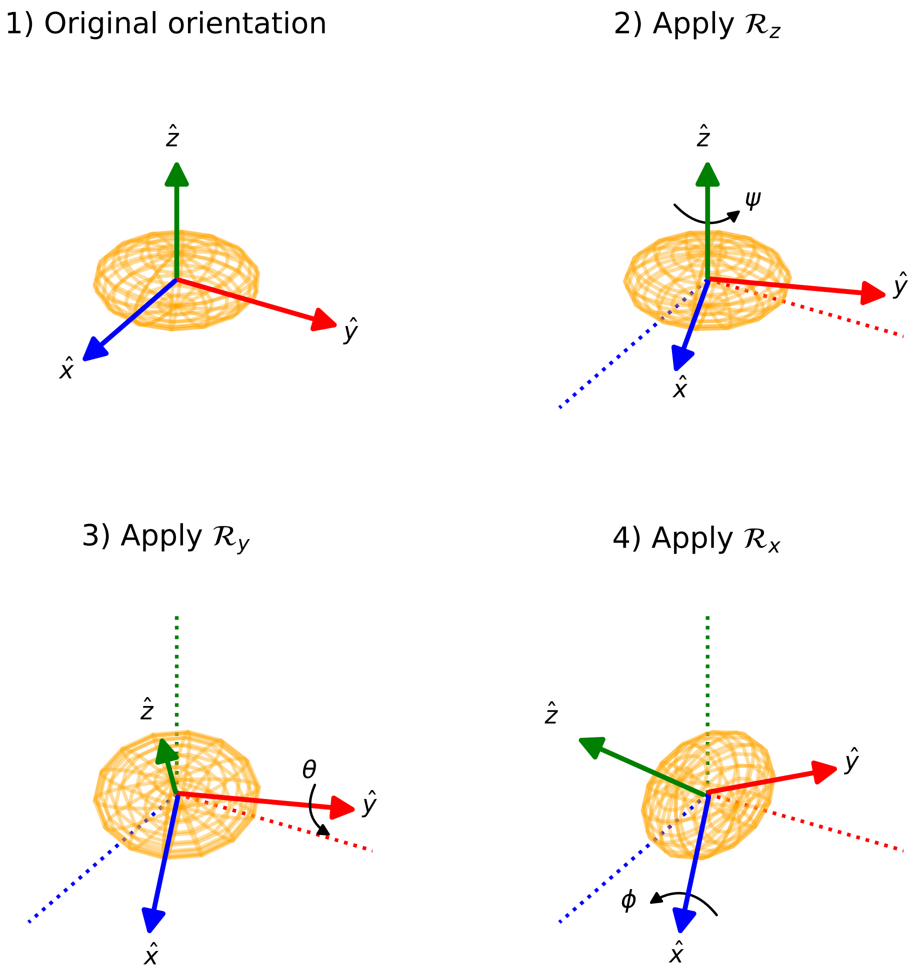

Figure 2.4: Rotation ordering using Tait-Bryan angles. The rotation matrix is defined by first rotating around the body-fixed z-axis (change of ψ), then around the body-fixed y-axis (change of θ), and finally around the body-fixed x-axis (change of ϕ). The dotted lines indicate the axis of the initial orientation.

2.3.2 Euler parameters

The Tait-Bryan convention may not be an optimal choice to describe the rotational motion, due to the singularities mentioned in the previous section. The Euler parameters (e_0, e_1, e_2, e_3) is a different convention that avoids the singularities associated with the Tait-Bryan angles. The rotation matrix for the Euler parameter convention is

$$\mathcal{R} = 2 \begin{bmatrix} e_0^2 + e_1^2 - \frac{1}{2} & e_1e_2 - e_0e_3 & e_1e_3 + e_0e_2 \\ e_1e_2 + e_0e_3 & e_0^2 + e_2^2 - \frac{1}{2} & e_2e_3 - e_0e_1 \\ e_1e_3 - e_0e_2 & e_2e_3 + e_0e_1 & e_0^2 + e_3^2 - \frac{1}{2} \end{bmatrix} \tag{2.46}$$

(Kane et al., 1983). The Euler parameters have the following constraint that must always be satisfied

$$e_0^2 + e_1^2 + e_2^2 + e_3^2 - 1 = 0. \tag{2.47}$$

Finally, the equations of motion to time step the Euler parameters are

$$\frac{de_0}{dt} = \frac{1}{2}\left(-e_1\hat{\omega}_x - e_2\hat{\omega}_y - e_3\hat{\omega}_z\right) \tag{2.48}$$

$$\frac{de_1}{dt} = \frac{1}{2}\left(e_0\hat{\omega}_x - e_3\hat{\omega}_y + e_2\hat{\omega}_z\right) \tag{2.49}$$

$$\frac{de_2}{dt} = \frac{1}{2}\left(e_3\hat{\omega}_x + e_0\hat{\omega}_y - e_1\hat{\omega}_z\right) \tag{2.50}$$

$$\frac{de_3}{dt} = \frac{1}{2}\left(-e_2\hat{\omega}_x + e_1\hat{\omega}_y + e_0\hat{\omega}_z\right). \tag{2.51}$$

2.3.3 Collision condition

The ellipsoidal potential given by Eq. (2.22) is only valid exterior to the body. If the bodies intersect, the surface integration method will calculate the gravitational potential at the interior, which may result in singularities. To prevent this from causing issues to the equations of motion, a collision condition is imposed when the ellipsoids intersect at any time step, in which the simulation terminates. The ellipsoid intersection algorithm is described in Appendix A.2.

Another reason to terminate the simulation when a collision occurs is the complexity of modeling the impact between the bodies. Modeling the fragments created by the impact is beyond the scope of this thesis. It is possible to model the impact as fully elastic, but the results post-collision would not be realistic as some of the energy should be converted to e.g. sound or deformation of the bodies.

2.3.4 Results from the surface integration method

The surface integration scheme for non-planar motion is demonstrated in the first paper of this thesis (Ho et al., 2021). The order 9(8) Runge-Kutta method by Verner (2010), with adaptive step-sizing, is used to solve the equations of motion. Because we consider a closed system, the total energy and total angular momentum of the system are conserved. We therefore measure the accuracy of the surface integration method by examining how the total energy and total angular momentum are conserved in the simulations.

Both spheroidal and ellipsoidal shapes are considered for dimensionless test simulations and also applied to simulate the binary system 1999 KW4 (Moshup and its satellite Squannit), which is a system commonly used to test methods that determine the mutual potential in the F2BP (Fahnestock and Scheeres, 2008; Compère and Lemaître, 2014; Hou et al., 2017; Shi et al., 2017). The 1999 KW4 simulations, using the surface integration method, are performed with two separate test cases. In one test simulation, both bodies are modeled as spheroids, while the second simulation modeled both bodies as ellipsoids. For both scenarios, the errors in the total energy and total angular momentum, relative to the first time step, in the simulations are smaller than 10^{-15} and 10^{-11} respectively. Figure 2.5 illustrates the conserved quantities of the ellipsoid simulation. It should be noted that the small errors in both the total energy and total angular momentum are also caused by the choice in the Runge-Kutta solver and using a lower-order Runge-Kutta method can increase the errors.

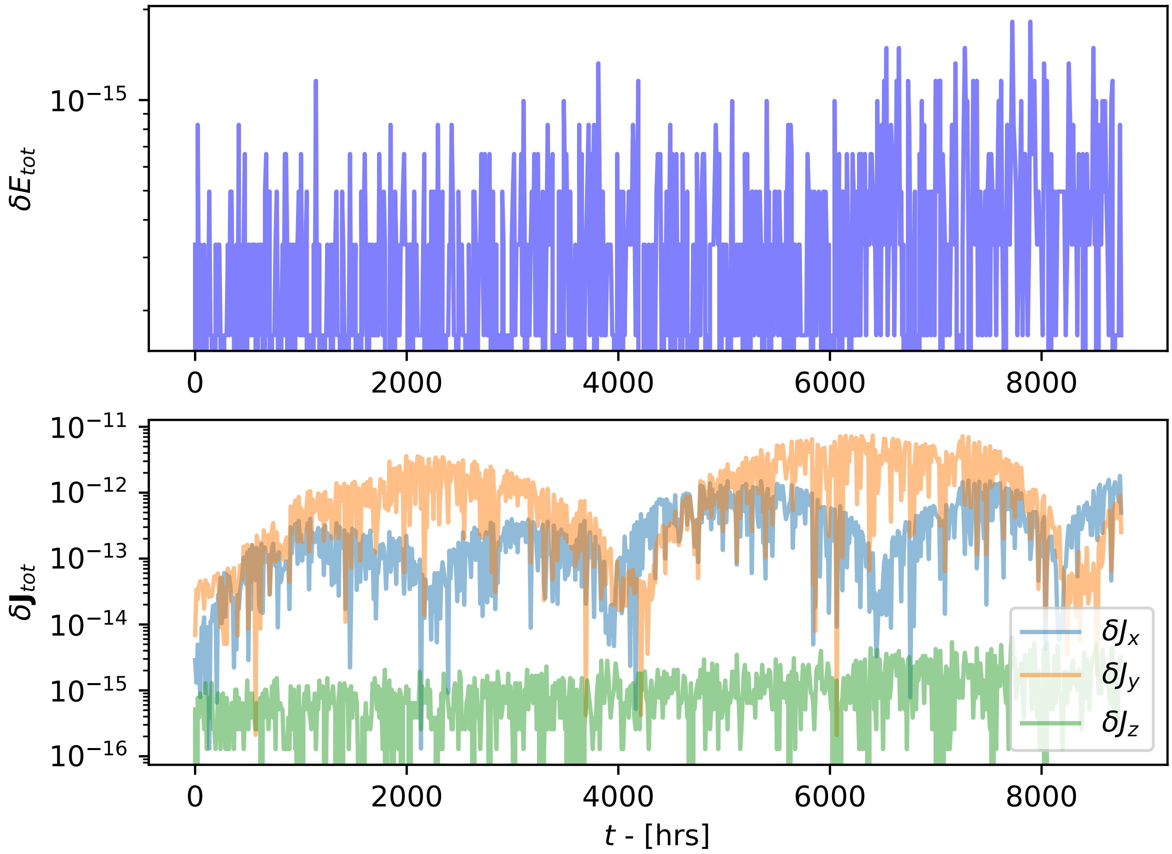

Figure 2.5: Accuracy of the surface integration, with data of the ellipsoid simulations from Ho et al. (2021). The top row shows the relative error in the total energy, while the bottom row shows the relative error in the total angular momentum components.

2.3.5 Computation time comparisons

Because we consider bodies of ellipsoidal shapes, the surface integration scheme yields exact values of the gravitational forces, torques, and mutual potential energies. However, a drawback is increased computation times. Methods that expand the mutual potential seldom require solving a large number of integrals, while the surface integration scheme must solve multiple two-dimensional integrals at every time step. We therefore expect higher computation times from the surface integration method compared to other approaches.

Previous studies have simulated the 1999 KW4 system with integration times of 200 hours. Here, we briefly compare the computation times from previous work with the surface integration scheme applied to the same system. The computation times are summarized in Table 2.1.

The approach by Compère and Lemaître (2014) is very efficient when the mutual gravitational potential is truncated to order two, in which the simulation completes in a few seconds. However, the simulation times, using their approach, increase significantly when higher orders are considered. Simulations performed by Hou et al. (2017) are even faster, using 0.2 seconds to complete the simulations when the mutual potential is truncated to order two, and 206 seconds with an order nine potential. The method by Shi et al.

Method	Computation time	Integrator
Compère and Lemaître (2014) (order 2)	few seconds	Bulirsch–Stoer
Compère and Lemaître (2014) (order 4)	4 hours	Bulirsch–Stoer
Compère and Lemaître (2014) (order 6)	36 days	Bulirsch–Stoer
Hou et al. (2017) (order 2)	0.2 seconds	RK-Fehlberg 7(8)
Hou et al. (2017) (order 4)	2.1 seconds	RK-Fehlberg 7(8)
Hou et al. (2017) (order 9)	206 seconds	RK-Fehlberg 7(8)
Shi et al. (2017) (order 2)	460 seconds	RK-Fehlberg 4(5)
Surface integration method	263 seconds	RK-Verner 9(8)

Table 2.1: The simulation times of the 1999 KW4 system, with integration times of 200 hours, from different methods (with different expansion orders). The right-most column shows the integrator used to solve the equations of motion, and RK is the acronym for Runge-Kutta. All methods except for Hou et al. (2017) make use of adaptive time stepping.

(2017), however, is slower than the other two approaches, even at the lowest order which completes the simulation in 460 seconds. Finally, the 1999 KW4 simulation performed with the surface integration scheme finishes in 263 seconds.

It is important to note that we, and also Hou et al. (2017), model the asteroids as ellipsoids, while Compère and Lemaître (2014) and Shi et al. (2017) consider polyhedral asteroid shapes. A polyhedron can accurately represent the shape of the asteroid and thus result in more realistic simulations. However, determining the mutual potential of polyhedral shapes is far more computationally demanding compared to that of ellipsoids. Therefore, it is more reasonable to compare the surface integration method with the results of Hou et al. (2017). If we were to use the surface integration method for polyhedral shapes, the simulation times are expected to increase significantly.

Agrusa et al. (2020) benchmarked four different mutual potential approaches to simulate the (65803) Didymos binary system. They find that the methodology by Hou et al. (2017) is sufficient to describe the dynamics of the Didymos-Dimorphos binary system when the mutual potential is truncated to order four. As shown in Table. 2.1, the fourth-order mutual potential by Hou et al. (2017) is approximately 125 times faster than the surface integration method. This shows the drawback in the computational speed of the surface integration scheme.

The choice of the integrator also affects the computation times. Higher-order Runge-Kutta methods are often more time-consuming compared to their lower-order counterparts, as higher-order methods have a higher number of stages. The number of stages corresponds to the number of times the equations of motion are calculated before the simulation advances with a single time step. For instance, the Runge-Kutta-Fehlberg order 4(5) scheme is a 6-stage method (Fehlberg, 1969), while the order 9(8) scheme by Verner (2010) is a 16-stage method.

2.4 Summary

In this chapter, we have introduced the surface integration method as an approach to study the dynamics of asteroid binary systems. The surface integrals to the gravitational force, torque, and mutual potential are obtained by applying the divergence theorem to the corresponding volume integrals. While the surface integral for the gravitational force was previously known, Conway (2016) introduced three new vector potentials that allowed the gravitational torque and mutual potential to take surface integration forms.

This surface integration method is applied to study the 1999 KW4 binary system, where the bodies are modeled as ellipsoids. The accuracy of the simulations, using the surface integration scheme, is determined by the conservation of the total energy and total angular momentum in the system, where the quantities were respectively conserved to the 15th and 11th decimal digits. We also compared the computation time from our simulation to other mutual potential approaches applied to the same binary system.

In the next chapter, the surface integration method is applied to study asteroid systems that are formed from rotational fission. The bodies of these systems are initially very close to each other when they first separate due to the fission process. For such systems, it is advantageous to use the surface integration scheme as the results are valid even when the bodies are close, unlike methods that expand the mutual potential.

Chapter 3

Dynamics of rotationally fissioned asteroid binaries

Previous studies on the dynamics of post-fissioned asteroid systems used approximations to determine the mutual gravitational potential, either by expanding the mutual potential with spherical harmonics (Boldrin et al., 2016) or expanded with inertia integrals (Scheeres, 2007, 2009; Jacobson and Scheeres, 2011; Davis and Scheeres, 2020a). However, methods that expand the mutual potential suffer from divergences when the bodies are close. Earlier works have circumvented this issue by ensuring that the initial conditions result in configurations where the bounding spheres of the two respective bodies do not intersect. By doing so, the expanded mutual potential remains valid.

In this thesis, we make use of the surface integration to study the dynamics of asteroid systems after the initial fission (Ho et al., 2022). Here, we take full advantage of the property of the surface integration scheme, in which the resulting mutual potential is still valid even when the bodies are close. This allows us to explore a larger range of initial conditions that previously were not considered.

3.1 Fission condition

Once a rubble pile asteroid reaches a critical spin rate due to the YORP effect, or tidal disruptions, its surface starts to shed mass. In this section, we calculate the spin limit required for rotational fission to occur on a rubble pile. This spin limit also serves as the initial angular velocity and translational velocity of the system.

In our work, we model the rubble pile asteroid as a contact binary, and rotational fission occurs when the contact binary separates into two components as illustrated in Fig. 3.1. Rotational fission occurs when the centrifugal force is equal to the gravitational force between the asteroids

$$\mathbf{F}_G = \mathbf{F}_c, \tag{3.1}$$

where $\mathbf{F}_G$ and $\mathbf{F}_c$ correspond to the gravitational and centrifugal force.

The centrifugal force can be written as

$$\mathbf{F}_c = -m_s \boldsymbol{\omega}_0 \times (\mathbf{r}_{cm} \times \boldsymbol{\omega}_0), \tag{3.2}$$

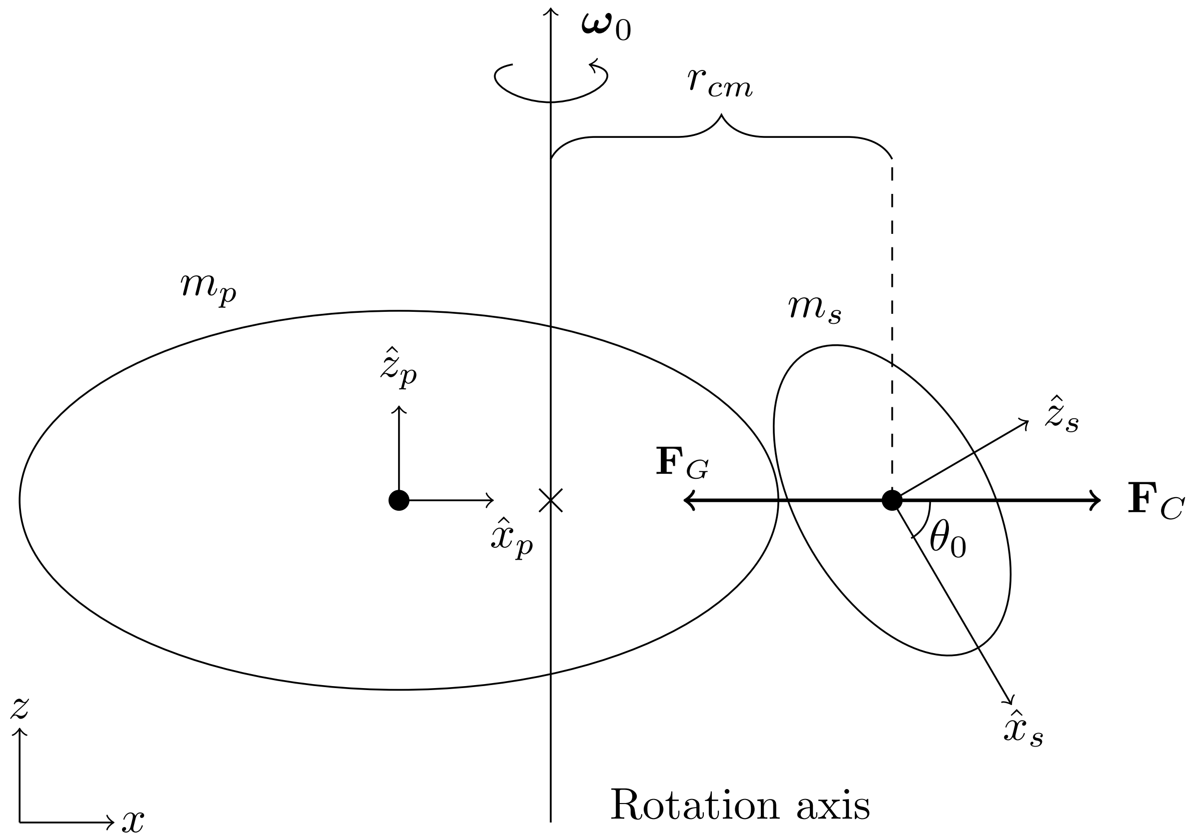

Figure 3.1: Illustration of a rotational fission scenario with the associated quantities required to compute the angular velocity that is needed for the two bodies to separate. The global y-axis points inwards the figure. Figure is similar to the one presented in Ho et al. (2022).

where m_s is the mass of the secondary, $\mathbf{r}_{cm}$ is the vector from the center of mass of the system to the center of mass of the secondary, and $\boldsymbol{\omega}_0$ the angular velocity vector through the center of mass of the system at the time of fission (see Fig. 3.1).

We simplify the model by displacing the secondary only along the long semiaxis of the primary, which, in the inertial frame, corresponds to a displacement only along the x-axis. Furthermore, the initial rotation axis of the contact binary passes through the mass center of the system perpendicular to the xy-plane of the primary. Equation (3.1) can then be rewritten to

$$F_G = m_s r_{cm} \omega_0^2, \tag{3.3}$$

and the angular velocity required for fission is then

$$\omega_0 = \sqrt{\frac{F_G}{m_s r_{cm}}}. \tag{3.4}$$

Equation (3.4) only considers the gravitational force between the two bodies. Ho et al. (2022) find that the limit computed from Eq. (3.4) had to be increased to obtain a reasonable number of simulations that did not end up with the two components colliding.

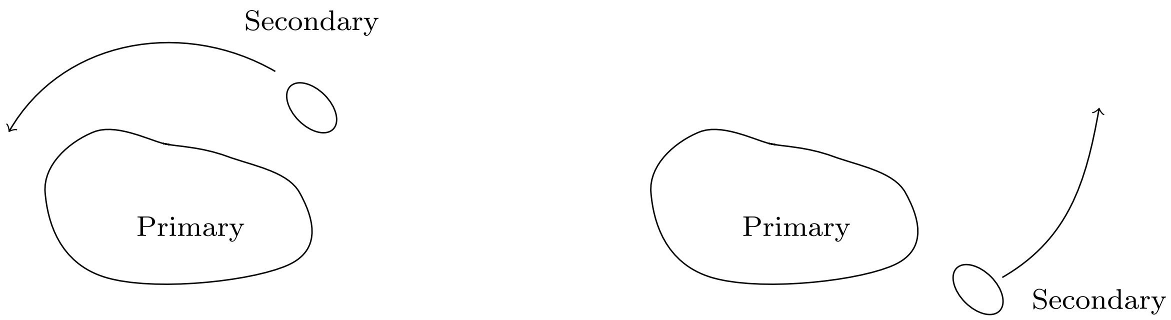

Negative system energy
Secondary remains in orbit

Positive system energy
Secondary escapes

Figure 3.2: Illustration of how the system energy determines whether the secondary remains in orbit or escapes. The left and right panels correspond to systems with negative and positive energies, respectively.

They model the initial angular velocity, required for surface disruption, as

$$\omega_0 = \beta \sqrt{\frac{F_G}{m_s r_{cm}}}, \tag{3.5}$$

where β is a correction factor used to increase the limit required for fission.

Along with gravity, a rubble pile asteroid can also be held together by weak cohesive forces, such as shear strength and tensile strength (Michel et al., 2001; Richardson et al., 2005). These cohesive forces are generally very weak, but can still increase the spin limit required for the rubble pile to break apart (Holsapple, 2001, 2004, 2007; Richardson et al., 2005; Sánchez and Scheeres, 2014; Hirabayashi et al., 2015; Li and Scheeres, 2021). By allowing $\beta > 1$, the factor can be considered as a cohesion factor. In this thesis, we consider $\beta = 1.01$. This choice is to ensure that there would be a reasonable number of simulations that did not end with the two bodies colliding.

3.2 Classifications of the outcome of newly formed binaries

When a rubble pile asteroid disrupts due to rotational fission, the outcome depends on the total energy of the system (often called free energy in other works, see e.g. Scheeres, 2007, 2009; Jacobson and Scheeres, 2011). Scheeres (2002) introduced various classifications of such systems, including; a fragment in a stable orbit around the parent body, the ejected fragment escaping the parent body (forming an asteroid pair), and a collision between the two components. The secondary remains in orbit around the primary if the total energy of the system is negative and escapes if the total energy is positive (see Fig. 3.2). In this thesis, we make similar classifications to distinguish the outcome of our simulations (Ho et al., 2022):

- Stable orbit: The total energy of the system is negative, and the secondary remains in stable orbit around the primary.

- Escaped secondary: The total energy of the system is positive, and the orbital eccentricity of the secondary is greater than one for at least 50 time steps. The system undergoes mutual escape and forms an asteroid pair.
- Unstable orbit: The total energy of the system is positive, but the secondary has not satisfied the escape condition above and remains in orbit around the primary.
- Collision: A collision/impact between the two bodies, regardless of the total energy of the system.

Systems with positive energies are separated into two categories (escape and unstable) due to the short simulation lengths. The simulation times we consider are 200 days, and the time before the system undergoes mutual escape increases for systems with higher mass ratios (Boldrin et al., 2016; Ho et al., 2022). If the simulation times are longer, the systems classified as "unstable" will eventually undergo mutual escape or result in an impact between the bodies.

3.3 The contact binary model

We model our contact binary as two ellipsoids, where the initial separation between the surfaces is 1 cm. The secondary is centered on the long semiaxis of the primary and is initially rotated about its body-fixed y-axis with an angle θ_0 (see Fig. 3.1). This contact binary model is similar to the work of Boldrin et al. (2016). We study six binary models, with varying densities and shapes of the secondary. Three different density models are considered, where the secondary has half, equal, and twice the density of the primary. The three shape models we consider vary the elongation of the secondary and is determined by the following parameters (Ho et al., 2022)

$$f_1 = \frac{a_s}{b_s} \tag{3.6}$$

$$f_2 = \frac{b_s}{c_s}, \tag{3.7}$$

where a_s, b_s, c_s are long, intermediate, and short semiaxes of the of the secondary respectively. Higher values of f_1 and f_2 correspond to more elongated secondaries. Three shape models of the secondary are studied where the parameters f_1 and f_2 are given by:

- $f_1 = 1.3, f_2 = 1.03$, which represents a secondary that is an oblate spheroid and fairly spherical.
- $f_1 = 1.6, f_2 = 1.2$, representing a cigar-shaped secondary.
- $f_1 = 2.5, f_2 = 1.2$, corresponding to an even more elongated cigar-shaped secondary.

When considering different initial angles for the secondary, the separation between the surfaces of the bodies will increase when θ_0 becomes larger. To ensure that the surface-to-surface distance is always kept at 1 cm, the secondary is moved closer after it has been given an initial angle, as illustrated in Fig. 3.3. This is not taken into account

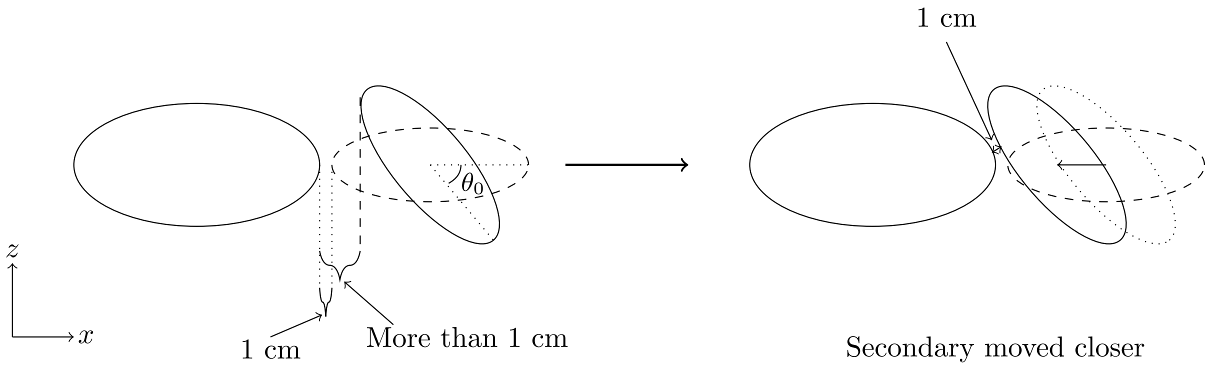

Figure 3.3: An illustration of how the secondary is moved closer to the primary so that the surface-to-surface distance is always kept at 1 cm, regardless of the initial tilt angle of the secondary component. Illustration is taken from Ho et al. (2022).

by Boldrin et al. (2016), where the surface-to-surface distance becomes larger when θ_0 increases in their model. When the surface-to-surface separation increases, the system no longer represents the binary system moments after the two components have separated due to rotational fission (see left panel of Fig. 3.3). However, because Boldrin et al. (2016) use spherical harmonics to determine the mutual gravitational potential, moving the secondary closer would result in divergences in the mutual potential. This is not an issue for the surface integration method, which allows us to explore more realistic initial conditions.

Moving the secondary closer to the primary, after it is rotated, causes the limiting angular velocity required for rotational fission to increase. For low mass ratio systems, increasing the initial angular velocity allows the secondary to escape earlier. Another consequence of moving the secondary closer is that collisions between the two bodies become more frequent. Ho et al. (2022) find that more than 80% of the simulations result in the two components impacting, whereas $\sim$ 30% of the simulations by Boldrin et al. (2016) end up as collisions. Figure 3.4 shows how the outcomes of the simulations (as described in the previous section) are distributed as functions of the mass ratio q and the initial tilt angle of the secondary θ_0. The majority of the collisions occur when the initial angle of the secondary is in the range of $\theta_0 \in [20°, 80°]$.

The separation between positive and negative energy regimes also differs between the models. Ho et al. (2022) find that the separation occurs at higher mass ratios when the density of the secondary increases, and at lower mass ratios when the shape of the secondary becomes more elongated (illustrated by the black dashed lines in Fig. 3.4). This also depends on the initial rotation angle of the secondary, as higher rotation angles of the secondary require higher spin rates to fission, resulting in higher energy configurations.

3.4 Comparisons with observations

Simulations that did not result in the bodies colliding are compared with observations of asteroid binaries and pairs. One observable quantity is the mass ratio of the system. For asteroid binaries, this can be measured by comparing the diameters of the bodies and

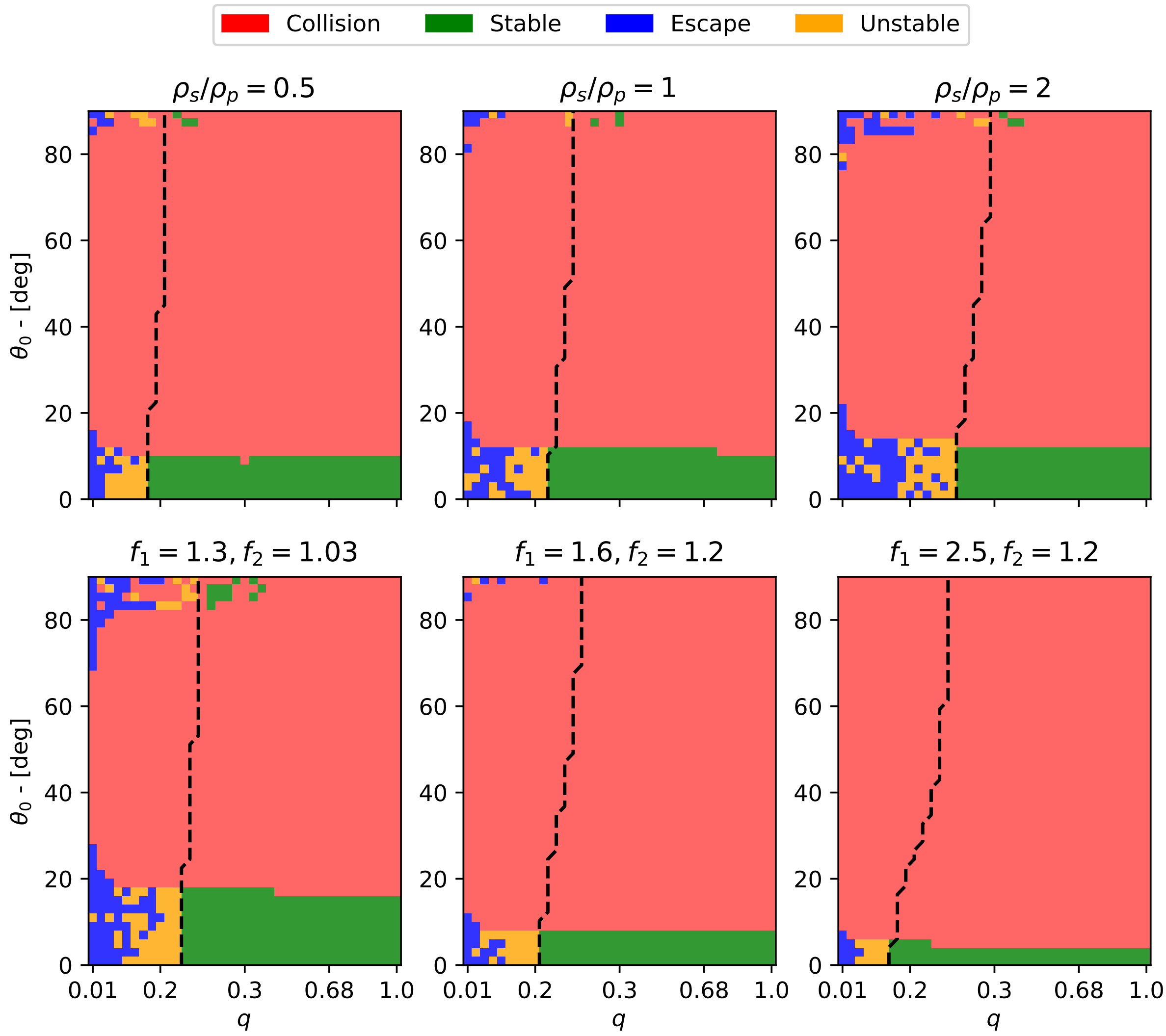

Figure 3.4: The outcome of the simulations for the six models. The simulation results are presented by Ho et al. (2022). The black dashed lines separate the positive and negative energy regimes.

assume equal bulk densities (Pravec et al., 2006, 2016), while for asteroid pairs, the mass ratio can be determined by comparing the absolute magnitudes (brightness) of the bodies (Pravec et al., 2019). Another parameter that can be observed is the rotation period. This can be achieved by studying light curves of asteroids, which is a technique that may also reveal their shape (Kaasalainen et al., 2001; Durech et al., 2015).

3.4.1 Comparisons with observed asteroid pairs

The simulations of the escape and unstable cases by Ho et al. (2022) are compared with asteroid pairs observed by Pravec et al. (2019). This is illustrated in Fig. 3.5. The gray crosses in the figure correspond to rotation periods of primaries and secondaries of observed asteroid pairs by Pravec et al. (2019), for pairs with mass ratios $q < 0.3$. It should be noted that our simulations only represent 200 days after the rotational process. Many of the observed pairs have existed for more than 10^5 years (Pravec et al., 2019),

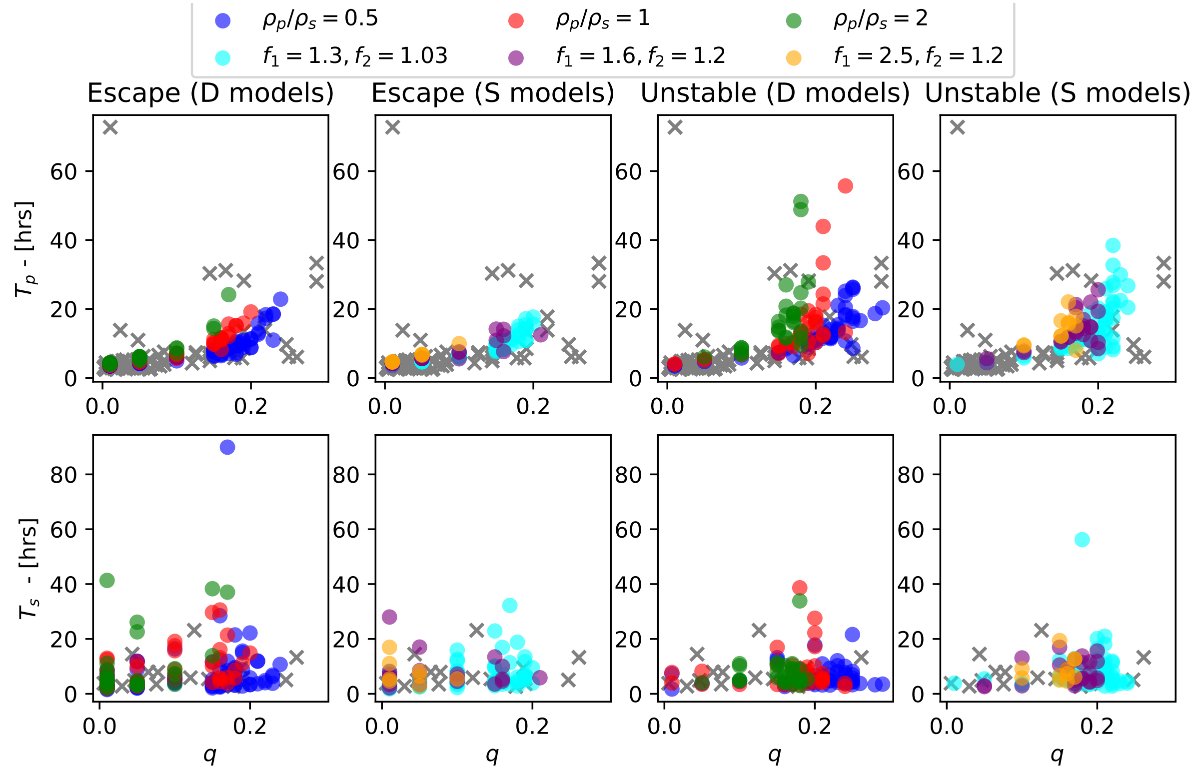

Figure 3.5: The top and bottom rows correspond to the rotation period of the primary and secondary, as functions of the mass ratio q, after $t = 200$ days, respectively. The simulation results are presented by Ho et al. (2022). The gray crosses are asteroid pair data from Pravec et al. (2019), and only asteroid pairs with $q < 0.3$ are included in the figure.

and each asteroid may have experienced many different dynamical events that change its rotation period, e.g. the YORP effect, tidal disruptions, or even collisions with other objects. Despite this, except for a few outliers, the simulation results of Ho et al. (2022) are within the range of the observed rotation periods of the asteroid pairs.

3.4.2 Comparisons with observed binaries

The rotation periods for the stable cases from Ho et al. (2022) are compared with data from observed asteroid binaries. The simulations give rotation periods of the primaries of typically 15-25 hours. However, observed primaries typically have short rotation periods. The rotation periods of Moshup and Didymos are estimated to 2.76 and 2.26 hours, respectively (Ostro et al., 2006; Naidu et al., 2020). Furthermore, Pravec et al. (2016) have collected data on the rotation periods of various binary and triple systems among the NEAs and in the main belt. They found that the primaries have rotation periods shorter than 4.4 hours. This therefore suggests that there must be some mechanism to increase the spin rate of the primary after the fission process, such as the YORP effect. On the other hand, the rotations of the secondaries observed by Pravec et al. (2016) range from 15 hours to 42 hours, and most of the simulations that are presented by Ho et al. (2022) result in secondaries with rotation periods in this observed range.

3.4.2.1 Energy loss to stabilise binary systems

Observed asteroid binaries, assuming that both the primary and secondary have equal bulk densities, have mass ratios smaller than 0.125 (Pravec et al., 2006, 2016). At these mass ratios, the rotational fission model predicts positive system energies of fissioned asteroids, which results in the secondary escaping and thus forming an asteroid pair (Scheeres, 2007; Pravec et al., 2010). In our model, all systems with mass ratios smaller than 0.125 result in the secondary escaping. To prevent the secondary from escaping, a form of energy dissipation must be applied to the binary system.

One method to dissipate energy is through collisions. When two asteroids impact, some of the energy is converted to, for instance, deformation of the asteroids. However, among the NEA population, it is unlikely that asteroids have collided with other objects. On the other hand, various studies have shown that it is possible for the secondary to re-collide with the primary after the initial break-up of the rubble pile (Scheeres, 2002; Boldrin et al., 2016; Davis and Scheeres, 2020a; Ho et al., 2022). If the impact speeds are great enough, the collisions may dissipate enough energy to help stabilize low mass ratio binaries and prevent the secondary from escaping.

Another energy dissipation mechanism is secondary fission (Jacobson and Scheeres, 2011), where the secondary experiences rotational fission if it spins fast enough. The newly formed component may escape the binary system, taking away energy from the system, or collide with one of the two original parent bodies. The shape and density of the secondary also affect its fission limit. Ho et al. (2022) find that secondary fission is more common when the secondary has a lower density than the primary, and when the secondary becomes more elongated.

3.5 Implications for asteroid system formation and evolution

As mentioned in the previous section, asteroid binaries observed by Pravec et al. (2016) have mass ratios that are too low to allow the secondary to remain in orbit, as the energy configuration of such systems is highly excited and will result in the secondary escaping. The energy of these low mass ratio systems must be dissipated, e.g. through collisions or secondary fission, to prevent the secondary from escaping.

Ho et al. (2022) found that more than 80% of the simulations end with the bodies colliding (see also Fig. 3.4). They also found that the impacts occur very early in the simulations, where more than 95% of the collisions occur within the first five hours after the initial fission event. If the collision speeds are large enough, it may contribute to significant amounts of energy dissipation. The rotational fission model of Walsh et al. (2008) found that collisions between fragmented asteroid materials, with collision speeds of order $0.2 - 0.5$ m s^{-1}, can dissipate significant amounts of energy, which may help stabilize low mass ratio binaries and prevent the secondary from escaping. However, collisions with low impact velocities may not be enough to stabilize the system, but it is also possible that the system experiences multiple collision events during its lifetime.

Davis and Scheeres (2020a) also find a high rate of re-collision events in their simulations and suggest this could result in craters on the asteroids in the binary systems.

Secondary fission is, in theory, mainly found for systems at the low mass ratio regime (Jacobson and Scheeres, 2011). On the other hand, Ho et al. (2022) find that secondary fission can occur at higher mass ratios if the shape of the secondary becomes more elongated. Their simulations also show that secondary fission events take place very early after the initial fission process if the secondary is highly elongated. This agrees with the work of Sharma (2014), who found that bodies are more likely to disrupt when they become more elongated, as they are less stable to finite structural perturbations compared to bodies that are more spherical. Moreover, Pravec et al. (2016) report that there are few binaries where the secondary is elongated. This suggests that secondaries with high initial elongations may experience multiple disruption events, and thus reshape and become less elongated over time. As the secondary reshapes over time, the shedded mass may accumulate to a third body. This third body may fall in a stable orbit around the primary (forming an asteroid triple system), collide with one of the other components, or escape and form a binary-pair system as observed by Pravec et al. (2019).

Pravec et al. (2019) propose a second mechanism to form binary-pair systems, in which the primary experiences a second (or multiple) rotational fission event. The idea is similar to secondary fission, and the newly formed component can escape the primary which also contributes to a dissipation of energy from the binary system. However, Ho et al. (2022) find that the primary does not experience a second rotational fission event in any of the simulations. However, Ho et al. (2022) do not include other forces, such as the YORP effect or tidal forces, which may increase the spin rate of the primary and thus allow it to fission a second time.

A combination of both collision and secondary fission may contribute to energy dissipation in a binary system. If the secondary has a low enough density or becomes highly elongated, secondary fission may occur very early after the initial separation of the contact binary (Ho et al., 2022). Many of these early secondary fission events correspond to simulations that end up with the two bodies impacting, and the impact may occur after the secondary has disrupted. However, once a third body is added to the system, the dynamics change and prevent the collisions from occurring.

Binary systems where the density of the secondary is lower than the density of the primary not only increase the probability of secondary fission, but also result in lower energy configurations. There is scarce data on the secondaries among the observed binaries. Radar observations from Naidu et al. (2015) estimate that the density of 2000 DP107 is 1.381 g cm^{-3}, while the secondary has a density of 1.047 g cm^{-3}. They also estimate that the mass ratio of this system is approximately 0.04. It is therefore likely that secondary fission has been the dominant part of stabilizing the 2000 DP107 system. Ostro et al. (2006) measured the binary system 1999 KW4 and estimated a density of 1.97 g cm^{-3} for the primary and a density of 2.81 g cm^{-3} for the secondary, and the system mass ratio to be roughly 0.06. The simulations from Ho et al. (2022) show that secondary fission is less likely when the secondary has a higher density than the primary. Results from Davis and Scheeres (2020a) show that approximately 36% of the 1999 KW4 simulations end with surface disruption of the secondary. Secondary fission may therefore have occurred for the 1999 KW4 system, but likely not often enough for the secondary to reshape. It is perhaps more likely that collisions are the main source of energy dissipation in the 1999 KW4 system.

Asteroids among the NEAs have been observed to tumble (Pravec et al., 2005, 2007). It is thought that tumbling motion emerges from impacts between asteroids and the YORP effect (Pravec et al., 2005). Tumbling may also arise if the bodies are rotating slowly and from rotationally fissioned asteroids due to non-planar effects (Boldrin et al., 2016; Ho et al., 2022). Tumbling motion causes stress-strain cycling in the interior of a body, which dissipates energy from the body (Pravec et al., 2005; Breiter and Murawiecka, 2015). However, Breiter and Murawiecka (2015) have shown that the tumbling damping time scales for ellipsoids can be millions of years. Due to these long damping time scales, tumbling motion is unlikely to have any significance on the energy loss from the system, as the time before a secondary escapes is typically under 100 years (Boldrin et al., 2016; Ho et al., 2022).

The stable simulations of Ho et al. (2022), where the secondary remains in orbit around the primary, show that the orbits are not synchronized and the bodies are in tumbling motion, as tidal forces are not included in the simulations. Several binaries are observed to be in some sort of synchronized state (see Jacobson and Scheeres, 2011, and references therein). Moreover, Wisdom (1987) points out that tumbling motion is a process all non-spherical natural satellites must undergo, and later stabilize to synchronous or doubly synchronous orbits due to tidal dissipation (Goldreich and Sari, 2009; Jacobson and Scheeres, 2011).

3.6 Summary

We have used the surface integration method to study the dynamics of newly fissioned asteroid systems. Unlike methods that expand the mutual potential, the advantage of the surface integration scheme is that the resulting mutual potential is still valid when bodies are close. This allows us to explore more realistic initial conditions, by letting the secondary start closer to the primary after the secondary is rotated relative to the primary. The simulations have been compared to the rotation periods of observed asteroid binaries and pairs.

The surface integration method allows us to move the secondary closer to the primary before the simulations are initialized. This is, however, not possible for methods that expand the mutual gravitational potential due to divergences in the mutual potential. In the next chapter, we will investigate the differences in the computed forces and torques, between the surface integration method and a method that expands the mutual potential with inertia integrals. We will also study how these differences may affect long-term simulations of existing binary systems and binaries formed from rotational fission.

Chapter 4

Comparisons of different mutual gravitational potential approaches

Expanding the mutual gravitational potential through power series is an efficient method to study the F2BP. Previous studies of the F2BP often expand the mutual potential up to order two (Scheeres, 2009; Jacobson and Scheeres, 2011; Boldrin et al., 2016), but some have truncated the potential at order four (Davis and Scheeres, 2020a; Agrusa et al., 2021). In this chapter, we investigate how the surface integration method compares with a method that expands the mutual up to order two and four. We also study how these differences may affect the dynamical outcome of asteroid binary systems.

4.1 Comparing the surface integration method with an expansion method

In this thesis, we aim to compare the surface integration method with the expansion-based approach by Hou et al. (2017) to compute the mutual gravitational potential, force, and torque. We consider bodies of ellipsoidal shapes, and the surface integration method will yield exact results of the mutual potential, force, and torque. The methodology by Hou et al. (2017) has been implemented in the software called "General Use Binary Asteroid Simulator" (GUBAS), developed by Davis and Scheeres (2020b), and is available as an open-source software[1].

The mutual potential derived by Hou et al. (2017) makes use of inertia integrals to describe the mass distribution of the bodies. These inertia integrals are analogous to spherical harmonics. As a consequence, the mutual potential derived from this approach diverges when the bodies are close. Tricarico (2008) showed that this method only converges for any point outside the bounding spheres, which are the spheres covering the circumference of each respective body, as long as the spheres do not intersect. Figure 4.1 shows examples of where the mutual potential converges and diverges. This limitation can impose restrictions to dynamical studies of post-fissioned asteroid systems, particularly in the early formation stages when the bodies are close.

---

[1] Github repository: `https://github.com/meyeralexj/gubas`

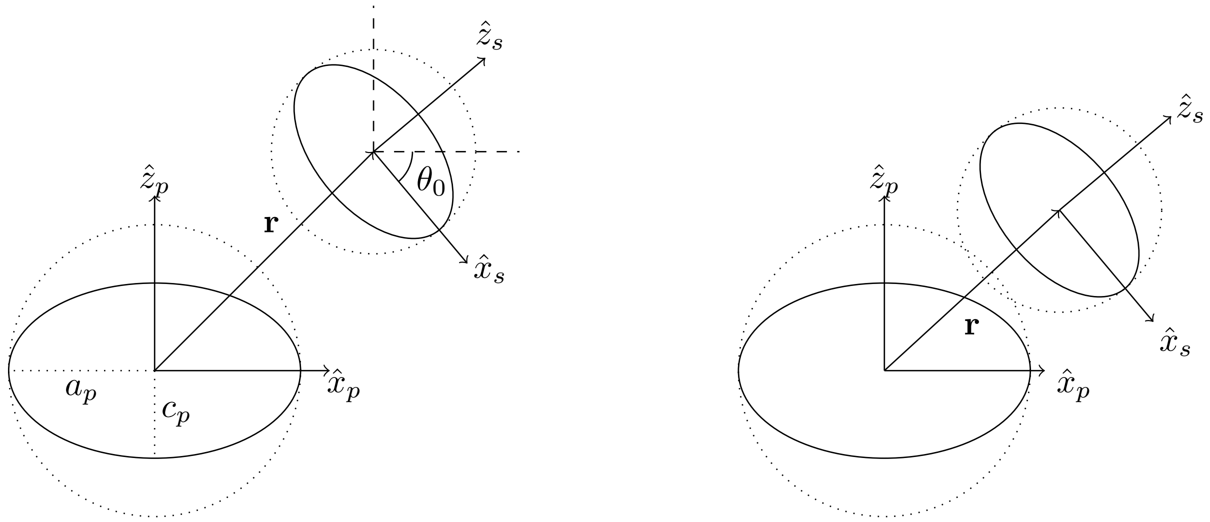

Convergent

Divergent

Figure 4.1: Example of configurations where the mutual potential, determined from inertia integrals, converges (left) and diverges (right). The dotted circles correspond to the bounding spheres around each respective body. The vector $\mathbf{r}$ describes the separation between the mass centers of the two bodies. Illustration is taken from Ho et al. (2023).

When the mutual potential is expressed as a power series, higher-order terms are neglected which results in truncation errors. The significance of higher-order terms, and how that affects the dynamics of binary asteroids, have been investigated by Hou et al. (2017) and Davis and Scheeres (2020a). Hou et al. (2017) considered the planar motion of two ellipsoids, and find that a second-order potential is sufficient to describe the dynamics of asteroid systems that are Hill stable (in a stable orbit) and when the bodies undergo mutual escape. However, if the bodies are highly elongated, higher-order terms become necessary for a more accurate description of the dynamics (Hou et al., 2017). Davis and Scheeres (2020a) applied the mutual potential approach by Hou et al. (2017) to study the dynamics of newly fissioned asteroid binaries, and model them with polyhedral shapes. They find that including additional terms does not significantly alter the formation process itself but can slow down the overall evolutionary process, e.g. mutual escape or collisions occur later in the simulations.

The surface integration method, however, does not make use of approximations and therefore does not suffer from truncation errors. For ellipsoidal shapes, the surface integration scheme yields exact results for the mutual potential. Moreover, as previously mentioned, the mutual gravitational potential calculated from this method is still valid when the bodies are close. Using this approach should therefore give more accurate results of the dynamics of binary asteroids compared to a method that expands the mutual potential.

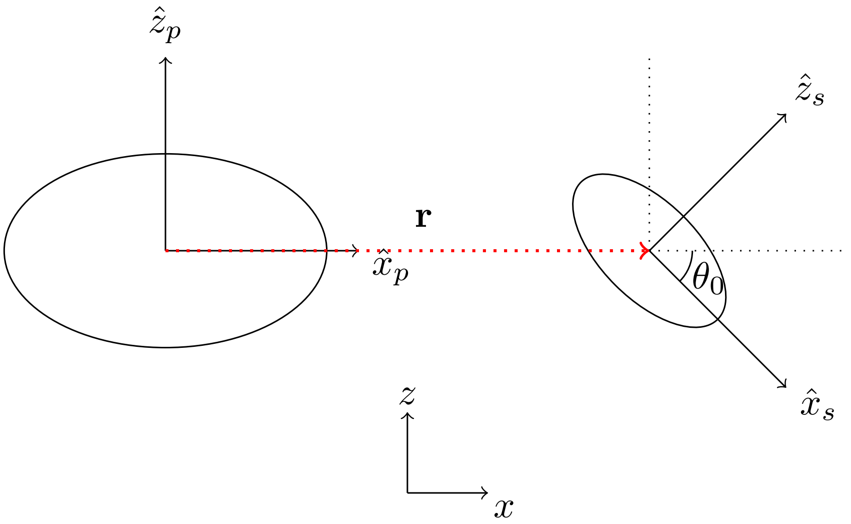

Figure 4.2: Example of how the secondary is rotated, relative to the primary, in the tests performed by Ho et al. (2023). The red dotted line corresponds to the separation vector between the mass centers of the bodies $\mathbf{r}$. The subscript p and s correspond to parameters of the primary and secondary respectively. Here, the vector $\mathbf{r}$ is parallel with the long principal axis of the primary, but not parallel with any of the principal axes of the secondary. This results in a zero torque on the primary, but not on the secondary, when the mutual potential is expanded to order two.

4.1.1 Force and torque differences with distance

When the separation between the bodies increases, the mutual potential of the surface integration method and the expansion approach should converge to the point mass solution. It is therefore expected that the two methods should give similar results as the bodies are separated further apart. However, when the bodies are close, we expect the discrepancies to increase. In this thesis, we investigate how the forces and torques differ between the surface integration method and the expansion-based approach. We consider configurations when the bodies have separations similar to some observed asteroid binaries, and configurations where the surfaces between the bodies are almost touching.

4.1.1.1 Differences at large distances

The first tests performed in Ho et al. (2023) investigate how the differences in the forces and torques change when the secondary is moved around the xy-plane of the primary and at varying distances. The secondary is rotated with an angle $\theta_0 = 45°$ to ensure non-zero torques, as illustrated in Fig. 4.2. Furthermore, the position of the secondary is limited to regions where the bounding spheres around each body do not intersect. This ensures that the mutual potential approach by Hou et al. (2017) is still valid. The separation between the bodies is increased up to five primary radii (where the primary radius is defined as its large semiaxis a_p, see Fig. 4.1), as some observed asteroid binaries have orbits of similar values (Pravec et al., 2016).

Figure 4.3 shows the differences of the computed forces and torques, relative to the

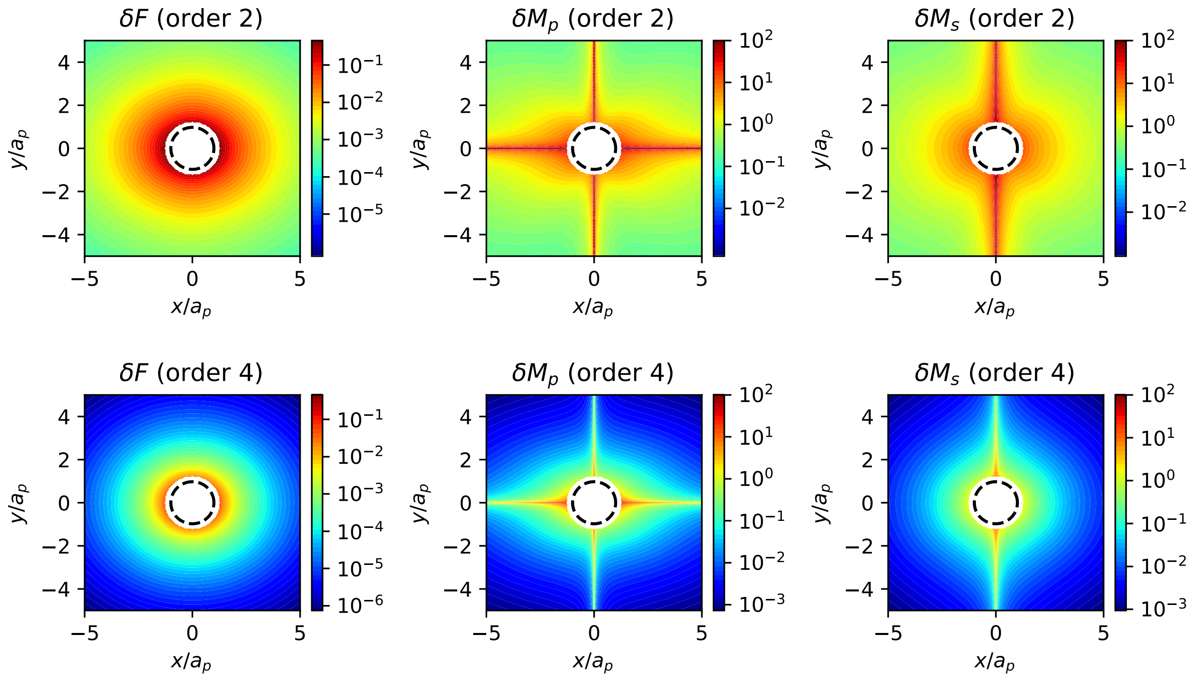

Figure 4.3: Percentage difference of the computed forces and torques from a second-order (top row) and fourth-order (bottom row) potential, relative to the surface integration method. The color bars are given in logarithmic scale. The left, middle, and right columns correspond to differences in the force $\mathbf{F}$, torque on the primary $\mathbf{M}_p$, and torque on the secondary $\mathbf{M}_s$. The pair-wise comparisons between second and fourth-order potentials share the same color scaling. The black dashed lines show the circumference of the primary, while the white regions correspond to the positions of the secondary where the two bounding spheres intersect. Illustration is taken from Ho et al. (2023).

surface integration method, when the secondary is displaced around the xy-plane. It can already be seen that the errors in the forces and torques are smaller from the fourth-order potential compared to the second-order potential, as the fourth-order potential is closer to the exact solution. Moreover, when the bodies are separated further apart, the differences decrease.

The difference in the forces from the second-order potential, relative to the surface integration method is approximately 0.4% when the bodies are close and 0.001% when the separation is $2-3$ primary radii. For the torques, the relative difference ranges from 10% at small separations and 1% at larger distances. For all three quantities, the relative differences decrease by a factor of 10 when the mutual potential is truncated to order four.

For the torques, there are some regions where the error from the second-order potential is 100%, regardless of the separation between the bodies. These are locations where the vector between the mass centers of the bodies, $\mathbf{r}$, is parallel with one of the principal axes of each respective body. This is a mathematical limitation to mutual potentials that expand inertia integrals up to order two, which result in zero torques when $\mathbf{r}$ is parallel with a principal axis (Kane et al. (see e.g. 1983), also shown in Appendix B.1). Figure 4.2

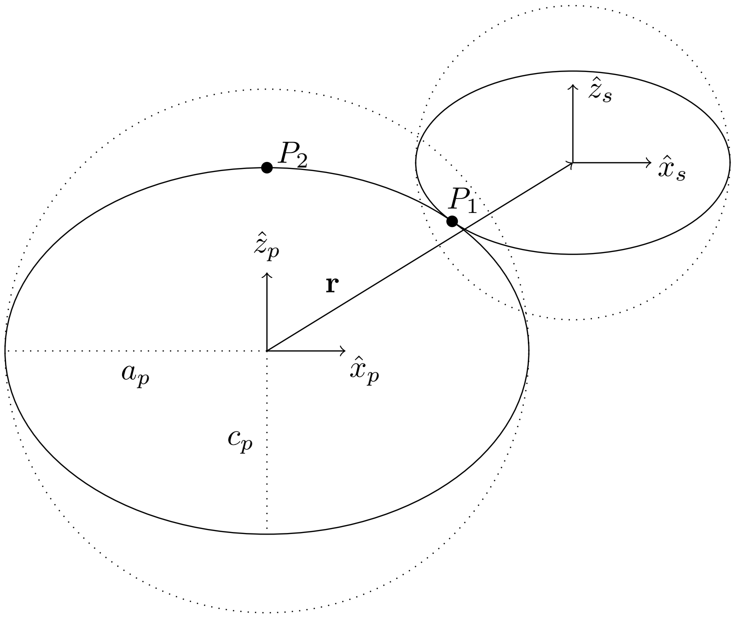

Figure 4.4: Configurations considered by Ho et al. (2023) where the two bodies are touching. Point P_1 is the point where the two bodies are in contact, while point P_2 is referred to as the "pole".

shows an example where $\mathbf{r}$ is parallel with one of the principal axes of the primary, but not the secondary, which result in 100% error in $\mathbf{M}_p$ but not $\mathbf{M}_s$. However, the configuration considered should result in non-zero torques, which is what is obtained from the surface integration method and the fourth-order potential.

4.1.1.2 Differences when the bodies are almost touching

Because the differences between the two approaches are expected to be at the maximum when the bodies are close, Ho et al. (2023) compares the results of these two approaches when the surfaces of the two bodies are almost touching (see Fig. 4.4). Three different shapes of the primary were considered while keeping the shape of the secondary constant. The axis ratios of the primary considered are

- Model 1: $a_p/b_p = 1.000$, $a_p/c_p = 1.067$.
- Model 2: $a_p/b_p = 1.231$, $a_p/c_p = 2.000$.
- Model 3: $a_p/b_p = 1.455$, $a_p/c_p = 4.000$.

Figure 4.5 shows the differences in the computed forces and torques increase as the primary becomes more elongated (higher values of a_p/b_p and a_p/c_p). When the ratio between the long and short semiaxes, a_p/c_p, becomes large enough, the fourth-order potential can give larger errors compared to the second-order counterpart. The largest errors are generally found when the contact point is located at the "pole" of the primary (see point P_2 in Fig. 4.4), which can exceed 1000% if the primary is highly elongated, as shown in the right-most panels of Fig. 4.5.

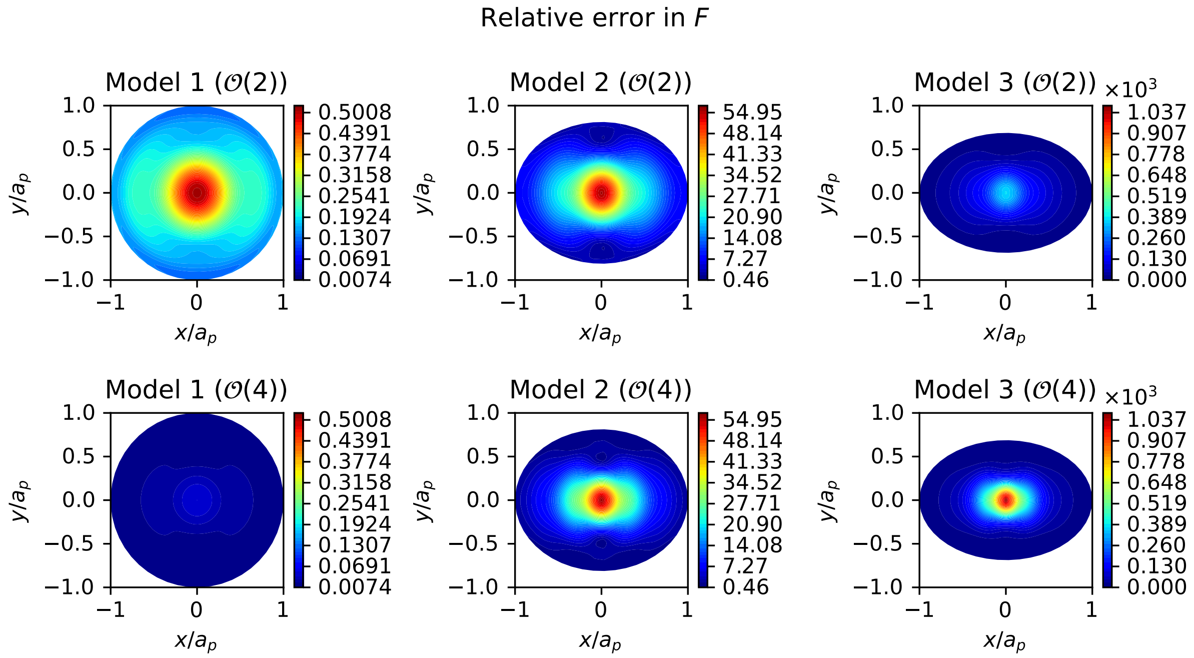

Figure 4.5: Percentage difference of the computed forces from an expansion method relative to the surface integration method. Each point corresponds to the location where the surfaces of the bodies are touching. The top and bottom rows correspond to errors in the second and fourth-order expansions outlined by Hou et al. (2017). The pair-wise comparisons between second and fourth-order potentials share the same color scaling. Illustration is taken from Ho et al. (2023).

To explain the accuracy reduction of the fourth-order approximation, it should be noted that the forces computed from an expansion method truncated to order N typically scale as $\mathcal{O}\left((r/a_p)^N\right)$, where a_p is the radius of the bounding sphere (see Fig. 4.4). When $r < a_p$, higher-order gravity terms in the mutual potential become larger than the lower-order terms, causing the resulting forces (and torques) to be inflated. If the primary becomes more elongated, the separation vector $\mathbf{r}$ may also become smaller compared to a more spherical primary, particularly near the pole of the primary. As a result, the errors from higher-order terms also increase. Similar behaviors are also observed in the computed torques on both the primary and the secondary, where the differences grow larger as the primary becomes more elongated.

When the bodies are touching, the bounding spheres of the bodies intersect, and the mutual potential approach by Hou et al. (2017) (and that of Tricarico (2008)) no longer converges. The large differences produced from the second and fourth-order potentials, when the bodies are touching, emphasize the necessity of using a more accurate model to compute the mutual potential to study the dynamics of post-fissioned asteroid systems.

4.1.2 Simulation differences between the methods

The differences in the computed forces and torques, between the surface integration method and an expansion method, become larger when the bodies are close. Ho et al.

(2023) study how these differences can potentially affect the dynamical behavior of the asteroids over longer time periods. Two test simulations are considered:

- Test 1: The two asteroids are initially separated by ~ 4.5 primary radii, corresponding to a binary system already in a stable orbit.
- Test 2: The secondary is located close to the primary, with a 1 cm separation between the surfaces of the two bodies. This corresponds to the moment after a contact binary has separated due to rotational fission. The initial conditions are identical to the work of Ho et al. (2022).

For test simulation 1, Ho et al. (2023) find that the differences in results, between the surface integration method and a fourth-order approximation, are negligible. The relative differences in the translational and angular velocities are smaller than 0.01% at each time step throughout the simulation. For the second-order approximation, on the other hand, the errors are approximately two orders of magnitude larger. Nevertheless, a fourth-order potential is sufficient to describe the dynamical evolution of asteroid binaries, provided that the initial separation is large enough (Agrusa et al., 2020; Ho et al., 2023).

In the second test simulation, the initial configuration of the system already results in large differences in the initial angular velocity required for the contact binary to fission. The rotation period required for the initial fission is 5.84 hours from the surface integration method, and 5.98 hours and 5.88 hours from the second and fourth-order approximations respectively (Ho et al., 2023). As a consequence, the outcome starts to significantly deviate within the first few hours of the simulations. After five hours, the discrepancies in the linear and angular velocities from both the second and fourth-order expansions, relative to the surface integration method, are more than 100%. Throughout the simulations, these differences average at $\sim 130\%$. Using the same initial conditions for all three methods results in similar differences. It is therefore reasonable to assume that the main discrepancies are caused by the choice in how the mutual potential is computed, and not only by the differences in the initial conditions. The use of an exact method is therefore important in order to correctly capture the dynamics of post-fissioned asteroid systems, particularly in the early stages when the bodies are close. However, once the bodies are separated far enough apart, it may be more beneficial to switch to an expansion-based method to determine the mutual potential. This could potentially reduce the computation time and, at the same time, give more accurate results.

4.1.3 System energy differences

The use of a mathematically exact method to compute the mutual gravitational potential, instead of an expansion-based method, also affects the system energy. For an asteroid binary, the total energy will determine if the secondary will remain in stable orbit around the primary, or escape (Pravec et al., 2010; Jacobson and Scheeres, 2011). Ho et al. (2023) show that the post-fissioned asteroid systems, with the initial conditions outlined in Ho et al. (2022), result in higher total energies when the surface integration method is used. As a result, the separation between the positive and negative energy regimes is located at higher mass ratios compared to a method that expands the mutual potential. Figure

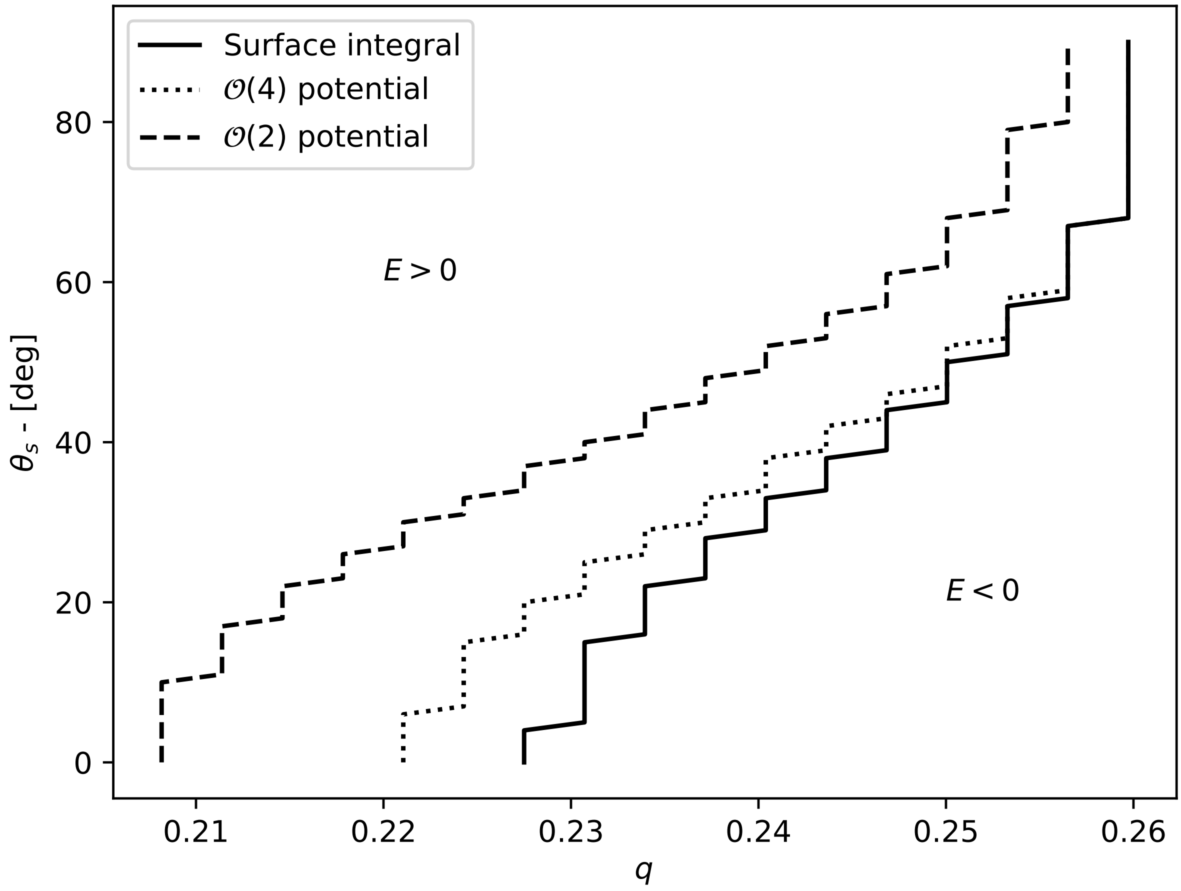

Figure 4.6: Zero-energy lines for the rotational fission scenario described by Ho et al. (2022), as functions of the mass ratio q and the initial tilt angle of the secondary θ_0. The solid, dotted, and dashed lines correspond to the zero-energies of the surface integration method, fourth-order, and second-order potentials. Regions to the left of each respective line correspond to systems with positive total energies.

4.6 shows the zero-energy lines that separate the positive and negative energy regimes for the different methods. The largest discrepancies occur at low mass ratios for smaller θ_0 values.

It is worth mentioning that the difference between the zero-energy lines also becomes smaller as θ_0 approaches 90 degrees. However, as θ_0 increases, the separation r must become smaller in order to maintain the 1 cm surface-to-surface separation. As a consequence of an increasing value of θ_0, the bounding spheres of both bodies will intersect more and more. It is therefore expected that the difference becomes larger when θ_0 increases. However, Fig. 4.7 shows that the relative differences in both the force and mutual potential energy become smaller when θ_0 takes higher values.

4.1.4 Computational efficiency

The methods considered by Ho et al. (2023) are benchmarked by comparing the CPU times. The benchmarking is performed in two parts. The first part compares the CPU

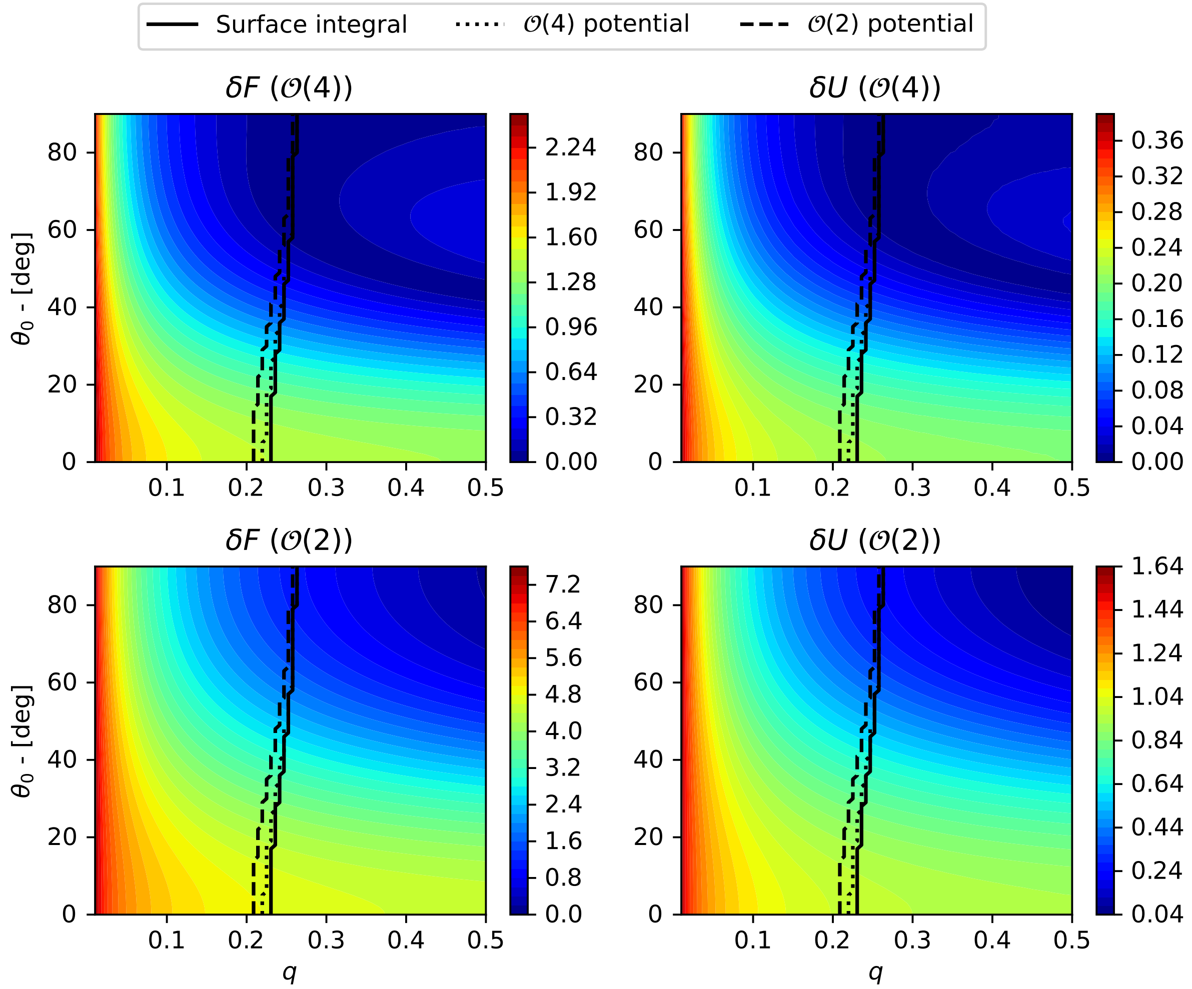

Figure 4.7: Percentage difference in the forces (left panels) and the mutual potential energy (right panels) from the expansion approach relative to the surface integration method. The top and bottom rows correspond to differences with respect to the fourth and second-order potentials. The black lines indicate the zero-energy lines (equivalent to Fig. 4.6).

times required to compute the forces and torques. The second part compares the CPU times for the full simulations, which includes the time required to initialize the software, solve the equations of motion, and save the resulting data.

Due to the nature of the surface integration method, it is expected that forces and torques calculated from this approach are more time-consuming than a method that expands the mutual potential. Ho et al. (2023) find that the time required to compute the forces and torques from the surface integration method is approximately 82 times and 4 times slower than the second and fourth-order potentials respectively. However, if the mutual potential is truncated to order eight, the surface integration scheme is roughly 16 times faster.

When comparing the full simulations, the CPU time from our software, utilizing the surface integration method, is similar to GUBAS when the mutual potential is truncated to order four. This is because of the differences in how the codes are optimized.

4.1.5 The importance of a more accurate mutual potential model

The results by Ho et al. (2023) indicate that a more accurate model to determine the mutual gravitational potential is important to properly determine the dynamics of newly fissioned asteroid systems. On the other hand, truncating the potential to order four is sufficient to study the dynamics of asteroid binaries with separations larger than ~ 4 primary radii. However, Agrusa et al. (2020) noted that the accuracy in the initial conditions is far more important to properly determine the dynamics of the (65803) Didymos binary system compared to the choice in the mutual potential.

4.2 Changes to the dynamics with different shape models

Up to now, we have only studied the dynamics of asteroids modeled as ellipsoids. However, real asteroids do not have perfect ellipsoidal shapes. In this section, we briefly investigate how changing the shape from an ellipsoid to a polyhedron may affect the dynamics of a two-body system.

This section will use, and also demonstrate, the polyhedron gravitational potential outlined by Conway (2015). Depending on the number of faces representing the polyhedron, the simulation times can increase by several orders of magnitude compared to ellipsoidal simulations. As a result, only polyhedra with a low number of vertices are used to demonstrate the method. A simulation consisting of a polyhedron with a large number of vertices and a point mass can be conducted within a reasonable time. This has previously been used to demonstrate how dust is emitted and transported around the comet 67P/Churyumov-Gerasimenko (Kramer et al., 2015; Kramer and Noack, 2015).

The polyhedron gravitational potential approach outlined by Werner (1997) can also be used together with the surface integration method in order to study the F2BP. However, this method makes use of spherical harmonics to determine the potential, and will therefore suffer from divergences when the bodies are close. The polyhedron potential outlined by Werner and Scheeres (1997) may also be used together with the surface integration method. However, this approach must also keep track of the edges of the polyhedron, such as the normal vectors of the edges. This is not required in the method by Conway (2015).

4.2.1 Surface integration

The equations of motion are mostly the same as described in chapter 2. However, unlike the ellipsoid, integrating over the polyhedron surface requires integration over each face representing the body. As a result, the force, torque, and mutual potential energy are sums of surface integrals over each face i. For instance, the force on the polyhedron, with a constant density ρ, is now

$$\hat{\mathbf{F}} = \rho \sum_{i}^{N_f} \iint_{S_i} \Phi(\mathbf{r}') \hat{\mathbf{n}}_i dS_i, \tag{4.1}$$

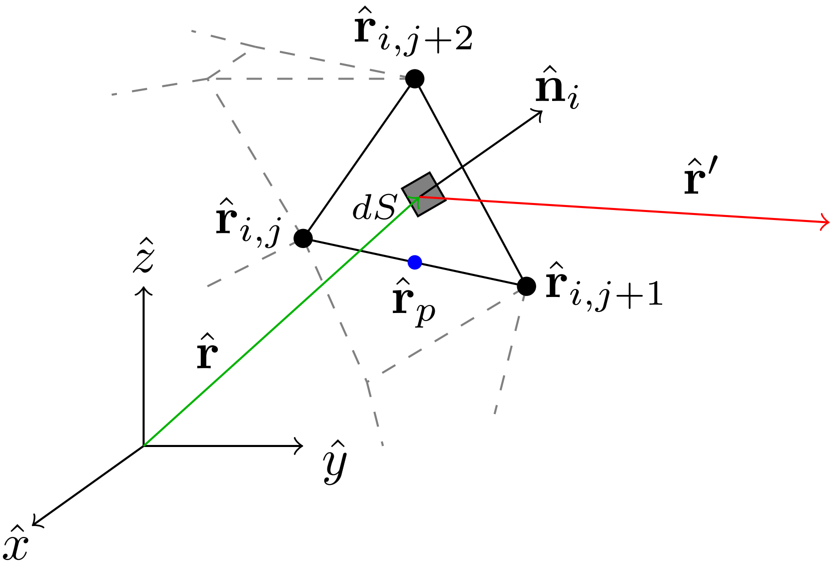

Figure 4.8: Vertices $\hat{\mathbf{r}}_{i,j}$ and normal vector $\hat{\mathbf{n}}_i$ of some face i of an arbitrary polyhedron. The blue point is a point $\hat{\mathbf{r}}_p$ along the edge of the face. The vectors $\hat{\mathbf{r}}$ and $\hat{\mathbf{r}}'$ correspond to those of Fig. 2.1. Only a small part of the polyhedron is shown, and the other faces of the polyhedron are marked with gray dashed lines. The blue dot is a point along the edge of the face. The coordinate axes are located at the center of mass of the polyhedron.

where N_f is the number of faces of the polyhedron, dS_i the surface element and $\hat{\mathbf{n}}_i$ the surface normal of face i.

In our model, we assume that the faces of the polyhedron are represented by triangles. Parametrizing a triangular surface is fairly simple. For a face i formed by vertices $\hat{\mathbf{r}}_{i,j}$, $\hat{\mathbf{r}}_{i,j+1}$ and $\hat{\mathbf{r}}_{i,j+2}$, the points on the triangle surface are given by (see Fig. 4.8)

$$\hat{\mathbf{r}} = (1-v)\hat{\mathbf{r}}_{i,j} + vu\hat{\mathbf{r}}_{i,j+1} + v(1-u)\hat{\mathbf{r}}_{i,j+2}, \quad \text{for } v \in [0,1], u \in [0,1]. \tag{4.2}$$

The infinitesimal displacement along v and u are

$$d\mathbf{r}_v = \left[-\hat{\mathbf{r}}_{i,j} + u\hat{\mathbf{r}}_{i,j+1} + (1-u)\hat{\mathbf{r}}_{i,j+2}\right] dv \tag{4.3}$$

$$d\mathbf{r}_u = \left[v\hat{\mathbf{r}}_{i,j+1} - v\hat{\mathbf{r}}_{i,j+2}\right] du. \tag{4.4}$$

The surface element and surface normal vector are then determined as $\hat{\mathbf{n}}_i dS_i = d\hat{\mathbf{r}}_v \times d\hat{\mathbf{r}}_u$.

It is crucial that the surface normals $\hat{\mathbf{n}}_i$ always point outward. A fourth arbitrary vertex of some face k, $\hat{\mathbf{r}}_{k,j}$, on the polyhedron is used to determine the direction of $\hat{\mathbf{n}}_i$ (See Fig. 4.9). The distance of $\hat{\mathbf{r}}_{k,j}$ to the vertex $\hat{\mathbf{r}}_{i,j}$ (or one of the other two vertices of face i) is

$$d = \hat{\mathbf{n}}_i \cdot (\hat{\mathbf{r}}_{k,j} - \hat{\mathbf{r}}_{i,j}). \tag{4.5}$$

If $d < 0$, the normal vector is already pointing outwards. Otherwise, the components of $\hat{\mathbf{n}}_i$ are multiplied by -1.

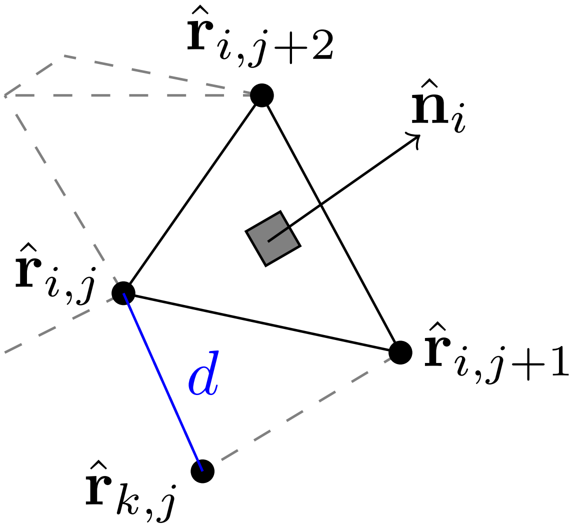

Figure 4.9: An example of an arbitrarily chosen vertex $\hat{\mathbf{r}}_{k,j}$ that is used to ensure that the surface normal vector $\hat{\mathbf{n}}_i$ points outwards. The blue line corresponds to the distance between $\hat{\mathbf{r}}_{i,j}$ and $\hat{\mathbf{r}}_{kj}$.

4.2.1.1 Inertia tensor for a general polyhedron

The inertia tensor for a polyhedron is also required to determine its rotational motion. The components of the moment of inertia tensor, of a general polyhedron, are given by (Dobrovolskis, 1996)

$$\mathcal{I}_{xx} = P_{yy} + P_{zz} \tag{4.6}$$

$$\mathcal{I}_{yy} = P_{xx} + P_{zz} \tag{4.7}$$

$$\mathcal{I}_{zz} = P_{xx} + P_{yy} \tag{4.8}$$

$$\mathcal{I}_{yz} = -P_{yz} \tag{4.9}$$

$$\mathcal{I}_{xz} = -P_{xz} \tag{4.10}$$

$$\mathcal{I}_{xy} = -P_{xy}, \tag{4.11}$$

where P_{ij} are the products of inertia.

The inertia tensor components are found by summing the inertia over every face. Consider a triangular face i with vertices $\hat{\mathbf{r}}_{i,j} = \mathbf{v}_1$, $\hat{\mathbf{r}}_{i,j+1} = \mathbf{v}_2$, $\hat{\mathbf{r}}_{i,j+2} = \mathbf{v}_3$, and the associated unit normal vector of the face $\hat{\mathbf{n}}_i$, then the inertia tensor component of each face, ΔP_{jk}, are given as

$$\begin{aligned}\Delta P_{jk} =& \frac{\rho \Delta V_i}{20}[2v_{1,j}v_{1,k} + 2v_{2,j}v_{2,k} + 2v_{3,j}v_{3,k} \\ &+ v_{1,j}v_{2,k} + v_{1,k}v_{2,j} + v_{1,j}v_{3,k} + v_{1,k}v_{3,j} + v_{2,j}v_{3,k} + v_{2,k}v_{3,j}]\end{aligned} \tag{4.12}$$

for $j, k = \{x, y, z\}$, and the volume element is determined as

$$\Delta V_i = \frac{1}{6}(\mathbf{v}_1 \cdot \hat{\mathbf{n}}_i) = \frac{1}{6}(\mathbf{v}_2 \cdot \hat{\mathbf{n}}_i) = \frac{1}{6}(\mathbf{v}_3 \cdot \hat{\mathbf{n}}_i). \tag{4.13}$$

The terms P_{kj} are then the sum of ΔP_{jk} over all the faces of the polyhedron. The inertia tensor of the polyhedron is also symmetric, e.g $\mathcal{I}_{xy} = \mathcal{I}_{yx}$ (Dobrovolskis, 1996).

4.2.2 Polyhedron potential

The gravitational potential of any general polyhedron, with uniform density ρ, is given by (Conway, 2015)

$$\Phi(\hat{\mathbf{r}}') = \frac{\rho G}{2} \sum_i \sum_j \hat{\mathbf{n}}_i \cdot (\hat{\mathbf{r}}_i - \hat{\mathbf{r}}')(Q_{i,j} + K_{i,j}), \tag{4.14}$$

and the gravitational field given as

$$\mathbf{g}(\hat{\mathbf{r}}') = -\rho G \sum_i \sum_j \hat{\mathbf{n}}_i (Q_{i,j} + K_{i,j}), \tag{4.15}$$

where $\hat{\mathbf{r}}'$ is an arbitrary point where the potential is evaluated, $\hat{\mathbf{n}}_i$ and outward pointing unit normal vector of the face i, and $\hat{\mathbf{r}}_i$ is an arbitrary point on the face. The parameter $Q_{i,j}$ is given by

$$\begin{aligned} Q_{i,j} = d_{i,j} \Bigg[\frac{c_{i,j}}{K_1} \left\{ \arctan\left(\frac{c_{i,j}(1 - b_{i,j})}{K_1 K_2} \right) + \arctan\left(\frac{c_{i,j} b_{i,j}}{a_{i,j} K_1} \right) \right\} \\ + \ln\left(\frac{1 - b_{i,j} + K_2}{a_{i,j} - b_{i,j}} \right) \Bigg], \end{aligned} \tag{4.16}$$

where

$$K_1 = \sqrt{a_{i,j}^2 - b_{i,j}^2 - c_{i,j}^2} \tag{4.17}$$

$$K_2 = \sqrt{1 + a_{i,j}^2 - 2b_{i,j}} \tag{4.18}$$

and

$$a_{i,j} = \frac{|\hat{\mathbf{r}}' - \hat{\mathbf{r}}_{i,j}|}{|\hat{\mathbf{r}}_{i,j+1} - \hat{\mathbf{r}}_{i,j}|} \tag{4.19}$$

$$b_{i,j} = \frac{(\hat{\mathbf{r}}' - \hat{\mathbf{r}}_{i,j}) \cdot (\hat{\mathbf{r}}_{i,j+1} - \hat{\mathbf{r}}_{i,j})}{|\hat{\mathbf{r}}_{i,j+1} - \hat{\mathbf{r}}_{i,j}|^2} \tag{4.20}$$

$$c_{i,j} = \frac{\hat{\mathbf{n}}_i \cdot (\hat{\mathbf{r}}' - \hat{\mathbf{r}}_{i,j})}{|\hat{\mathbf{r}}_{i,j+1} - \hat{\mathbf{r}}_{i,j}|} \tag{4.21}$$

$$d_{i,j} = \frac{(\hat{\mathbf{n}}_i \times (\hat{\mathbf{r}}' - \hat{\mathbf{r}}_{i,j})) \cdot (\hat{\mathbf{r}}_{i,j+1} - \hat{\mathbf{r}}_{i,j})}{|\hat{\mathbf{r}}_{i,j+1} - \hat{\mathbf{r}}_{i,j}|}. \tag{4.22}$$

Here, $\hat{\mathbf{r}}_{i,j}$ represents the j^{th} vertex of face i on the polyhedron. The term $K_{i,j}$ is given by

$$K_{i,j} = -|\hat{\mathbf{n}}_i \cdot (\hat{\mathbf{r}}' - \hat{\mathbf{r}}_{i,j})| \theta_{i,j} \tag{4.23}$$

with

$$\theta_{i,j} = \operatorname{sgn}\left(\hat{\mathbf{n}}_i \cdot ((\hat{\mathbf{r}}_{i,j} - \hat{\mathbf{r}}_p) \cdot (\hat{\mathbf{r}}_{i,j+1} - \hat{\mathbf{r}}_p))\right) \arccos\left(\frac{(\hat{\mathbf{r}}_{i,j} - \hat{\mathbf{r}}_p) \cdot (\hat{\mathbf{r}}_{i,j+1} - \hat{\mathbf{r}}_p)}{|\hat{\mathbf{r}}_{i,j} - \hat{\mathbf{r}}_p| \, |\hat{\mathbf{r}}_{i,j+1} - \hat{\mathbf{r}}_p|} \right). \tag{4.24}$$

where $\operatorname{sgn}(x)$ is the sign function, and $\mathbf{r}_p$ is a point along the edge of the face on the polyhedron (see Fig. 4.8) which takes the form

$$\hat{\mathbf{r}}_p = (\hat{\mathbf{n}}_i \cdot \hat{\mathbf{r}}_i)\, \hat{\mathbf{n}}_i - \hat{\mathbf{n}}_i \times (\hat{\mathbf{n}}_i \times \hat{\mathbf{r}}_i). \tag{4.25}$$

Tetrahedron vertices	Octahedron vertices	Ellipsoid semiaxes (a, b, c)
(0.5, -0.5, -0.5)	(1, 0, 0)	(1.0, 0.7, 0.5)
(-0.5, -0.5, 0.5)	(-1, 0, 0)	
(-0.5, 0.5, -0.5)	(0, 1, 0)	
(0.5, 0.5, 0.5)	(0, -1, 0)	
	(0, 0, 1)	
	(0, 0, -1)	

Table 4.1: The shape models used for the polyhedron test simulations. The units of the vertices and the semiaxes are given in dimensionless quantities.

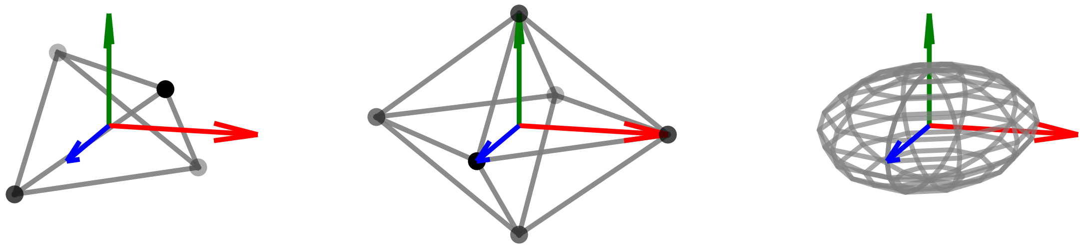

Figure 4.10: Illustration of the tetrahedron, octahedron and ellipsoid shapes used from Table 4.1. The blue, red and green arrows correspond to the local x, y and z-axes of the bodies.

4.2.3 Polyhedron simulation models

Due to the nature of the surface integration method and the polyhedron potential described by Eq. (4.14), the computation time increases significantly for polyhedral shapes with many faces. Therefore, we only consider polyhedra with low number of faces in these demonstrations.

Three shapes are considered; ellipsoid, tetrahedron, and octahedron. The vertices of the polyhedra, and the semiaxes of the ellipsoid, are listed in Table 4.1 and illustrated in Fig. 4.10. In the test simulations, all variables are given in dimensionless quantities, i.e. the gravitational constant is $G = 1$, similar to the work performed in the first paper (Ho et al., 2021).

The initial condition positions of body A and B are

$$\mathbf{r}_{0,A} = (-4, 0, 0) \tag{4.26}$$
$$\mathbf{r}_{0,B} = (4, 0, 0) \tag{4.27}$$

and the initial velocities are

$$\mathbf{v}_{0,A} = (0, 0.3, 0) \tag{4.28}$$
$$\mathbf{v}_{0,B} = (0, -0.3, 0). \tag{4.29}$$

Both bodies are initially rotating about their body-fixed axes, with initial angular velocities of $\hat{\omega}_z = 0.25$ radians per time unit. The rotation angles of both bodies are initially zero. Furthermore, both bodies have equal masses of $m = 2$. The shape of body A and B are specified in their respective section. We also run the simulations up to $t = 1000$, four times longer than the work of Ho et al. (2021). The embedded Runge-Kutta method of order 5(4) by Dormand and Prince (1980), with adaptive time-stepping, is used for the test simulations.

4.2.4 Interaction between ellipsoid and polyhedron

We first consider simulations where the system consists of an ellipsoid and a polyhedron. These simulations are compared to simulations with two ellipsoids. The ellipsoid is considered as body A, while the polyhedron is considered as body B. In all the test simulations, swapping the body shapes, i.e. the polyhedron is body A and body B the ellipsoid, does not change the outcome of the simulations in any significant manner.

4.2.4.1 Ellipsoid-Tetrahedron system

In the first test simulation, we consider the interaction between an ellipsoid and a tetrahedron. Here, the most notable difference in the dynamics of the bodies is the angular velocity component $\hat{\omega}_z$, illustrated in the top panels of Fig. 4.11. The change in the $\hat{\omega}_z$ of the tetrahedron is roughly two orders of magnitude smaller than the ellipsoid. Upon further inspection, the magnitude of the torque acting on the tetrahedron is also two orders of magnitude smaller than the torque acting on the ellipsoid. This may be because the torque contributions from each face cancel out.

Despite starting with no initial tilt angles, the shape symmetry of the tetrahedron will result in a small force along the z-direction, leading to non-planar motion. This is illustrated in the bottom left panel of Fig. 4.11. However, the motion along the z-direction is 4 orders of magnitude smaller than the motion along the x and y-directions.

The bottom right panel of Fig. 4.11 shows the error in the total energy, relative to the energy at the first time step. The green line corresponds to the simulation where force is computed by integrating over the ellipsoid surface, while the orange line corresponds to the simulation where the force is computed by integrating over the tetrahedron surface. Both approaches result in energy errors at the fifth decimal digit, which is reasonable for an order five Runge-Kutta method. The small differences between the two approaches are negligible and are mainly caused by the errors associated with the surface integration routine. Compared to the simulations in Ho et al. (2021), the energy errors for the ellipsoid-tetrahedron system are roughly three orders of magnitude larger. This is because the order 9(8) Runge-Kutta method by Verner (2010) is used in Ho et al. (2021), hence resulting in smaller errors in the total energy. Using the order 9(8) method by Verner (2010) will give energy errors four magnitudes smaller than what is shown in Fig. 4.11, but also significantly increases the computation time.

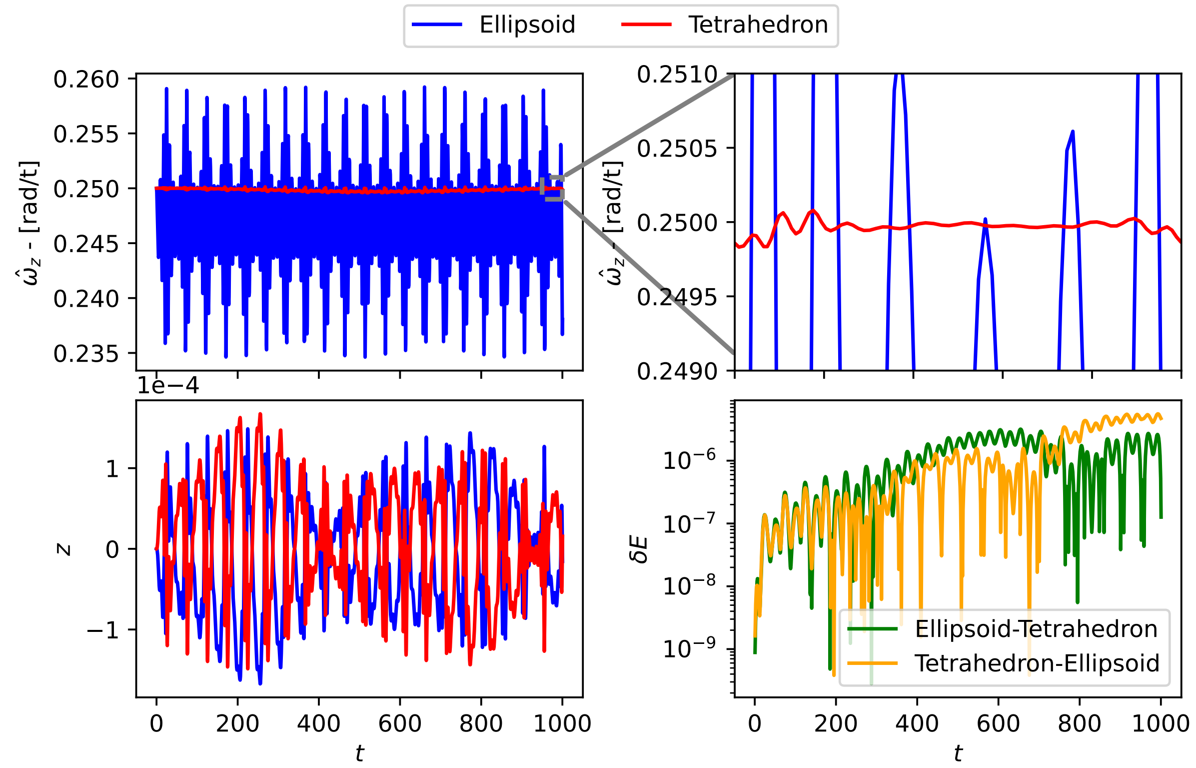

Figure 4.11: Results of a simulation consisting of an ellipsoid and a tetrahedron. The top left panel shows the $\hat{\omega}_z$ component of the bodies, while the top right panel shows a zoomed-in segment of $\hat{\omega}_z$. The bottom left panel shows the z-positions of the bodies in the inertial frame. Finally, the bottom right panel shows the error in the total energy of the system for two simulation types: One where the force is computed by integrating over the ellipsoid surface (green), and the other by integrating over the tetrahedron surface (orange).

4.2.4.2 Ellipsoid-Octahedron system

Changing the shape of the tetrahedron to an octahedron mainly affects the rotational motion of the octahedron. For the tetrahedron case, all angular velocity components are fluctuating over time. For the octahedron, however, the $\hat{\omega}_x$ and $\hat{\omega}_y$ components remain zero throughout the simulation, as illustrated in Fig. 4.12. This is due to the sphere-like symmetry of the octahedron, in which all sides are equal. Furthermore, similarly to the ellipsoid-tetrahedron simulation, the change in the $\hat{\omega}_z$ component of the octahedron is also two orders of magnitude smaller compared to the ellipsoid.

Because of the shape symmetry of the octahedron, there will, in theory, be no motion along the z-direction. However, because of round-off errors in the surface integration scheme from each face, a small force along the z-direction arises and results in non-planar motion. Despite this, the magnitude of this motion is of order 10^{-10} and can be neglected. The energy for this case is conserved to the 6th decimal digit.

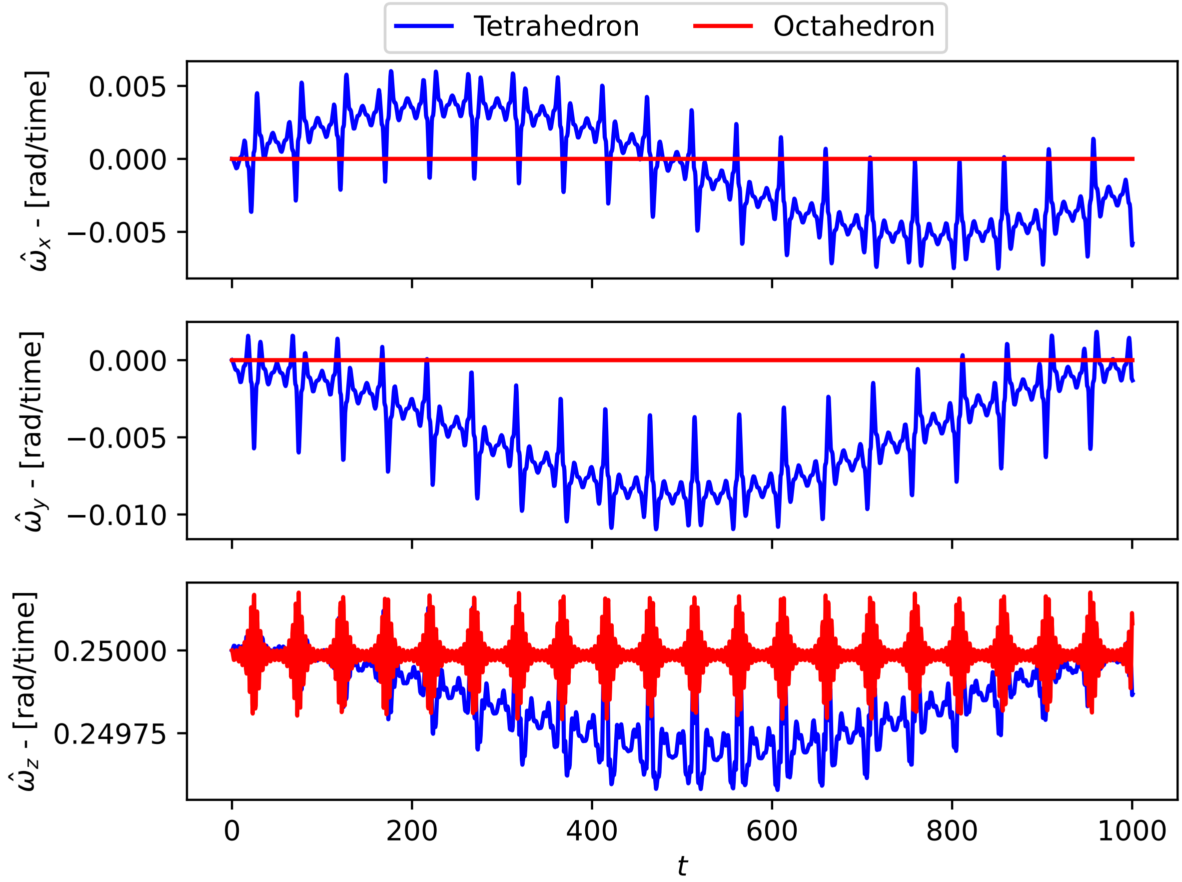

Figure 4.12: The difference in the angular velocity, when body B is either a tetrahedron (blue) or an octahedron (red), in the ellipsoid-polyhedron simulations. The top, middle and bottom rows correspond to the $\hat{\omega}_x$, $\hat{\omega}_y$ and $\hat{\omega}_z$ components respectively.

4.2.5 Interaction between two polyhedra

Allowing both bodies to take polyhedral shapes, instead of allowing one to be an ellipsoid, mainly affects the rotational motion of the bodies. The angular velocity components of the bodies, for the two-tetrahedron and tetrahedron-octahedron simulations, are shown in Fig. 4.13. The rotational motions of each respective body do not deviate much from the ellipsoid-polyhedron scenarios. For the two-tetrahedron simulation, the $\hat{\omega}_x$ and $\hat{\omega}_y$ components are opposite. This is due to the gravitational interactions caused by the shape symmetry of the bodies, resulting in the x and y components of the torque becoming equal but opposite. The $\hat{\omega}_z$ components, on the other hand, are practically identical. Changing body B to an octahedron does not alter the angular velocity components of the tetrahedron, and the rotational motion of the octahedron is also identical to what was seen in the ellipsoid-octahedron simulation.

A notable difference in the translational motion is the motion along the z-direction. This is illustrated in Fig. 4.14, which shows the z-position of body B relative to body A. The differences in the z-position are almost indistinguishable between the ellipsoid-tetrahedron and the tetrahedron-octahedron simulations. However, for the two-tetrahedron simulation, the motion along the z-direction is of order 10^{-9}, five orders of magnitude

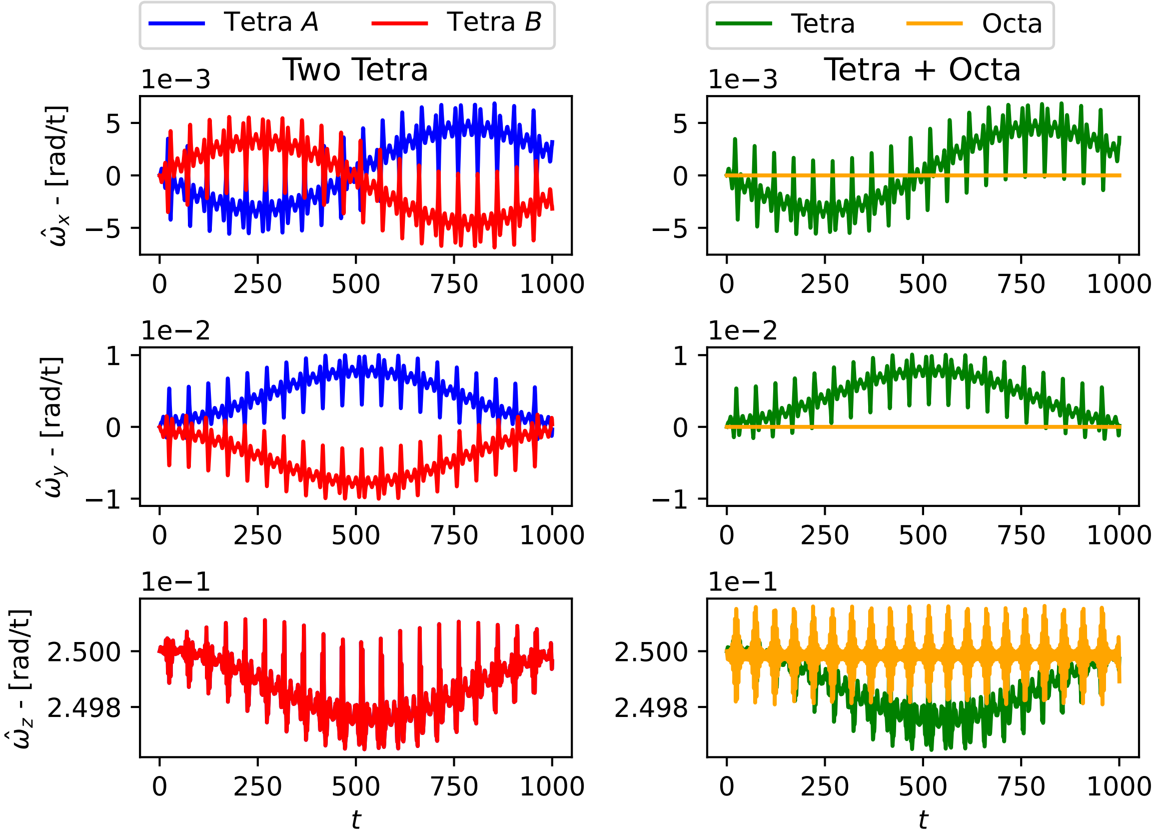

Figure 4.13: Simulation results of the angular velocity components of the bodies. The left panel shows the two-tetrahedron simulation, while the right panel shows the tetrahedron-octahedron simulation. "Tetra" and "Octa" labels correspond to tetrahedron and octahedron respectively.

smaller than the former two test cases. The z-component of the force cancels out due to the shape symmetry of the tetrahedra.

4.2.6 Significance of polyhedral shapes

From the simulations in the previous two sections, changing the asteroid shape from an ellipsoid to a polyhedron mainly affects the rotational motion of the bodies. This result is similar to the results in the third paper, in which the differences in the torque, between an exact method and an approximation, are larger than the differences in the forces, thus resulting in larger discrepancies in the rotational motion (Ho et al., 2023). Accurate shape models should therefore be used if one desires high precision to the rotational motion. However, the polyhedron models considered in this chapter are very simple and do not accurately represent the true shape of an asteroid. Using a more detailed polyhedron shape may have different results from what is shown in this chapter.

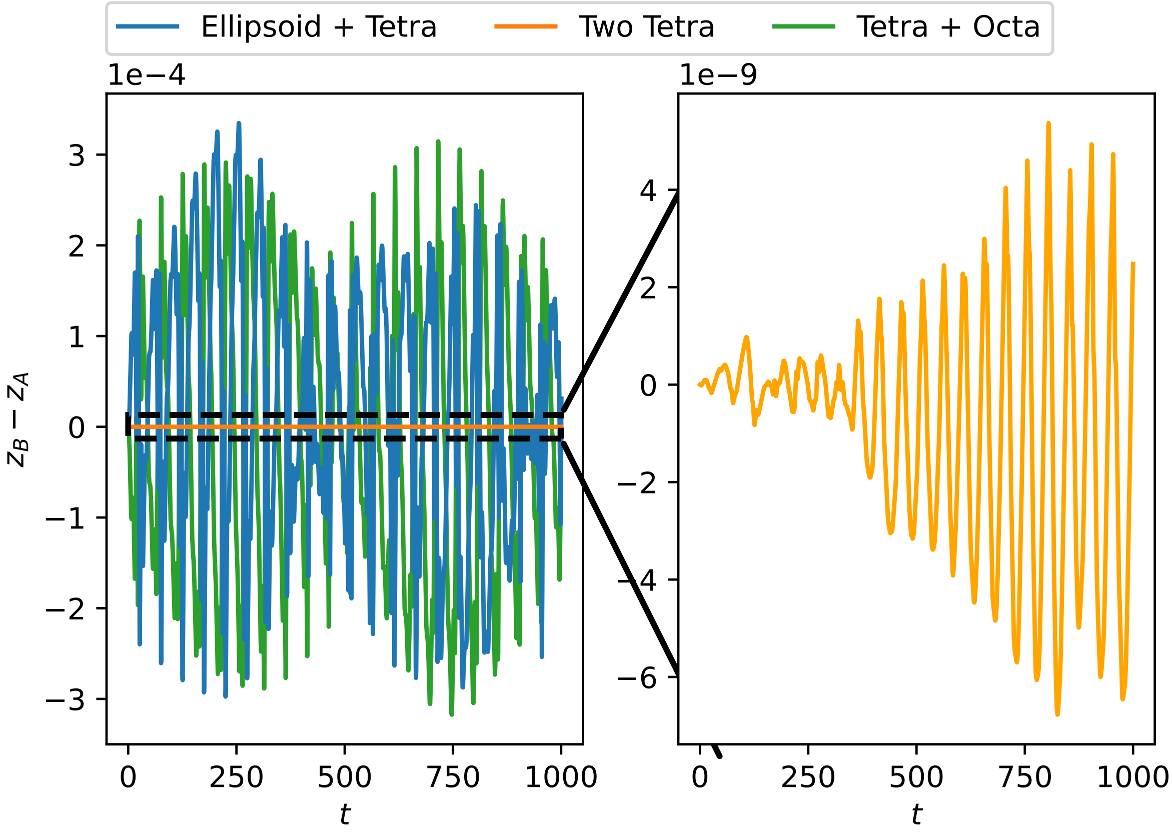

Figure 4.14: Simulation results of the z-positions of body B, relative to body A, as functions of time. The right panel shows a zoomed-in segment of the position. The first named shape in the labels corresponds to body A, while the second corresponds to body B. "Tetra" and "Octa" correspond to tetrahedron and octahedron respectively.

4.3 Numerical limitations

As with all numerical methods, round-off errors always take place due to limitations in the computer arithmetic in representing floating-point numbers. In this section, different limitations associated with the project are considered, and the significance of these constraints is discussed.

4.3.1 Numerical limitations to the ellipsoid potential

During the comparisons of the mutual potential approaches (as discussed in Sect. 4.1.1), we noticed that the differences in the computed forces and torques approached 100% when the separation between the two ellipsoids becomes too large. Upon closer inspection, when the separation reaches a limit, the force computed from the surface integration method increases with separation, while it is expected that the force to continuously decrease when the distance increases. The issue is caused by round-off errors in the ellipsoid potential. However, these round-off errors will not affect the majority of the full-two body problems, as the errors arise at distances far beyond the orbits of observed secondaries in NEA binary systems.

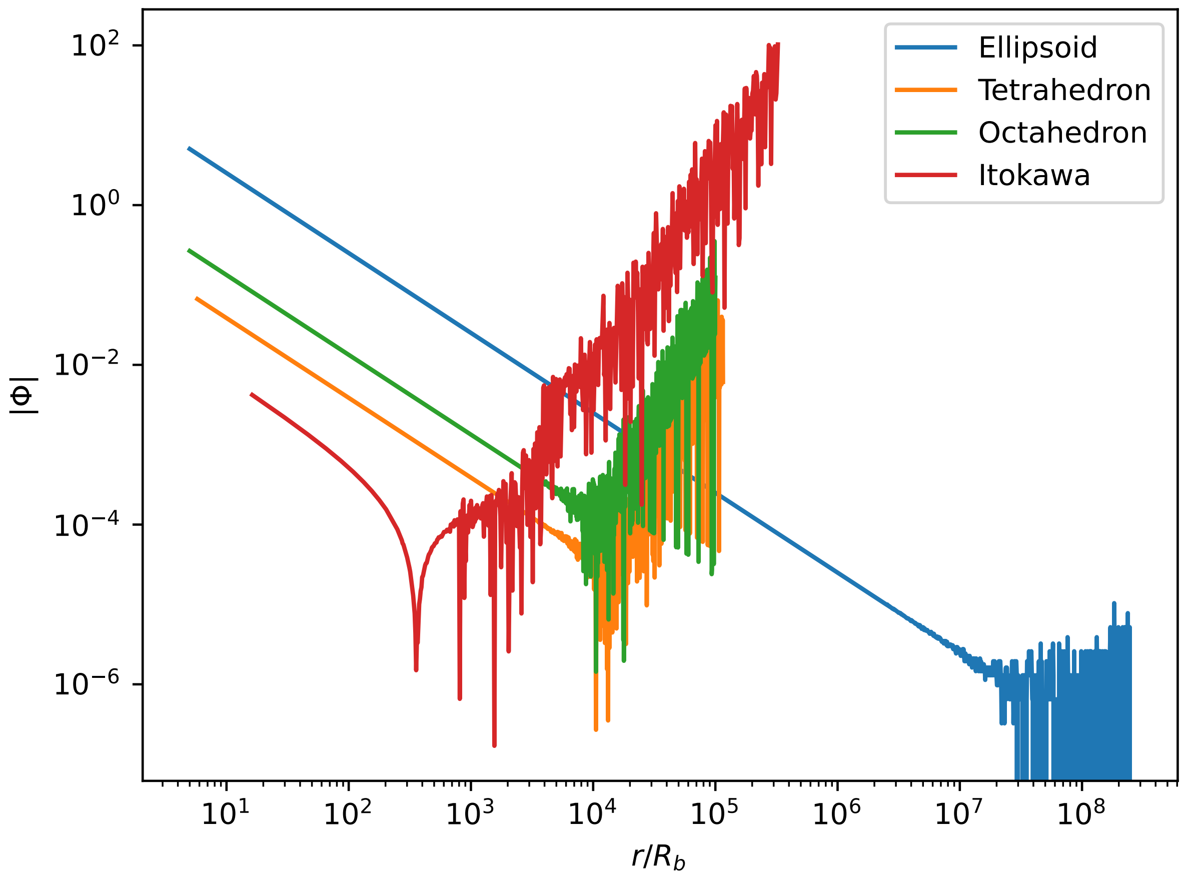

Figure 4.15: Illustration of round-off errors in the ellipsoid and polyhedron potentials when the separation becomes large. Three polyhedron shapes are considered. The ellipsoid semiaxes, tetrahedron, and octahedron shapes are given in Table 4.1, while the Itokawa polyhedron shape is given by Gaskell et al. (2006). R_b is the radius of the bounding sphere of the body, and $R_b = a$ for the ellipsoid. All parameters have dimensionless quantities.

Here, we briefly illustrate the round-off error behavior to the ellipsoid potential evaluated at arbitrary points. We consider dimensionless quantities, i.e. $G = 1$. An ellipsoid with semiaxes $(a, b, c) = (1.0, 0.7, 0.5)$ and density $\rho = 1$ is used as a demonstration. The value of the ellipsoid potential should become smaller if the evaluation point is further away from the ellipsoid. If the separation surpasses $\sim 10^8 a$, the calculated potential starts to increase, as illustrated by the blue line in Fig. 4.15. However, at these distances, the translational and rotational motion in a two-body problem effectively decouples, and the spin rates of the bodies remain constant (Scheeres, 2002). The bodies can therefore be treated as point masses, and using the point mass potential may be more beneficial to reduce the computation times. Furthermore, observations of NEA binary systems show that most secondaries have orbits within 7 primary radii (Pravec et al., 2016), which is far below the limit where round-off errors cause issues to the ellipsoidal potential.

The reason for the round-off errors is due to a small number being multiplied by a larger one. As $r \to \infty$, the elliptic integrals associated with the ellipsoid potential approach zero. These elliptic integrals are then multiplied with the Cartesian coordinates (x, y, z), which take large values as the separation increases. Because a float-point number can only be represented by a limited number of digits, the digits from the elliptic integrals are lost when multiplied by a large number. As a consequence, the resulting ellipsoid potential becomes larger and larger.

The limitation on the ellipsoid potential is purely numerical. It can be analytically shown that the ratio between the ellipsoid potential and the point mass potential converges to one as $r \to \infty$ (see Appendix B.2). A similar proof can also be shown for the gravitational fields between an ellipsoid and a point mass.

4.3.2 Numerical limitations to the polyhedron potential

Similar to the ellipsoid potential, the polyhedron potential outlined by Conway (2015) also suffers from round-off errors when the separation becomes large. However, the round-off errors take place at far smaller separations compared to that of an ellipsoid. The polyhedron potential is the sum of the gravitational potential contributions from all faces of the body. Round-off errors from each term will therefore add up, and become more apparent if the polyhedron is made up of more faces.

Three polyhedral shapes are considered to illustrate the round-off errors to the polyhedron potential; the tetrahedron and octahedron shapes from Table 4.1, and the Itokawa polyhedron shape from Gaskell et al. (2006). The Itokawa vertices are given as dimensionless quantities. The body radius, R_b, of the polyhedron is defined by the distance between the center of mass of the polyhedron and the vertex furthest away from the center of mass.

Figure 4.15 illustrates how the polyhedron potential of the various polyhedral shapes changes with the separation. Similar to the ellipsoid potential, the value of the polyhedron potential decreases with increasing separation. However, when the separation surpasses roughly $10^4 R_b$, the gravitational potentials of the tetrahedron and octahedron increase due to round-off errors. For reference, the ellipsoid potential starts to experience similar issues when $r \gtrsim 10^8 R_b$. For the Itokawa shape model, the potential suffers from round-off errors when $r \gtrsim 250 R_b$. Despite these round-off errors, the separations considered are still far beyond the orbits of observed NEA binaries.

Another issue with the polyhedron potential outlined by Conway (2015) is that the resulting potential becomes imaginary. Round-off errors may cause the term under the square root in Eq. (4.17) to become a very small number. This may sometimes be rounded to a small negative number, causing the potential to become imaginary. This can be mitigated by increasing the float point precision of the variables when the potential is computed, but that also significantly increases the computation time.

4.4 Summary

In this chapter, we have explored the significance of using the surface integration method to study the dynamics of ellipsoidal bodies by comparing it to a method that expands the mutual potential with inertia integrals. Using a more accurate model to determine the mutual potential becomes more important when the bodies are very close. However, expanding the mutual potential up to order four is sufficient to determine the dynamics of binary asteroids, provided that they are far apart.

We have also investigated how changing the shape models change the dynamics of a two-body system. Modeling an asteroid with a polyhedron instead of an ellipsoid mainly affected the rotational motion of the body.

Finally, numerical round-off errors that may arise have been studied and discussed. Round-off errors are only significant if the separation between the bodies is very large. This is, however, not an issue for most F2BP simulations, as asteroid binaries have separations far smaller than the distances required for the round-off errors to take place.

Chapter 5

Concluding remarks

5.1 Summary of research

In this thesis, the surface integration method outlined by Conway (2016) is numerically implemented. The main application of the approach is to study the dynamics of non-spherical objects, such as asteroids. It is common to utilize approximations in order to determine the mutual potential of two non-spherical bodies, for instance, through series expansions. These approximation-based approaches suffer from truncation errors and divergence problems when the interacting bodies are close. This is, however, not an issue for the surface integration method, which can yield exact results for ellipsoidal bodies even when the bodies are close.

The surface integration method was first demonstrated by Wold and Conway (2021), and later extended in the first paper to include non-planar motion (Ho et al., 2021). The method was demonstrated on two dimensionless spheroidal systems, and also on the 1994 KW4 binary system with ellipsoidal shapes. The simulations conserved both the total energy and total angular momentum to the 11th decimal digit. To our knowledge, this is the first study of the full F2BP with ellipsoids using an exact method without using approximations. Furthermore, the tool developed from this work is published as an open-source software. The code is also generalized as an N-body code, allowing one to study multi-body problems for extended bodies.

In the second paper of the thesis, we applied the surface integration approach to study the dynamics of asteroid systems after a contact binary has separated due to rotational fission (Ho et al., 2022). In this work, we made use of the advantage of the surface integration method by starting the two bodies closer to each other, thus allowing us to study more realistic initial conditions compared to the work of Boldrin et al. (2016). We considered six models, with varying densities and shapes of the secondary. The results were compared to other theoretical works, such as the reason for an increased number of secondary fission events when the secondary becomes more elongated. Furthermore, the rotation periods of both bodies from the simulations were compared to observed data of asteroid binaries and pairs. Despite limiting the simulations to 200 days, the rotation periods from the simulations are within the range of the rotation periods of asteroid pairs. Moreover, for simulations labeled as 'stable', the rotation periods of the secondaries is also within the range of those among observed NEA binaries. However, the rotation periods of the primaries in our simulations range between $15 - -25$ hours, while primaries among NEA binaries have rotation periods shorter than 4.4 hours.

The significance of the use of an exact method to determine the mutual potential energy of non-spherical objects was demonstrated in the third paper (Ho et al., 2023). The surface integration method was compared to the mutual potential formulation of Hou et al. (2017). Truncating the mutual potential to order four is sufficient to describe the dynamics of asteroid binaries if the separation is large enough. For a binary system with an initial separation of ~ 4.5 primary radii, the differences in the translational and rotational motion of the bodies were smaller than 0.01% when the fourth-order potential was compared to the surface integration method. On the other hand, when a rotational fission scenario was considered, the differences in the dynamics surpassed 100% within the first five hours of the simulations. Using a mathematically exact method to calculate the mutual potential between two non-spherical bodies is therefore important to accurately determine the dynamics of rotationally fissioned asteroid systems.

Using different methods to determine the mutual gravitational potential between two non-spherical bodies has a larger effect on the rotational motion compared to the translational motion. When the surface integration method was compared to the mutual potential approach by Hou et al. (2017), it was shown that the difference in the gravitational forces were roughly an order magnitude smaller than the gravitational torques. This is also the case when ellipsoidal shapes are changed to polyhedral shapes.

5.2 Future work

Previous studies on the F2BP have used approximations to study the dynamics of two irregular bodies. However, we have used an exact method, through the use of surface integrals. Several project may arise with the use of the code developed in this thesis.

Correia (2018) studied the stability of the (47171) Lempo triple system as a 3-body problem. The stability was investigated by considering different shapes of the bodies, and the mutual potential was modeled through series expansions. Because the software of this project is generalized as an N-body code, future work may involve a similar stability study of asteroid triple systems. This can be applied to the Lempo system, or NEA triple systems such as (136617) 1994 CC (Brozović et al., 2011) or (153591) 2001 SN263 (Becker et al., 2015).

An accurate shape model of an asteroid may produce more realistic simulations. Future research may involve simulations with detailed asteroid polyhedron shapes. The work of Davis and Scheeres (2020a) used polyhedra to model the asteroids and used the mutual potential description by Hou et al. (2017) to study the dynamics. This may therefore be used to compare the results produced by an exact method.

Similar to the work of Davis and Scheeres (2020a), it may be of interest to include non-gravitational effects, such as tidal forces, together with the surface integration scheme. This can be used to study how the rotational motion of the asteroids may stabilize over time, and thus result in synchronized orbits.

The work in Ho et al. (2023) showed that the use of an exact method to determine the mutual potential results in higher energy configurations for post-fissioned asteroid systems, compared to a method that expands the mutual potential. It may be of interest to study how the dynamics of such systems differ. For instance, one can compare the number of systems that end up with an impact between the two bodies or how long it takes for the secondary to escape. It may also be beneficial to compare the surface integration scheme with expansion methods for an ellipsoid-polyhedron system, as one of the bodies is now modeled with higher precision.

Reducing the integral dimensions is of great importance for computational efficiency. Whether or not the surface integrals presented by Conway (2016) can be further reduced down to line integrals may be worth investigating.

Appendix A

Numerical methods

A.1 Runge-Kutta solvers

Solving ordinary differential equations (ODEs) is a central part of the full two-body problem (and also N-body problems). A Runge-Kutta method is one of the most common approaches to solve ODEs. The advantage of Runge-Kutta methods is that they are efficient and can give very accurate results. Another advantage is that adaptive time steppers can be implemented through the use of embedded Runge-Kutta methods (see e.g. Hairer et al., 2000). Adaptive time steppers can speed up the simulations considerably but also slow down in order to solve the ODEs more accurately near difficult points, e.g. when the bodies are close, by reducing the time step.

Several Runge-Kutta methods, from the standard order four to an embedded order 12, have been implemented in the software. The scheme by Dormand and Prince (1980) is included in the project and is perhaps one of the most common embedded Runge-Kutta methods as it can be found as the default ODE solver in many scientific libraries, such as `scipy` and `matlab`. Verner has presented a number of embedded Runge-Kutta solvers, ranging from order 6(5) to 9(8) (Verner, 1991, 2010). Another order 9(8) method by Tsitouras (2001) has also been implemented in the software and can give results that can be even more accurate than the one by Verner. Even higher-order methods, such as the order 10(8) and 12(10) by Feagin are also implemented (Feagin, 2007, 2012).

One drawback with Runge-Kutta methods is that they are unable to maintain energy conservation for long time periods, resulting in a drift in the orbits. Symplectic integration methods can be used as an alternative, as they can conserve the energy of the system for long time periods (see e.g. Sanz-Serna, 1992). However, implementation of adaptive time steppers for symplectic integrators has been a long-standing problem (see e.g. Richardson and Finn, 2012), and symplectic methods with variable step-sizes are often not as efficient as those with constant step-sizes (Sanz-Serna, 1992).

A.1.1 Benchmarking

To illustrate their accuracies, we conduct a benchmarking on the implemented Runge-Kutta solvers, using adaptive time stepping. The simulation scenario is the ellipsoid simulation of the 1999 KW4 binary system studied by Ho et al. (2021), but the simulation time is now 100 hours instead of 1 year. It was already illustrated by Ho et al. (2021) that the relative error in the total energy can be as low as 10^{-15} using the order 9(8) by Verner (2010).

Different error tolerance values are considered, from $\epsilon_{user} = 10^{-6}$ to $\epsilon_{user} = 10^{-15}$, which are used to determine when the step size must be reduced. A lower tolerance value corresponds to a more accurate simulation, but at a cost of added computation time. To measure the accuracy, we measure the change in the total energy of the system. Because no external forces are acting on the system, the total energy should be constant. To study how the total energy is conserved, we compute the relative error as

$$\delta E = \left| \frac{E_{i+1} - E_0}{E_0} \right|, \quad \text{for } i = 0, 1, 2, ..., N_s - 1, \tag{A.1}$$

where N_s is the number of time steps. Ideally, the relative error should be zero. However, because of numerical round-off errors, this will rarely be the case. In all test scenarios, the minimum step size allowed is set to be $h_{min} = 0.4$ hrs. This ensures that the errors and computation times between the methods are comparable, as some of the adaptive time step implementations may vary which may cause the time steps to become far smaller than this limit despite using the same tolerance values.

The relative error will vary with the simulation time. We therefore compare the average of Eq. (A.1) and compare it with the CPU time, which is the time required for the software to complete the simulation. Figure A.1 shows the average error in the total energy as a function of the CPU time. The accuracy of the majority of the methods can reach below 10^{-10}, and lower-order methods often take a longer time to reach this accuracy. Despite this, the evaluation times are typically below 150 CPU seconds, unless the user-specified tolerance is low enough or a higher-order method is used. As expected, the errors from the lower-order schemes are larger than the higher-order methods, but the CPU time is also lower. Despite being a lower-order scheme, the order 10(8) algorithm by Feagin can be both faster and more accurate than the 12(8) method. The order 9(8) schemes by Verner (2010) and Tsitouras (2001) are similar when $\epsilon_{user} \lesssim 10^{-9}$. However, when the user-specified tolerance is small enough, the errors from Verner's method become almost 2 orders of magnitude smaller than the ones from Tsitouras. While the errors become smaller with increased CPU time, if the tolerance value becomes too small, the errors start to increase again for the methods of order 8 or higher. However, this increase is small enough to be negligible, but using slightly larger tolerance values may be more beneficial for the higher-order methods in order to obtain optimal efficiency and accuracy.

It should also be noted that the evaluation time will also depend on the required accuracy of the surface integration methods. The software utilizes the QAG adaptive integration algorithm, implemented by the GNU Scientific Library (GSL) (Galassi et al., 2002). The integration scheme can take different orders from one to six, where higher orders correspond to more accurate results, but at the cost of additional computation time. Using an order four integration scheme can run twice as fast compared to an order six scheme, and the difference in the results are less than 10^{-11}, unless the bodies are initially very close (Ho et al., 2023). The benchmark results shown in Fig. A.1 use an order six QAG integration scheme.

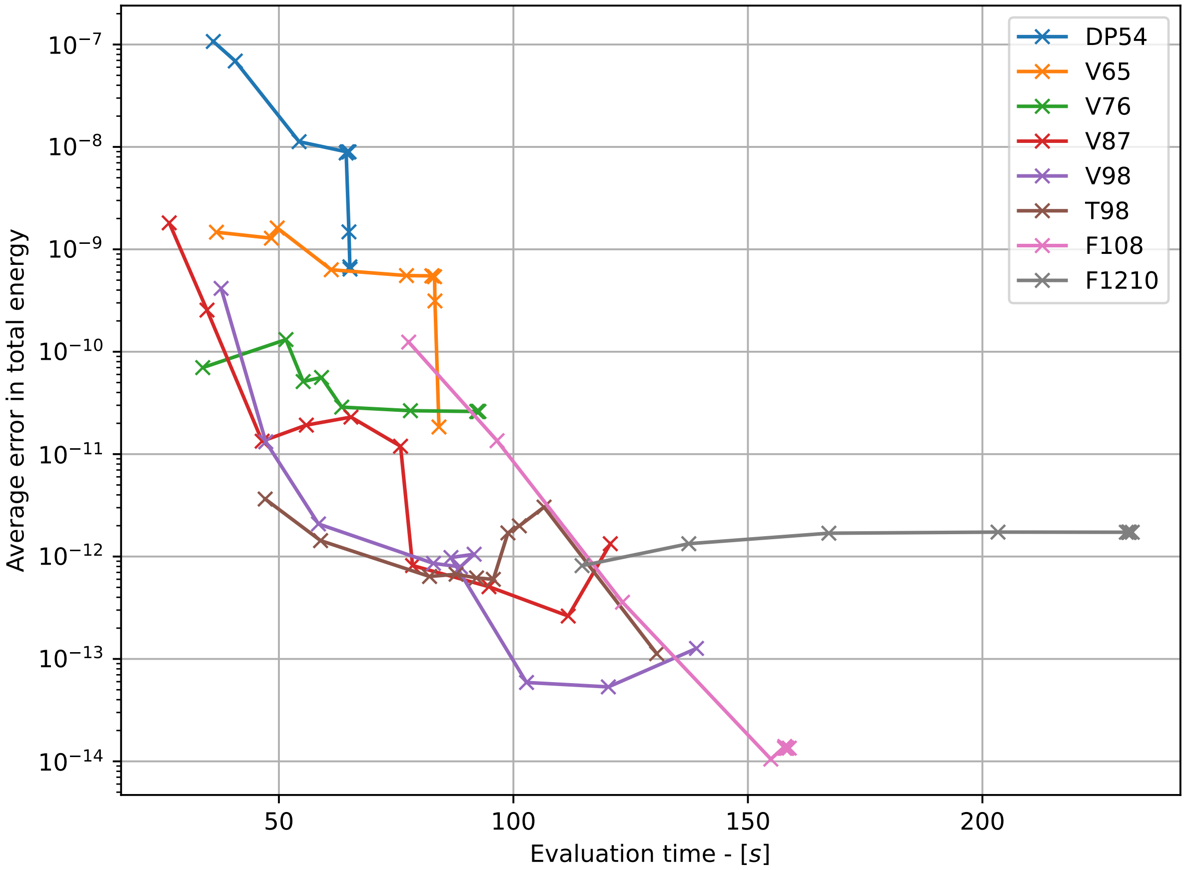

Figure A.1: The accuracy of the implemented Runge-Kutta methods as functions of the evaluation time. The accuracy is based on the average of the relative error computed by Eq. A.1. The simulation is that of the 1999 KW4 system studied by Ho et al. (2021) using ellipsoidal shapes, but the simulation time is now 100 hours instead of 1 year.

Despite the drawbacks of energy conservation from the Runge-Kutta methods, the errors in the energy conservation are smaller than 10^{-7}. Using a higher-order Runge-Kutta method, with a reasonably small error tolerance, should therefore not suffer from the effects of energy loss for most types of simulations related to this project.

A.2 Ellipsoid intersection algorithm

The algorithm that determines the intersection of two ellipsoids follows the work of Alfano and Greer (2003). This algorithm is an eigenvalue problem that solves the following system of equations

$$\left(S'_A\right)^{-1} S'_B X = \lambda X, \tag{A.2}$$

where λ is the eigenvalue, $X = [x_i, y_i, z_i, 1]$ the vector that determines the intersection point and S'_j represents the shape of ellipsoid j. For any general ellipsoid with semi-axes $a > b > c$, centered at position $[x_0, y_0, z_0]$, the matrix S takes the form

$$S_j = \frac{1}{2}\begin{bmatrix} 2a_j^{-2} & 0 & 0 & -2x_{0,j}a_j^{-2} \\ 0 & 2b_j^{-2} & 0 & -2y_{0,j}b_j^{-2} \\ 0 & 0 & 2c_j^{-2} & -2z_0c_j^{-2} \\ -2x_{0,j}a_j^{-2} & -2y_{0,j}b_j^{-2} & -2z_{0,j}c_j^{-2} & K_j \end{bmatrix} \tag{A.3}$$

$$K_j = \left(\frac{x_{0,j}}{a_j}\right)^2 + \left(\frac{y_{0,j}}{b_j}\right)^2 + \left(\frac{z_{0,j}}{c_j}\right)^2 - 1. \tag{A.4}$$

In order to take into account the rotation of the ellipsoid, the matrix S is modified as

$$S' = \bar{\mathcal{R}} S \bar{\mathcal{R}}^T, \tag{A.5}$$

where $\bar{\mathcal{R}}$ is a 4×4 rotation matrix and the superscript T denotes the transpose. This rotation matrix is similar to any other rotation matrices described either through Tait-Bryan angles or Euler parameters, and takes the form

$$\bar{\mathcal{R}} = \begin{bmatrix} & & & 0 \\ & \mathcal{R} & & 0 \\ & & & 0 \\ 0 & 0 & 0 & 1 \end{bmatrix}, \tag{A.6}$$

where $\mathcal{R}$ is the 3×3 rotation matrix described either by Tait-Bryan angles or Euler parameters.

The eigenvalues, λ, are used to determine if the ellipsoids intersect or not. Despite satisfying four equations, there are only two solutions of λ that are of importance. There are three possible outcomes:

1. If both solutions of λ are imaginary, the ellipsoids intersect, i.e. there is an overlap of the surfaces.

2. If both solutions are real and equal, i.e. $\lambda_1 = \lambda_2$, then the ellipsoids are touching at exactly one spot on each respective surface.

3. If neither of the conditions above are satisfied, then there are no contact between the ellipsoids.

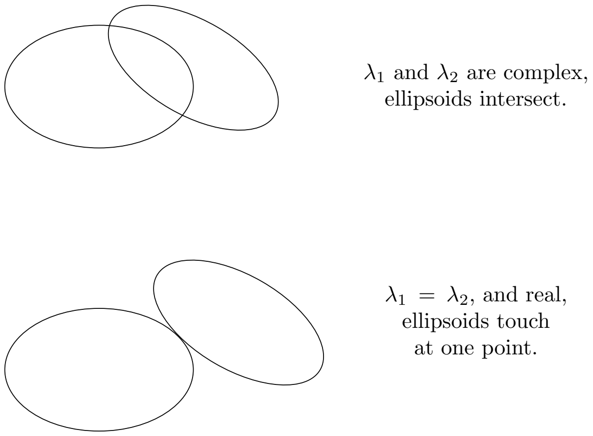

Figure A.2: Illustration of the solutions of the ellipsoid intersection algorithm by Alfano and Greer (2003).

Figure A.2 illustrates possible configurations when points 1 or 2 are satisfied.

This algorithm can also be used in reverse. If an intersection point is known and one of the ellipsoids is centered at the origin, then it is possible to find the coordinate of the centroid of the second ellipsoid. This approach is used in the third paper to determine the location of the secondary while it is touching the surface of the primary. These configurations are then used to compare the differences in the computed forces and torques between the surface integration method and a method that approximates the mutual potential (Ho et al., 2023).

Consider two ellipsoids A and B, with ellipsoid A centered at the origin and ellipsoid B centered around x_0, y_0, z_0. Assuming that the ellipsoids are touching (satisfying condition 2) at the point x_i, y_i, z_i, we have to solve the following equations

$$\left(\frac{a_A}{a_B}\right)^2 (x_i - x_0) = \lambda x_i \tag{A.7}$$

$$\left(\frac{b_A}{b_B}\right)^2 (y_i - y_0) = \lambda y_i \tag{A.8}$$

$$\left(\frac{c_A}{c_B}\right)^2 (z_i - z_0) = \lambda z_i \tag{A.9}$$

$$\frac{x_0 x_i}{a_B^2} + \frac{y_0 y_i}{b_B^2} + \frac{z_0 z_i}{c_B^2} - K_B = \lambda. \tag{A.10}$$

These equations also assume that none of the ellipsoids are rotated, i.e. $\bar{\mathcal{R}}$ is an identity matrix. Because there are two solutions of λ, one solution will result in ellipsoid B residing inside ellipsoid A, and the other where it is outside. Checking the distance between the centroids is then used to determine which solution corresponds to the latter solution.

Appendix B

Analytical proofs

B.1 Gravitational torque from second order expansion of inertia integrals

The results of chapter 4.1.1 showed that the gravitational torques become zero when the separation vector, $\mathbf{r}$, is parallel with one of the principal axes if the mutual potential is truncated to order two. This is a mathematical limitation to the mutual potential. In this section, we briefly inspect where this limitation arises.

Consider two extended bodies A and B (see Fig. B.1). The gravitational force from body A induces a torque on body B about its rotation axis B^*, which can be expressed as (Kane et al., 1983)

$$\mathbf{M}_B = \frac{3Gm_B}{r^3}\left[\mathbf{b}_1(I_3 - I_2)C_2C_3 + \mathbf{b}_2(I_1 - I_3)C_3C_1 + \mathbf{b}_3(I_2 - I_1)C_1C_2\right]. \tag{B.1}$$

Here, m_B is the mass of body B, r the separation between the mass centers of the two bodies, $\mathbf{b}_i$ the unit vector components parallel to the principal axis of body B (for $i = 1, 2, 3$), and

$$I_i = \mathbf{b}_i \cdot \mathcal{I}_B \cdot \mathbf{b}_i, \tag{B.2}$$

where $\mathcal{I}_B$ is the inertia tensor of body B. The parameter C_i is

$$C_i = \mathbf{a} \cdot \mathbf{b}_i, \tag{B.3}$$

where $\mathbf{a}$ is the unit vector parallel to the separation vector $\mathbf{r}$.

From these expressions, if $\mathbf{r}$ is parallel with one of the principal axes, corresponding to $\mathbf{a}$ becoming parallel to one of the $\mathbf{b}_i$ components, then two of the three C_i factors become zero. This therefore results in a zero torque acting on body B if the mutual potential is truncated to order two.

B.2 Convergence of potentials

From what was shown in chapter 4.3.1, the errors that arise from the ellipsoid potential are due to numerical round-off errors as a result of a large number multiplied by a small

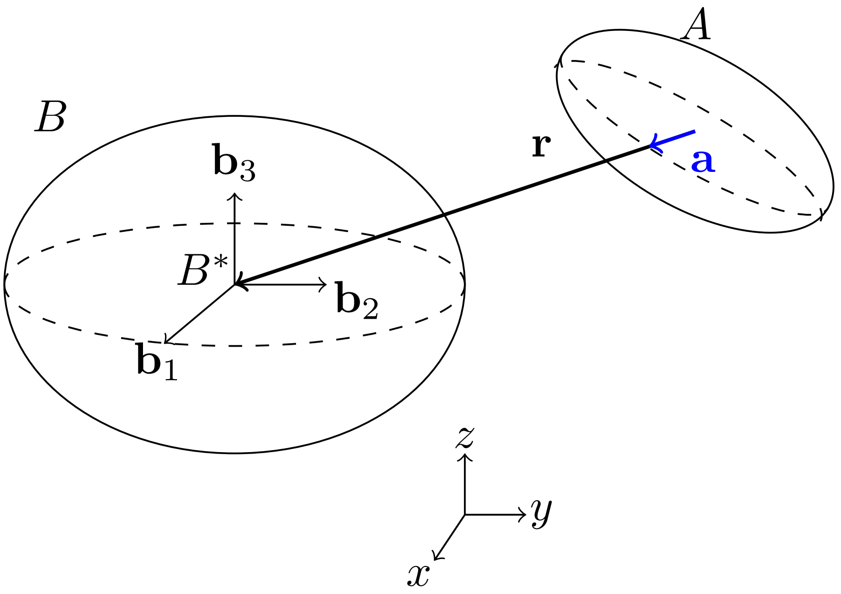

Figure B.1: Illustration of the vector quantities required to compute the gravitational torque when the mutual potential is truncated to order two using inertia integrals.

number. As a consequence, when two bodies are separated far enough, the ellipsoid potential no longer converges to the point mass solution numerically. To verify that this is indeed a numerical problem, we show an analytic proof that the ellipsoid potential and the point mass potential converge to the same solution when the separation approaches infinity. For convenience, the variables indicating the elliptic integrals are written as $F(\omega_\kappa, k) = F$ and $E(\omega_\kappa, k) = E$ (not to be confused with the force and total energy).

B.2.1 Known limits

When the separation r approaches infinity, the variable κ, given by Eq. (2.27), will also converge to infinity (see MacMillan, 1930, for details)

$$\lim_{r\to\infty} \kappa = \infty. \tag{B.4}$$

As a consequence, the limit of ω_κ, given by Eq. (2.25) becomes

$$\lim_{r\to\infty} \omega_\kappa = 0. \tag{B.5}$$

We also need to consider the limit of the elliptic integrals. For the elliptic integral of the first kind, we have

$$\lim_{r\to\infty} F(\omega_\kappa, k) = \lim_{r\to\infty} \int_0^{\omega_\kappa} \frac{d\alpha}{\sqrt{1-k^2\sin^2\alpha}} \tag{B.6}$$

The only thing that is directly dependent on r is the ω_κ variable, which approaches zero when $r \to \infty$. Therefore

$$\lim_{r\to\infty} \int_0^{\omega_\kappa} \frac{d\alpha}{\sqrt{1-k^2\sin^2\alpha}} = \int_0^{0} \frac{d\alpha}{\sqrt{1-k^2\sin^2\alpha}} = 0. \tag{B.7}$$

This limit will not experience any issues with the denominator as k, given by Eq. (2.26), is always less than one. Similarly, the limit of the elliptic integral of the second kind is

$$\lim_{r\to\infty} E(\omega_\kappa, k) = 0. \tag{B.8}$$

Furthermore, as r approaches infinity, the semi-axes a, b, c in Eq. (2.27) become negligible, so that

$$\kappa = x^2 + y^2 + z^2 = r^2, \quad \text{when } r \to \infty. \tag{B.9}$$

B.2.2 Proof of convergence - Ellipsoid potential

When $r \to \infty$, we expect that

$$\lim_{r\to\infty} \left| \frac{\Phi_e - \Phi_{pm}}{\Phi_{pm}} \right| = \lim_{r\to\infty} \left| \frac{\Phi_e}{\Phi_{pm}} - 1 \right| = 0, \tag{B.10}$$

where Φ_e is the ellipsoid potential given by Eq. (2.22), and Φ_{pm} the point mass potential

$$\Phi_{pm} = \frac{4\pi\rho G a_p b_p c_p}{r}. \tag{B.11}$$

In order to prove that the ellipsoid potential converges to the point mass potential, it is sufficient to show that

$$\lim_{r\to\infty} \frac{\Phi_e}{\Phi_{pm}} = 1. \tag{B.12}$$

The ellipsoid potential is given with Cartesian coordinates. We instead use spherical coordinates

$$x = r\tilde{x} = r\cos\phi\sin\theta \tag{B.13}$$
$$y = r\tilde{y} = r\sin\phi\sin\theta \tag{B.14}$$
$$z = r\tilde{z} = r\cos\theta. \tag{B.15}$$

where ϕ and θ are azimuthal and polar angles respectively. For an ellipsoid with semi-axes a, b, c, mass m, and constant density ρ, we have the following relation

$$3m = 4\pi\rho abc. \tag{B.16}$$

The ellipsoid potential can then be rewritten as

$$\begin{aligned}\Phi_e = \frac{3Gm}{2\sqrt{a^2-c^2}} \Bigg(&\left[1 - \frac{\tilde{x}^2}{a^2-b^2} + \frac{\tilde{y}^2}{a^2-b^2}\right] r^2 F \\ &+ \left[\frac{\tilde{x}^2}{a^2-b^2} - \frac{(a^2-c^2)\tilde{y}^2}{(a^2-b^2)(b^2-c^2)} + \frac{\tilde{z}^2}{b^2-c^2}\right] r^2 E \\ &+ \left[\frac{c^2+\kappa}{b^2-c^2}\tilde{y}^2 - \frac{b^2+\kappa}{b^2-c^2}\tilde{z}^2\right] \frac{r^2\sqrt{a^2-c^2}}{\sqrt{(a^2+\kappa)(b^2+\kappa)(c^2+\kappa)}} \Bigg).\end{aligned} \tag{B.17}$$

With a little bit of rewriting, we have that

$$\frac{\Phi_e}{\Phi_{pm}} = \frac{3}{2\sqrt{a^2-c^2}}\left[rF + r^3\delta_1 + r^3\delta_2 + r^3\delta_3\right] \tag{B.18}$$

where we have defined the following parameters

$$\delta_1 = \tilde{x}^2\left(\frac{E-F}{a^2-b^2}\right) \tag{B.19}$$

$$\delta_2 = \tilde{y}^2\left(\frac{F}{a^2-b^2} - \frac{(a^2-c^2)E}{(a^2-b^2)(b^2-c^2)} + \frac{\sqrt{a^2-c^2}}{b^2-c^2}B(\kappa)\right) \tag{B.20}$$

$$\delta_3 = \tilde{z}^2\left(\frac{E}{b^2-c^2} - \frac{\sqrt{a^2-c^2}}{b^2-c^2}C(\kappa)\right) \tag{B.21}$$

$$B(\kappa) = \sqrt{\frac{c^2+\kappa}{(a^2+\kappa)(b^2+\kappa)}} \tag{B.22}$$

$$C(\kappa) = \sqrt{\frac{b^2+\kappa}{(a^2+\kappa)(c^2+\kappa)}}. \tag{B.23}$$

When the limit is taken on Eq. (B.18), there are four terms that are considered. For each term, L'Hopital's rule is applied, where the r and r^3 factors are differentiated in the denominator, e.g.

$$\lim_{r\to\infty} rF = \lim_{r\to\infty}\frac{\frac{\partial F}{\partial r}}{\frac{\partial(r^{-1})}{\partial r}} = \lim_{r\to\infty}\left[-r^2\frac{\partial F}{\partial r}\right]. \tag{B.24}$$

The resulting limits then become

$$\lim_{r\to\infty} rF = \sqrt{a^2-c^2} \tag{B.25}$$

$$\lim_{r\to\infty} r^3\delta_1 = -\frac{1}{3}\sqrt{a^2-c^2} \tag{B.26}$$

$$\lim_{r\to\infty} r^3\delta_2 = -\frac{1}{3}\sqrt{a^2-c^2} \tag{B.27}$$

$$\lim_{r\to\infty} r^3\delta_3 = -\frac{1}{3}\sqrt{a^2-c^2}. \tag{B.28}$$

Finally, by combining the results we find that

$$\lim_{r\to\infty}\frac{\Phi_e}{\Phi_{pm}} = \frac{3}{2\sqrt{a^2-c^2}}\left(\sqrt{a^2-c^2} - \frac{\sqrt{a^2-c^2}}{3}(\tilde{x}^2+\tilde{y}^2+\tilde{z}^2)\right) \tag{B.29}$$

$$= 1 \tag{B.30}$$

where $\tilde{x}^2+\tilde{y}^2+\tilde{z}^2 = 1$.

B.2.3 Proof of convergence - Ellipsoid gravitational field

The previous section only considered the limit of the ellipsoid potential Φ_e. Naturally, as the separation between two bodies increases, the gravitational field, $\mathbf{g} = \nabla\Phi$, of an ellipsoid should also converge towards the point mass solution. However, the gravitational field also suffers from round-off errors, similar to the scalar potential. In this section, we show that the following limit is true

$$\lim_{r\to\infty} \frac{|\mathbf{g}_e|}{|\mathbf{g}_{pm}|} = 1, \tag{B.31}$$

where $|\mathbf{g_e}| = \sqrt{g_x^2 + g_y^2 + g_z^2}$ and $|\mathbf{g}_{pm}| = Gm/r^2$. The components of ellipsoid gravitational field $\mathbf{g}_e = [g_x, g_y, g_z]$ are given by Eqs. (2.28)-(2.30). We have that

$$\begin{aligned}
\frac{|\mathbf{g}_e|}{|\mathbf{g}_{pm}|} &= \frac{-3r^3}{\sqrt{a^2-c^2}} \Bigg[\left(\frac{E-F}{a^2-b^2}\right)^2 \tilde{x}^2 \\
&+ \left(\frac{F}{a^2-b^2} - \frac{(a^2-c^2)E}{(a^2-b^2)(b^2-c^2)} + \frac{\sqrt{a^2-c^2}}{b^2-c^2} B(\kappa)\right)^2 \tilde{y}^2 \\
&+ \left(\frac{E}{b^2-c^2} - \frac{\sqrt{a^2-c^2}}{b^2-c^2} C(\kappa)\right)^2 \tilde{z}^2 \Bigg]^{1/2} \\
&= \frac{-3r^3}{\sqrt{a^2-c^2}} \sqrt{(\tilde{x}T_1)^2 + (\tilde{y}T_2)^2 + (\tilde{z}T_3)^2} \\
&= \frac{-3r^3}{\sqrt{a^2-c^2}} \sqrt{\gamma(\kappa)},
\end{aligned} \tag{B.32}$$

where

$$T_1 = \frac{E-F}{a^2-b^2} \tag{B.33}$$

$$T_2 = \frac{F}{a^2-b^2} - \frac{(a^2-c^2)E}{(a^2-b^2)(b^2-c^2)} + \frac{\sqrt{a^2-c^2}}{b^2-c^2} B(\kappa) \tag{B.34}$$

$$T_3 = \frac{E}{b^2-c^2} - \frac{\sqrt{a^2-c^2}}{b^2-c^2} C(\kappa). \tag{B.35}$$

L'Hopital's rule is once again used to differentiate the r^3 factor in the denominator. It can then be shown that the resulting limit is

$$\lim_{r\to\infty} \frac{|\mathbf{g}_e|}{|\mathbf{g}_{pm}|} = \lim_{r\to\infty} \left[\frac{-3}{\sqrt{a^2-c^2}} r^3 \sqrt{\gamma}\right] = 1. \tag{B.36}$$

This shows that the ellipsoid gravitational potential and gravitational field behave as expected. The numerical round-off errors caused by large distances are therefore mainly caused by numerical round-off errors.

Bibliography

H. F. Agrusa et al. A benchmarking and sensitivity study of the full two-body gravitational dynamics of the DART mission target, binary asteroid 65803 Didymos. *Icarus*, 349: 113849, October 2020. doi: 10.1016/j.icarus.2020.113849.

H. F. Agrusa et al. The excited spin state of Dimorphos resulting from the DART impact. *Icarus*, 370:114624, December 2021. doi: 10.1016/j.icarus.2021.114624.

M. F. A'Hearn. Comets as Building Blocks. *Annual Review of Astronomy and Astrophysics*, 49(1):281–299, September 2011. doi: 10.1146/annurev-astro-081710-102506.

S. Alfano and M. L. Greer. Determining if two solid ellipsoids intersect. *Journal of guidance, control, and dynamics*, 26(1):106–110, 2003.

T. M. Becker et al. Physical modeling of triple near-Earth Asteroid (153591) 2001 SN_{263} from radar and optical light curve observations. *Icarus*, 248:499–515, March 2015. doi: 10.1016/j.icarus.2014.10.048.

J. Bellerose and D. J. Scheeres. Energy and stability in the Full Two Body Problem. *Celestial Mechanics and Dynamical Astronomy*, 100(1):63–91, January 2008. doi: 10.1007/s10569-007-9108-3.

L. A. G. Boldrin, D. J. Scheeres, and O. C. Winter. Dynamics of rotationally fissioned asteroids: non-planar case. *Monthly Notices of the Royal Astronomical Society*, 461(4): 3982–3992, October 2016. doi: 10.1093/mnras/stw1607.

G. Boué. The two rigid body interaction using angular momentum theory formulae. *Celestial Mechanics and Dynamical Astronomy*, 128(2-3):261–273, June 2017. doi: 10.1007/s10569-017-9751-2.

S. Breiter and M. Murawiecka. Tumbling asteroid rotation with the YORP torque and inelastic energy dissipation. *Monthly Notices of the Royal Astronomical Society*, 449 (3):2489–2497, May 2015. doi: 10.1093/mnras/stv433.

M. Brozović et al. Radar and optical observations and physical modeling of triple near-Earth Asteroid (136617) 1994 CC. *Icarus*, 216(1):241–256, November 2011. doi: 10.1016/j.icarus.2011.09.002.

B. Carry. Density of asteroids. *Planetary and Space Science*, 73(1):98–118, December 2012. doi: 10.1016/j.pss.2012.03.009.

A. Compère and A. Lemaître. The two-body interaction potential in the STF tensor formalism: an application to binary asteroids. *Celestial Mechanics and Dynamical Astronomy*, 119(3-4):313–330, August 2014. doi: 10.1007/s10569-014-9568-1.

G. Consolmagno, D. Britt, and R. Macke. The significance of meteorite density and porosity. *Chemie der Erde / Geochemistry*, 68(1):1–29, April 2008. doi: 10.1016/j.chemer.2008.01.003.

J. T. Conway. Vector potentials for the gravitational interaction of extended bodies and laminas with analytical solutions for two disks. *Celestial Mechanics and Dynamical Astronomy*, 125:161–194, June 2016. doi: 10.1007/s10569-016-9679-y.

J. T. Conway. Analytical solution from vector potentials for the gravitational field of a general polyhedron. *Celestial Mechanics and Dynamical Astronomy*, 121(1):17–38, Jan 2015. doi: 10.1007/s10569-014-9588-x.

A. C. M. Correia. Chaotic dynamics in the (47171) Lempo triple system. *Icarus*, 305: 250–261, May 2018. doi: 10.1016/j.icarus.2018.01.008.

A. B. Davis and D. J. Scheeres. High-fidelity Modeling of Rotationally Fissioned Asteroids. *The Planetary Science Journal*, 1(1):25, June 2020a. doi: 10.3847/PSJ/ab9a39.

A. B. Davis and D. J. Scheeres. Doubly synchronous binary asteroid mass parameter observability. *Icarus*, 341:113439, May 2020b. doi: 10.1016/j.icarus.2019.11343910.48550/arXiv.1910.04720.

A. R. Dobrovolskis. Inertia of any polyhedron. *Icarus*, 124(2):698 – 704, 1996. ISSN 0019-1035. doi: https://doi.org/10.1006/icar.1996.0243.

J. R. Dormand and P. J. Prince. A family of embedded runge-kutta formulae. *Journal of computational and applied mathematics*, 6(1):19–26, 1980.

J. Durech et al. Asteroid Models from Multiple Data Sources. In *Asteroids IV*, pages 183–202. University of Arizona Press, 2015. doi: 10.2458/azu_uapress_9780816532131-ch010.

E. G. Fahnestock and D. J. Scheeres. Simulation of the full two rigid body problem using polyhedral mutual potential and potential derivatives approach. *Celestial Mechanics and Dynamical Astronomy*, 96(3-4):317–339, November 2006. doi: 10.1007/s10569-006-9045-6.

E. G. Fahnestock and D. J. Scheeres. Simulation and analysis of the dynamics of binary near-Earth Asteroid (66391) 1999 KW4. *Icarus*, 194(2):410–435, April 2008. doi: 10.1016/j.icarus.2007.11.007.

P. Fatka et al. Recent formation and likely cometary activity of near-Earth asteroid pair 2019 PR2-2019 QR6. *Monthly Notices of the Royal Astronomical Society*, 510(4): 6033–6049, March 2022. doi: 10.1093/mnras/stab3719.

T. Feagin. A tenth-order runge-kutta method with error estimate. In *Proceedings of the IAENG Conference on Scientific Computing*, 2007.

T. Feagin. High-order explicit runge-kutta methods using m-symmetry. *Neural, Parallel & Scientific Computations*, 20, 09 2012.

E. Fehlberg. *Low-order Classical Runge-Kutta Formulas with Stepsize Control and Their Application to Some Heat Transfer Problems.* NASA technical report. National Aeronautics and Space Administration, 1969.

J. Feng and X. Hou. Dynamics of Equilibrium Points in a Uniformly Rotating Second-Order and Degree Gravitational Field. *The Astronomical Journal*, 154(1):21, July 2017. doi: 10.3847/1538-3881/aa75d0.

T. Fossen. *Handbook of Marine Craft Hydrodynamics and Motion Control.* Wiley, 2011. ISBN 9781119991496.

M. Galassi et al. *GNU scientific library.* Network Theory Limited, 2002.

Y. Gao, Y. Yu, B. Cheng, and H. Baoyin. Accelerating the finite element method for calculating the full 2-body problem with CUDA. *Advances in Space Research*, 69(5): 2305–2318, March 2022. doi: 10.1016/j.asr.2021.11.037.

R. Gaskell et al. Global Topography of Asteroid 25143 Itokawa. In S. Mackwell and E. Stansbery, editors, *37th Annual Lunar and Planetary Science Conference*, Lunar and Planetary Science Conference, page 1876, March 2006.

A. Ginsburg et al. astroquery: An Astronomical Web-querying Package in Python. *The Astronomical Journal*, 157(3):98, March 2019. doi: 10.3847/1538-3881/aafc33.

B. Gladman, P. Michel, and C. Froeschlé. The Near-Earth Object Population. *Icarus*, 146(1):176–189, July 2000. doi: 10.1006/icar.2000.6391.

P. Goldreich and R. Sari. Tidal Evolution of Rubble Piles. *The Astrophysical Journal*, 691(1):54–60, January 2009. doi: 10.1088/0004-637X/691/1/54.

E. Hairer, S. P. Norsett, and G. Wanner. *Solving Ordinary, Differential Equations I, Nonstiff problems/E. Hairer, SP Norsett, G. Wanner, with 135 Figures, Vol.: 1.* Number BOOK. 2Ed. Springer-Verlag, 2000, 2000.

M. Hirabayashi and D. J. Scheeres. Recursive computation of mutual potential between two polyhedra. *Celestial Mechanics and Dynamical Astronomy*, 117(3):245–262, November 2013. doi: 10.1007/s10569-013-9511-x.

M. Hirabayashi, D. P. Sánchez, and D. J. Scheeres. Internal structure of asteroids having surface shedding due to rotational instability. *The Astrophysical Journal*, 808(1):63, 2015.

A. Ho, M. Wold, J. T. Conway, and M. Poursina. Extended two-body problem for rotating rigid bodies. *Celestial Mechanics and Dynamical Astronomy*, 133(8):35, August 2021. doi: 10.1007/s10569-021-10034-8.

A. Ho, M. Wold, M. Poursina, and J. T. Conway. Dynamics of asteroid systems post-rotational fission. *Astronomy and Astrophysics*, 665:A43, September 2022. doi: 10.1051/0004-6361/202243706.

A. Ho, M. Wold, M. Poursina, and J. T. Conway. The accuracy of mutual potential approximations in simulations of binary asteroids. *Astronomy and Astrophysics*, 671:A38, March 2023. doi: 10.1051/0004-6361/202245552.

K. A. Holsapple. On Equilibrium Shapes of Solid Solar System Bodies. In *Lunar and Planetary Science Conference*, Lunar and Planetary Science Conference, page 1992, March 2001.

K. A. Holsapple. Equilibrium figures of spinning bodies with self-gravity. *Icarus*, 172(1):272–303, November 2004. doi: 10.1016/j.icarus.2004.05.023.

K. A. Holsapple. Spin limits of Solar System bodies: From the small fast-rotators to 2003 EL61. *Icarus*, 187(2):500–509, April 2007. doi: 10.1016/j.icarus.2006.08.012.

X. Hou, D. J. Scheeres, and X. Xin. Mutual potential between two rigid bodies with arbitrary shapes and mass distributions. *Celestial Mechanics and Dynamical Astronomy*, 127(3):369–395, March 2017. doi: 10.1007/s10569-016-9731-y.

W. Hu and D. J. Scheeres. Spacecraft Motion About Slowly Rotating Asteroids. *Journal of Guidance Control Dynamics*, 25(4):765–775, July 2002. doi: 10.2514/2.4944.

W. Hu and D. J. Scheeres. Numerical determination of stability regions for orbital motion in uniformly rotating second degree and order gravity fields. *Planetary and Space Science*, 52(8):685–692, July 2004. doi: 10.1016/j.pss.2004.01.003.

S. A. Jacobson and D. J. Scheeres. Dynamics of rotationally fissioned asteroids: Source of observed small asteroid systems. *Icarus*, 214(1):161–178, July 2011. doi: 10.1016/j.icarus.2011.04.009.

D. Jewitt and J. Luu. Discovery of the candidate Kuiper belt object 1992 QB$_1$. *Nature*, 362(6422):730–732, April 1993. doi: 10.1038/362730a0.

A. Johansen et al. New Paradigms for Asteroid Formation. In *Asteroids IV*, pages 471–492. 2015. doi: 10.2458/azu_uapress_9780816532131-ch025.

M. Kaasalainen, J. Torppa, and K. Muinonen. Optimization Methods for Asteroid Lightcurve Inversion. II. The Complete Inverse Problem. *Icarus*, 153(1):37–51, September 2001. doi: 10.1006/icar.2001.6674.

T. Kane, P. Likins, and D. Levinson. *Spacecraft Dynamics*. McGraw-Hill series in aeronautical and aerospace engineering. McGraw-Hill Book Company, 1983. ISBN 9780070378438.

T. Kramer and M. Noack. Prevailing Dust-transport Directions on Comet 67P/Churyumov-Gerasimenko. *Astrophys. J.*, 813(2):L33, Nov 2015. doi: 10.1088/2041-8205/813/2/L33.

T. Kramer et al. Dust and gas emission from cometary nuclei: the case of comet 67P/Churyumov-Gerasimenko. *arXiv e-prints*, art. arXiv:1505.08041, May 2015.

X. Li and D. J. Scheeres. Analysis of Cohesion in Fast-spinning Small Bodies. *The Planetary Science Journal*, 2(6):229, December 2021. doi: 10.3847/PSJ/ac2df5.

A. J. Maciejewski. Reduction, Relative Equilibria and Potential in the Two Rigid Bodies Problem. *Celestial Mechanics and Dynamical Astronomy*, 63(1):1–28, March 1995. doi: 10.1007/BF00691912.

W. MacMillan. *The Theory of the Potential.* (MacMillan: Theoretical Mechanics). McGraw-Hill Book Company, Incorporated, 1930.

J. L. Margot et al. Binary Asteroids in the Near-Earth Object Population. *Science*, 296 (5572):1445–1448, May 2002. doi: 10.1126/science.1072094.

W. J. Merline et al. *Asteroids Do Have Satellites*, pages 289–312. University of Arizona Press, 2002.

P. Michel, W. Benz, P. Tanga, and D. C. Richardson. Collisions and Gravitational Reaccumulation: Forming Asteroid Families and Satellites. *Science*, 294(5547):1696–1700, November 2001. doi: 10.1126/science.1065189.

P. Michel, A. Morbidelli, and W. F. Bottke. Origin and dynamics of Near Earth Objects. *Comptes Rendus Physique*, 6(3):291–301, April 2005. doi: 10.1016/j.crhy.2004.12.013.

A. Morbidelli, J. Bottke, W. F., C. Froeschlé, and P. Michel. Origin and Evolution of Near-Earth Objects. In *Asteroids III*, pages 409–422. University of Arizona Press, 2002.

H. Moritz. *Advanced Physical Geodesy.* Sammlung Wichmann : Neue Folge : Buchreihe. Wichmann, 1980. ISBN 9780856261954.

N. A. Moskovitz et al. A common origin for dynamically associated near-Earth asteroid pairs. *Icarus*, 333:165–176, November 2019. doi: 10.1016/j.icarus.2019.05.030.

S. P. Naidu et al. Radar Imaging and Characterization of the Binary Near-Earth Asteroid (185851) 2000 DP107. *The Astronomical Journal*, 150(2):54, August 2015. doi: 10.1088/0004-6256/150/2/54.

S. Naidu et al. Radar observations and a physical model of binary near-earth asteroid 65803 didymos, target of the dart mission. *Icarus*, 348:113777, 2020.

S. J. Ostro et al. Radar Imaging of Binary Near-Earth Asteroid (66391) 1999 KW4. *Science*, 314(5803):1276–1280, November 2006. doi: 10.1126/science.1133622.

M. K. Paul. An Expansion in Power Series of Mutual Potential for Gravitating Bodies with Finite Sizes. *Celestial Mechanics*, 44(1-2):49–59, March 1988. doi: 10.1007/BF01230706.

P. Pravec and A. W. Harris. Binary asteroid population. 1. Angular momentum content. *Icarus*, 190(1):250–259, September 2007. doi: 10.1016/j.icarus.2007.02.023.

P. Pravec et al. Tumbling asteroids. *Icarus*, 173(1):108–131, January 2005. doi: 10.1016/j.icarus.2004.07.021.

P. Pravec et al. Photometric survey of binary near-Earth asteroids. *Icarus*, 181(1):63–93, March 2006. doi: 10.1016/j.icarus.2005.10.014.

P. Pravec et al. Formation of asteroid pairs by rotational fission. *Nature*, 466(7310):1085–1088, August 2010. doi: 10.1038/nature09315.

P. Pravec et al. Binary asteroid population. 2. Anisotropic distribution of orbit poles of small, inner main-belt binaries. *Icarus*, 218(1):125–143, March 2012. doi: 10.1016/j.icarus.2011.11.026.

P. Pravec et al. Binary asteroid population. 3. Secondary rotations and elongations. *Icarus*, 267:267–295, March 2016. doi: 10.1016/j.icarus.2015.12.019.

P. Pravec et al. Asteroid pairs: A complex picture. *Icarus*, 333:429–463, November 2019. doi: 10.1016/j.icarus.2019.05.014.

P. Pravec and A. W. Harris. Fast and Slow Rotation of Asteroids. *Icarus*, 148(1):12–20, November 2000. doi: 10.1006/icar.2000.6482.

P. Pravec, A. W. Harris, and B. D. Warner. NEA rotations and binaries. In G. B. Valsecchi, D. Vokrouhlický, and A. Milani, editors, *Near Earth Objects, our Celestial Neighbors: Opportunity and Risk*, volume 236, pages 167–176, May 2007. doi: 10.1017/S1743921307003201.

A. S. Richardson and J. M. Finn. Symplectic integrators with adaptive time steps. *Plasma Physics and Controlled Fusion*, 54(1):014004, January 2012. doi: 10.1088/0741-3335/54/1/014004.

D. C. Richardson, W. F. Bottke, and S. G. Love. Tidal Distortion and Disruption of Earth-Crossing Asteroids. *Icarus*, 134(1):47–76, July 1998. doi: 10.1006/icar.1998.5954.

D. C. Richardson, P. Elankumaran, and R. E. Sanderson. Numerical experiments with rubble piles: equilibrium shapes and spins. *Icarus*, 173(2):349–361, February 2005. doi: 10.1016/j.icarus.2004.09.007.

D. C. Richardson, P. Elankumaran, and R. E. Sanderson. Numerical experiments with rubble piles: equilibrium shapes and spins. *Icarus*, 173(2):349–361, 2005. ISSN 0019-1035. doi: https://doi.org/10.1016/j.icarus.2004.09.007.

D. P. Rubincam. Radiative Spin-up and Spin-down of Small Asteroids. *Icarus*, 148(1): 2–11, November 2000. doi: 10.1006/icar.2000.6485.

P. Sánchez and D. J. Scheeres. The strength of regolith and rubble pile asteroids. *Meteoritics & Planetary Science*, 49(5):788–811, May 2014. doi: 10.1111/maps.12293.

J. M. Sanz-Serna. Symplectic integrators for Hamiltonian problems: an overview. *Acta Numerica*, 1:243–286, January 1992. doi: 10.1017/S0962492900002282.

D. Scheeres. Stability of Relative Equilibria in the Full Two-Body Problem. *Annals of the New York Academy of Sciences*, 1017(1):81–94, May 2004. doi: 10.1196/annals.1311.006.

D. J. Scheeres. Stability of Binary Asteroids. *Icarus*, 159(2):271–283, October 2002. doi: 10.1006/icar.2002.6908.

D. J. Scheeres. Rotational fission of contact binary asteroids. *Icarus*, 189(2):370–385, August 2007. doi: 10.1016/j.icarus.2007.02.015.

D. J. Scheeres. Stability of the planar full 2-body problem. *Celestial Mechanics and Dynamical Astronomy*, 104(1-2):103–128, June 2009. doi: 10.1007/s10569-009-9184-7.

D. J. Scheeres et al. Dynamical Configuration of Binary Near-Earth Asteroid (66391) 1999 KW4. *Science*, 314(5803):1280–1283, November 2006. doi: 10.1126/science.1133599.

D. J. Scheeres, D. Britt, B. Carry, and K. A. Holsapple. Asteroid Interiors and Morphology. In *Asteroids IV*, pages 745–766. University of Arizona Press, 2015. doi: 10.2458/azu_uapress_9780816532131-ch038.

D. Scheeres, S. Ostro, R. Hudson, and R. Werner. Orbits close to asteroid 4769 castalia. *Icarus*, 121(1):67 – 87, 1996. ISSN 0019-1035. doi: https://doi.org/10.1006/icar.1996.0072.

I. Sharma. Stability of rubble-pile satellites. *Icarus*, 229:278–294, February 2014. doi: 10.1016/j.icarus.2013.09.023.

Y. Shi, Y. Wang, and S. Xu. Mutual gravitational potential, force, and torque of a homogeneous polyhedron and an extended body: an application to binary asteroids. *Celestial Mechanics and Dynamical Astronomy*, 129(3):307–320, November 2017. doi: 10.1007/s10569-017-9776-6.

S. A. Stern and J. E. Colwell. Collisional Erosion in the Primordial Edgeworth-Kuiper Belt and the Generation of the 30-50 AU Kuiper Gap. *The Astrophysical Journal*, 490 (2):879–882, December 1997. doi: 10.1086/304912.

K. Sugiura, H. Kobayashi, and S. Inutsuka. Toward understanding the origin of asteroid geometries. Variety in shapes produced by equal-mass impacts. *Astronomy & Astrophysics*, 620:A167, December 2018. doi: 10.1051/0004-6361/201833227.

P. Tricarico and M. V. Sykes. The dynamical environment of Dawn at Vesta. *Planetary and Space Science*, 58(12):1516–1525, October 2010. doi: 10.1016/j.pss.2010.07.017.

P. Tricarico. Figure figure interaction between bodies having arbitrary shapes and mass distributions: a power series expansion approach. *Celestial Mechanics and Dynamical Astronomy*, 100(4):319–330, April 2008. doi: 10.1007/s10569-008-9128-7.

C. Tsitouras. Optimized explicit runge–kutta pair of orders 9 (8). *Applied numerical mathematics*, 38(1-2):123–134, 2001.

J. H. Verner. Some runge-kutta formula pairs. *SIAM Journal on Numerical Analysis*, 28 (2):496–511, 1991. ISSN 00361429.

J. H. Verner. Numerically optimal runge–kutta pairs with interpolants. *Numerical Algorithms*, 53(2):383–396, Mar 2010. ISSN 1572-9265. doi: 10.1007/s11075-009-9290-3.

D. Vokrouhlický et al. *The Yarkovsky and YORP Effects*, pages 509–531. University of Arizona Press, 2015. doi: 10.2458/azu_uapress_9780816532131-ch027.

D. Vokrouhlický and D. Nesvorný. Pairs of Asteroids Probably of a Common Origin. *The Astronomical Journal*, 136(1):280–290, July 2008. doi: 10.1088/0004-6256/136/1/280.

K. J. Walsh and S. A. Jacobson. *Formation and Evolution of Binary Asteroids*, pages 375–393. University of Arizona Press, 2015. doi: 10.2458/azu_uapress_9780816532131-ch020.

K. J. Walsh and D. C. Richardson. Binary near-Earth asteroid formation: Rubble pile model of tidal disruptions. *Icarus*, 180(1):201–216, January 2006. doi: 10.1016/j.icarus.2005.08.015.

K. J. Walsh and D. C. Richardson. A steady-state model of NEA binaries formed by tidal disruption of gravitational aggregates. *Icarus*, 193(2):553–566, February 2008. doi: 10.1016/j.icarus.2007.08.020.

K. J. Walsh, D. C. Richardson, and P. Michel. Rotational breakup as the origin of small binary asteroids. *Nature*, 454(7201):188–191, July 2008. doi: 10.1038/nature07078.

B. D. Warner, A. W. Harris, and P. Pravec. Asteroid Lightcurve Database (LCDB) Bundle V4.0. *NASA Planetary Data System*, page 10, September 2021. doi: 10.26033/j3xc-3359.

S. J. Weidenschilling. Hektor: Nature and origin of a binary asteroid. *Icarus*, 44(3): 807–809, December 1980. doi: 10.1016/0019-1035(80)90147-5.

R. A. Werner. Spherical harmonic coefficients for the potential of a constant-density polyhedron. *Computers and Geosciences*, 23(10):1071–1077, December 1997. doi: 10.1016/S0098-3004(97)00110-6.

R. A. Werner and D. J. Scheeres. Exterior Gravitation of a Polyhedron Derived and Compared with Harmonic and Mascon Gravitation Representations of Asteroid 4769 Castalia. *Celestial Mechanics and Dynamical Astronomy*, 65(3):313–344, Jan 1997.

R. A. Werner and D. J. Scheeres. Mutual Potential of Homogeneous Polyhedra. *Celestial Mechanics and Dynamical Astronomy*, 91(3-4):337–349, March 2005. doi: 10.1007/s10569-004-4621-0.

J. Wisdom. Rotational Dynamics of Irregularly Shaped Natural Satellites. *Astronomical Journal*, 94:1350, November 1987. doi: 10.1086/114573.

M. Wold and J. T. Conway. The planar two-body problem for spheroids and disks. *Celestial Mechanics and Dynamical Astronomy*, 133(6):27, June 2021. doi: 10.1007/s10569-021-10023-x.

Y. Yu et al. A finite element method for computational full two-body problem: I. The mutual potential and derivatives over bilinear tetrahedron elements. *Celestial Mechanics and Dynamical Astronomy*, 131(11):51, November 2019. doi: 10.1007/s10569-019-9930-4.

Paper 1 - Extended two-body problem for rotating rigid bodies

Alex Ho, Margrethe Wold, John T. Conway, and Mohammad Poursina

This paper has been published as:

Alex Ho, Margrethe Wold, John T. Conway, and Mohammad Poursina, Extended two-body problem for rotating rigid bodies. *Celestial Mechanics and Dynamical Astronomy*, 133(8):35, August 2021. doi: 10.1007/s10569-021-10034-8.

Extended two-body problem for rotating rigid bodies

Alex Ho, Margrethe Wold, John T. Conway, Mohammad Poursina
University of Agder, Jon Lilletuns vei 9, 4879 Grimstad, Norway

Abstract

A new technique that utilizes surface integrals to find the force, torque and potential energy between two non-spherical, rigid bodies is presented. The method is relatively fast, and allows us to solve the full rigid two-body problem for pairs of spheroids and ellipsoids with 12 degrees of freedom. We demonstrate the method with two dimensionless test scenarios, one where tumbling motion develops, and one where the motion of the bodies resemble spinning tops. We also test the method on the asteroid binary (66391) 1999 KW4, where both components are modelled either as spheroids or ellipsoids. The two different shape models have negligible effects on the eccentricity and semi-major axis, but have a larger impact on the angular velocity along the z-direction. In all cases, energy and total angular momentum is conserved, and the simulation accuracy is kept at the machine accuracy level.

1 Introduction

Asteroids are remnants from the formation of the solar system. It is hoped that detailed study of asteroids may improve our understanding on how the solar system was formed. One way to obtain a better knowledge of asteroids is to study the dynamics of multi-body systems. Roughly two decades ago, the existence of asteroid satellites was still uncertain (Weidenschilling et al., 1989). Not long after, the first asteroid binary, (243) Ida and its satellite Dactyl,was discovered by the Galileo spacecraftmission in 1993 (Chapman et al., 1995). Since then, many more binaries have been observed and it is believed that roughly 15% of near-Earth asteroids, larger than 200 meters in diameter, are binaries (Margot et al., 2002). A few asteroid binaries have also been observed amongst the main-belt asteroids, but the frequency of such systems is generally lower (Merline et al., 2002).

Studying the dynamical evolution of two rigid bodies, including both their translational and rotational motion, is known as the full two-body problem. In the full two-body problem, the rotational and translational motion of both bodies are fully coupled (Maciejewski, 1995). However, studying the full two-body problem is not trivial for irregular bodies, such as asteroids, as no analytical solution exists to compute the gravitational force between two non-spherical objects. Therefore, several numerical approaches have been developed to solve the full-two body problem.

A straightforward method of modelling the gravitational field of an asteroid is the mascon model (Geissler et al., 1996). In this approach, a set of point masses are placed in a grid, forming the shape of the asteroid. The total gravitational field of the asteroid will then be the sum of all the point mass fields. The advantage of the mascon model is that it can produce an accurate shape representation of an arbitrary body. Despite this advantage, the mascon model also has several drawbacks. For instance, the accuracy of the model depends on the number of point masses included in the body, and including a large number of point masses is computationally expensive. Furthermore Werner and Scheeres (1997) have shown that, despite including a large number of point masses, there exists significant errors in the force computation. This is due to the errors in the resolution of the surface of the asteroid, as the topology of the body is replaced with spherical balls. Wittick and Russell (2017) have revisited and optimized the model to make it less computationally demanding and increased the numerical accuracy.

A different, yet common method to model the gravitational field of non-spherical bodies is through the application of series expansions. The most common case is generated by using expansions of spherical harmonics (Konopliv et al., 2011). However, for spherical harmonics, the potential can only be computed outside a given sphere, known as the Brillouin sphere, as the potential will diverge inside this region (Moritz, 1980). Spherical harmonics are also utilized in the full two-body problem to describe the mutual gravitational potential (Scheeres et al., 1996; Boldrin et al., 2016; Boué, 2017).

Alternative parametrizations are also used to mitigate the divergence problem present in the spherical harmonics approach. For example, ellipsoidal harmonics has been used to compute the gravity field on various small solar system bodies (Garmier and Barriot, 2001; Garmier et al., 2002; Dechambre and Scheeres, 2002; Reimond and Baur, 2016). However, the use of ellipsoidal harmonics can be cumbersome, due to the mathematical and numerical complexity. Alternatively, prolate spheroidal harmonics (Fukushima, 2014; Sebera et al., 2016) provides simpler mathematical expressions compared to ellipsoidal harmonics, while providing a good geometric fit for non-spherical objects. Furthermore, Reimond and Baur (2016) have shown that, although ellipsoidal harmonics are far more accurate than spherical harmonics, there are virtually no difference between prolate spheroidal and ellipsoidal harmonics. Nevertheless, because all these methods use mathematical expansions, there exists a limit to the number of terms included in the model. Neglecting higher order terms, therefore, results in truncation errors.

Another way to expand potentials is to expand the inertia integrals. Scheeres (2009) used this approach to study the stability of two ellipsoids restricted in the plane. Hou et al. (2017) present a fast method to compute the mutual potential, also using inertia integrals, between two arbitrary bodies using recurrence relations. Compère and Lemaître (2014) utilize the STF tensor formalism, which allows one to determine the coupling between spherical harmonics in a compact way, to determine the mutual potential and applied the method to study the (66391) 1999 KW4 binary system.

Another approach is to model an asteroid as a polyhedron of constant density. Similar to the mascon model, the polyhedron model allows one to include finer geometric details of an asteroid. Werner and Scheeres (1997) present a method to compute the gravitational potential of a polyhedron and use it to model the gravity field of the asteroid (4769) Castalia. Conway (2015) gives an alternative formulation of the gravitational potential of a polyhedron through the use of vector potentials, a method used to study how the dust is emitted and transported around Comet 67P (Kramer and Noack, 2015; Kramer et al., 2015). For two bodies, a method was presented by Werner and Scheeres (2005) to determine the mutual potential between two polyhedra. This approach has been used to study the dynamical evolution of the asteroid binary (66391) 1999 KW4 (Scheeres et al., 2006; Fahnestock and Scheeres, 2006). Shi et al. (2017) present a different model for the mutual potential between a polyhedron and a rigid body of an arbitrary mass distribution and use this method to also study the (66391) 1999 KW4 system.

For most asteroids, detailed shape models are not available. An alternative to the polyhedron model is to approximate an asteroid with a well-defined shape, such as an ellipsoid. The gravitational potential of such bodies can be expressed analytically (MacMillan, 1930). However, the potential of an ellipsoid requires computation of elliptic functions, which may be computationally demanding. Nevertheless, using ellipsoid shape approximation to model asteroids has been e.g. used to study an ellipsoid-sphere system (Scheeres, 2004; Bellerose and Scheeres, 2008).

A new approach, based on vector potentials, to compute the gravitational potential between two extended bodies is presented by Conway (2016). Here, the force, torque and mutual potential energy are formulated as surface integrals under the assumption of constant density. This could potentially be a faster and more accurate technique, as the force and torque integrals are converted from volume integrals to surface integrals. Moreover, this approach does not rely on series expansions and will therefore not suffer from truncation errors. This approach was recently tested on coplanar spheroids and thin disks by Wold and Conway (2021). In this paper, we extend the work of Wold & Conway by giving a full three-dimensional treatment of the dynamics between the two bodies, including the coupling between translational and rotational motion.

In Sect. 2, we introduce the equations used to determine the translational and rotational motion and describe how we treat the rotational kinematics. In Sect. 3, we present the results of two dimensionless test scenarios, while in Sect. 4 we apply our method on the asteroid binary system (66391) 1999 KW4. In this paper, all dotted variables denote the time derivative of the corresponding term. All vectors with a hat (e.g. $\hat{\mathbf{x}}$) show the vector expressions in the body-fixed frame (local frame), while those without a hat are in an inertial frame.

2 Mathematical model

The main objective of the method is to calculate the force $\mathbf{F}$, torque $\mathbf{M}$ and potential U of a solid body of uniform density ρ in a gravitational field $\mathbf{g}(\mathbf{r})$ in terms of surface integrals over the surface of the body.

The force of an extended body with constant density ρ, due to an external gravitational field $\mathbf{g}(\mathbf{r})$, can be expressed through a volume integral

$$\hat{\mathbf{F}} = \rho \iiint\limits_V \mathbf{g}(\mathbf{r}) dV, \tag{1}$$

where $\mathbf{r}$ is a position vector to a point on the surface of the body being integrated over. If the gravitational field is given by the gradient of a scalar potential $\Phi(\mathbf{r})$, so that $\mathbf{g}(\mathbf{r}) = \nabla\Phi(\mathbf{r})$, we can apply the divergence theorem such that the force can be computed through a surface integral

$$\hat{\mathbf{F}} = \rho \iint\limits_{S} \Phi(\mathbf{r})\mathbf{n} dS. \tag{2}$$

It can also be shown that the torque about the mass center of an extended body is given by

$$\hat{\mathbf{M}} = -\rho \iint\limits_{S} \Phi(\mathbf{r})\mathbf{n} \times \mathbf{r} dS \tag{3}$$

and the mutual potential as

$$U = \frac{\rho}{3} \iint\limits_{S} \left(\mathbf{r}\Phi(\mathbf{r}) - \frac{1}{2} |\mathbf{r}|^2 \mathbf{g}(\mathbf{r}) \right) \cdot \mathbf{n} dS \tag{4}$$

(Conway, 2016). In these formulas $\mathbf{n}$ is a unit normal to the body surface. The above surface integrals are thus alternative expressions for the force, torque and potential between two bodies. In the following when we consider two interacting bodies, we replace the scalar potential $\Phi(\mathbf{r})$ with known analytical formulae for spheroids and ellipsoids as the first body, and integrate over either a spheroid or an ellipsoid as the second body. The surface integration method is outlined in detail by Wold and Conway (2021).

Analytical formulas for $\mathbf{g}(\mathbf{r})$ and $\Phi(\mathbf{r})$ in terms of elementary functions are given for spheroids and triaxial ellipsoids in (MacMillan, 1930). The Macmillan formulas for $\mathbf{g}(\mathbf{r})$ were validated using Eq. (2) by taking $\Phi(\mathbf{r})$ to be the scalar potential of a unit point mass and integrating this over a spheroid. Exact agreement was obtained between Eq. (2) and the MacMillan formulas. The analytical expressions for the moments of inertia of spheroids and ellipsoids are already available. Therefore, it is straightforward to set up surface integration schemes in a local body-fixed coordinate system for spheroids and ellipsoids.

Here, we analyze the motion of the bodies in a global inertial coordinate system using the forces and torques acting on each body and applying Newton's laws. As we consider a two-body problem, if $\mathbf{F}_A$ and $\mathbf{F}_B$ are the global forces acting on the two bodies A and B, then from Newton's third law

$$\mathbf{F}_B = -\mathbf{F}_A. \tag{5}$$

It should be noted that $\hat{\mathbf{M}}_A$, which is the torque of $\hat{\mathbf{F}}_A$ about the origin of the body-fixed frame of body A, may not necessarily be equal to $\hat{\mathbf{M}}_B$, which is the torque of $\hat{\mathbf{F}}_B$ about the origin of the body-fixed frame of body B. However, the torque of all forces about any arbitrary predefined point in the system must be zero in order to maintain the conservation of the angular momentum.

When the forces and torques are computed, the equations of motion can be solved as a standard initial value problem, where the velocities $\mathbf{v}$ and positions $\mathbf{r}$ can be integrated as

$$\frac{d\mathbf{v}}{dt} = \frac{\mathbf{F}}{m} \tag{6}$$

$$\frac{d\mathbf{r}}{\mathrm{d}t} = \mathbf{v} \tag{7}$$

and the angular velocity $\hat{\boldsymbol{\omega}}$ integrated from

$$\frac{d\mathbf{J}}{dt} = \mathbf{M}, \tag{8}$$

where $\mathbf{J}$ is the angular momentum of the body.

We use the embedded Runge-Kutta method of order 9(8) by Verner (Verner, 2010) to solve the equations of motion. The coefficients of the Butcher tableau are taken from Verner's web page [1], using the 'most efficient' coefficients provided in the web page.

2.1 Rotation angles and rotational motion

The force and torque integrals given in Eqs. (2) and (3) are computed in the body-fixed frames. However, because we are interested in the motion in the inertial frame, the equations of motion must be projected back to the inertial frame. To move between different reference frames, we use a rotation matrix. In this paper, we adopt the Tait-Bryan convention where the rotation matrix $\mathcal{R}$ takes the form

$$\mathcal{R}_x = \begin{bmatrix} 1 & 0 & 0 \\ 0 & \cos\phi & -\sin\phi \\ 0 & \sin\phi & \cos\phi \end{bmatrix} \tag{9}$$

$$\mathcal{R}_y = \begin{bmatrix} \cos\theta & 0 & \sin\theta \\ 0 & 1 & 0 \\ -\sin\theta & 0 & \cos\theta \end{bmatrix} \tag{10}$$

$$\mathcal{R}_z = \begin{bmatrix} \cos\psi & -\sin\psi & 0 \\ \sin\psi & \cos\psi & 0 \\ 0 & 0 & 1 \end{bmatrix} \tag{11}$$

$$\mathcal{R}(\phi,\theta,\psi) = \mathcal{R}_z\mathcal{R}_y\mathcal{R}_x. \tag{12}$$

The angles (ϕ, θ, ψ) are the Tait-Bryan angles, and correspond to rotations around the body-fixed x, y, z axes respectively[2]. The rotation matrix given in Eq. (12) is then used to project the force in the body-fixed frame, from Eq. (2), back to the inertial frame using the equation

$$\mathbf{F} = \mathcal{R}\hat{\mathbf{F}}. \tag{13}$$

The computed torque in Eq. (3) is used to determine how the angular velocity changes over time, using the equations of motion for each body in its body-fixed frame, given as

$$I_{11}\dot{\hat{\omega}}_x + (I_{33} - I_{22})\hat{\omega}_y\hat{\omega}_z = \hat{M}_x \tag{14}$$

$$I_{22}\dot{\hat{\omega}}_y + (I_{11} - I_{33})\hat{\omega}_x\hat{\omega}_z = \hat{M}_y \tag{15}$$

$$I_{33}\dot{\hat{\omega}}_z + (I_{22} - I_{11})\hat{\omega}_x\hat{\omega}_y = \hat{M}_z \tag{16}$$

---

[1] http://people.math.sfu.ca/~jverner/

[2] These angles are also known as roll, pitch and yaw.

(Curtis, 2013), where $(\hat{\omega}_x, \hat{\omega}_y, \hat{\omega}_z)$ are the angular velocity components in the body-fixed frame, I is the moment of inertia tensor and $(\hat{M}_x, \hat{M}_y, \hat{M}_z)$ are the components of the torque computed in the body-fixed frame. The angular velocity $(\hat{\omega}_x, \hat{\omega}_y, \hat{\omega}_z)$ is related to the angular velocity in the inertial frame as

$$\begin{bmatrix} \omega_x \\ \omega_y \\ \omega_z \end{bmatrix} = \mathcal{R} \begin{bmatrix} \hat{\omega}_x \\ \hat{\omega}_y \\ \hat{\omega}_z \end{bmatrix}. \tag{17}$$

The rotation angles (ϕ, θ, ψ) change over time, and the following kinematic equations relate the time rate of change of these angles to the angular velocity of the body

$$\dot{\phi} = \hat{\omega}_x + (\hat{\omega}_y \sin\phi + \hat{\omega}_z \cos\phi) \tan\theta \tag{18}$$

$$\dot{\theta} = \hat{\omega}_y \cos\phi - \hat{\omega}_z \sin\phi \tag{19}$$

$$\dot{\psi} = (\hat{\omega}_y \sin\phi + \hat{\omega}_z \cos\phi) \sec\theta \tag{20}$$

(Fossen, 2011). These kinematic equations become singular when $\theta = n\pi/2$ for any odd integer n. This singularity is a mathematical problem and is normally resolved by using Euler parameters (see e.g. Kane et al., 1983). Nevertheless, this singularity is generally not a problem for our cases in question.

2.2 Surface integration

The expressions for the surface elements in the surface integrals given by Eqs. (2)-(4), as well as the components of the moment of inertia tensor, vary depending on the shape of the bodies. This can be generalized to any arbitrary ellipsoidal shapes.

Consider a general ellipsoid with semiaxes (a, b, c). The surface elements $\mathbf{n}dS$ and $\mathbf{n} \times \mathbf{r}dS$, used in Eqs. (2)-(4) respectively, for a general ellipsoid, are given as

$$\mathbf{n}dS = \begin{bmatrix} \frac{b\sqrt{c^2-z^2}}{c} \cos\alpha \\ \frac{a\sqrt{c^2-z^2}}{c} \sin\alpha \\ \frac{ab}{c^2} z \end{bmatrix} d\alpha dz \tag{21}$$

$$\mathbf{n} \times \mathbf{r}dS = \begin{bmatrix} \frac{a}{c^3}(c^2 - b^2)\sqrt{c^2 - z^2} z \sin\alpha \\ -\frac{b}{c^3}(c^2 - a^2)\sqrt{c^2 - z^2} z \cos\alpha \\ \frac{b^2-a^2}{c^2}(c^2 - z^2) \cos\alpha \sin\alpha \end{bmatrix} d\alpha dz \tag{22}$$

(Wold and Conway, 2021), where α is the angle of the cylindrical coordinates (written as ϕ in Wold & Conway) and z is the generalized latitude line on the ellipsoid. For a general ellipsoid with density ρ, the only non-zero components of the moment of inertia tensor I_{ij} can be expressed analytically as

$$I_{11} = \frac{4\pi\rho abc}{15}(b^2 + c^2) \tag{23}$$

$$I_{22} = \frac{4\pi\rho abc}{15}(c^2 + a^2) \tag{24}$$

$$I_{33} = \frac{4\pi\rho abc}{15}(a^2 + b^2). \tag{25}$$

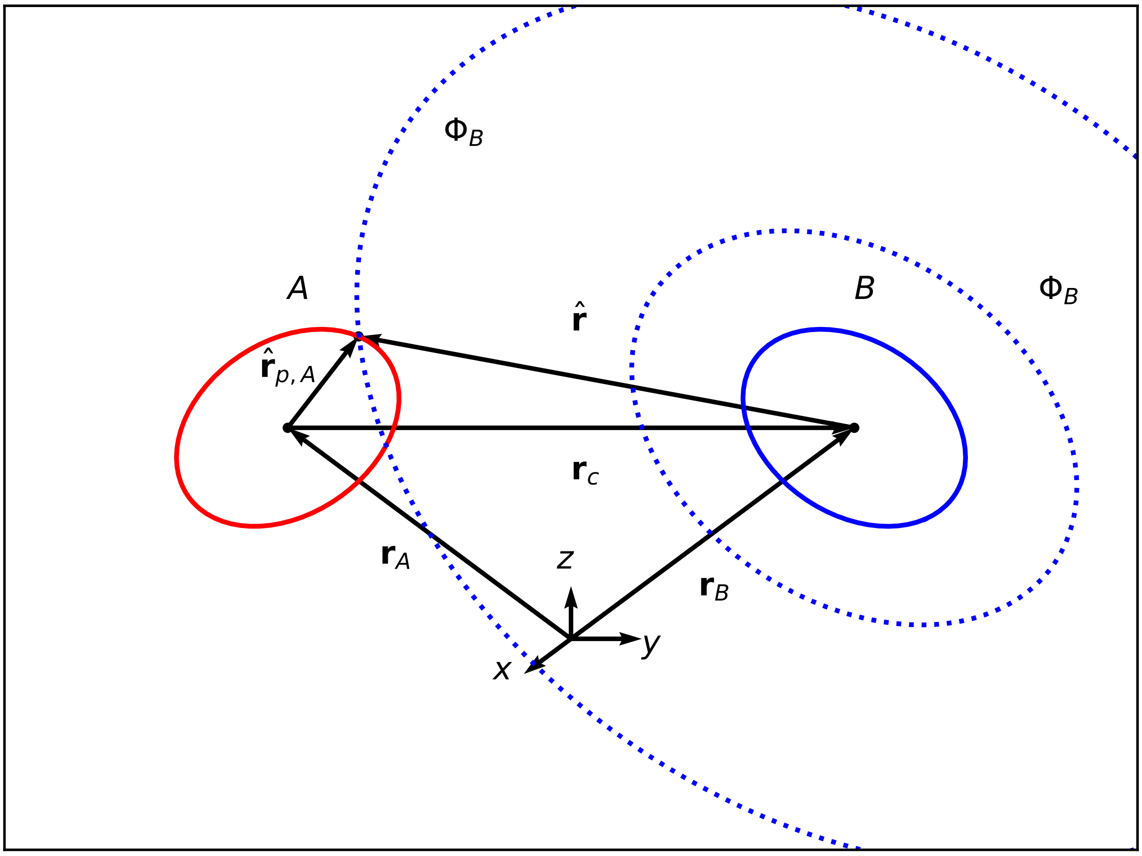

Figure 1: An illustration on how the gravitational field is computed after the bodies have rotated. The gravitational potential Φ_B (blue dotted lines) is rotated according to the rotation of spheroid B. The axes x, y, z denotes the inertial frame of the system.

2.2.1 Rotated gravitational potential

In this section, we will describe how to incorporate the change in the gravitational potential $\Phi(\mathbf{r})$ and gravitational field $\mathbf{g}(\mathbf{r})$ when the bodies are rotated.

Consider two bodies A and B whose mass centers are respectively positioned by $\mathbf{r}_A$ and $\mathbf{r}_B$ from the origin of the inertial reference frame and with their respective rotation matrices $\mathcal{R}_A$ and $\mathcal{R}_B$. The vector linking the two centroids therefore becomes

$$\mathbf{r}_c = \mathbf{r}_B - \mathbf{r}_A. \tag{26}$$

Let us consider the case where we compute the force on body A. In the inertial frame, the position vector of an arbitrary point located on the surface of A is expressed as

$$\mathbf{r}_p = \mathcal{R}_A \hat{\mathbf{r}}_{p,A} + \mathbf{r}_A, \tag{27}$$

where $\hat{\mathbf{r}}_{p,A}$ is a vector describing the surface points of A in its body-fixed frame. For a general ellipsoid, this becomes

$$\hat{\mathbf{r}}_{p,A} = \begin{bmatrix} \frac{a}{c}\sqrt{c^2 - z^2}\cos\alpha \\ \frac{b}{c}\sqrt{c^2 - z^2}\sin\alpha \\ z \end{bmatrix}. \tag{28}$$

The term $\mathbf{r}$ used as input argument in the $\Phi(\mathbf{r})$ and $\mathbf{g}(\mathbf{r})$ functions is a vector that points from the centroid of B to any point on the surface of A. This can be written as

$$\mathbf{r} = \mathbf{r}_p - \mathbf{r}_B = \mathcal{R}_A\hat{\mathbf{r}}_{p,a} - \mathbf{r}_c, \tag{29}$$

which can be expressed in the body frame of reference as

$$\hat{\mathbf{r}} = \mathcal{R}_B^T\mathbf{r} = \mathcal{R}_B^T(\mathcal{R}_A\hat{\mathbf{r}}_{p,A} - \mathbf{r}_c). \tag{30}$$

Equation (30) is then used as the input argument of both the gravitational potential $\Phi(\mathbf{r})$ and the gravitational field $\mathbf{g}(\mathbf{r})$. As the bodies rotate, so must the relative gravitational field $\mathbf{g}(\mathbf{r})$. This can be achieved using the following equation

$$\mathbf{g}_A(\hat{\mathbf{r}}) = \mathcal{R}_A^T\mathcal{R}_B\mathbf{g}_B(\hat{\mathbf{r}}). \tag{31}$$

2.3 Total energy

When all the differential equations are solved, we use the computed velocities, positions, angular velocities and rotation angles to determine the energy of the system. The translational kinetic energy of each body is computed as

$$E_k = \frac{1}{2}m\mathbf{v}^2, \tag{32}$$

where m and $\mathbf{v}$ are the mass and the center of mass velocity of the body, respectively. For an ellipsoid with constant density, the kinetic energy of rotational motion is

$$E_{\text{rot}} = \frac{1}{2}\left(I_{11}\hat{\omega}_x^2 + I_{22}\hat{\omega}_y^2 + I_{33}\hat{\omega}_z^2\right). \tag{33}$$

The mutual potential energy U is computed by Eq. (4). The total energy of the system is the sum of the kinetic, rotational and potential energies.

2.4 Angular momentum

Because we do not include external forces and moments to model the system, the angular momentum and total energy of the system must be conserved. The total angular momentum, in the inertial frame, is

$$\mathbf{J}_{tot} = \mathbf{J}_A + \mathbf{J}_B, \tag{34}$$

where the angular momentum of each body is given by

$$\mathbf{J} = \mathbf{r} \times m\mathbf{v} + \mathcal{R}I\hat{\boldsymbol{\omega}}. \tag{35}$$

As previously stated, for a general ellipsoid, the only non-zero components of the moment of inertia are I_{11}, I_{22} and I_{33}. Therefore, the total angular momentum becomes

$$\mathbf{J}_{tot} = \mathbf{r} \times m\mathbf{v} + \mathcal{R} \begin{bmatrix} I_{11}\hat{\omega}_x \\ I_{22}\hat{\omega}_y \\ I_{33}\hat{\omega}_z \end{bmatrix} . \tag{36}$$

2.5 Gravitational potential

To compute the force and torque given in Eqs. (2) and (3), we require an expression for the gravitational potential $\Phi(\mathbf{r})$. This potential can take different forms depending on the shape of the body. In this paper, we consider spheroids and triaxial ellipsoids, for which analytical expressions for $\Phi(\mathbf{r})$ are available.

For a general ellipsoid with semiaxes $a > b > c$ and constant density ρ, the gravitational potential is given by

$$\begin{aligned} \Phi(\mathbf{r}) = \frac{2\pi\rho abc}{\sqrt{a^2-c^2}} \Bigg(&\left[1 - \frac{x^2}{a^2-b^2} + \frac{y^2}{a^2-b^2}\right] F(\omega_\kappa, k) \\ &+ \left[\frac{x^2}{a^2-b^2} - \frac{(a^2-c^2)y^2}{(a^2-b^2)(b^2-c^2)} + \frac{z^2}{b^2-c^2}\right] E(\omega_\kappa, k) \\ &+ \left[\frac{c^2+\kappa}{b^2-c^2}y^2 - \frac{b^2+\kappa}{b^2-c^2}z^2\right] \frac{\sqrt{a^2-c^2}}{\sqrt{(a^2+\kappa)(b^2+\kappa)(c^2+\kappa)}} \Bigg) \end{aligned} \tag{37}$$

(MacMillan, 1930), where $F(\omega_\kappa, k)$ and $E(\omega_\kappa, k)$ are the elliptic integrals of the first and second kind respectively, κ is the largest root of the equation

$$\frac{x^2}{a^2+\kappa} + \frac{y^2}{b^2+\kappa} + \frac{z^2}{c^2+\kappa} = 1 \tag{38}$$

and

$$\omega_\kappa = \sin^{-1}\sqrt{\frac{a^2-c^2}{a^2+\kappa}} \tag{39}$$

$$k = \sqrt{\frac{a^2-b^2}{a^2-c^2}}. \tag{40}$$

For an oblate spheroid with semiaxes $a = b > c$, the gravitational potential can be expressed as

$$\begin{aligned} \Phi(\mathbf{r}) = \frac{2\pi\rho a^2 c}{\sqrt{a^2-c^2}} &\left(1 - \frac{x^2+y^2-2z^2}{2(a^2-c^2)}\right) \times \sin^{-1}\sqrt{\frac{a^2-c^2}{a^2+\kappa}} \\ &+ \frac{\pi\rho a^2 c\sqrt{c^2+\kappa}}{a^2-c^2}\frac{x^2+y^2}{a^2+\kappa} - \frac{\pi\rho a^2 c}{a^2-c^2}\frac{2z^2}{\sqrt{c^2+\kappa}} \end{aligned} \tag{41}$$

(MacMillan, 1930), where κ still satisfies Eq. (38). It should be noted that the gravitational potentials given in Eqs. (37) and (41) are exterior potentials. The expression for the gravitational field $\mathbf{g}(\mathbf{r})$, which is required to compute the mutual potential energy in Eq. (4), is derived in Appendix A.

Scenario	$\mathbf{r}_0$	$\mathbf{v}_0$	$(\phi_0, \theta_0, \psi_0)$	$\hat{\boldsymbol{\omega}}_0$	(a, b, c)	m
Case 1	$(-4, 0, 0)$	$(0, 0.3, 0)$	$(\frac{\pi}{32}, 0, 0)$	$(0, 0, 0)$	$(1, 1, 0.25)$	2
(Rotated)	$(4, 0, 0)$	$(0, -0.3, 0)$	$(-\frac{\pi}{32}, 0, 0)$	$(0, 0, 0)$	$(1, 1, 0.25)$	2
Case 2 (Spinning)	$(-4, 0, 0)$	$(0, 0.3, 0)$	$(0, \frac{\pi}{32}, 0)$	$(0, 0, 2)$	$(1, 1, 0.25)$	2
	$(4, 0, 0)$	$(0, -0.3, 0)$	$(0, -\frac{\pi}{32}, 0)$	$(0, 0, 2)$	$(1, 1, 0.25)$	2

Table 1: The initial parameters used for the two dimensionless test cases. The second and third columns show initial positions $\mathbf{r}_0$ and velocities $\mathbf{v}_0$ in the inertial frame, respectively. The fourth column indicates the initial rotation angles in radians. The fifth column shows the initial angular velocities in the body-fixed frames, in units of radians per unit time. The sixth and seventh columns show the semiaxes (a, b, c) of the spheroids and their masses, respectively. The top and bottom rows, for each case, correspond to body A and B respectively.

3 Dimensionless test scenarios

We first test our method for two dimensionless cases, where the gravitational constant is set to unity, i.e. $G = 1$. In these scenarios, we let both bodies take spheroidal shapes. The initial conditions and spheroid parameters for the simulations are summarized in Table 1. The time span of the simulations is $t \in [0, 200]$. The actual simulation times on an ordinary laptop computer for these test scenarios varied from 20 seconds to two minutes.

3.1 Case 1: Small initial rotation of the spheroids

We first consider a case where the spheroids have a small initial rotation angle $\phi_{0,A} = -\phi_{0,B} = \pi/32$ about the x-axis and zero angular velocity. Their physical parameters and initial conditions are listed in Tab. 1 under "Case 1 (Rotated)".

Figure 2a shows the spheroid orbits projected into the xy-plane, while Fig. 2b shows their z-positions as functions of time. Because forces are acting parallel to the z-axis, as seen in Fig. 3, the motions of the spheroids are no longer restricted to one plane. The motion along the z-axis is 11 orders of magnitude smaller than the motions along the x and y-axes. The motion in the z-direction grows with simulation time, and becomes of the order 10^{-1} at $t \approx 2200$. The motion along the x and y-directions, unlike the motion in z-direction, did not have any significant changes in the same time duration.

The rotation angles (ϕ, θ, ψ), plotted as sine functions, for spheroids A and B, are shown in Fig. 2c and Fig. 2d, respectively. Both spheroids rotate multiple times about their x and z-axes, and therefore have tumbling motion. The angular velocities, projected onto the respective body-fixed frames, are shown in Fig. 2e and 2f for spheroids A and B. Due to the rotational symmetry of the bodies about their z-axes, no gravitational forces can change the rotational speeds about the z-axes. Hence, the body-fixed component $\hat{\omega}_z$ remains constant for both spheroids.

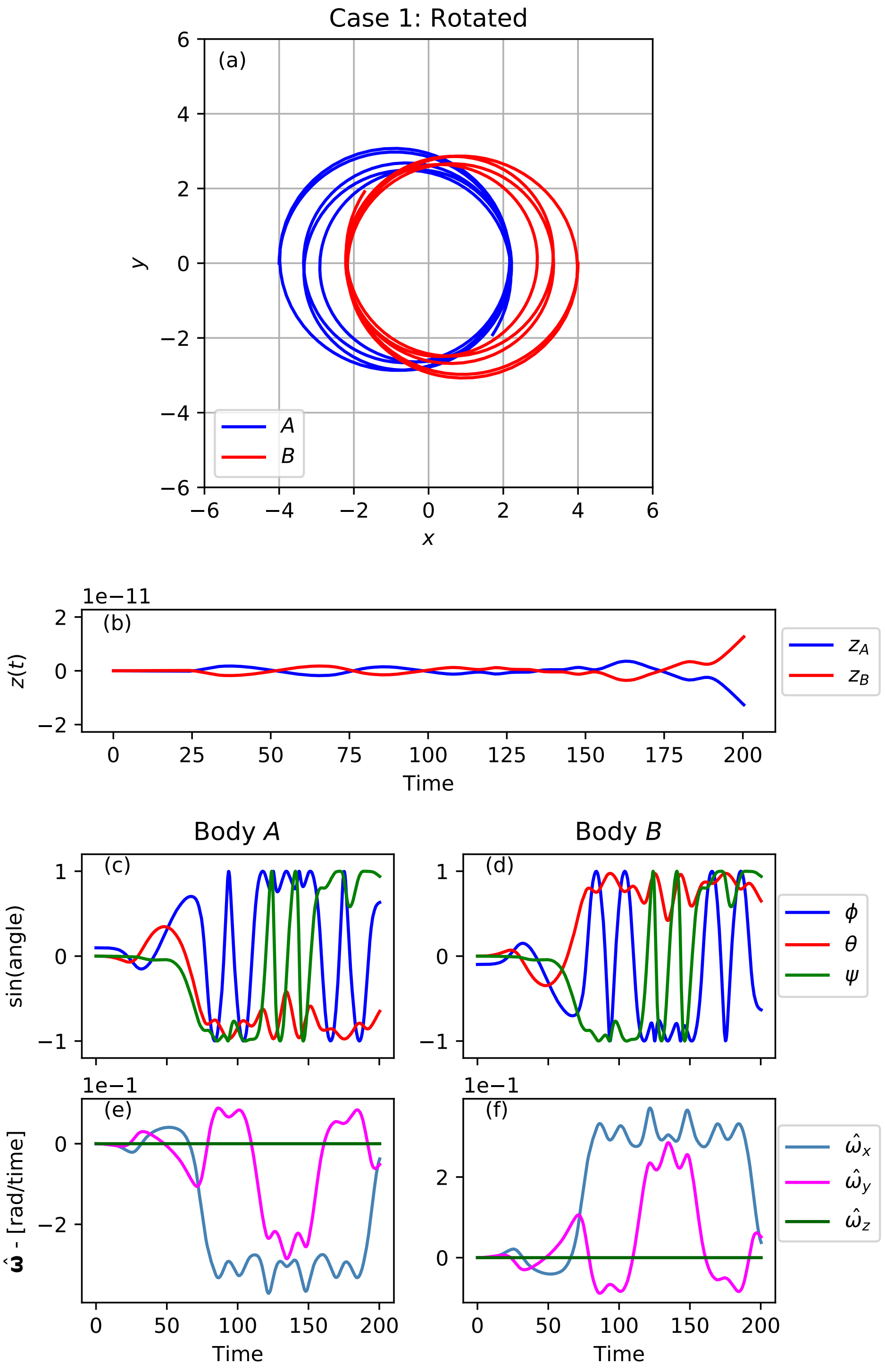

Figure 2: For case 1, where the spheroids are initially rotated about their respective x-axes. **(a)** The orbits of spheroids A and B in the inertial frame projected into the xy-plane. **(b)** The z-position of the spheroids as a function of time. **(c,d)** The rotation angles of bodies A and B as sine functions. **(e,f)** The angular velocity in the body-fixed frames of bodies A and B as a function of time. The unit of the angular velocity $\hat{\boldsymbol{\omega}}$ is radians per unit time.

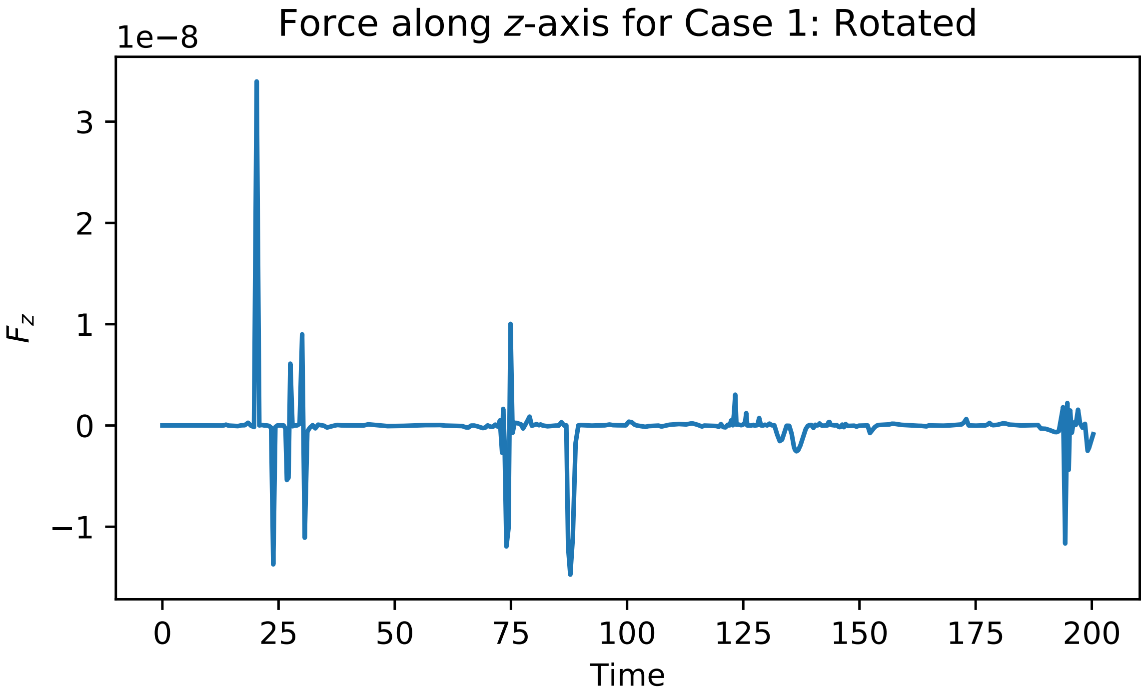

Figure 3: F_z component on body A for case 1. The F_x and F_y components are not included in the figure as they take values of order 10^{-1}.

The top panel of Fig. 4 shows the energies in the system. While both spheroids have no initial rotational motion, the rotational energy starts to make a noticeable contribution near $t \approx 75$, which is consistent with Figs. 2e and 2f, indicating that the angular velocities start to increase around $t = 75$. The middle panel of Fig. 4 shows the relative error in the total energy as a function of time. The relative error is computed as

$$\delta E = \left| \frac{E_{i+1} - E_i}{E_i} \right|, \quad i = 0, 1, 2, ..., (N_s - 1) \tag{42}$$

where N_s is the number of data points. Because the relative error is smaller than 10^{-12}, the total energy can be considered as conserved in our simulation. Finally, the absolute error of the three total angular momentum components are shown in the bottom panel of Fig. 4. The absolute error is computed as

$$\delta J = |J_{i+1} - J_i|, \quad i = 0, 1, 2, ..., (N_s - 1). \tag{43}$$

Similar to the total energy, the error in the total angular momentum is smaller than 10^{-12}, and we conclude that also the total angular momentum is conserved in the simulation.

3.2 Case 2: Adding initial angular velocity to the spheroids

We now consider a system where both spheroids are initially spinning around their z-axes, with $\hat{\omega}_{0,z} = 2$, while the other angular velocity components are initially set to zero. We also

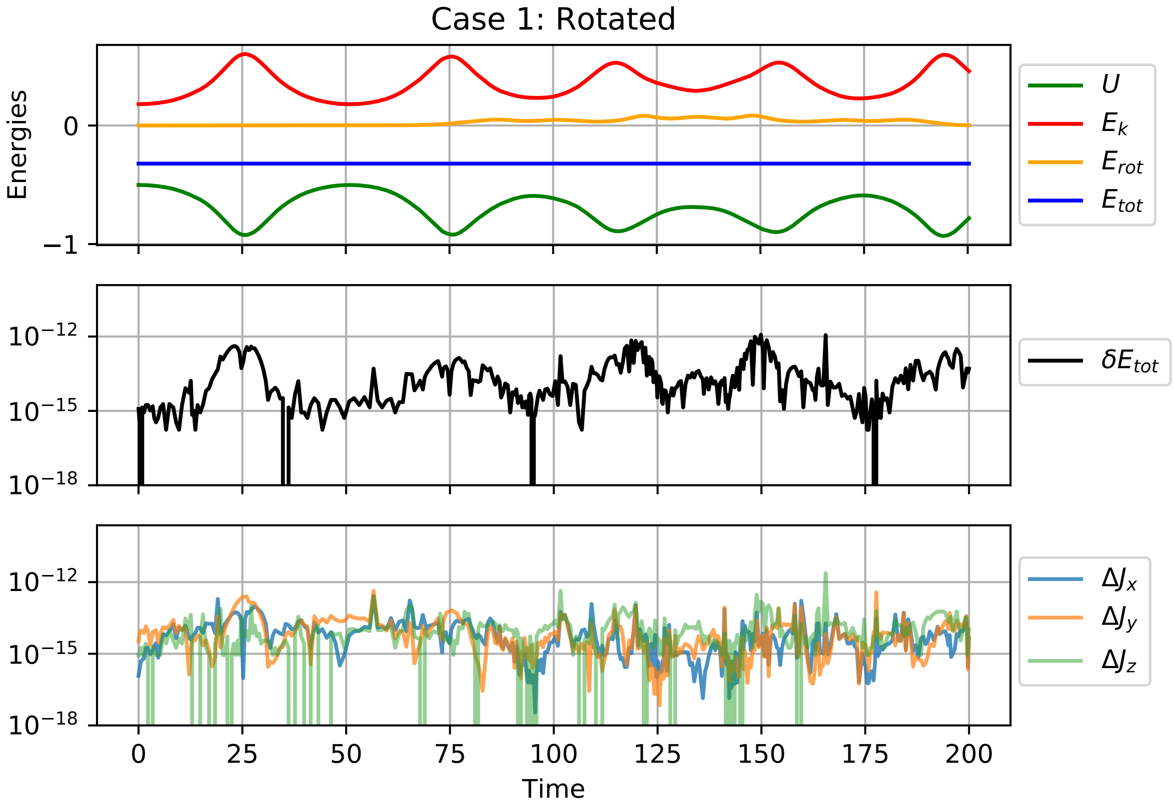

Figure 4: For case 1. *Top*: The potential energy U (green), translational kinetic energy E_k (red), rotational kinetic energy E_{rot} (orange) and the total energy E_{tot} (blue). *Middle*: The relative error of the total energy. *Bottom*: The absolute errors in the components of the total angular momentum. The errors in both the total energy E_{tot} as well as the total angular momentum $\mathbf{J}_{tot}$ are smaller than 10^{-12}, which demonstrates that these quantities are conserved in our simulations.

let both spheroids start with a slight tilt, in which $\theta_{0,A} = -\theta_{0,B} = \pi/32$, while the other angles are initially zero. The other parameters are the same as those in case 1.

Figure 5a shows the spheroid orbits projected onto the xy-plane. The orbits for this case closely resemble the case for two spheroids in co-planar motion (Wold and Conway, 2021). Figure 5b shows their z-positions as a function of time. As in Case 1, a force along the z-axis can occur, but the motion in the z-direction is 11 orders of magnitude smaller than the motion in the x and y-directions for both spheroids.

Figure 5c and 5d show the rotation angles ϕ and θ, plotted as sine functions, of bodies A and B respectively. As the spheroid spins around its z-axis, the angle ψ increases linearly and will appear as a straight line with constant slope in the figures. Meanwhile, the angles (ϕ,θ) oscillate between $-\pi/32$ and $\pi/32$. As ψ is increasing linearly and (ϕ, θ) are both oscillating, the rotational motion of the two spheroids is very similar to that of a spinning top or a precessing gyroscope. Compared to case 1 in Sect. 3.1, where the spheroids tumbled, by spinning the spheroids around their corresponding axes of symmetry, the rotational motion

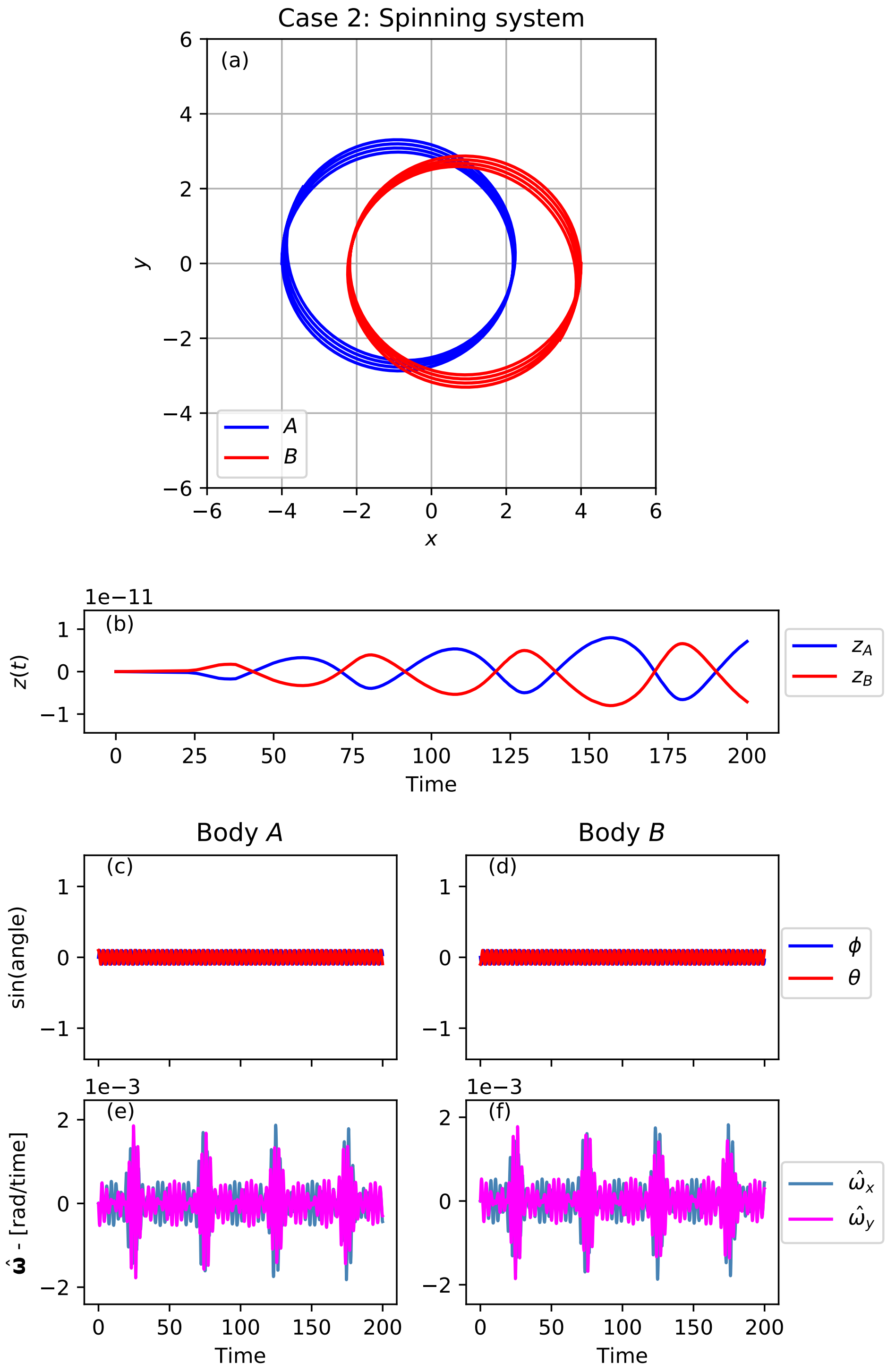

Figure 5: Results of the translational and rotational motion of the spheroids for case 2. We have not shown $\hat{\omega}_z$ since it has a constant value of $\hat{\omega}_z = 2$.

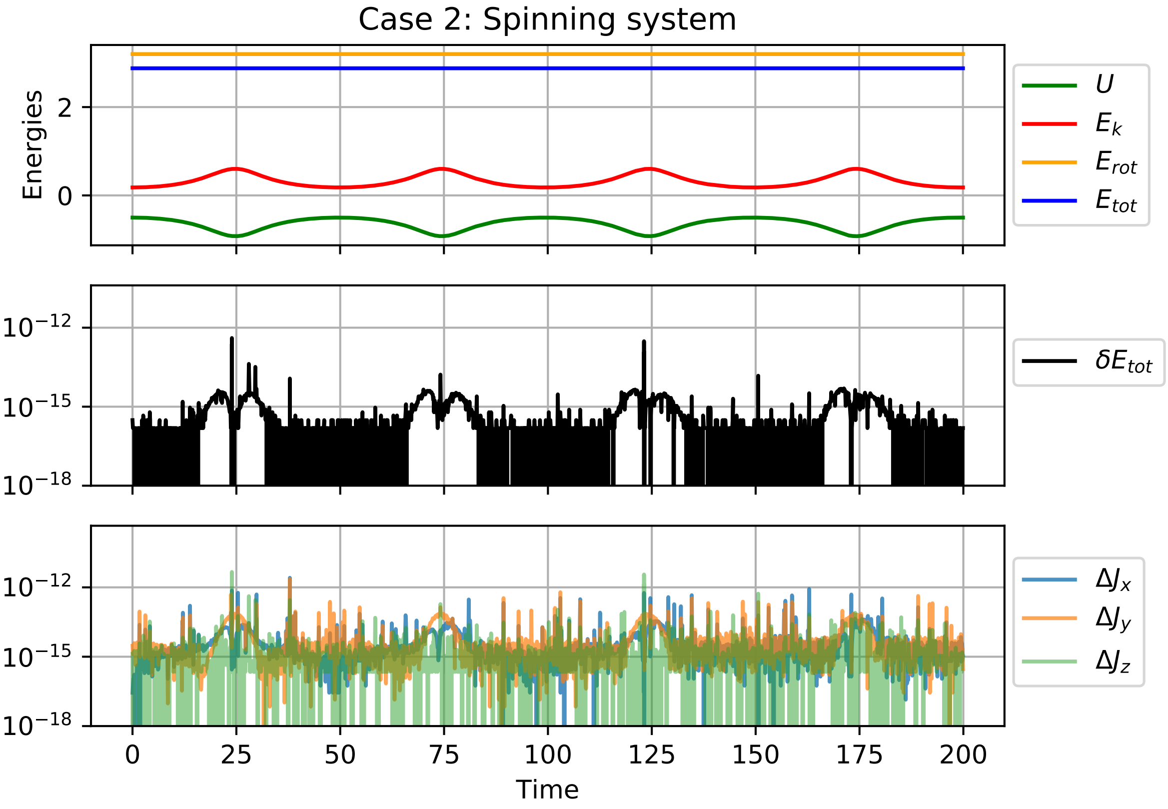

Figure 6: Same as Fig. 4 but for case 2, where both spheroids have an initial angular velocity. The total energy and total angular momentum of the system is conserved, as demonstrated by the small relative error in these two quantities.

stabilises.

The angular velocity components $(\hat{\omega}_x, \hat{\omega}_y)$ are shown in Figs. 5e and 5f for bodies A and B, respectively. Because of the rotational symmetry of the spheroid, $\hat{\omega}_z$ will remain constant at the value $\hat{\omega}_z = 2$ throughout the simulation, and is therefore excluded from the figures. The values of the $\hat{\omega}_x$ and $\hat{\omega}_y$ components peaks when the two spheroids are in close proximity. By increasing the initial angles by a factor of four, i.e. $\theta_0 = \pi/8$, the amplitude of both the $\hat{\omega}_x$ and $\hat{\omega}_y$ components nearly doubles, indicating that the amplitude of these two angular velocity components is sensitive to initial angle.

The different parts of the total energy are shown in the top panel of Fig. 6. Due to the spheroids' rotations, the rotational energy now makes a significant contribution to the total energy, being greater than the kinetic energy from the translational motion. However, because $\hat{\omega}_x$ and $\hat{\omega}_y$ are roughly 3 orders of magnitude smaller than $\hat{\omega}_z$, and $\hat{\omega}_z$ is constant, the rotational energy is nearly constant. Furthermore, both the total energy and total angular momentum remain constant in the simulation, as their respective errors are smaller than 10^{-12}.

Parameter	Alpha	Beta
a, semiaxis along x [km]	0.766	0.285
b, semiaxes along y [km]	0.748	0.232
c, semiaxes along z [km]	0.674	0.175
m, mass [10^{12} kg]	2.353	0.135
ϕ_0, initial rotation angle around x-axis [°]	3.2	0.0
$\hat{\omega}_{z,0}$, initial angular velocity [rad hr^{-1}]	2.2728	0.3611
a_s, semi-major axis [km]		2.548
e, eccentricity		0.0004
i, inclination [°]		156.1
Ω, longitude of ascending node [°]		105.4
ω, argument of periapsis [°]		319.7
M_0, mean anomaly [°]		0.0

Table 2: The parameters and initial conditions used for the simulations. The orbital elements, obtained from Ostro et al. (2006), are those of Beta in orbit around Alpha. For the spheroid simulations, we set the semiaxes to be $a = b$.

4 Application to (66391) 1999 KW4

In this section, we apply our method to the asteroid binary system (66391) 1999 KW4, where we refer to the primary as Alpha, and to the secondary as Beta. We will study the dynamical evolution of the bodies and see how the outcome changes when the body shapes are changed from ellipsoids to spheroids by setting the semiaxes to be $a = b > c$. The simulations run with a timespan of 1 year.

The physical parameters, as well as initial conditions, used in the simulations are shown in Table 2. We let Alpha start at rest from the origin of the inertial frame in the simulations. We also assume that Beta is located at the pericenter at $t = 0$, and thus set the mean anomaly M_0 to be initially zero. Ostro et al. (2006) also find that the angle between the rotation pole of Alpha and the binary orbit is between 0° and 7.5° with a nominal separation of 3.2°. As such, we let Alpha be initially rotated with $\phi_0 = 3.2°$, whereas Beta initially remains non-rotated. It is assumed that the orbit of Beta is synchronous, and the initial angular velocity of Beta is set so that its rotation period is equal to its orbital period.

The top, middle and bottom panels of Fig. 7 shows the eccentricity, semi-major axis and inclination of Beta respectively. The inclination is calculated with respect to the original plane of orbit. For a spheroidal model, the eccentricity can take slightly higher values, where the eccentricity peaks at $e = 0.0140$ for the spheroidal model, while it peaks at $e = 0.0126$ for the ellipsoidal model. This is lower to the eccentricity in the excited state of Fahnestock and Scheeres (2008) (see also Compère and Lemaître, 2014; Hou et al., 2017; Shi et al., 2017), which find that the eccentricity can surpass $e = 0.03$. The range of the semi-major axis are similar in both simulation types, where it takes values between $a_s \in [2.5418, 2.5526]$

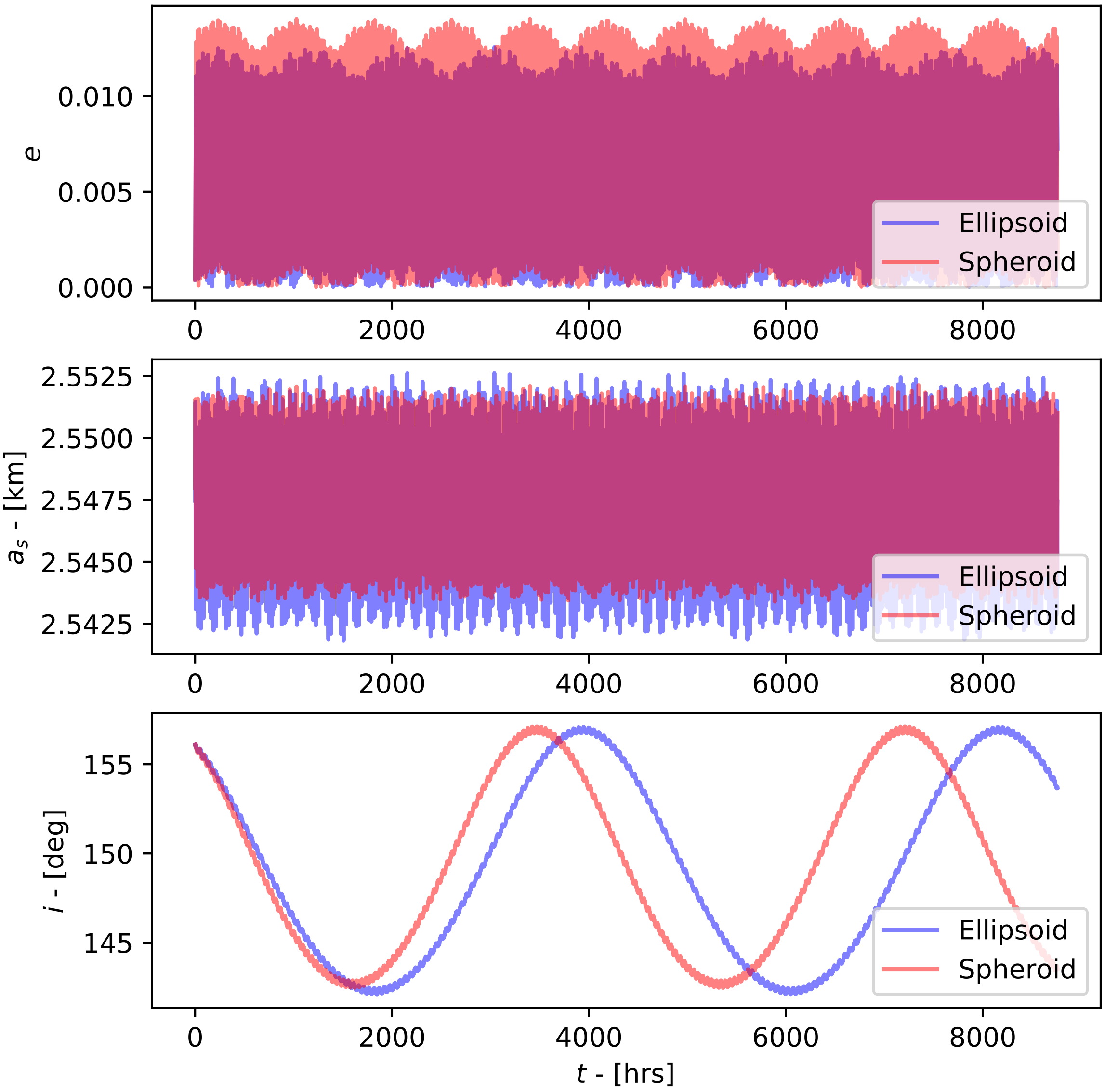

Figure 7: Time evolution of the eccentricity, semi-major axis and inclination with respect to the original plane of orbit.

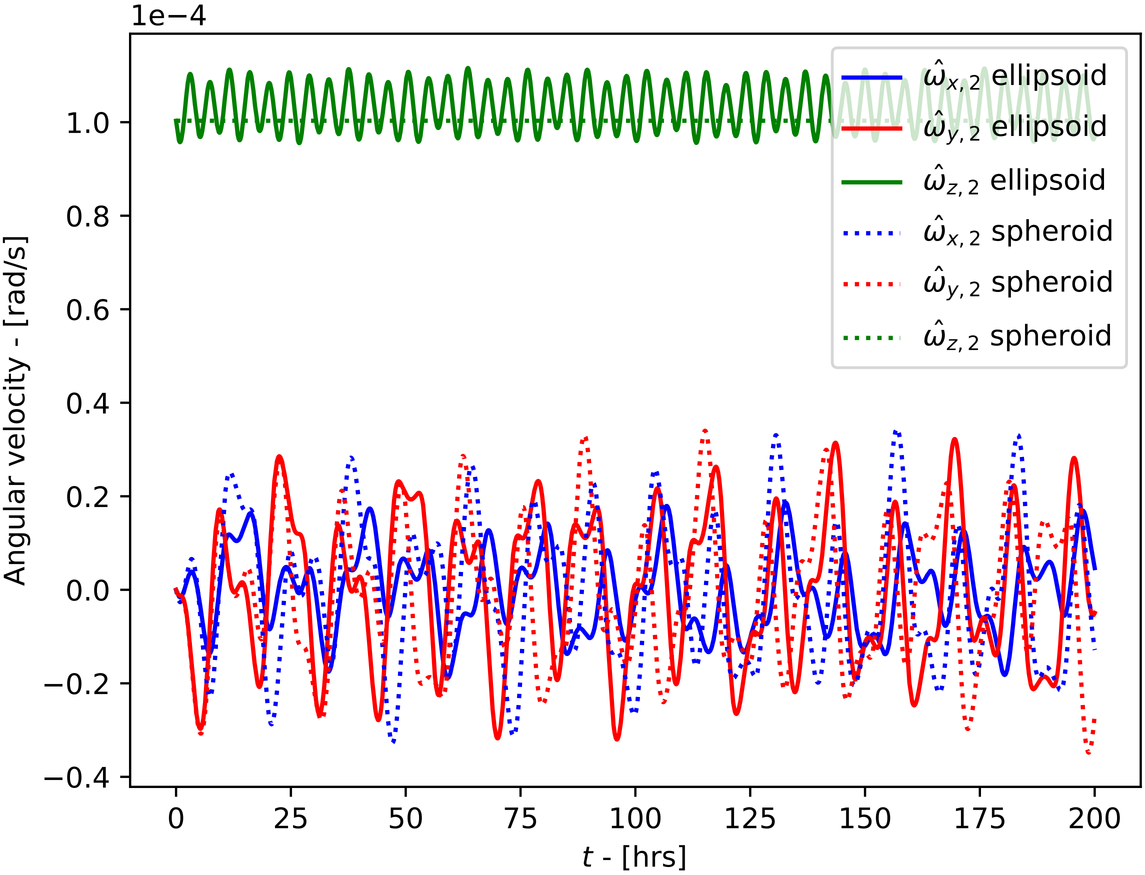

Figure 8: The angular velocity components of Beta as a function of time. Solid lines corresponds to the bodies take ellipsoidal shapes, while the dotted lines correspond to the bodies with spheroidal shapes.

km and averaging at $\bar{a}_s = 2.5471$ km for the ellipsoidal model, and $a_s \in [2.5433, 2.5521]$ km and averages at $\bar{a}_s = 2.5477$ km for the spheroidal model.

Because the orbital period is proportional to the semi-major axis, the fact that the average semi-major axis is larger in the spheroidal simulation, indicates that the orbital period is also longer. We find that the average orbital period of Squannit is $\bar{T} = 17.4116$ hrs for the ellipsoidal simulation and $\bar{T} = 17.4177$ for the spheroidal simulation. The period of the inclination is longer for the ellipsoidal model, where the period is approximately 3900 hrs between the two maxima, whereas the period is approximately 3400 hrs for the spheroidal model.

Figure 8 shows the angular velocity components of the secondary for the first 200 hours of the simulation. Here, we find that the range of $\hat{\omega}_z$ is $\hat{\omega}_z \in [9.55, 11.16] \cdot 10^{-5}$ rad/s. Compared to the findings of Fahnestock and Scheeres (2008), the range range is smaller than the excited state, but also larger than the relaxed state, than that of Fahnestock and Scheeres. Another major difference is in the components of both $\hat{\omega}_x$ and $\hat{\omega}_y$. The work of Fahnestock and Scheeres find that both of these components change very insignificantly for both the excited

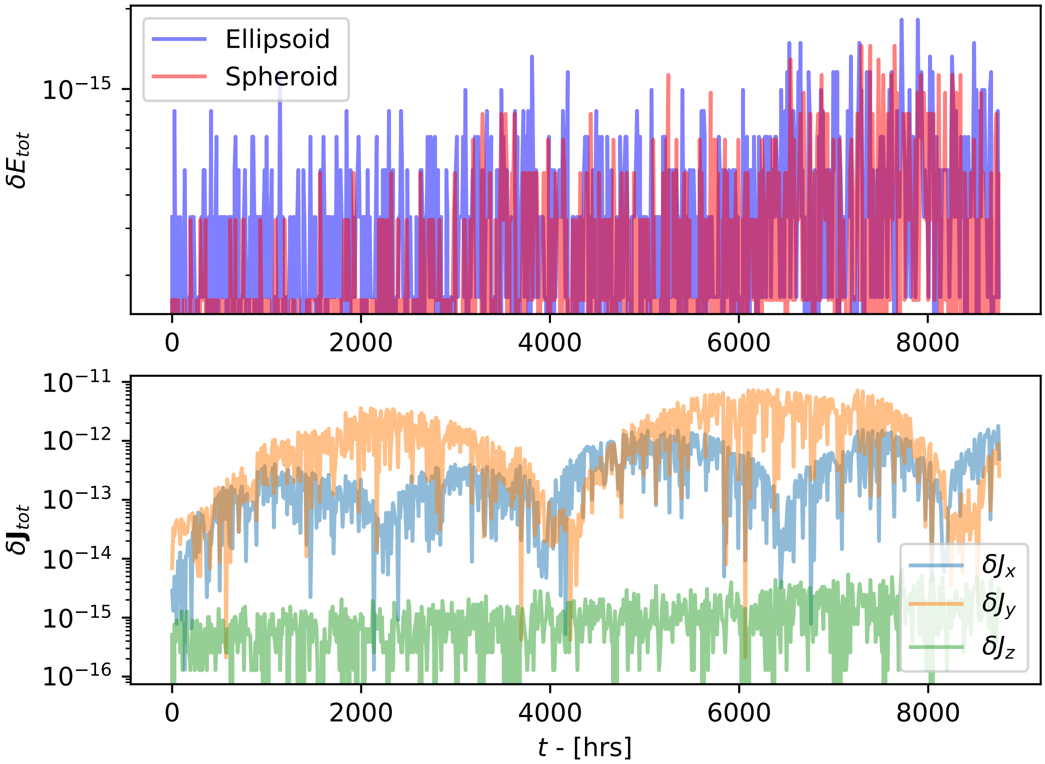

Figure 9: *Top*: The relative error of the total energy of the (66391) 1999 KW4 system, where the blue and red curves correspond to the ellipsoidal and spheroidal simulations respectively. *Bottom*: The relative error of the components of the total angular momentum for the ellipsoidal simulation.

and relaxed configurations. Our findings, however, show that the components respectively oscillates around the values $\hat{\omega}_x \in [-1.89, 1.86] \cdot 10^{-5}$ rad/s, $\hat{\omega}_y \in [-3.20, 3.23] \cdot 10^{-5}$ rad/s. As previously mentioned in dimensionless test scenario "spinning system" (see Sect. 3.2), the amplitude of the $\hat{\omega}_x$ and $\hat{\omega}_y$ components could be affected by the initial angle. The difference in our result, and the one of Fahnestock and Scheeres, could therefore be due to the difference in the initial angles.

Changing the body shapes from ellipsoids to spheroids significantly affects $\hat{\omega}_z$. As seen in Fig. 8, by allowing the bodies to take a spheroidal shapes, $\hat{\omega}_z$ for Beta becomes constant as opposed to oscillating when it had an ellipsoidal shape. This is because spheroids are rotationally symmetric, and no torques can act to change the angular velocity in the z-direction. This is also what was seen in the dimensionless test scenarios in Sect. 3. The $\hat{\omega}_x$ and $\hat{\omega}_y$ components, on the other hand, still oscillates between the values seen for an ellipsoidal shape. The angular velocity of Beta in the spheroidal case is similar to the result that was previously shown in Fig. 5e and 5f, in which $\hat{\omega}_z$ was constant and both $\hat{\omega}_x$ and $\hat{\omega}_y$ were oscillating over time.

Figure 9 shows the relative error in the total energy and the relative error of the components of the total angular momentum in the top and bottom panels respectively. The blue and red curves correspond to simulations where the bodies take ellipsoidal and spheroidal shapes. The relative error of the total energy is smaller than 10^{-14} for both the ellipsoidal and spheroidal simulations. For the total angular momentum, we only show the relative error in the ellipsoidal simulation. Here, the relative errors in each component are smaller than 10^{-11}. The errors in the spheroidal simulation are similar to the ellipsoidal simulation. Although, throughout the simulation, there is a drift in the total angular momentum, causing the errors in each component to increase over time.

5 Summary and discussion

We have validated and explored an alternative method for simulating the dynamics of a fully three dimensional rigid two-body problem suggested by Conway (2016). The method, which is based on vector potentials instead of scalar potentials, uses surface integrals to determine the force, torque and mutual potential energy between two bodies. Wold and Conway (2021) outlined the surface integration method in detail, and tested it for a pair of coplanar spheroids and thin disks. In this work, we extend the work and apply the method to pairs of ellipsoids and spheroids that can be randomly oriented with respect to each other, hence torques and angular momentum exchange is included.

Table 3 shows a summary on the CPU time used for each simulation. The CPU time used for the dimensionless simulations varied between 20 seconds to two minutes. For the (66391) 1999 KW4 system, the CPU time required varied between one hour to four hours.

Two dimensionless cases were studied, where both test scenarios considered spheroidal body shapes. In the first case, both the spheroids are initially rotated around their body-fixed x-axes. Despite the lack of initial motion along the z-direction, the initial rotational tilt allowed a small force component along the z-direction to take place. This results to a small motion along the z-direction over time, although the motion is 11 orders of magnitude smaller than the motion along the x and y direction. Furthermore, the rotational motion of the spheroids develops into tumbling motion. The second dimensionless case considered is similar to the first one, where both bodies are now initially rotated around their body-fixed y-axes. However, in this scenario, both bodies also start with an angular velocity about their body-fixed z-axes. The motions of the spheroids' in this case closely resembled two tops spinning in orbit around the common center of mass. By spinning the spheroids about their axes of symmetry, the rotational motion stabilises so that it is no longer tumble-like.

Finally, we apply the method on the asteroid binary system (66391) 1994 KW4. In this scenario, we consider two types of simulations: one where both bodies have ellipsoidal shapes and one where both have spheroidal shapes.

We compare the difference in the dynamical evolution of Beta when the bodies had ellipsoidal and spheroidal shapes. The eccentricity, on average, is larger in the spheroidal simulation. Furthermore, the values of the eccentricity is smaller than the findings of of Fahnestock and Scheeres (2008). The values of the semi-major axis are similar for both simulation types, but the average semi-major axis is slightly larger for the spheroidal simulation compared to the ellipsoidal simulation. This also indicates that the orbital period becomes longer when the bodies take ellipsoidal shapes. We also find that the time period it would take for the inclination to reach its maximum are longer when both bodies took

Scenario	CPU time	Simulation time
Case 1	22.8 s	200
Case 2	129.0 s	200
1999 KW4, ellipsoids	4.6 hrs	1 yr
1999 KW4, spheroids	1.1 hrs	1 yr

Table 3: CPU time used for each simulation, as well as simulation time, presented in the paper. Note that the simulation time for Case 1 and Case 2 have a dimensionless quantity.

ellipsoidal shapes.

The angular velocity components of Beta is also studied. The results are also compared to the findings of Fahnestock and Scheeres (2008), where we find that the $\hat{\omega}_z$ component, for the ellipsoidal simulation, is similar to the findings of Fahnestock and Scheeres. However, the evolution of both $\hat{\omega}_x$ and $\hat{\omega}_y$ are different, in which we find that these components are oscillating with larger amplitudes compared to the findings of Fahnestock and Scheeres, which is due to the difference in the initial conditions.

Studying the errors in the total energy and total angular momentum serves as a check of simulation accuracy. We find that the errors for both the total energy and total angular momentum are smaller than 10^{-12} for all simulations presented. The errors, which are numerical in origin, are small enough to demonstrate that our model conserves energy and angular momentum.

While our method has only been demonstrated here for a handful of scenarios, the method can also be generalized to an N-body simulation, which can be used to simulate e.g. an asteroid triple system and even include the gravitational pull from the planets in the Solar system.

The authors thank the anonymous referee for the helpful comments and suggestions that improved the manuscript.

A Gravitational field of an ellipsoid and spheroid

The gravitational field is required to compue the mutual potential energy in Eq. (4). We will here derive an analytical expression of $\mathbf{g} = (g_x, g_y, g_z) = \nabla\Phi$ based on the expression in Eqs. (37) and (41). It should be noted that, while κ is a function of (x, y, z), when taking the partial derivatives of the gravitational potential Φ, κ can be treated as a constant (MacMillan, 1930).

For a general ellipsoid, the components of the gravitational field thus become

$$g_x = \frac{4x\pi\rho abc}{\sqrt{a^2 - c^2}} \frac{E(\omega_\kappa) - F(\omega_\kappa)}{a^2 - b^2} \tag{44}$$

$$\begin{aligned} g_y = \frac{4y\pi\rho abc}{\sqrt{a^2 - c^2}} \Bigg[& \frac{F(\omega_\kappa)}{a^2 - b^2} - \frac{(a^2 - c^2)E(\omega_\kappa)}{(a^2 - b^2)(b^2 - c^2)} \\ & + \frac{(c^2 + \kappa)}{b^2 - c^2} \frac{\sqrt{a^2 - c^2}}{\sqrt{(a^2 + \kappa)(b^2 + \kappa)(c^2 + \kappa)}} \Bigg] \end{aligned} \tag{45}$$

$$g_z = \frac{4z\pi\rho abc}{\sqrt{a^2 - c^2}} \left[\frac{E(\omega_\kappa)}{b^2 - c^2} - \frac{(b^2 + \kappa)}{b^2 - c^2} \frac{\sqrt{a^2 - c^2}}{\sqrt{(a^2 + \kappa)(b^2 + \kappa)(c^2 + \kappa)}} \right]. \tag{46}$$

For an oblate spheroid, the components of **g** are

$$g_x = \frac{2\pi\rho x a^2 c}{a^2 - c^2} \left[\frac{\sqrt{c^2 + \kappa}}{a^2 + \kappa} - \frac{1}{\sqrt{a^2 - c^2}} \sin^{-1}\left(\sqrt{\frac{a^2 - c^2}{a^2 + \kappa}} \right) \right] \tag{47}$$

$$g_y = \frac{2\pi\rho y a^2 c}{a^2 - c^2} \left[\frac{\sqrt{c^2 + \kappa}}{a^2 + \kappa} - \frac{1}{\sqrt{a^2 - c^2}} \sin^{-1}\left(\sqrt{\frac{a^2 - c^2}{a^2 + \kappa}} \right) \right] \tag{48}$$

$$g_z = \frac{4\pi\rho z a^2 c}{a^2 - c^2} \left[\frac{1}{\sqrt{a^2 - c^2}} \sin^{-1}\left(\sqrt{\frac{a^2 - c^2}{a^2 + \kappa}} \right) - \frac{1}{\sqrt{c^2 + \kappa}} \right]. \tag{49}$$

The value of κ, for both the ellipsoid and spheroid cases, still satisfies Eq. (38).

References

J. Bellerose and D. J. Scheeres. Energy and stability in the Full Two Body Problem. *Celestial Mechanics and Dynamical Astronomy*, 100(1):63–91, January 2008. doi: 10.1007/s10569-007-9108-3.

L. A. G. Boldrin, D. J. Scheeres, and O. C. Winter. Dynamics of rotationally fissioned asteroids: non-planar case. *Monthly Notices of the Royal Astronomical Society*, 461(4): 3982–3992, October 2016. doi: 10.1093/mnras/stw1607.

G. Boué. The two rigid body interaction using angular momentum theory formulae. *Celestial Mechanics and Dynamical Astronomy*, 128(2-3):261–273, June 2017. doi: 10.1007/s10569-017-9751-2.

C. R. Chapman et al. Discovery and physical properties of Dactyl, a satellite of asteroid 243 Ida. *Nature*, 374(6525):783–785, Apr 1995. doi: 10.1038/374783a0.

A. Compère and A. Lemaître. The two-body interaction potential in the STF tensor formalism: an application to binary asteroids. *Celestial Mechanics and Dynamical Astronomy*, 119(3-4):313–330, August 2014. doi: 10.1007/s10569-014-9568-1.

J. T. Conway. Vector potentials for the gravitational interaction of extended bodies and laminas with analytical solutions for two disks. *Celestial Mechanics and Dynamical Astronomy*, 125:161–194, June 2016. doi: 10.1007/s10569-016-9679-y.

J. T. Conway. Analytical solution from vector potentials for the gravitational field of a general polyhedron. *Celestial Mechanics and Dynamical Astronomy*, 121(1):17–38, Jan 2015. doi: 10.1007/s10569-014-9588-x.

H. Curtis. *Orbital Mechanics for Engineering Students*. Aerospace Engineering. Elsevier Science, 2013. ISBN 9780080977485.

D. Dechambre and D. J. Scheeres. Transformation of spherical harmonic coefficients to ellipsoidal harmonic coefficients. *Astron. Astrophys.*, 387:1114–1122, Jun 2002. doi: 10.1051/0004-6361:20020466.

E. G. Fahnestock and D. J. Scheeres. Simulation of the full two rigid body problem using polyhedral mutual potential and potential derivatives approach. *Celestial Mechanics and Dynamical Astronomy*, 96(3-4):317–339, November 2006. doi: 10.1007/s10569-006-9045-6.

E. G. Fahnestock and D. J. Scheeres. Simulation and analysis of the dynamics of binary near-Earth Asteroid (66391) 1999 KW4. *ICARUS*, 194(2):410–435, April 2008. doi: 10.1016/j.icarus.2007.11.007.

T. Fossen. *Handbook of Marine Craft Hydrodynamics and Motion Control*. Wiley, 2011. ISBN 9781119991496.

T. Fukushima. Prolate Spheroidal Harmonic Expansion of Gravitational Field. *Astron. J.*, 147(6):152, Jun 2014. doi: 10.1088/0004-6256/147/6/152.

R. Garmier and J.-P. Barriot. Ellipsoidal Harmonic expansions of the gravitational potential: Theory and application. *Celestial Mechanics and Dynamical Astronomy*, 79(4): 235–275, April 2001. doi: 10.1023/A:1017555515763.

R. Garmier, J.-P. Barriot, A. S. Konopliv, and D. K. Yeomans. Modeling of the eros gravity field as an ellipsoidal harmonic expansion from the near doppler tracking data. *Geophysical Research Letters*, 29(8):72–1–72–3, 2002. doi: 10.1029/2001GL013768.

P. Geissler et al. Erosion and Ejecta Reaccretion on 243 Ida and Its Moon. *ICARUS*, 120 (1):140–157, Mar 1996. doi: 10.1006/icar.1996.0042.

X. Hou, D. J. Scheeres, and X. Xin. Mutual potential between two rigid bodies with arbitrary shapes and mass distributions. *Celestial Mechanics and Dynamical Astronomy*, 127(3):369–395, March 2017. doi: 10.1007/s10569-016-9731-y.

T. Kane, P. Likins, and D. Levinson. *Spacecraft Dynamics*. McGraw-Hill series in aeronautical and aerospace engineering. McGraw-Hill Book Company, 1983. ISBN 9780070378438.

A. S. Konopliv et al. The dawn gravity investigation at vesta and ceres. *Space Science Reviews*, 163(1):461–486, Dec 2011. ISSN 1572-9672. doi: 10.1007/s11214-011-9794-8.

T. Kramer and M. Noack. Prevailing Dust-transport Directions on Comet 67P/Churyumov-Gerasimenko. *Astrophys. J.*, 813(2):L33, Nov 2015. doi: 10.1088/2041-8205/813/2/L33.

T. Kramer et al. Dust and gas emission from cometary nuclei: the case of comet 67P/Churyumov-Gerasimenko. *arXiv e-prints*, art. arXiv:1505.08041, May 2015.

A. J. Maciejewski. Reduction, Relative Equilibria and Potential in the Two Rigid Bodies Problem. *Celestial Mechanics and Dynamical Astronomy*, 63(1):1–28, March 1995. doi: 10.1007/BF00691912.

W. MacMillan. *The Theory of the Potential.* (MacMillan: Theoretical Mechanics). McGraw-Hill Book Company, Incorporated, 1930.

J. L. Margot et al. Binary Asteroids in the Near-Earth Object Population. *Science*, 296 (5572):1445–1448, May 2002. doi: 10.1126/science.1072094.

W. J. Merline et al. *Asteroids Do Have Satellites*, pages 289–312. University of Arizona Press, 2002.

H. Moritz. *Advanced Physical Geodesy.* Sammlung Wichmann : Neue Folge : Buchreihe. Wichmann, 1980. ISBN 9780856261954.

S. J. Ostro et al. Radar Imaging of Binary Near-Earth Asteroid (66391) 1999 KW4. *Science*, 314(5803):1276–1280, November 2006. doi: 10.1126/science.1133622.

S. Reimond and O. Baur. Spheroidal and ellipsoidal harmonic expansions of the gravitational potential of small Solar System bodies. Case study: Comet 67P/Churyumov-Gerasimenko. *Journal of Geophysical Research (Planets)*, 121(3):497–515, Mar 2016. doi: 10.1002/2015JE004965.

D. Scheeres. Stability of Relative Equilibria in the Full Two-Body Problem. *Annals of the New York Academy of Sciences*, 1017(1):81–94, May 2004. doi: 10.1196/annals.1311.006.

D. J. Scheeres. Stability of the planar full 2-body problem. *Celestial Mechanics and Dynamical Astronomy*, 104(1-2):103–128, June 2009. doi: 10.1007/s10569-009-9184-7.

D. J. Scheeres et al. Dynamical Configuration of Binary Near-Earth Asteroid (66391) 1999 KW4. *Science*, 314(5803):1280–1283, November 2006. doi: 10.1126/science.1133599.

D. Scheeres, S. Ostro, R. Hudson, and R. Werner. Orbits close to asteroid 4769 castalia. *Icarus*, 121(1):67 – 87, 1996. ISSN 0019-1035. doi: https://doi.org/10.1006/icar.1996.0072.

J. Sebera, A. Bezděk, I. Pešek, and T. Henych. Spheroidal models of the exterior gravitational field of asteroids bennu and castalia. *ICARUS*, 272:70 – 79, 2016. ISSN 0019-1035. doi: https://doi.org/10.1016/j.icarus.2016.02.038.

Y. Shi, Y. Wang, and S. Xu. Mutual gravitational potential, force, and torque of a homogeneous polyhedron and an extended body: an application to binary asteroids. *Celestial Mechanics and Dynamical Astronomy*, 129(3):307–320, November 2017. doi: 10.1007/s10569-017-9776-6.

J. H. Verner. Numerically optimal runge–kutta pairs with interpolants. *Numerical Algorithms*, 53(2):383–396, Mar 2010. ISSN 1572-9265. doi: 10.1007/s11075-009-9290-3.

S. J. Weidenschilling, P. Paolicchi, and V. Zappala. Do asteroids have satellites? In R. P. Binzel, T. Gehrels, and M. S. Matthews, editors, *Asteroids II*, pages 643–658, Jan 1989.

R. A. Werner and D. J. Scheeres. Exterior Gravitation of a Polyhedron Derived and Compared with Harmonic and Mascon Gravitation Representations of Asteroid 4769 Castalia. *Celestial Mechanics and Dynamical Astronomy*, 65(3):313–344, Jan 1997.

R. A. Werner and D. J. Scheeres. Mutual Potential of Homogeneous Polyhedra. *Celestial Mechanics and Dynamical Astronomy*, 91(3-4):337–349, March 2005. doi: 10.1007/s10569-004-4621-0.

P. T. Wittick and R. P. Russell. Mascon models for small body gravity fields. In *AAS/AIAA Astrodynamics Specialist Conference*, volume 162, pages 17–162, 2017.

M. Wold and J. T. Conway. The planar two-body problem for spheroids and disks. *Celestial Mechanics and Dynamical Astronomy*, 133(6):27, June 2021. doi: 10.1007/s10569-021-10023-x.

Paper 2 - Dynamics of asteroid systems post-rotational fission

Alex Ho, Margrethe Wold, Mohammad Poursina, and John T. Conway

This paper has been published as:

Alex Ho, Margrethe Wold, Mohammad Poursina and John T. Conway, Dynamics of asteroid systems post-rotational fission. *Astronomy & Astrophysics*, 665:A43, September 2022. doi: 10.1051/0004-6361/202243706.

Dynamics of asteroid systems post-rotational fission

Alex Ho, Margrethe Wold, Mohammad Poursina, John T. Conway
University of Agder, Jon Lilletuns vei 9, 4879 Grimstad, Norway

Abstract

Asteroid binaries found among the near-Earth objects are believed to have formed from rotational fission. In this paper we study the dynamical evolution of asteroid systems the moment after fission. The model considers two bodies the moment after a contact binary separates due to rotational fission. Both bodies are modeled as ellipsoids, and the secondary is given an initial rotation angle about its body-fixed y-axis. Moreover, we consider six different cases, three where the density of the secondary varies and three where the shape of the secondary varies. The simulations consider 45 different initial tilt angles of the secondary, each with 37 different mass ratios. We start the dynamical simulations at the moment the contact binary reaches a spin fission limit, and our model ensures that the closest distance between the surfaces of the two bodies is always kept at 1 cm. The forces, torques, and gravitational potential between the two bodies are modeled using a newly developed surface integration scheme, giving exact results for two ellipsoids. We find that more than 80% of the simulations end with the two bodies impacting, and collisions between the bodies are more common when the density of the secondary is lower, or when it becomes more elongated. In comparison with observed data on asteroid pairs, we find that variations in density and shape of the secondary can account for some of the spread seen in the rotation period for observed pairs. Furthermore, the secondary may also reach a spin limit for surface disruption, creating a ternary or multiple system. We find that secondary fission typically occurs within the first five hours after the contact binary separates, and is more common when the secondary is less dense or more elongated.

1 Introduction

Since the first binary asteroid system, (243) Ida and its moon Dactyl, were discovered by the Galileo spacecraft (Chapman et al., 1995), many more have been identified among near-Earth objects, in the main belt, and in the Kuiper belt (see, e.g., Margot et al., 2015, and references therein). Roughly 27 000 near-Earth asteroids (NEAs) are currently known, the majority of them with diameters less than 1 km (Harris and Chodas, 2021). NEAs are thought to originate from the main belt and, due to resonances with Jupiter, to have migrated into Earth-crossing orbits with perihelion distances of ¡ 1.3 AU (Morbidelli et al., 2002). It is estimated that roughly 16% of near-Earth objects are binaries (Margot et al., 2002).

It is believed that smaller binary systems among asteroids are formed through rotational fission (Margot et al., 2002; Pravec and Harris, 2007). Small asteroids, typically with diameters $\sim 0.1 - 10$ km (Walsh, 2018), are "rubble piles", porous collections of irregularly shaped boulders and finer grains held together by gravity and possibly weak cohesion forces (Hirabayashi et al., 2015; Li and Scheeres, 2021). In the rotational fission model a rubble pile asteroid is spun up by the Yarkovsky-O'Keefe-Radzievskii-Paddack (YORP) effect (Rubincam, 2000). Once the asteroid reaches a critical spin rate, it will start to shed some of its mass (Scheeres, 2007; Walsh et al., 2008). This model also matches the observations of rapidly rotating primaries of asteroid pairs (Pravec et al., 2010, 2019).

Other binary creation processes have also been proposed, such as binary creation by collisions and even creation via tidal disruptions from nearby planets (see, e.g., Margot et al., 2002; Merline et al., 2002; Richardson and Walsh, 2006). The first mechanism is likely to describe formation of binaries of large asteroid systems (see, e.g., Walsh and Jacobson, 2015). However, it is believed that creation of binaries among the NEA population is highly unlikely through these mechanisms.

Various works have studied the dynamics of an asteroid binary system during and after the fission process. Walsh et al. (2008) modeled asteroids as rubble piles consisting of numerous self-gravitating spheres. In their model, the YORP spin-up would eject some of these spheres, and they found that the formation of a satellite was more efficient for a spherical and oblate primary. The work of Scheeres (2007) considered a slightly different scenario in which the asteroids are initially resting on each other; these are known as contact binaries. Scheeres studied the limits in which fission would take place, considering an ellipsoid–sphere model and extended this to a two-ellipsoid model to study the stability of the binary system post-fission (Scheeres, 2009). However, the systems predicted by these theories are highly energetically excited. In order to stabilize the systems and prevent the secondary from escaping, a form of energy dissipation mechanism is necessary.

Work by Jacobson and Scheeres (2011) studied the creation of various NEA binary systems, including doubly synchronous binaries, high-e binaries, ternary systems and contact binaries. They introduced a new binary process, secondary fission, as a mechanism to decrease the energy level of the system. This was extended by Boldrin et al. (2016) to include nonplanar effects, and they found that secondary fission can take place at higher mass ratios, compared to Jacobson and Scheeres (2011), as a nonplanar configuration allows for higher energy levels. They also found that the secondary acquired nonprincipal axis rotations as a consequence of the nonplanar effects. Davis and Scheeres (2020) further studied post-fission dynamics by including higher order gravity terms in addition to nonplanar effects, and also included tidal torques. Davis and Scheeres compared their results with Jacobson and Scheeres (2011), and found that the formation processes remain unaltered, but that the process itself is slower. Additionally, due to the possibility of re-collision in their model, they found that the rate of escaping secondaries is lower.

In this paper we study the dynamical evolution of asteroid binary systems immediately after fission occurs. Our work is similar to the work of Boldrin et al. (2016), who assumed rotational fission of a contact binary where the secondary was given different initial tilt angles about its body-fixed y-axis. We investigate the outcome of the rotational fission for a number of different mass ratios and configurations of the contact binary. Whereas the

Boldrin et al. study was restricted to systems with mass ratios $q \leq 0.3$ where the density and shape of the secondary was identical to that of the primary, we include the whole range of mass ratios from 0.01 to 1, and also allow for different densities and shapes of the secondary. Our work applies the method we recently developed that computes the forces and mutual torques between two bodies without using approximations (Wold and Conway, 2021; Ho et al., 2021). When expanding the mutual potential, for instance through spherical harmonics, higher order terms have a more significant role in the dynamics of the system when the bodies are closer. Furthermore, Hou et al. (2017) showed that higher order terms are required when the bodies are also more elongated. This means that using an exact method may provide more accurate results of the dynamics of asteroid binaries or pairs after the initial separation.

The structure of this paper is as follows. In Sect. 2 we present the mathematical framework and initial conditions used for our models. In Sect. 3 we describe the models used and present the results of the simulations. Finally, we summarize and discuss our results in Sect. 4.

2 Dynamical model

The model consists of two triaxial ellipsoids. Initially they are attached to each other as a contact binary. We assume that the contact binary undergoes rotational fission, a process where the two components separate when a certain limiting rotational speed is reached (Bottke et al., 2002; Scheeres, 2007; Walsh et al., 2008). The initial setup is shown in Fig. 1, and is similar to that used by Boldrin et al. (2016), with the secondary centered on the long semiaxis of the primary and rotated an angle θ_0 about its body-fixed y-axis.

To compute the force and torque on body i in the gravitational field of body j, we apply the surface integral equations described by Conway (2016)

$$\mathbf{F}_G = G\rho_i \iint\limits_{S_i} \Phi_j(\mathbf{r})\mathbf{n}dS, \tag{1}$$

$$\mathbf{M} = -G\rho_i \iint\limits_{S_i} \Phi_j(\mathbf{r})\mathbf{n} \times \mathbf{r}dS, \tag{2}$$

where the mutual potential between the two bodies is written as

$$U = \frac{G\rho_i}{3} \iint\limits_{S_i} \left(\mathbf{r}\Phi_j(\mathbf{r}) - \frac{1}{2}|\mathbf{r}|^2\mathbf{g}_j(\mathbf{r}) \right) \cdot \mathbf{n}dS. \tag{3}$$

In these formulae ρ_i is the density of body i (assumed to be constant throughout the body), and $\Phi_j(\mathbf{r})$ and $\mathbf{g}_j(\mathbf{r}) = \nabla\Phi_j$ are the scalar potential and gravitational field of body j at a position $\mathbf{r}$ on the surface of body i. The vector normal to the surface of body i at position $\mathbf{r}$ is $\mathbf{n}$, and dS is the surface element at that position. The gravitational constant is denoted as G.

It is customary to use second- or fourth-order approximations of the mutual gravitational potential for two-body interactions of nonspherical bodies, and from that compute force and torque (Fahnestock and Scheeres, 2008; Boldrin et al., 2016; Hou et al., 2017; Davis and Scheeres, 2020). The mutual potential is thus expressed as a sum of several terms, which in fact suffers from a truncation error. However, our approach uses exact expressions in the form of surface integrals, and will therefore not suffer from truncation errors. For ellipsoids the potential of the bodies (Φ) can be expressed using well-known analytical expressions (MacMillan, 1930). The surface integration scheme thus becomes a surface integration over an ellipsoid surface (see Wold and Conway, 2021, for a more detailed outline of the surface integration).

We propagate the binary after rotational fission by solving the rotational and translational equations of motion in an inertial frame of reference, formulating it as a standard initial value problem. The rotational motion of the bodies is solved in the body-fixed reference frames using Euler parameters (e_0, e_1, e_2, e_3) in order to avoid the singularities related to Euler angles. For the integration of the equations of motion, we use the ninth-order Runge-Kutta method by Verner (2010). While it is convenient to use an adaptive time stepper, we use the solver with a fixed time step of $\Delta t = 19$ minutes in order to compare the time evolutions between various simulations. Furthermore, we do not make use of an adaptive time stepper because our simulations are relatively short. The end results did not have significant changes when the time step was smaller, nor did an adaptive time stepper affect the outcome.

2.1 Rotational fission

Throughout the rest of this paper, all variables with subscript p and s correspond to variables describing the primary and secondary, respectively.

Initially, before separation, the contact binary rotates about an axis passing through the center of mass of the system and perpendicular to the xy-plane of the primary, as shown in Fig. 1. When the rotational speed reaches a certain limit ω_0, the centrifugal force on the secondary matches the gravitational attraction between the primary and secondary, and the contact binary fissions.

The initial angular velocity ω_0, which we use to start our simulations, is therefore the limit for rotational fission given by

$$\omega_0 = \beta\sqrt{\frac{F_G}{m_s r}}, \tag{4}$$

where m_s is the mass of the secondary and r is the distance between the centroid of the secondary and the center of mass of the system (see Fig. 1). We found during our simulations that it was necessary to assume a value of ω_0 that is slightly higher than the theoretical limit, hence we multiplied the theoretical limit by the factor $\beta = 1.01$. The β-factor can be interpreted as some cohesion between the two components, and small amounts of cohesion may allow rubble pile asteroids to rotate faster than the theoretical limit (Holsapple, 2007; Sánchez and Scheeres, 2014).

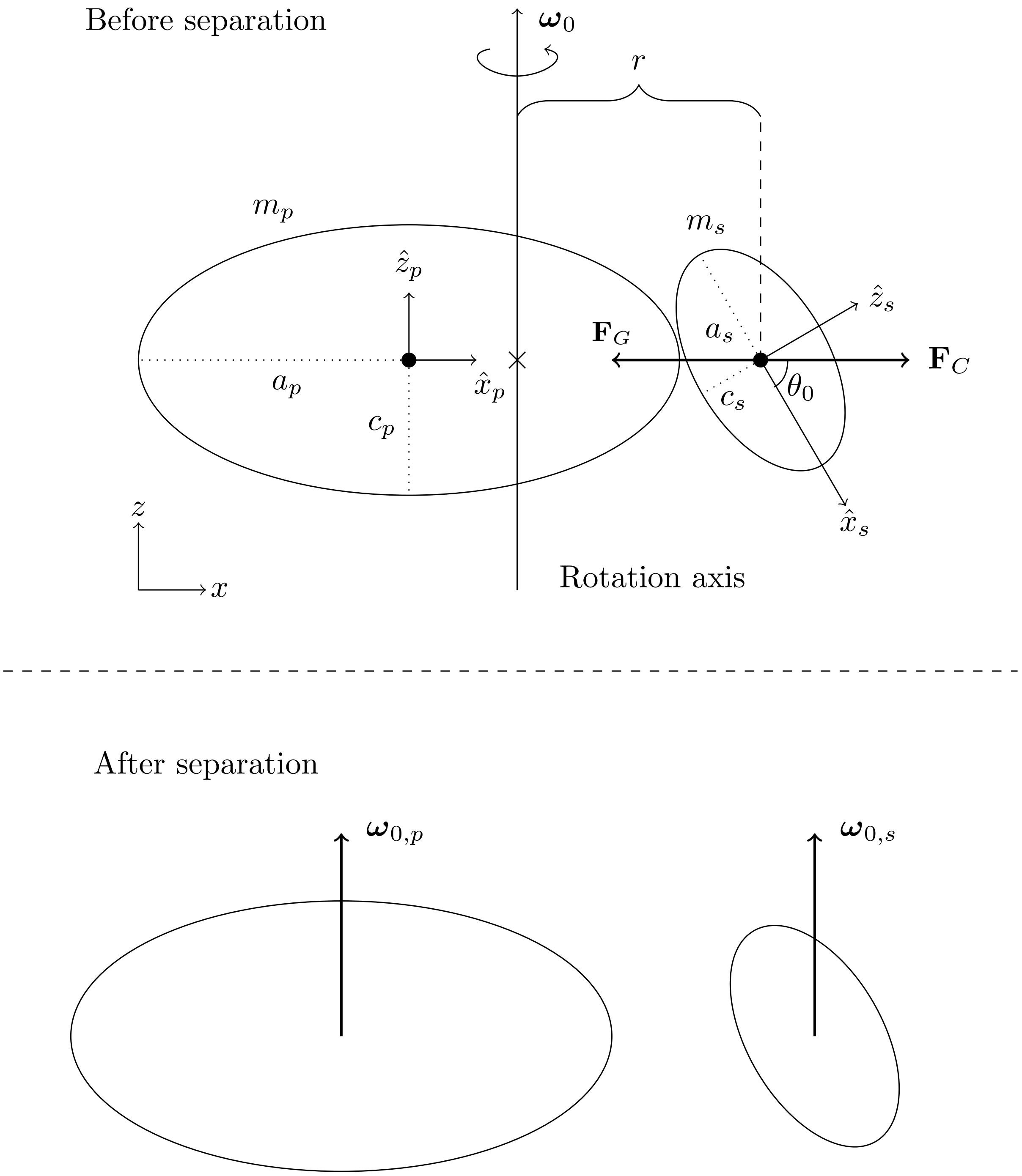

Figure 1: Contact binary before separation (top) and after separation (bottom). Top: Configuration of the contact binary the moment of fission where the gravitational force $\mathbf{F}_G$ and the centrifugal force $\mathbf{F}_C$ are equal. The cross indicates the center of mass of the system. The long and short semiaxes (a and c) are aligned with the body-fixed x- and z-axes of the respective bodies. Bottom: Angular velocities of the bodies after the contact binary separates.

2.2 Initial conditions

As the system is not affected by external forces or torques, linear and angular momentum is conserved. Furthermore, no energy is added or removed at the instant of fission. Thus, immediately after fission the primary and the secondary both experience the same angular velocity ω_0. Therefore, the initial translational velocities of these two objects right after fission can be found as

$$\mathbf{v}_{0,p} = \boldsymbol{\omega}_0 \times (\mathbf{r}_{0,p} - \mathbf{r}_{cm}), \tag{5}$$

$$\mathbf{v}_{0,s} = \boldsymbol{\omega}_0 \times (\mathbf{r}_{0,s} - \mathbf{r}_{cm}), \tag{6}$$

where $\mathbf{r}_{0,p}$ and $\mathbf{r}_{0,s}$ are respectively the initial positions of the primary and secondary in the inertial frame, $\mathbf{r}_{cm}$ is the position of the center of mass of the system, and $\boldsymbol{\omega}_0 = [0, 0, \omega_0]$ is the initial angular velocity vector in the center of mass system. After the bodies have separated, the angular velocities of the bodies in the inertial frame are equal to those of the contact binary before separation, as shown below the dashed line in Fig. 1. The angular velocities in the body-fixed frames are determined as

$$\hat{\boldsymbol{\omega}}_0 = R^T \boldsymbol{\omega}_0, \tag{7}$$

where R^T is the transpose of the rotation matrix at the time of separation.

The configuration is varied by changing simultaneously the initial angle θ_0 of the secondary and the centroid-to-centroid distance between the primary and secondary, under the condition that the separation between the two surfaces at their closest point is kept at $\Delta r = 1$ cm. When $\theta_0 = 0°$, the initial positions of the primary and the secondary are

$$\mathbf{r}_{0,p} = [0, 0, 0], \tag{8}$$

$$\mathbf{r}_{0,s} = [a_s + a_p + \Delta r, 0, 0], \tag{9}$$

where a_p and a_s are respectively the long semiaxes of the primary and secondary and $\Delta r = 1$ cm is the separation between the surfaces.

When θ_0 increases from 0 to 90°, the surface-to-surface distance increases. In order to keep this distance at 1 cm, the secondary's centroid has to be moved closer to the primary's centroid, as illustrated in Fig. 2. In this manner we ensure that the initial separation between the surfaces is always 1 cm. In practice, when θ_0 changes, the initial position of the secondary $\mathbf{r}_{0,s}$ is recalculated by a separate algorithm.

By keeping the initial distance between the surfaces to 1 cm regardless of the value of θ_0, the limiting value of ω_0 for the initial fission will increase. This is a consequence of r becoming smaller in Eq. (4). The variation in ω_0 with θ_0 is shown in Fig. 3. The top panel shows that ω_0 increases as a function of θ_0 when $\Delta r = 1$ cm (blue crosses). However, when the centroid-to-centroid distance is kept constant, which leads to an increasing gap between the surfaces, the value of ω_0 decreases slightly as a function of θ_0 (red crosses). Our model therefore takes into account that the limiting rotational speed for fission changes as the tilt angle of the secondary changes. The bottom panel shows the relative difference between these two cases for three different mass ratios of the primary to the secondary. The relative difference amounts to ≈15–20 % when θ_0 approaches 90°. We also note that the relative difference grows larger as the mass ratio increases.

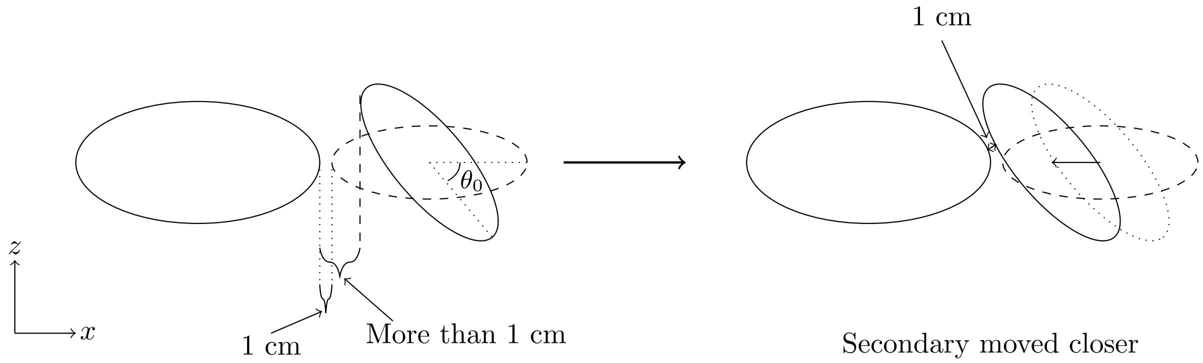

Figure 2: How the secondary moves closer to the primary when the angle θ_0 of the secondary is increased.

Throughout all the simulations the shape and density of the primary are fixed. The semiaxes are $(a_p, b_p, c_p) = (1.0, 0.7, 0.65)$ km, equal to the numbers used by Boldrin et al. (2016), and the density is $\rho_p = 2.0$ g cm^{-3}, which is a commonly used density to model rubble pile asteroids (Pravec et al., 2010; Jacobson and Scheeres, 2011; Boldrin et al., 2016). Some observed asteroids also have densities close to this value, for example 25143 Itokawa (Fujiwara et al., 2006; Kanamaru et al., 2019), as do some primaries of asteroid binaries, such as (66391) 1994 KW4 (Moshup) (Ostro et al., 2006; Scheirich et al., 2021) and (88710) 2001 SL9 (Scheirich et al., 2021).

For each configuration defined by sets of θ_0 (and consequently $\mathbf{r}_{0,s}$), our aim is to study how the dynamics of the binary system evolve while varying the mass ratio $q = m_s/m_p$. We ran simulations for 37 different mass ratios $q = 0.01, 0.05, 0.10$, $q \in [0.15, 0.30]$ in increments of 0.01 and $q \in [0.32, 1.00]$ in increments of 0.04. For each mass ratio q, we considered 45 different initial angles θ_0 of the secondary in the range $\theta_0 \in [0.001°, 90°]$. All simulations were run with a time span of 4800 hr (200 days), unless they were terminated earlier due to collision (or impact) between the two bodies.

3 Results

We examined the dynamics as a function of q and the initial tilt angle θ_0. The mass ratio can be written as

$$q = \frac{\rho_s}{\rho_p}\frac{a_s b_s c_s}{a_p b_p c_p}. \tag{10}$$

Because we keep the shape and density of the primary fixed, varying the mass ratio of the system mainly affects the mass and volume of the secondary. Moreover, increasing the mass ratio also changes the total energy of the system, as shown in Fig. 4. The total energy is the sum of kinetic and potential energy. The systems where the total energy is negative are bound; in systems where the total energy is positive the two components can undergo mutual escape.

First, we consider models with three fixed values of ρ_s/ρ_p while keeping the ratio of the secondary's semiaxes equal to that of the primary. In the next three models the secondary

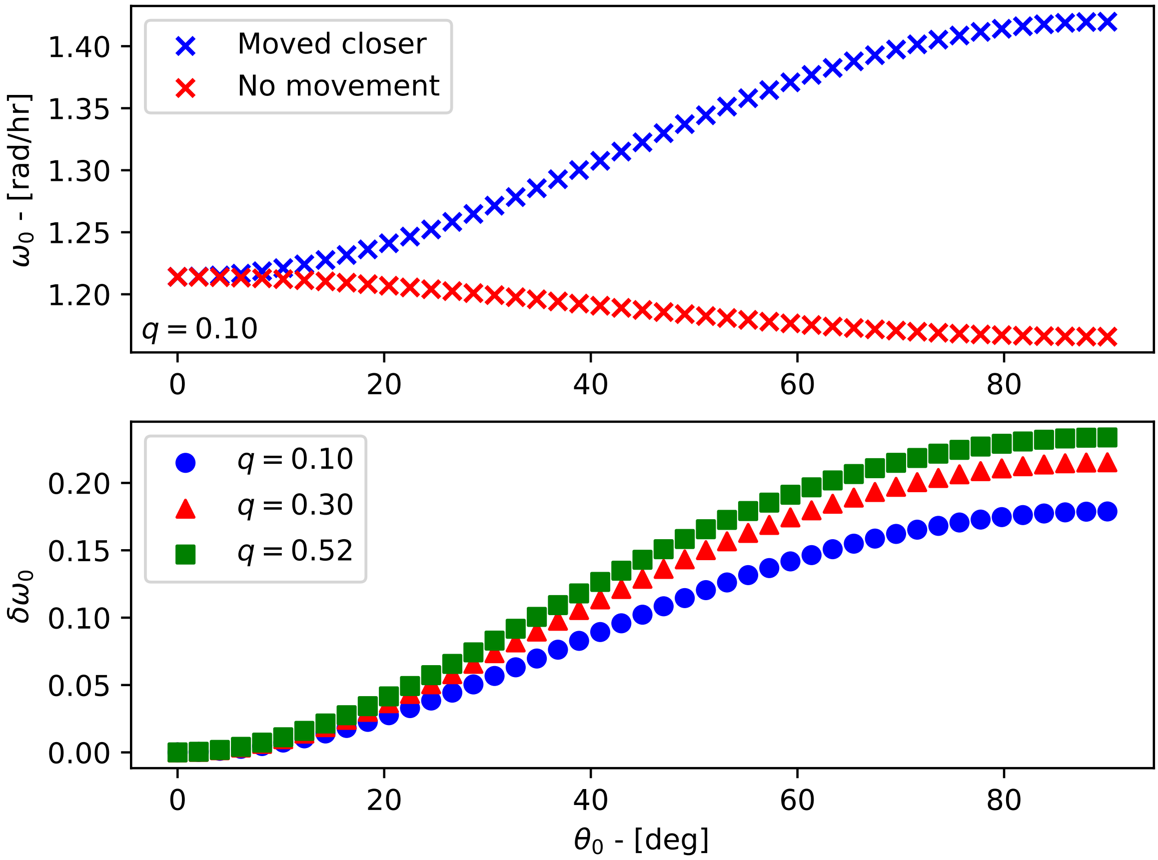

Figure 3: How angular velocity changes with the initial tilt angle θ_0 of the secondary. Top panel: ω_0 is affected when there is contact between the surfaces (blue) and when the surface-to-surface distance increases (red) as the secondary is tilted (see also Fig. 2. The mass ratio is $q = 0.1$ for the data in the top panel. Bottom panel: Relative difference in ω_0 between the two approaches shown in Fig. 2, but for three different mass ratios q. The mass ratio is defined as $q = m_s/m_p$.

can take different geometrical shapes, but now the density is kept constant and equal to that of the primary.

In order to determine whether the secondary has escaped or exists in an unstable orbit, we utilize its orbital eccentricity e. The eccentricity is an osculating Keplerian element, and therefore changes with time. The secondary is considered to have escaped when $e \geq 1$ for at least 50 time steps. This is to ensure that cases where $e \geq 1$ for only a shorter period of time are not classified as already escaped. Increasing this limit to more than 50 time steps did not change the outcome. If, however, the eccentricity is less than unity at the end of the simulation, and the total energy of the system is positive, we classify it as residing in an unstable orbit. The secondary in systems with negative total energies is classified as being in a stable orbit. If the ellipsoid surfaces intersect at any time during the simulation, we consider it a collision and end the simulation.

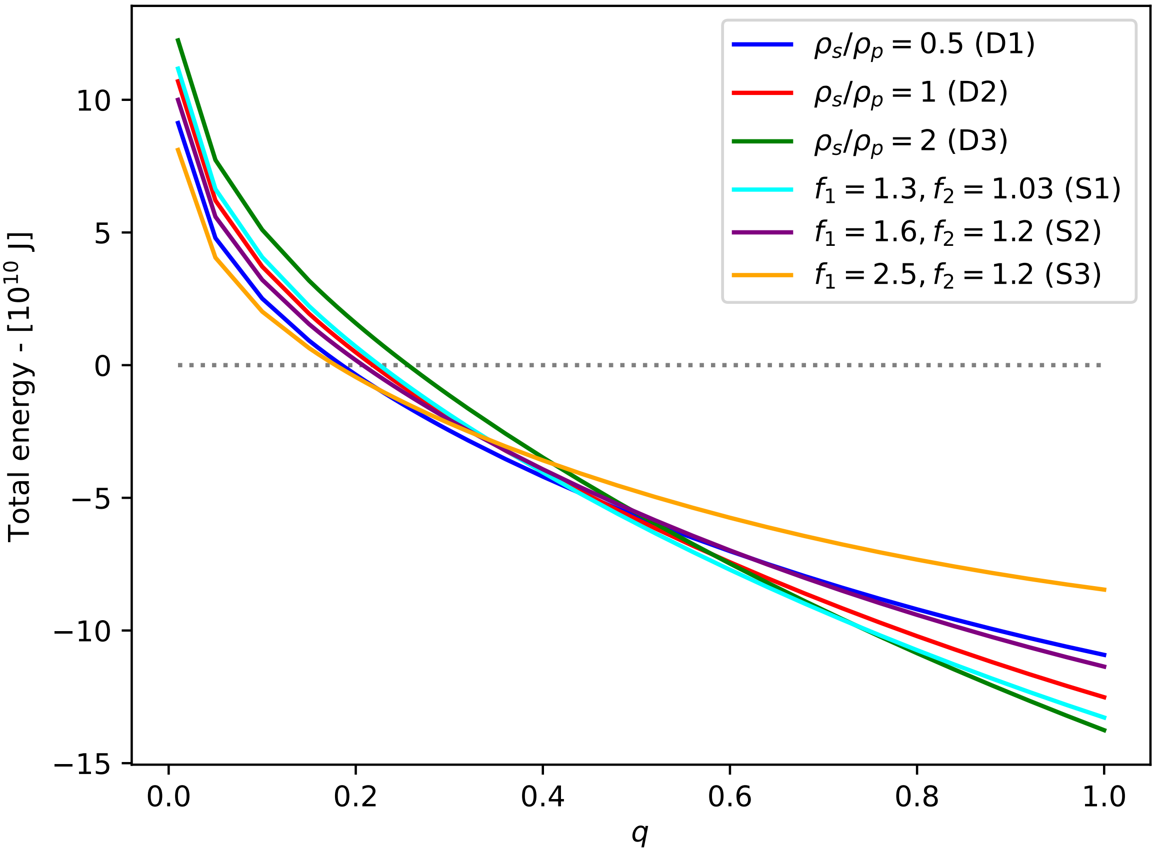

Figure 4: Total energy of the system as a function of the mass ratio q, for each model, using $\theta_0 = 0.001°$. The gray dotted line shows the zero energy line.

These definitions share some similarities with the definitions provided by Scheeres (2002). For instance, the outcome "eventual escape" outlined by Scheeres, where there are multiple periapsis passages that will eventually terminate, is similar to our definition of an unstable case scenario. The "nonimpacting and nonescaping" outcome is equivalent to our stable orbit outcome. However, we do not classify immediate escape scenarios, nor we do distinguish between different reimpact events.

3.1 Varied densities, models D1–D3

The first set of models considered involves varying the density of the secondary while keeping the semiaxis ratio equal to that of the primary, that is $a_s/b_s = a_p/b_p$ and $b_s/c_s = b_p/c_p$. In this case the semiaxes of the secondary can be derived from Eq. (10), with a_s written as

$$a_s = \left(\frac{\rho_p}{\rho_s} q\right)^{1/3} a_p. \tag{11}$$

The equations of b_s and c_s take similar forms.

We examine models with three different density ratios:

- Model D1: $\rho_s/\rho_p = 0.5$;
- Model D2: $\rho_s/\rho_p = 1.0$;
- Model D3: $\rho_s/\rho_p = 2.0$.

As the density of the primary is fixed at $\rho_p = 2.0$ g/cm^3, models D1, D2, and D3 have secondaries with densities of 1.0 g/cm^3, 2.0 g/cm^3, and 4.0 g/cm^3, respectively. Model D2 is identical to the model discussed by Boldrin et al. (2016).

3.2 Varied shapes, models S1–S3

In these models we investigate cases where we vary the axis ratio of the secondary, but keep the density of the secondary equal to that of the primary. We write the secondary's semiaxis ratios as

$$\frac{a_s}{b_s} = f_1, \tag{12}$$

$$\frac{b_s}{c_s} = f_2. \tag{13}$$

We select three combinations of f_1 and f_2:

- Model S1: $f_1 = 1.3, f_2 = 1.03$, a secondary that is fairly spherical and almost an oblate spheroid;
- Model S2: $f_1 = 1.6, f_2 = 1.2$, a cigar-shaped secondary with $a \gg b > c$;
- Model S3: $f_1 = 2.5, f_2 = 1.2$, similar to model S2, but even more elongated.

3.3 Outcome distribution

First we study the outcome of the secondary at the end of the simulations. Figure 5 shows the distribution of the outcomes as functions of mass ratio and initial tilt angle for the six different models. In all six models, most of the simulations (more than 80% of the case results) end up with the two bodies colliding (red area in the figure). These collision events are typically found when $\theta_0 \gtrsim 15°$.

In general, there are two regions ($\theta_0 \lesssim 15°$ and $\theta_0 \gtrsim 80°$) where the components do not impact, but where the secondary either escapes or orbits the primary. Most of these cases are found for configurations with $\theta_0 < 10 - 15°$ over the entire range of q. Those found at higher initial angles mainly take place at low mass ratios, and the number of them residing in this region is low for most models. These two ranges of θ_0 correspond to regions near two configurations ($\theta_0 = 0°$ and $\theta_0 = 90°$) where the contact binary is in a relative equilibrium (Scheeres, 2009).

The separation between the positive and negative total energy regimes in Fig. 5 occurs between the yellow and green areas. For two spheres this separation occurs at $q = 0.2$, and

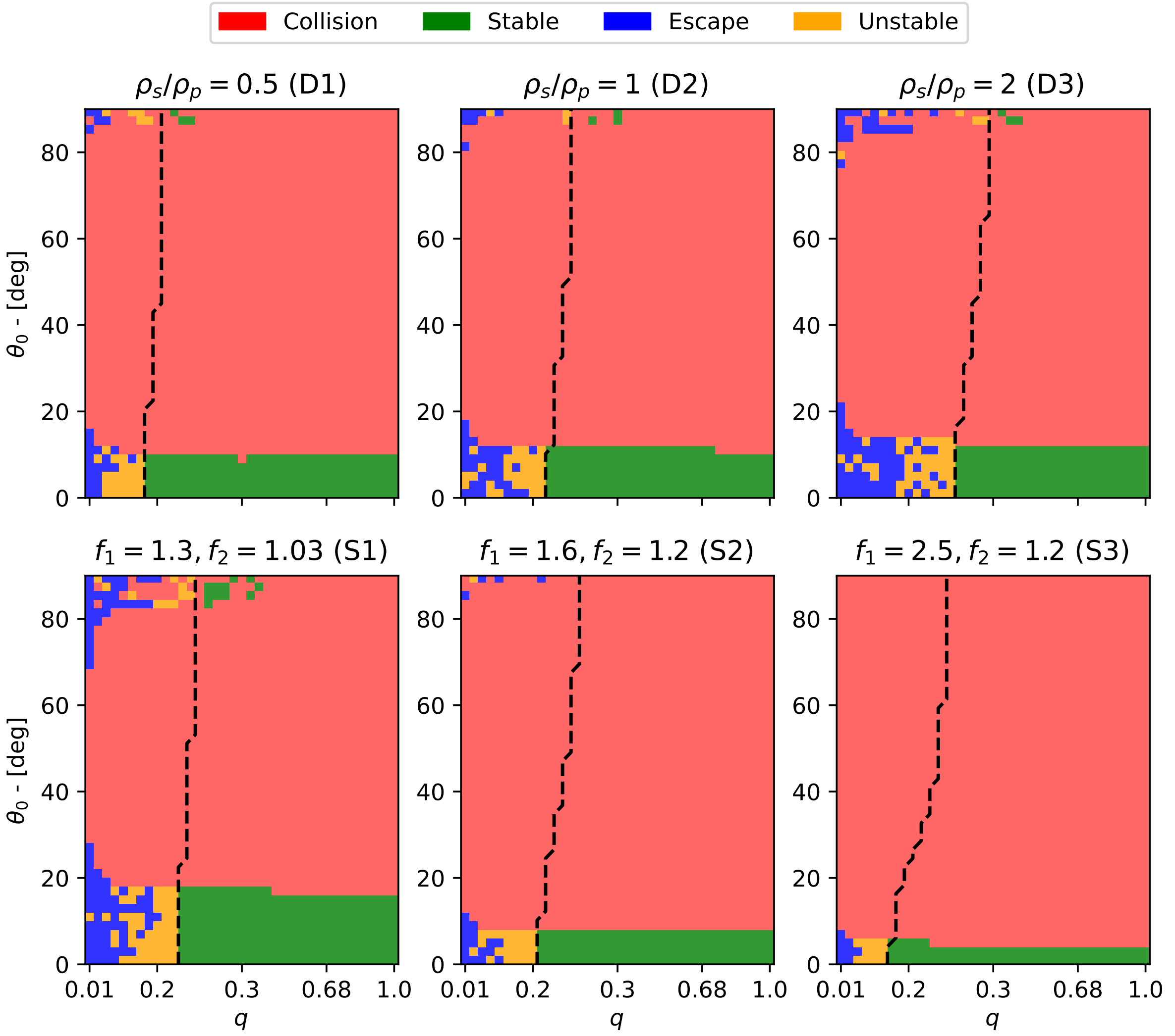

Figure 5: Model outcomes as functions of mass ratio q and initial tilt angle θ_0. In the top row, the left, middle, and right panels correspond to models D1, D2, and D3, respectively. In the bottom row, the left, middle, and right panels correspond to models S1, S2, and S3. The dashed lines indicate the value of q where the total energy is zero.

for triaxial ellipsoids, as in our case, the separateion fluctuates around this value depending on both shape and configuration (see discussion in Scheeres 2009 and Jacobson and Scheeres 2011). We find that the separation occurs at $q = 0.19 - 0.20$, $q = 0.22 - 0.24$, and $q = 0.26 - 0.32$ for models D1, D2, and D3, respectively. Hence the separation occurs at successively higher mass ratios when the density of the secondary increases. The separation shifts toward slightly higher mass ratios when θ_0 increases, as seen in the top regions of the panels. This occurs because the total energy is raised for these configurations, and also reflects an increased value of ω_0, as illustrated in Fig. 3. A similar trend is seen in the varied shape models, where the separation between positive and negative energy regimes occurs at lower mass ratios when the secondary becomes more elongated.

At low mass ratios where the total system energy is positive, we find a mix of cases where the secondary has escaped and where it is still orbiting the primary in an unstable orbit. With a longer simulation time, we expect to see fewer cases of secondaries in unstable orbits. Boldrin et al. (2016) call these secondaries "escape survivors", and only find them at $q > 0.27$ (they only include systems with $q < 0.3$) after a simulation time of 200 yrs. As our simulations are 200 days long, they represent a snapshot of the situation after a fraction of this time. We therefore have survivor cases also at the lowest mass ratios, as opposed to Boldrin et al. (2016).

Of all the cases at $\theta_0 \gtrsim 80°$ that do not collide, a relatively large fraction have escaped compared to those at lower θ_0, typically making up more than 70% for most models. This indicates that the secondary may escape earlier the more tilted its initial position is. A higher initial angle corresponds to a higher energy configuration of the system, and may therefore be the cause of an earlier escape for the high initial angle systems.

At higher mass ratios $q \gtrsim 0.2$ the system total energy is negative, hence all secondaries are gravitationally bound to the primary (unless sufficient energy is added to the system). These are shown in green in Fig. 5. Some also appear when $\theta_0 \gtrsim 85°$.

3.4 Collisions

The majority of the simulations end up with a collision. The collisions tend to occur for configurations with $\theta_0 \gtrsim 15°$, but can also take place at lower initial angles when the density ratio ρ_s/ρ_p is lower, when the secondary becomes more elongated, or when the mass ratio increases. Allowing the secondary to become less dense or more elongated also increases the overall number of collision cases.

Although we find that collisions typically happen at $\theta_0 \gtrsim 15°$ (with the exception of model S3, where collisions can happen as low as $\theta_0 \gtrsim 8°$), Boldrin et al. (2016) report that in their simulations collisions occur for initial tilt angles of $\theta_0 \gtrsim 40°$. This cannot be due to our study having a shorter simulation time, as we would expect the opposite to happen if that were the case (as we expect more systems to collide over time). The most likely explanation is that the secondary in our study starts out closer to the primary when it is rotated (see Fig. 2). By moving the secondary closer, the probability of collision is also expected to increase. This is especially true when θ_0 is nonzero, as the secondary will fall onto the surface of the primary due to the gravitational torque. This also explains why there are significantly more collisions for the more elongated secondaries, as the gravitational torque is stronger when the secondary becomes more elongated. The simulations that survive at high angles are likely due to higher initial velocities as a result of higher system energies, which thus prevent this type of collision.

There is a sharp horizontal division separating collision and stable cases when $\theta_0 \sim 10^\circ - 15^\circ$. However, this is not found at higher angles. This may be because when θ_0 approaches 90 degrees, the secondary approaches an unstable equilibrium, whereas a lower initial angle is closer to a stable equilibrium.

Most of the collisions take place very early in the simulations. More than 95% of the impact events occur within the first five hours. Some of these impacts can occur even within the first two time steps, which make up 82% of the collision outcomes. The collisions that occur between the first and second time step may be considered the "immediate reimpact" events that are mentioned by Scheeres (2002). These early impacts are due to the secondary falling onto the primary as a result of the gravitational torque.

Finally, we study the remaining collision cases that occur later one in the simulation, at $t > 5$ hr. These are shown in Fig. 6, distributed as functions of both q and θ_0. The top panels show that cases that survive longest, in all six models, have intermediate values of the mass ratio, typically between 0.18 and 0.4. Compared to models D1 and D2, there is a tendency for model D3 to survive longer at both lower and higher mass ratios than this range. For instance, there are a few cases with $q \approx 0.5$ and $q \approx 0.1$ with a survival time $\gtrsim 500$ hr which is not found in models D1 and D2. The collision time of model S1 is, on average, greater than those in models S2 and S3. In model S2 there are only two simulations that experience collision after 500 hr, and only one in model S3, that occur when $q \approx 0.25$. The bottom panels in Fig. 6 show that nearly all collisions that take place after 5 hr have elapsed have secondaries with large initial tilt angles $\theta_0 > 80^\circ$. The one exception is for model D1, where the time before collision is approximately 59 hr for a case with $\theta_0 \approx 8^\circ$ and $q = 0.3$ (corresponding to the "dent" in the green region in the top left panel of Fig. 5). On average, the time before collision, for simulations that last longer than 5 hr, is 133 hr, 166 hr, and 143 hr for models D1, D2, and D3, respectively, while for the varied shape models the averages are 170 hr, 192 hr, and 79 hr for models S1, S2, and S3.

3.5 Escape cases

The escape cases are mainly found at the low end of the mass ratio spectrum, typically $q < 0.2$ for most models, as these low mass ratio systems have positive energies. Simulations that result in the secondary escaping make up 1.38%, 2.40%, and 4.86% of the simulations for models D1, D2, and D3, respectively. Thus, it appears that the secondary escapes more easily when the secondary is denser than the primary. Meanwhile, for the varied shape models we find that the escape cases make up 5.23%, 1.20% and 0.48% of the simulations for models S1, S2, and S3, respectively. The lower number of escape cases in models S2 and S3 is likely a consequence of a lower energy configuration in the system, due to the elongated shape of the secondary. However, the torque applied on the secondary, due to the primary, is stronger when it becomes more elongated. It is therefore possible that the small number of escaped secondaries is due to the early collisions.

How long it takes for the secondary to escape varies with both its density and its shape.

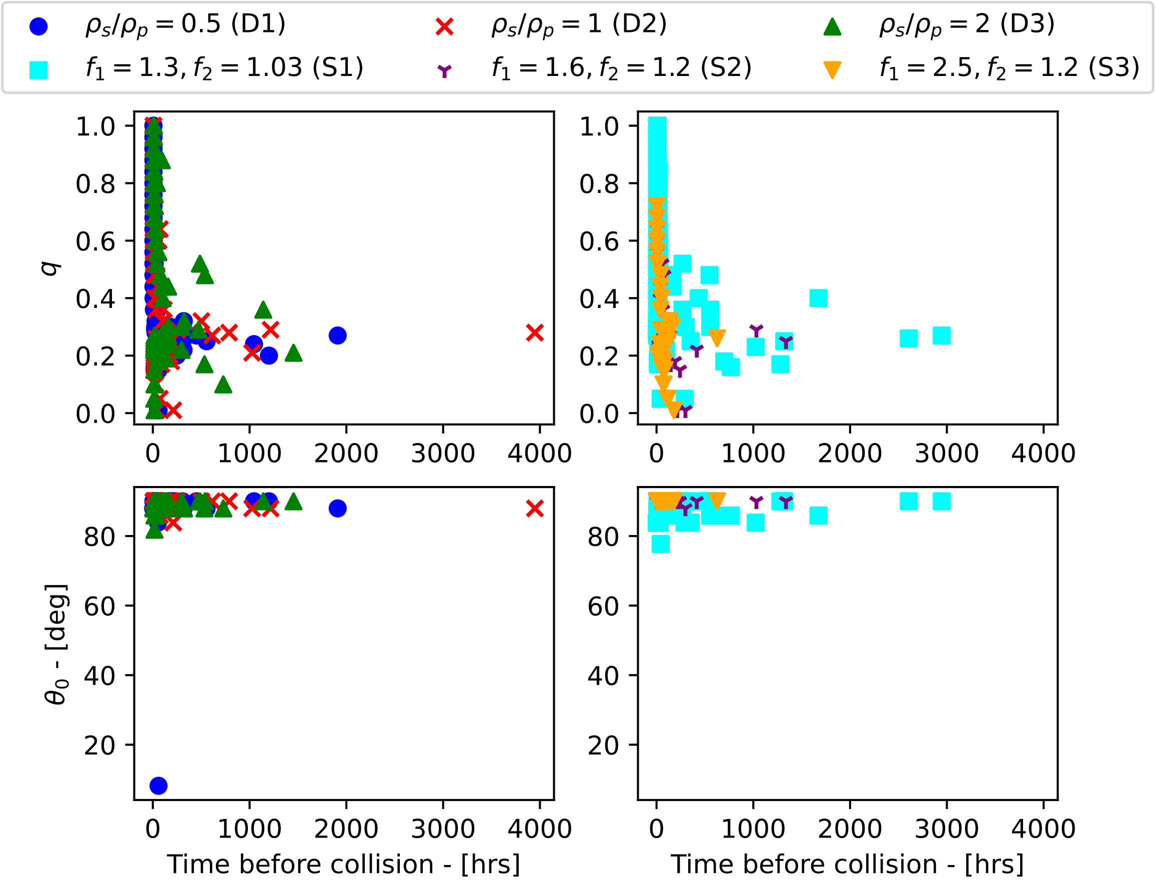

Figure 6: Distribution of mass ratio (top) and initial tilt angle (bottom) as functions of time before collision. The left and right panels show the models with varied density and varied shape, respectively. Collisions that occur before 5 hours have elapsed are excluded from this plot. For the remaining simulations shown in the figure, the average time it takes to collide is 143 hr, 166 hr, and 133 hr for models D1, D2, and D3, respectively, while the average is 171 hr, 193 hr and 79 hr for models S1, S2, and S3 models, respectively.

In Fig. 7, we plot the escape time t_e, averaged over the 45 initial angles, as a function of q. From this figure we can see that there is a trend that the secondary takes longer to escape as the mass ratio increases, which is similar to the findings of Boldrin et al. (2016). We find that the average escape time is roughly twice as short in model D2 as in the results of Boldrin et al. (2016) at corresponding mass ratios. However, as described in Sect. 2.2, the value of ω_0 becomes larger when the secondary is moved closer, due to an increase in θ_0, and the probability of an early escape increases as the system energy increases. The escape time trends of models D1 and D3 are similar to that of D2, but the escape times are slightly longer when density of the secondary is lower. The average escape times of models S1 and S2 are similar up to $q = 0.11$. However, the escape time increases significantly with mass ratio in model S3.

For systems where the secondary takes longer to escape, we expect that rotational energy

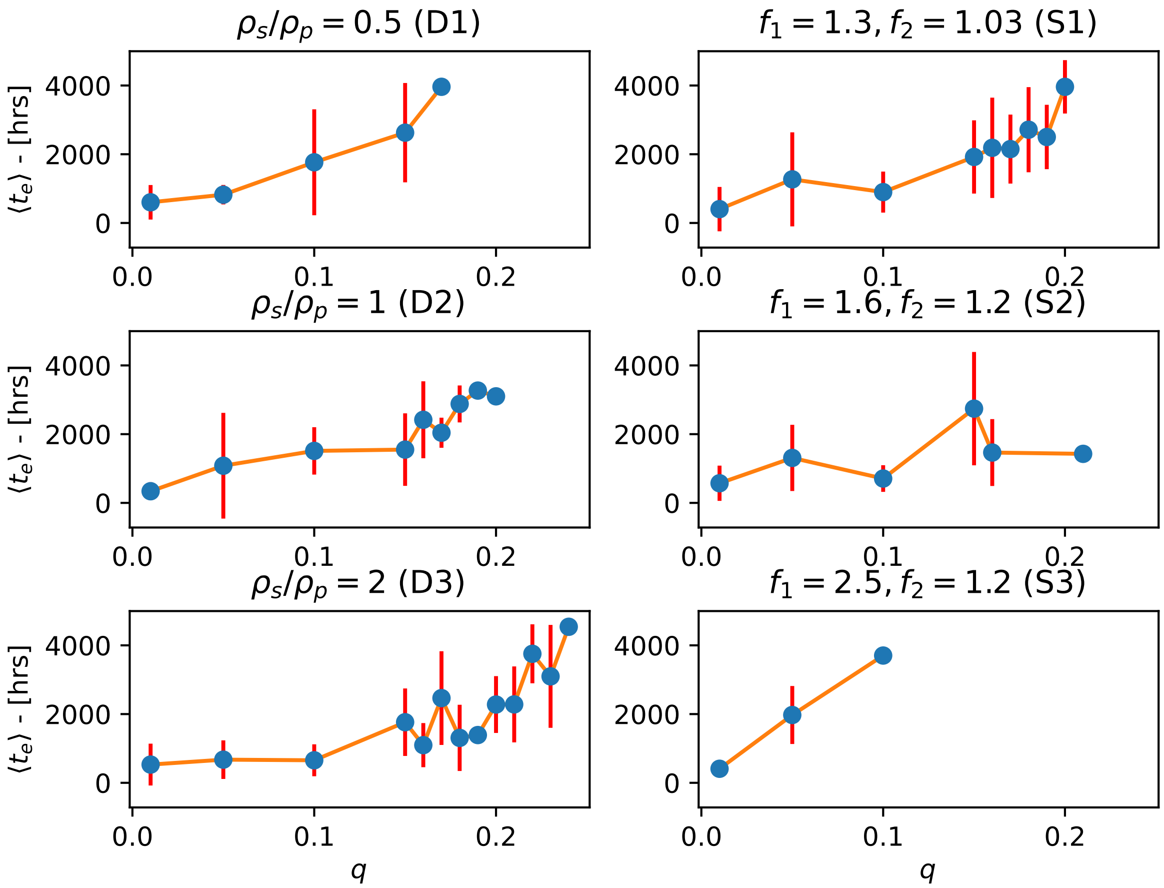

Figure 7: Escape times, averaged over the 45 initial values of θ_0, as functions of the mass ratio. The left columns show the varied density models, while the right columns show the varied shape models. The error bars show the standard deviation of the escape times at the given mass ratio.

gets transferred to translational energy before the secondary is expelled. At the time of escape (when the eccentricity exceeds 1), the separation between the two bodies is large enough for the rotational and translational motion to be decoupled (Scheeres, 2002). Hence, we expect the rotation of the bodies to slow down as time passes in our simulations; after escape we expect the rotation period to stay roughly constant. Because it takes longer for the secondary to escape in systems with higher mass ratios, we expect the rotation of the primary to slow down more in systems with higher mass ratios. We first investigate the rotation of the primary after mutual escape. We calculate the (instantaneous) rotation period of a body as $T = 2\pi/\omega$, where ω is the magnitude of the angular velocity of the body. The rotation period of the primary, at the time of escape, is displayed in the two top left panels in Fig. 8, showing the rotation period of the primary T_p at the final time step as a function of q. In the figure it can be seen that T_p in all six models, is longer at higher mass ratios after escape of the secondary, indicating a correlation between T_p and q. The Spearman correlation coefficients between T_p and q are shown in Table 1. For all models

Model	r_s (T_p and q)	p-value
D1	0.943	$1.828 \cdot 10^{-11}$
D2	0.980	$3.485 \cdot 10^{-28}$
D3	0.964	$2.996 \cdot 10^{-47}$
S1	0.976	$2.954 \cdot 10^{-58}$
S2	0.924	$5.958 \cdot 10^{-9}$
S3	0.913	$1.547 \cdot 10^{-3}$

Table 1: Correlation between the rotation period of the primary T_p and the mass ratio q, for all the escape cases. The second column shows the Spearman correlation coefficient r_s between the two variables, while the third column shows the corresponding p-values.

the correlation coefficients are $r_s > 0.9$. Furthermore, with the exception of model S3, the p-values are lower than 10^{-9}. The high p-value in model S3 is likely due to the smaller number of escape scenarios for this model.

We also include the data of asteroid pairs from Pravec et al. (2019) in the figure, for pairs with $q < 0.3$ (indicated with gray crosses), and most of our results are within the range of the observed data. However, some outliers also exist in the data provided by Pravec et al. (2019), where some asteroid pairs have mass ratios that are too high and some pairs where the primary is rotating too slowly. Pravec et al. believe that these outlier asteroid pairs are not formed by rotational fission.

We also briefly studied the rotation period of the secondary after escape, which is shown in the two bottom left panels in Fig. 8. Unlike the primary, there are no obvious patterns of an increasing rotation period of the secondary when the mass ratio increases. We have also included the rotation period of the secondary of asteroid pairs from Pravec et al. (2019). With the exception of a few outliers in our results, most of the escaped secondaries have rotation periods that are in the range of the data from Pravec et al. (2019).

3.6 Unstable binaries

Some of our simulations, with positive total energy, are still in orbit around the primary after 200 days (the orange regions in Fig. 5). These systems are typically found near the same values of θ_0 as the escape cases, and we refer to them as “unstable”. Of all non-collision systems with positive energy, the unstable scenarios typically make up roughly one-half of them, with the exception of model D3 where the unstable cases make up approximately one-third of the simulations. However, we expect the number of unstable scenarios to decrease and to become either an escape or a collision case if a longer time span is considered.

In the third and fourth columns of Fig. 8 we give the rotation periods of the bodies at the end of the simulations for all unstable cases. The rotation periods of both bodies of these simulations, similar to the scenarios where the secondary has escaped, are also within the range of the observed data from Pravec et al. (2019). The primary is again seen to have longer rotation periods as the mass ratio increases.

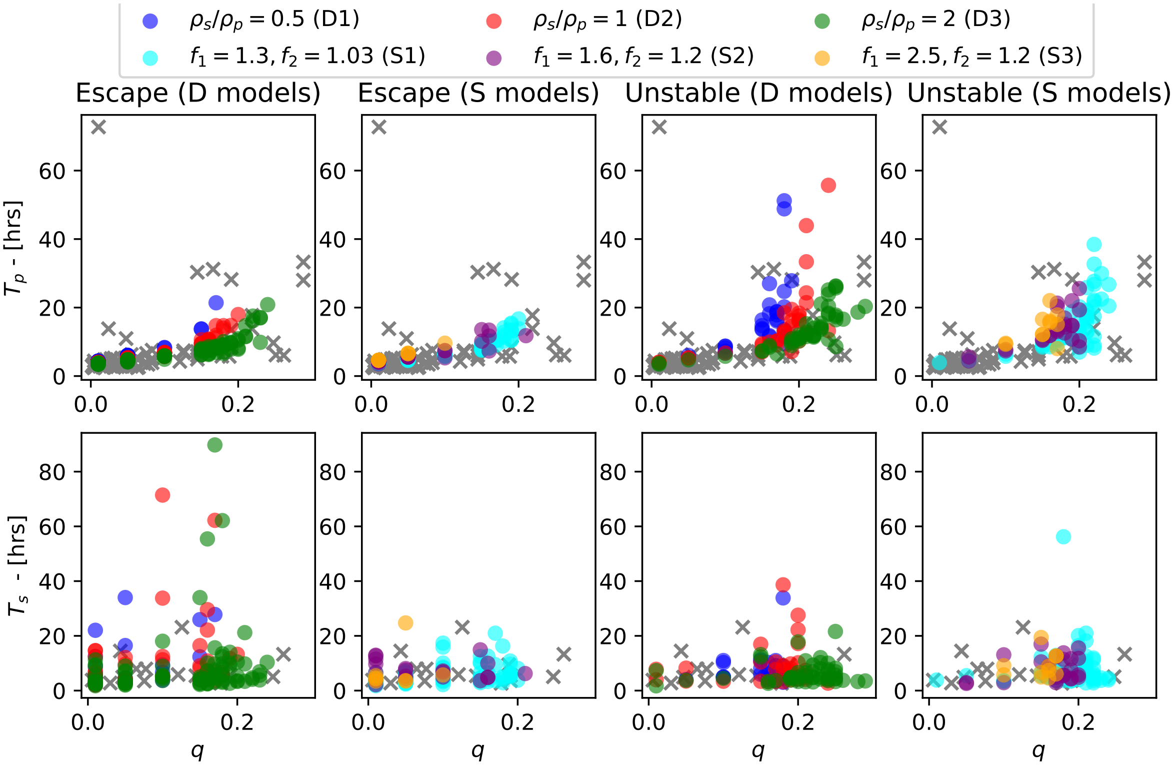

Figure 8: Distribution of rotation periods, as functions of mass ratio, for non-collision systems with positive total energy. The top and bottom rows correspond to the rotation period of the primary and secondary, at $t = 200$ days, respectively. The first and second columns show the escape cases, while the third and fourth columns show the unstable cases. The D and S models correspond to models D1–D3 and S1–S3, respectively. The gray crosses are data from Pravec et al. (2019), and only asteroid pairs with $q < 0.3$ are included in the figure.

Body	Rotation state	Model D1	Model D2	Model D3	Model S1	Model S2	Model S3
Primary	LAM	30.05%	27.59%	27.04%	26.91%	36.54%	32.56%
	SAM	54.19%	51.29%	45.19%	48.02%	46.79%	51.16%
	Uniform	15.75%	21.12%	27.78%	25.07%	25.07%	16.28%
Secondary	LAM	58.62%	59.91%	57.78%	65.70%	55.77%	58.14%
	SAM	36.95%	34.91%	37.41%	25.07%	39.10%	39.53%
	Uniform	4.43%	5.17%	4.81%	3.43%	5.13%	2.33%

Table 2: Distribution of the rotation modes of the primary and secondary for all the non-collision cases. The rotation mode is considered uniform if the difference between I_D and I_z (or I_x) is smaller than 10^{-5}.

3.7 Stable binaries

Finally, at mass ratios of $q \gtrsim 0.2$ the systems have negative total energy, forming binary systems that are stable against mutual escape. They correspond to the green regions in Fig. 5, and most of them appear at $\theta_0 \lesssim 15°$. Although this is called a stable orbit, the secondary may still collide with the primary if a longer time span is considered. Some systems with negative total energies do end up with an impact after 1000 hr. The case with the longest time before impact (as seen in Fig. 6) is actually a system with negative total energy. However, we also saw in Fig. 6 that the time before impact is generally shorter at higher mass ratios. It is therefore possible that, for high enough mass ratios, systems that survive longer than ~ 100 hr will never collide.

3.8 Rotational motion

In order to examine the rotational state of the bodies at the end of the simulation, we follow Boldrin et al. (2016) and utilize the dynamic inertia I_D, defined as

$$I_D = \frac{L^2}{2E_r} \tag{14}$$

(Scheeres et al., 2000), where L is the magnitude of the angular momentum and E_r is the rotational kinetic energy of the body. A body has a uniform rotational motion when $I_D = I_z$ or $I_D = I_x$, which corresponds to rotations about the short and long axes, respectively[1]. Nonuniform rotation (or tumbling motion) happens when $I_x < I_D < I_z$. This can be categorized as long-axis mode (LAM) when $I_x < I_D < I_y$, and as short-axis mode (SAM) when $I_y < I_D < I_z$ (Scheeres et al., 2000). Here we only take into consideration the rotational motion in simulations that do not result in the two bodies impacting.

Initially, the primary has uniform rotational motion, where the dynamic inertia is equal to I_z, while the secondary starts off in a tumbling state. For low values of θ_0 the initial dynamic inertia of the secondary is close to I_z, and approaches I_x as θ_0 increases.

---

[1] This assumes that $I_x \leq I_y \leq I_z$.

At the end of the simulations, we find that both the primary and the secondary, in most cases, are in some state of tumbling. Table 2 summarizes the final rotation state of the two bodies. The primary is mainly found with SAM rotation, which is close to its initial state. For $q \lesssim 0.25$, the primary may be able to retain its uniform rotational motion throughout the whole simulation, and these are mainly found at mass ratios of $q \lesssim 0.2$, as shown in Fig. 9. Most of these situations are found among the escape cases; however, some are also found among the unstable cases. This is a consequence of the secondary being unable to act with a gravitational torque on the primary due to the large separation between the bodies. This is similar to the results of Davis and Scheeres (2020), as they found that the spin state of the primary is, for the most part, unaffected when the secondary escapes. Moreover, simulations where the primary ends with a LAM rotation are more common at high mass ratios.

The secondary is also mostly in a tumbling state. Unlike the primary, LAM rotation is more common for the secondary because most simulations have a secondary with initial LAM rotation. Typically, the initial rotation mode of the secondary is SAM when $\theta_0 \lesssim 27^\circ$ and LAM otherwise, but it also depends on its shape. For the non-collision cases when $\theta_0 > 60^\circ$, nearly all simulations end with the secondary in a LAM rotation, as shown in Fig. 10, with one exception found in model D3. In some of the simulations ($\lesssim 5\%$), the secondary has uniform rotational motion at the end of the simulation, either along the short or the long axis. These are mainly found when $q \leq 0.1$, when the secondary has escaped, and when $\theta_0 = 0.001^\circ$. Uniform rotational motion is less common among the stable cases because both the primary and secondary act with torques on each other for a longer time period.

If we isolate the escaped secondaries in this analysis, we find that approximately $35-50\%$ have SAM rotation at the end of the simulation for every model except the S3, where the percentage is 63% instead. Boldrin et al. (2016) found in their study that most escaped secondaries are SAM rotators. Our results are therefore slightly different in that we seem to find fewer with SAM rotation. In particular, we find fewer SAM rotators as the secondary becomes less dense. Davis and Scheeres (2020) also investigated the rotational state of escaped secondaries, and found that every escaped secondary is in tumbling motion.

We also wanted to study how the rotation period of the bodies changes with time when the secondary is still in orbit around the primary. Figure 11 shows the average rotation period of the primary and secondary as functions of time in the top and bottom rows, respectively. The left and right panels correspond to stable and unstable cases, respectively. The averaged data are binned in 48 hour periods.

In the figure it can be seen that the average rotation period of the primary increases over time, both for the stable and unstable cases. Furthermore, the rotation period of the unstable cases are lower than the stable cases, which is a consequence of the large separations between the bodies, effectively decoupling the translational and rotational motions, similar to the escape cases. The secondary, as shown in the bottom two panels, has rotation periods of typically 10–15 hr in the stable systems and, similarly to the primary, rotates slightly faster, typically 8–12 hr in the unstable systems. The time evolution of the rotation period of the secondary is far more volatile within the first ~ 2500 hr of the simulations, and the figure shows that it experiences frequent speed-ups and slow-downs during this time period.

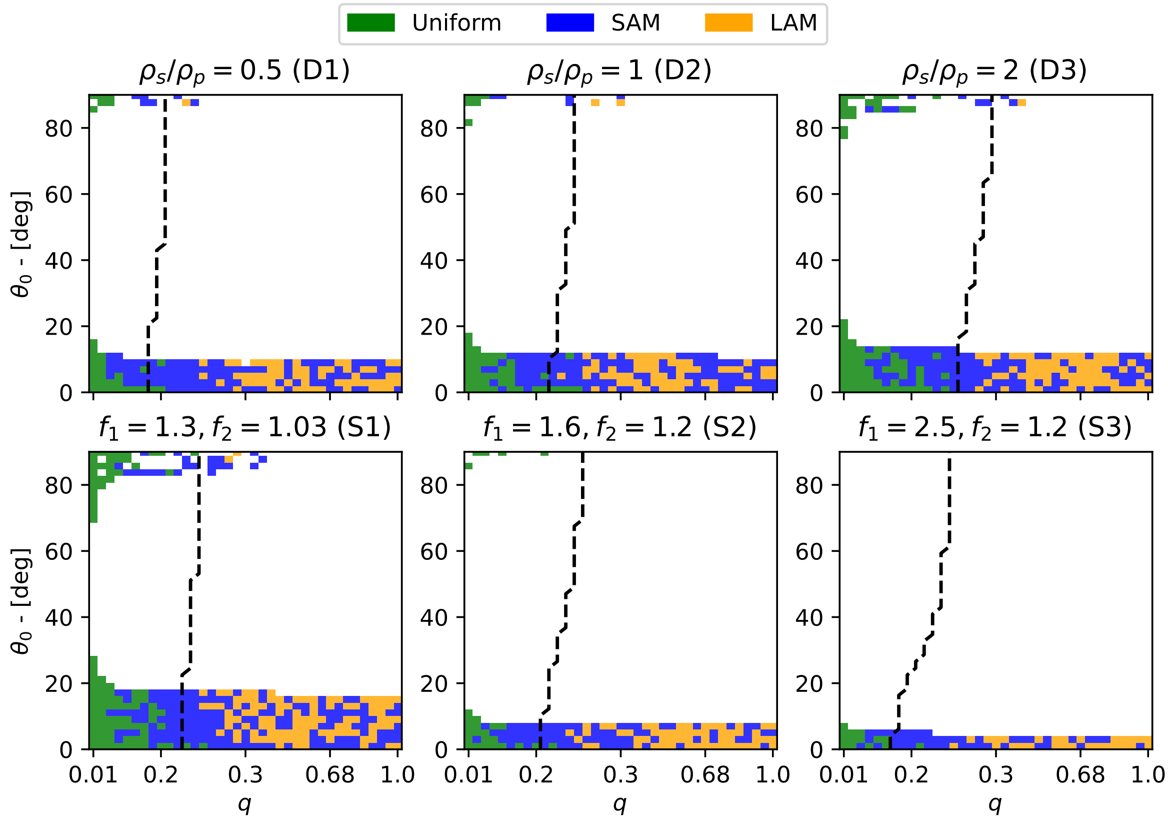

Figure 9: Distribution of the rotation state of the primary, at the end of the simulation, as functions of q and θ_0. The white regions correspond to simulations that result in collisions. The dashed lines indicate the value of q where the total energy is zero.

After this, the rotation period of the secondary stabilizes.

We also see that the rotation period of the primary increases with mass ratio for the escape cases. Because the escape times are longer at higher mass ratios, the secondary can act with a gravitational torque for a longer time period.

We also show how the rotation periods change over time for four simulations with different outcomes for model D2. This is illustrated in Fig. 12. As previously mentioned, when the separation between the two bodies becomes large enough, the translational and rotational motion will decouple. As seen in the figure, for the escape and the unstable cases, when the bodies are sufficiently far apart, their rotation periods become approximately constant. For the stable and collision cases, the rotation periods vary far more as the bodies are relatively close to each other.

3.9 Secondary fission

Jacobson and Scheeres (2011) introduced secondary fission as a mechanism to form stable binaries from systems with low mass ratios. During secondary fission, the secondary disrupts

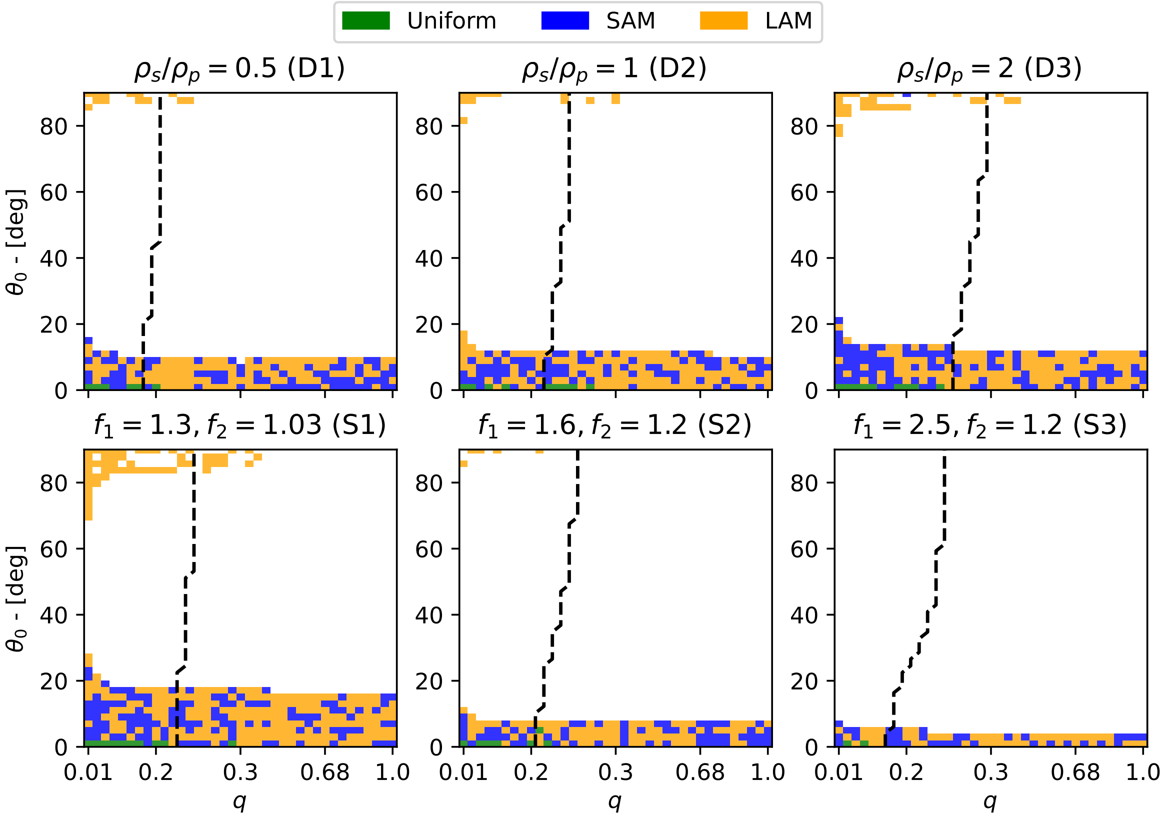

Figure 10: Same as Fig. 9, but for the secondary.

or fissions when it is spun up by gravitational torques. Through secondary fission, parts of the energy in the system can be removed if the newly fissioned component escapes or impacts with the primary.

We wanted to investigate whether fission of the secondary can take place in our simulations, and similarly to Boldrin et al. (2016), we applied the rotation limit for surface disruption of the secondary as the critical limit for achieving secondary fission. We define this critical limit T_r as the rotation rate at which a point mass is lifted off the surface by centrifugal forces. We use Eq. (4) with $\beta = 1.0$ to determine this limit. The value of T_r depends on the density, shape, and rotation state of the body. The rotation period required for secondary fission becomes longer when the density becomes smaller or when the body becomes more elongated. Tumbling motion may further increase the spin rate required for fission, and is taken into account during our analysis.

As is evident from the previous section, the average rotation period of the secondary has frequent speed-ups and slow-downs. The secondaries of some systems might obtain rotation periods short enough for secondary fission to occur. Figure 13 shows the percentages of simulations that experience secondary fission as functions of the mass ratio, based on the rotation criterion described above. Secondary fission events are most common when $q = 0.01$, and decrease as the mass ratio increases. These events may take place up to $q = 0.4$,

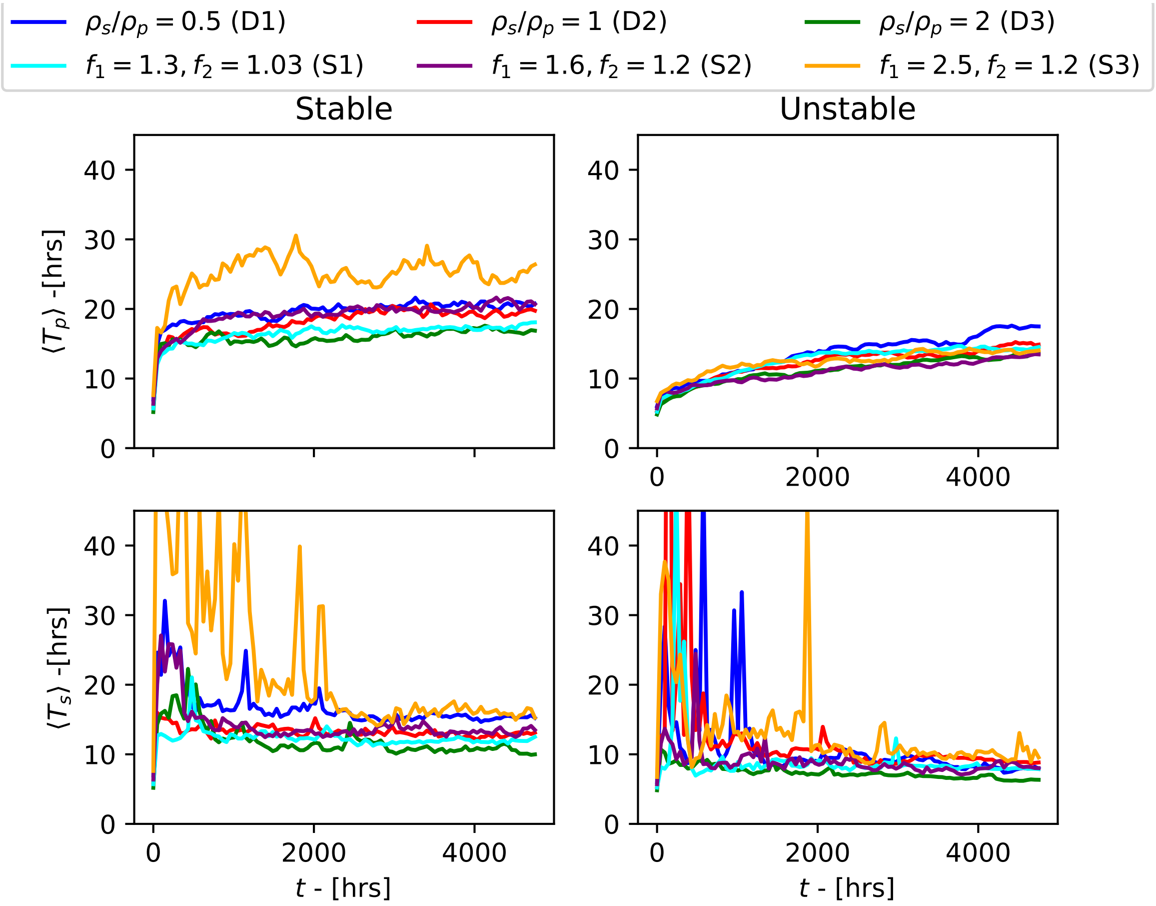

Figure 11: Average rotation period of the primary (*top*) and the secondary (*bottom*), averaged over all the stable *(left)* and unstable *(right)* cases, as functions of time. The averages, for $t > 0$, are binned over 48 hour intervals.

with the exception of models S3, where the secondary can still disrupt at mass ratios as high as $q = 0.72$. The work of Jacobson and Scheeres (2011) and Sharma (2014) also suggests disruption events are more common if the body is more elongated. However, unlike the findings of Jacobson and Scheeres (2011), we find that secondary fission may occur also in systems with positive total energy.

As previously seen, the rotation of the secondary slows down rapidly during the first few hours of the simulation, and spins up again further into the simulation. It is therefore likely that secondary fission events occur early on in the simulation, but they may also take place toward the end of the 200 day simulations. We find that roughly half the secondary fission events may occur before 5 hr have elapsed for most models, and for D1 and S3 the percentage is even higher, at 100% and 82%, respectively. Many of these events belong to simulations where the two bodies impact. Thus, for these systems, a ternary (or multiple) can be created early on, and may change the dynamics of the system, possibly preventing the early collisions.

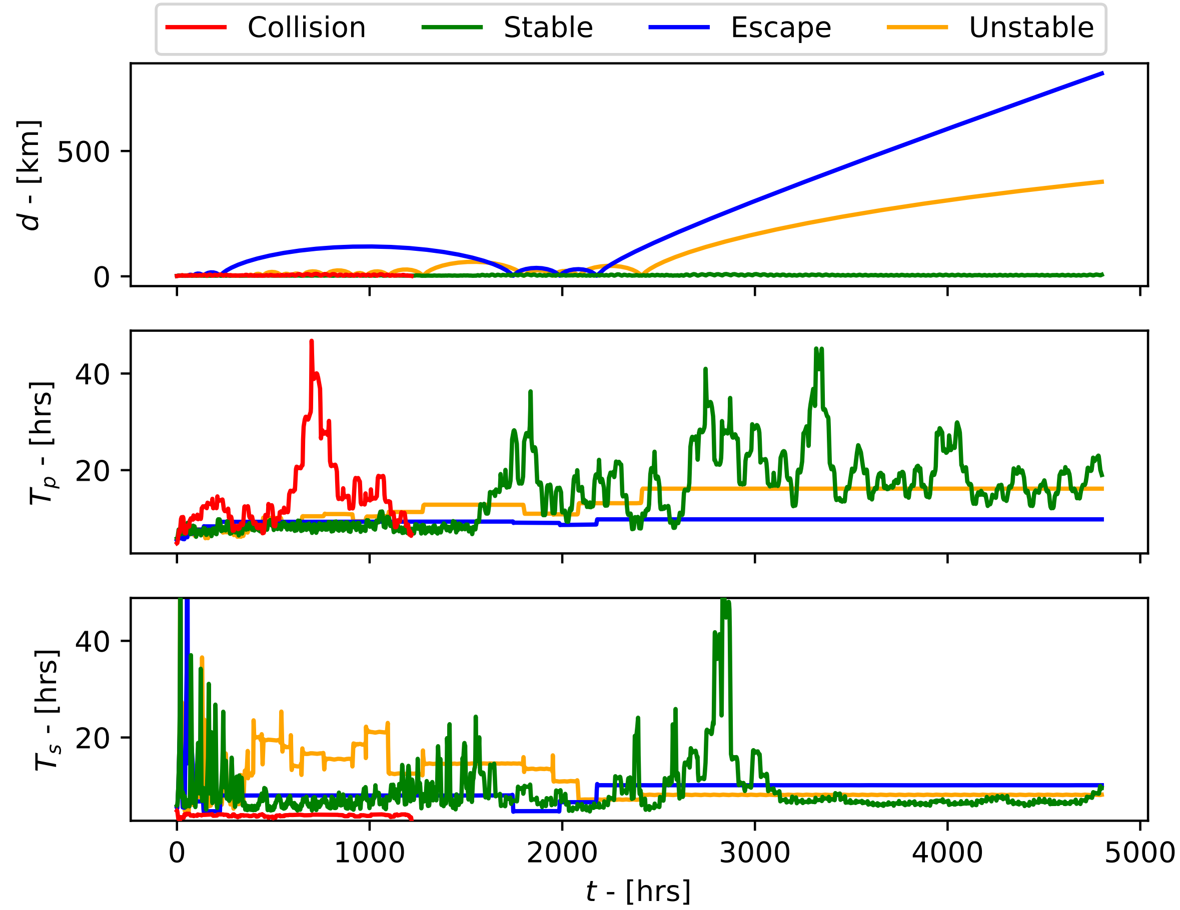

Figure 12: How the separation between bodies and rotation periods changes over time, for four selected simulations. The top row shows the separation, while the middle and bottom rows show the rotation period of the primary and secondary, respectively. The mass ratios of the collision, stable, escape, and unstable examples are $q = 0.29, 0.32, 0.15$, and 0.19 respectively, with corresponding initial rotation periods of $T_0 = 4.87, 5.87, 5.42$, and 5.56 hr.

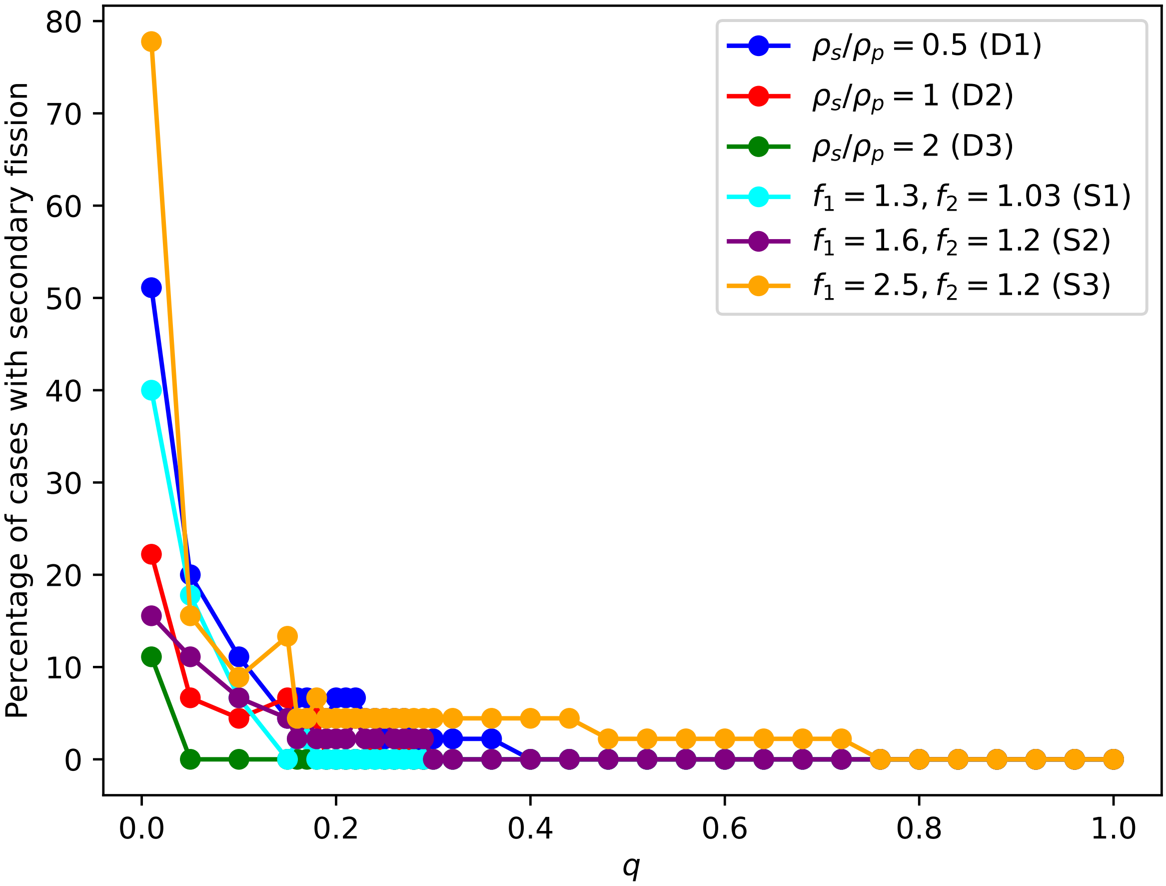

Figure 13: Percentage of cases that experience secondary fission as a function of mass ratio.

Cases where secondary fission may occur after the initial 5 hr are spread out in time. For some models the secondary can disrupt at $t > 3000$ hr as the secondary's rotation slowly speeds up over time, although the number of these events is small (less than ten in total).

4 Discussion

Table 3 shows a summary of the percentage of each end-case scenario for the models presented. The collision cases make up approximately 80% of the simulations, while the remaining cases are categorized as stable, unstable, or escape. The collisions typically occur when the secondary has a tilt angle in the range $\theta_0 = 15° - 80°$. However, for tilt angles smaller or larger than this the system can develop into a stable binary, an unstable binary, or a system with an escaped secondary.

The difference in the end-case distribution does not change significantly when the density of the secondary is changed, but rather when the secondary take different shapes. By allowing the secondary to become more elongated, the number of collisions increases. In the model where the secondary's shape is close to spheroidal (model S1), $\sim 77\%$ of the

Model	Submodel	Collisions	Stable	Escape	Unstable
Varied densities	D1	87.81%	9.13%	1.38%	1.68%
	D2	86.07%	9.49%	2.40%	2.04%
	D3	83.78%	8.47%	4.86%	2.88%
Varied shapes	S1	77.24%	13.81%	5.23%	3.72%
	S2	90.63%	6.73%	1.20%	1.44%
	S3	94.84%	4.02%	0.48%	0.66%

Table 3: Summary of the percentage of end-case results for each model presented.

simulations end with an impact. This percentage increases to above 90% for the model with the most elongated secondary (model S3).

Most of the collision events take place very early in the simulations. We find that 90% of the collisions occur before 5 hr have elapsed. This occurs because we move the secondary closer to the primary when it is rotated with an angle θ_0, such that the surface-to-surface distance is always 1 cm, as described in Sect. 2.2. One consequence of this is that the secondary rotates into the primary early in the simulation, due to the gravitational torque. The gravitational torque is also stronger on the secondary when it is more elongated, and hence the increased fraction of collision events in model S3 compared to S1 and S2. The early impact between the two bodies may help contribute to stabilizing the system. The energy dissipation from these collision events may prevent the secondary from escaping, and thus allow formation of asteroid binaries with low mass ratios. The early collisions we find are similar to the 1996 HW1 simulations and also shorter than the Moshup simulations of Davis and Scheeres (2020), who found that the median collision time is 2.1 hr and 0.52 days, respectively.

One of our models is the same as the model used by Boldrin et al. (2016), and when comparing with their work, a larger percentage of our simulations end up with the two bodies impacting. This is another consequence of keeping the surface separation to 1 cm. Furthermore, because the surface-to-surface distance is always 1 cm, we find that collisions can occur at angles as low as $\theta_0 \sim 8°$, while Boldrin et al. (2016) find that collisions do not occur when $\theta_0 \lesssim 40°$.

Escape scenarios, which is the likely mechanism behind the formation of some asteroid pairs (Pravec et al., 2010), exist for systems with low mass ratios, and we find that the time it takes for mutual escape to happen is longer when the mass ratio is higher. However, there are cases where the escape time is longer than 1000 hr at low mass ratios, but these cases are not frequent. At the lowest mass ratios the escape time tends to be the longest when the secondary has a more elongated shape, as it was seen in model S3, because the energy configuration in S3 is lower than the other models at equal mass ratios. We also found that escape cases were more frequent when the secondary has a higher density, and asteroid pairs with secondaries of higher density may therefore be more frequent in the asteroid pair population.

Because we consider relatively short simulation times, some of the systems will remain as unstable systems throughout the duration of the simulation (200 days). These systems are generally found at intermediate mass ratios, but this will also vary based on the density of the secondary as well as its shape. If a longer time span is considered, such as 200 years as done by Boldrin et al. (2016), these unstable cases either become escape cases, or end up with an impact between the two bodies.

We find that the rotation period of the primary increases with time, hence it loses rotational energy because the rotational energy is converted to translational energy (Scheeres, 2002). The rate at which the rotation period increases is slower for the unstable cases compared to the stable cases as the average separation between the bodies is larger for the former case. This is also seen among the escape cases. Higher mass ratios result in both longer escape times and longer rotation periods of the primary. Moreover, changing the shape of the secondary has a larger effect on the rotation of the primary in the stable cases, compared to changing its density. The average rotation period of the primary in model S3 can be nearly twice as long as in model S1.

The average rotation period of the primary is much longer in our simulations compared to that in some of the observed asteroid binaries. For instance, the rotation period of Moshup is estimated to be 2.76 hr (Ostro et al., 2006) and 2.26 hr for Didymos (Naidu et al., 2020), where the mass ratio of the former system is estimated to be $q = 0.057$ (Ostro et al., 2006) and $q = 0.048$ for the latter (Pravec et al., 2006). Observations by Pravec et al. (2016) estimate that the primary bodies have rotation periods of less than ~ 4.4 hr. Meanwhile, the average rotation periods of the primary we find, for the stable cases, are in the range 15–25 hr. Although, our simulation time span is very short, adding other physical effects such as tidal torques and the YORP effect may be able to allow the primary to spin up after a longer time period. On the other hand, rotation periods of the secondaries observed by Pravec et al. (2016) range from ~ 14 hr all the way up to ~ 37 hr, which is within the range of what we find in our results for the stable cases. However, the mass ratio of the binary systems presented by Pravec et al. (2016) are lower than 0.125 (assuming equal bulk densities), while our stable cases are found when $q > 0.2$. Energy dissipation of the system is therefore required, for example from collision or secondary fission.

We compare rotation periods from our simulations with that of observed asteroids pairs by Pravec et al. (2019), and find that there is an overall agreement for systems with $q < 0.3$, as illustrated in Fig. 8. The primaries of low mass ratio asteroid pairs were observed to be rapidly rotating, which indicates that the secondary may have escaped very early after the initial fission process. However, some systems observed by Pravec et al. (2019) have mass ratios that are too high or have a primary with a rotation period that is too long. These systems are considered outliers, and the rotational fission theory is unable to explain their existence (Pravec et al., 2019). Kyrylenko et al. (2021) suggest that the mass ratio of the asteroid pair 1999 XF200 and 2008 EL40, which reside in the main belt, is $q < 0.01$. The rotation period of 1999 XF200 is estimated to be 4.903 hr[2], which is within the range of the escape rotation periods of the primary for $q = 0.01$ in our models. Furthermore, Kyrylenko et al. (2021) estimate that the age of this asteroid pair is 265.8 kyr. Under this time period, the rotation period of the bodies have likely changed by a significant amount due to the

---

[2] Obtained from the JPL Small-Body Database,
`https://ssd.jpl.nasa.gov/sbdb.cgi`

YORP effect and possibly also via collisions with other bodies in the main belt.

Jacobson and Scheeres (2011) find that the separation between positive and negative energy regimes can be approximated to $q \approx 0.2$, and that it should not change much if the bodies are more elongated. We find that this separation regime can go as high as $q = 0.29$ when the secondary has twice the density of the primary (model D3), and as low as $q = 0.17$ when the secondary is more elongated (model S3). This indicates that asteroid pairs formed through rotational fission may occur at higher mass ratios, up to $q \sim 0.3$, if the secondary has a higher density than the primary, or if it becomes less elongated.

If the secondary also fissions, then ternary or multiple systems may be formed. If any of the components escape or collide with the primary, this can stabilize the system (Jacobson and Scheeres, 2011). We find that this process generally occurs at low mass ratios, as predicted by Jacobson and Scheeres (2011), and also fits the findings of Boldrin et al. (2016). On the other hand, unlike the work of Jacobson and Scheeres (2011), we find that secondary fission may still occur in systems where the total energy is negative. We also find that it is more likely for the secondary to disrupt when it has a lower density or when it is more elongated. The latter possiblity is in agreement with the work of Sharma (2014), who shows that more elongated bodies are less stable to finite structural perturbations compared to the less elongated ones. Observations of Pravec et al. (2016) find that there is a scarce number of binaries with secondary elongations of $a_s/b_s \gtrsim 1.5$. This suggests that elongated secondaries may experience multiple fission events, and may thus reshape over time. The results of Davis and Scheeres (2020) also suggest a form of energy dissipation, such as secondary fission, is required to stabilize the 1994 KW4 and 2000 DP107 systems in their current state.

Boldrin et al. (2016) used second-order spherical harmonics to study the dynamical evolution of fissioned systems, while we use an exact expression. Higher order terms become more important when the bodies are more elongated (Hou et al., 2017) or when the bodies are close. A future study that compares an exact method with an approximation may give better insights into the importance of exact mathematical expressions used to study asteroid systems immediately after fission.

We want to thank the anonymous referee for their valuable feedback that improved the manuscript.

A Ellipsoid potential

For any general ellipsoid with semiaxes $a > b > c$ and constant density ρ, the gravitational potential is given by (MacMillan, 1930)

$$\begin{aligned}\Phi(\mathbf{r}) = \frac{2\pi\rho abc}{\sqrt{a^2-c^2}}\Bigg(&\left[1 - \frac{x^2}{a^2-b^2} + \frac{y^2}{a^2-b^2}\right] F(\omega_\kappa, k) \\ &+ \left[\frac{x^2}{a^2-b^2} - \frac{(a^2-c^2)y^2}{(a^2-b^2)(b^2-c^2)} + \frac{z^2}{b^2-c^2}\right] E(\omega_\kappa, k) \\ &+ \left[\frac{c^2+\kappa}{b^2-c^2}y^2 - \frac{b^2+\kappa}{b^2-c^2}z^2\right] \frac{\sqrt{a^2-c^2}}{\sqrt{(a^2+\kappa)(b^2+\kappa)(c^2+\kappa)}}\Bigg),\end{aligned} \tag{15}$$

where $F(\omega_\kappa, k)$ and $E(\omega_\kappa, k)$ are respectively the elliptic integrals of the first and second kind, κ is the largest root of the equation

$$\frac{x^2}{a^2+\kappa} + \frac{y^2}{b^2+\kappa} + \frac{z^2}{c^2+\kappa} = 1, \tag{16}$$

and

$$\omega_\kappa = \sin^{-1}\sqrt{\frac{a^2-c^2}{a^2+\kappa}} \tag{17}$$

$$k = \sqrt{\frac{a^2-b^2}{a^2-c^2}}. \tag{18}$$

The components of the gravitational field $\mathbf{g} = \nabla\Phi$ then become

$$g_x = \frac{4x\pi\rho abc}{\sqrt{a^2-c^2}} \frac{E(\omega_\kappa,k) - F(\omega_\kappa,k)}{a^2-b^2}, \tag{19}$$

$$\begin{aligned} g_y = \frac{4y\pi\rho abc}{\sqrt{a^2-c^2}} \Bigg[& \frac{F(\omega_\kappa,k)}{a^2-b^2} - \frac{(a^2-c^2)E(\omega_\kappa,k)}{(a^2-b^2)(b^2-c^2)} \\ & + \frac{(c^2+\kappa)}{b^2-c^2} \frac{\sqrt{a^2-c^2}}{\sqrt{(a^2+\kappa)(b^2+\kappa)(c^2+\kappa)}} \Bigg], \end{aligned} \tag{20}$$

$$g_z = \frac{4z\pi\rho abc}{\sqrt{a^2-c^2}} \left[\frac{E(\omega_\kappa,k)}{b^2-c^2} - \frac{(b^2+\kappa)}{b^2-c^2} \frac{\sqrt{a^2-c^2}}{\sqrt{(a^2+\kappa)(b^2+\kappa)(c^2+\kappa)}} \right]. \tag{21}$$

Despite being functions of x, y, and z, the variable κ is treated as a constant when the partial derivatives are taken (see MacMillan, 1930, for details).

B Verification of accuracy

The accuracy of the integration scheme can be demonstrated by inspecting the conservation of total energy E, total linear momentum $\mathbf{p}$, and total angular momentum $\mathbf{J}$. This is shown in Fig. 14 for one of the models (D2 with $q = 0.32$, $\theta_0 = 6.1°$). In the figure we plot, for each of these three quantities, the difference between the initial value at $t = 0$ and the value at each subsequent time step. For the energy and angular momentum, the difference is normalized by the initial values E_0 and J_0. We find that these quantities are conserved to the 11th decimal place; the error on the linear momentum fluctuates between the 4th and 7th decimal places.

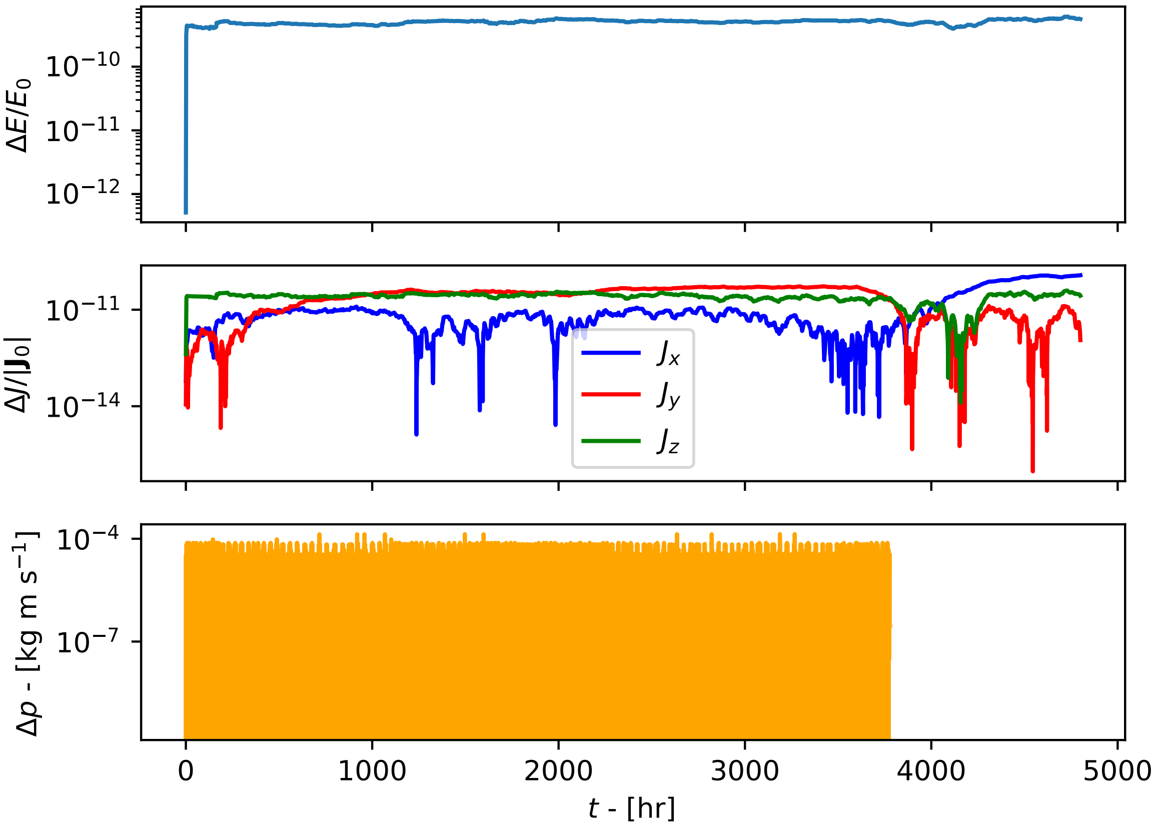

Figure 14: Illustration of energy, angular, and linear momentum conservation for one of the simulations.

References

L. A. G. Boldrin, D. J. Scheeres, and O. C. Winter. Dynamics of rotationally fissioned asteroids: non-planar case. *Monthly Notices of the Royal Astronomical Society*, 461(4): 3982–3992, October 2016. doi: 10.1093/mnras/stw1607.

J. Bottke, W. F., D. Vokrouhlický, D. P. Rubincam, and M. Broz. *The Effect of Yarkovsky Thermal Forces on the Dynamical Evolution of Asteroids and Meteoroids*, pages 395–408. University of Arizona Press Tucson, 2002.

C. R. Chapman et al. Discovery and physical properties of Dactyl, a satellite of asteroid 243 Ida. *Nature*, 374(6525):783–785, Apr 1995. doi: 10.1038/374783a0.

J. T. Conway. Vector potentials for the gravitational interaction of extended bodies and laminas with analytical solutions for two disks. *Celestial Mechanics and Dynamical Astronomy*, 125:161–194, June 2016. doi: 10.1007/s10569-016-9679-y.

A. B. Davis and D. J. Scheeres. High-fidelity Modeling of Rotationally Fissioned Asteroids. *The Planetary Science Journal*, 1(1):25, June 2020. doi: 10.3847/PSJ/ab9a39.

E. G. Fahnestock and D. J. Scheeres. Simulation and analysis of the dynamics of binary near-Earth Asteroid (66391) 1999 KW4. *Icarus*, 194(2):410–435, April 2008. doi: 10.1016/j.icarus.2007.11.007.

A. Fujiwara et al. The Rubble-Pile Asteroid Itokawa as Observed by Hayabusa. *Science*, 312(5778):1330–1334, June 2006. doi: 10.1126/science.1125841.

A. W. Harris and P. W. Chodas. The population of near-earth asteroids revisited and updated. *Icarus*, 365:114452, September 2021. doi: 10.1016/j.icarus.2021.114452.

M. Hirabayashi, D. P. Sánchez, and D. J. Scheeres. Internal structure of asteroids having surface shedding due to rotational instability. *The Astrophysical Journal*, 808(1):63, 2015.

A. Ho, M. Wold, J. T. Conway, and M. Poursina. Extended two-body problem for rotating rigid bodies. *Celestial Mechanics and Dynamical Astronomy*, 133(8):35, August 2021. doi: 10.1007/s10569-021-10034-8.

K. A. Holsapple. Spin limits of Solar System bodies: From the small fast-rotators to 2003 EL61. *Icarus*, 187(2):500–509, April 2007. doi: 10.1016/j.icarus.2006.08.012.

X. Hou, D. J. Scheeres, and X. Xin. Mutual potential between two rigid bodies with arbitrary shapes and mass distributions. *Celestial Mechanics and Dynamical Astronomy*, 127(3):369–395, March 2017. doi: 10.1007/s10569-016-9731-y.

S. A. Jacobson and D. J. Scheeres. Dynamics of rotationally fissioned asteroids: Source of observed small asteroid systems. *Icarus*, 214(1):161–178, July 2011. doi: 10.1016/j.icarus.2011.04.009.

M. Kanamaru, S. Sasaki, and M. Wieczorek. Density distribution of asteroid 25143 itokawa based on smooth terrain shape. *Planetary and Space Science*, 174:32 – 42, 2019. ISSN 0032-0633. doi: https://doi.org/10.1016/j.pss.2019.05.002.

I. Kyrylenko, Y. N. Krugly, and O. Golubov. Asteroid pairs: method validation and new candidates. *Astronomy & Astrophysics*, 655:A14, November 2021. doi: 10.1051/0004-6361/202140365.

X. Li and D. J. Scheeres. Analysis of Cohesion in Fast-spinning Small Bodies. *The Planetary Science Journal*, 2(6):229, December 2021. doi: 10.3847/PSJ/ac2df5.

W. MacMillan. *The Theory of the Potential.* (MacMillan: Theoretical Mechanics). McGraw-Hill Book Company, Incorporated, 1930.

J. L. Margot et al. Binary Asteroids in the Near-Earth Object Population. *Science*, 296 (5572):1445–1448, May 2002. doi: 10.1126/science.1072094.

J. L. Margot et al. *Asteroid Systems: Binaries, Triples, and Pairs*, pages 355–374. University of Arizona Press Tucson, 2015. doi: 10.2458/azu_uapress_9780816532131-ch019.

W. J. Merline et al. *Asteroids Do Have Satellites*, pages 289–312. University of Arizona Press, 2002.

A. Morbidelli, J. Bottke, W. F., C. Froeschlé, and P. Michel. Origin and Evolution of Near-Earth Objects. In *Asteroids III*, pages 409–422. University of Arizona Press, 2002.

S. Naidu et al. Radar observations and a physical model of binary near-earth asteroid 65803 didymos, target of the dart mission. *Icarus*, 348:113777, 2020.

S. J. Ostro et al. Radar Imaging of Binary Near-Earth Asteroid (66391) 1999 KW4. *Science*, 314(5803):1276–1280, November 2006. doi: 10.1126/science.1133622.

P. Pravec and A. W. Harris. Binary asteroid population. 1. Angular momentum content. *Icarus*, 190(1):250–259, September 2007. doi: 10.1016/j.icarus.2007.02.023.

P. Pravec et al. Photometric survey of binary near-Earth asteroids. *Icarus*, 181(1):63–93, March 2006. doi: 10.1016/j.icarus.2005.10.014.

P. Pravec et al. Formation of asteroid pairs by rotational fission. *Nature*, 466(7310):1085–1088, August 2010. doi: 10.1038/nature09315.

P. Pravec et al. Binary asteroid population. 3. Secondary rotations and elongations. *Icarus*, 267:267–295, March 2016. doi: 10.1016/j.icarus.2015.12.019.

P. Pravec et al. Asteroid pairs: A complex picture. *Icarus*, 333:429–463, November 2019. doi: 10.1016/j.icarus.2019.05.014.

D. C. Richardson and K. J. Walsh. Binary Minor Planets. *Annual Review of Earth and Planetary Sciences*, 34:47–81, May 2006. doi: 10.1146/annurev.earth.32.101802.120208.

D. P. Rubincam. Radiative Spin-up and Spin-down of Small Asteroids. *Icarus*, 148(1):2–11, November 2000. doi: 10.1006/icar.2000.6485.

P. Sánchez and D. J. Scheeres. The strength of regolith and rubble pile asteroids. *Meteoritics & Planetary Science*, 49(5):788–811, May 2014. doi: 10.1111/maps.12293.

D. J. Scheeres. Stability of Binary Asteroids. *Icarus*, 159(2):271–283, October 2002. doi: 10.1006/icar.2002.6908.

D. J. Scheeres. Rotational fission of contact binary asteroids. *Icarus*, 189(2):370–385, August 2007. doi: 10.1016/j.icarus.2007.02.015.

D. J. Scheeres. Stability of the planar full 2-body problem. *Celestial Mechanics and Dynamical Astronomy*, 104(1-2):103–128, June 2009. doi: 10.1007/s10569-009-9184-7.

D. J. Scheeres et al. Effects of Gravitational Interactions on Asteroid Spin States. *Icarus*, 147(1):106–118, September 2000. doi: 10.1006/icar.2000.6443.

P. Scheirich et al. A satellite orbit drift in binary near-Earth asteroids (66391) 1999 KW4 and (88710) 2001 SL9 - Indication of the BYORP effect. *Icarus*, 360:114321, May 2021. doi: 10.1016/j.icarus.2021.114321.

I. Sharma. Stability of rubble-pile satellites. *Icarus*, 229:278–294, February 2014. doi: 10.1016/j.icarus.2013.09.023.

J. H. Verner. Numerically optimal runge–kutta pairs with interpolants. *Numerical Algorithms*, 53(2):383–396, Mar 2010. ISSN 1572-9265. doi: 10.1007/s11075-009-9290-3.

K. J. Walsh and S. A. Jacobson. Formation and Evolution of Binary Asteroids. In *Asteroids IV*, pages 375–393. University of Arizona Press Tucson, 2015. doi: 10.2458/azu_uapress_9780816532131-ch020.

K. J. Walsh. Rubble Pile Asteroids. *Annual Review of Astronomy and Astrophysics*, 56: 593–624, September 2018. doi: 10.1146/annurev-astro-081817-052013.

K. J. Walsh, D. C. Richardson, and P. Michel. Rotational breakup as the origin of small binary asteroids. *Nature*, 454(7201):188–191, July 2008. doi: 10.1038/nature07078.

M. Wold and J. T. Conway. The planar two-body problem for spheroids and disks. *Celestial Mechanics and Dynamical Astronomy*, 133(6):27, June 2021. doi: 10.1007/s10569-021-10023-x.

Paper 3 - The accuracy of mutual potential approximations in simulations of binary asteroids

Alex Ho, Margrethe Wold, Mohammad Poursina, and John T. Conway

This paper has been published as:

Alex Ho, Margrethe Wold, Mohammad Poursina and John T. Conway, The accuracy of mutual potential approximations in simulations of binary asteroids, *Astronomy & Astrophysics*, 671:A38, March 2023. doi: 10.1051/0004-6361/202245552.

Dynamics of asteroid systems post-rotational fission

Alex Ho, Margrethe Wold, Mohammad Poursina, John T. Conway
University of Agder, Jon Lilletuns vei 9, 4879 Grimstad, Norway

Abstract

Context. Simulations of asteroid binaries commonly use mutual gravitational potentials approximated by series expansions, leading to truncation errors, and also preventing correct computations of force and torque for certain configurations where the bodies have overlapping bounding spheres, such as in the rotational fission model for creating asteroid binaries and pairs.

Aims. We address errors encountered when potentials truncated at order two and four are used in simulations of binaries, as well as other errors related to configurations with overlapping bounding spheres where the series diverge.

Methods. For this we utilized a recently developed method where the gravitational interaction between two triaxial ellipsoids can be calculated without approximations for any configuration. The method utilizes surface integration for both force and torque calculations, and it is exact for ellipsoidal shapes. We also computed approximate solutions using potentials truncated at second and fourth order, and we compare these with the solutions obtained with the surface integral method. The approximate solutions were generated with the "General Use Binary Asteroid Simulator" (GUBAS).

Results. If the secondary is located with its centroid in the equatorial plane of the primary, the error in the force increases as the secondary is moved closer to the primary, but is still relatively small for both second and fourth order potentials. For torque calculations, the errors become more significant, especially if the other body is located close to one of the extended principal axes. On the axes themselves, the second order series approximation fails by 100%. For dynamical simulations of components separated a few primary radii apart, the fourth order approximation is significantly more accurate than the second order. Furthermore, because of larger errors in the torque calculations, the rotational motion is subject to greater inaccuracies than the translational motion. For configurations resembling contact binaries where the bounding spheres overlap, the errors in both force and torque in the initial stages of the simulation are considerable, regardless of the approximation order, because the series diverge. A comparison of the computational efficiency of the force and torque calculations shows that the surface integration method is approximately 82 times and four times slower than the second and fourth order potentials, respectively, but approximately 16 times faster than the order eight potential. Comparing the computation efficiency of full simulations, including the calculations of the equations of motion, shows that the surface integration scheme is comparable with GUBAS when an order four potential is used.

Conclusions. The errors generated when mutual gravitational potentials are truncated at second or fourth order lead to larger errors in the rotational than in the translational motion. Using a mathematically exact method for computing forces and torques becomes important when the bodies are initially close and the bounding spheres overlap, in which case both the translational and rotational motion of the bodies have large errors associated with them. For simulations with two triaxial ellipsoids, the computational efficiency of the surface integral method is comparable to fourth order approximations with GUBAS, and superior to eight order or higher.

1 Introduction

Dynamical simulations of binary asteroids are relevant for understanding their formation processes, and their evolution over time. Among the near-Earth population of asteroids, smaller asteroids get spun up by the Yarkovsky – O'Keefe – Radzievskii – Paddack effect (YORP) effect, and break apart when they reach a critical spin limit via rotational fission (Weidenschilling, 1980; Margot et al., 2002; Pravec and Harris, 2007). Studying the dynamics of post-fissioned asteroids allows us to understand how such systems evolve over time, as they can either remain in stable orbits about each other (as binaries or multiple systems), reimpact, or undergo mutual escape thus forming asteroid pairs (Pravec et al., 2010; Jacobson and Scheeres, 2011; Boldrin et al., 2016; Davis and Scheeres, 2020; Ho et al., 2022).

Asteroids have nonspherical shapes, and for binaries where the components are close, there is a continuous exchange of energy and angular momentum, leading to a significant spin-orbit coupling. The dynamics of nonspherical binary asteroids is described by the solution to the full two-body problem (F2BP) for rigid bodies (Maciejewski, 1995). However, solving the F2BP is not a trivial task as there is no analytical solution for the mutual potential between two nonspherical bodies (apart from between two thin disks (Conway, 2016; Wold and Conway, 2021)). Therefore, approximations of the mutual potential are often made in order to solve the F2BP.

The most common approach is to expand the potential through the use of spherical harmonics (Scheeres et al., 1996; Hu and Scheeres, 2002; Boldrin et al., 2016; Feng and Hou, 2017). However, a drawback with this is that the power series only converges outside the bounding sphere (Brillouin sphere), which is the smallest sphere that can completely contain the circumference of the body. Inside the Brillouin sphere, the power series approximating the gravitational potential diverges (Moritz, 1980). Furthermore, when using series approximations to the potential, higher order terms are often neglected, which leads to truncation errors.

Paul (1988) presents a different approach to compute the mutual potential of two bodies of finite sizes using power series. The mass distribution of the bodies is described through inertia integrals. Unlike spherical harmonics, where the potential is expressed in spherical coordinates, the method by Paul (1988) uses Cartesian coordinates. Tricarico (2008) has further applied this method to bodies with arbitrary shapes and mass distributions. The power series of Paul (1988) converts the six-dimensional volume integral of the mutual potential to six open summations. The method was improved by Hou et al. (2017), who reduced the six open summations to one single summation in order to make it more computationally efficient. Moreover, the formulation of Hou et al. (2017) allows the inertia integrals to be stored before the mutual potential is calculated, while the approaches by Paul (1988) and Tricarico (2008) require the inertia integrals to be recomputed before the mutual potential is evaluated. Even though this approach is computationally very efficient, it will still suffer from divergence problems within the bounding spheres of the bodies (Tricarico, 2008), and truncation errors.

The potential of an arbitrarily shaped body can also be modeled with a homogeneous polyhedron. This approach has been utilized to determine the gravitational potential of an asteroid (Werner, 1997; Werner and Scheeres, 1997; Tsoulis, 2012; Conway, 2015), and the mutual potential of two polyhedra (Werner and Scheeres, 2005; Fahnestock and Scheeres, 2006, 2008; Scheeres et al., 2006). However, this method can be very time consuming if the polyhedron is represented by many triangular faces. A different method is the mascon model (Muller and Sjogren, 1968, 1969; Geissler et al., 1996), where the body is modeled by point masses to represent its mass distribution. On the other hand, despite using many point masses, the mascon model can yield large errors in the forces and the resolution of the surface is poorly represented by spherical balls (Werner and Scheeres, 1997). The mascon model has been modified to become more accurate by replacing the point masses with tetrahedrons (Chanut et al., 2015; Aljbaae et al., 2017, 2020, 2021), which provides the gravitational potential to that of a polyhedron. Chanut et al. (2015) found that their method results in more accurate estimation of the gravitational potential close to the body, and is also computationally faster, compared to the polyhedron approach by Tsoulis (2012). Aljbaae et al. (2021) showed that the approach by Chanut et al. (2015) reduced the computation time by more than 95%, while losing less than 2% of the precision, compared to the polyhedron approach outlined by Tsoulis and Petrović (2001).

Previous works that have studied the dynamics of asteroid binaries after fission typically consider a mutual potential approximation order of order two (Scheeres, 2009; Jacobson and Scheeres, 2011; Boldrin et al., 2016), or order four (Davis and Scheeres, 2020). However, only a few authors have considered the significance of higher order terms in simulations, and how the order of the series approximation affects the dynamics. Hou et al. (2017) investigate the importance of higher order terms for a planar two-ellipsoid system where the ellipsoids are initially in contact. They find that truncating the potential at second order is sufficient to describe systems where the mutual orbit is Hill stable, and also when the bodies undergo mutual escape. On the other hand, they find that additional terms become necessary to describe the trajectory if the bodies are highly elongated. Davis and Scheeres (2020) find that higher order terms in the gravitational potential and nonplanar effects do not significantly change the formation process (rotational fission) itself of asteroid binaries, but can slow down the overall evolutionary process, for example, mutual escape occurs later in the simulations. Agrusa et al. (2020) compare four different full two-body codes to determine the most optimal method to simulate the motion of the (65803) Didymos binary system. The two-body codes they consider model the asteroids as polyhedral or mascon shapes. They find that expanding the mutual potential up to order four is sufficient to describe the motion of the Didymos binary system.

However, an accurate shape model of an asteroid is often not available. Modeling an asteroid as a triaxial ellipsoid is commonly used to approximate the shape of the body to study the F2BP (Scheeres, 2009; Jacobson and Scheeres, 2011; Boldrin et al., 2016; Ho et al., 2021, 2022), and the gravitational potential of such bodies can be expressed analytically (MacMillan, 1930).

Approximating the shape of asteroids as ellipsoids have previously been used to study the dynamics of post-fissioned asteroid systems (Jacobson and Scheeres, 2011; Boldrin et al., 2016; Ho et al., 2022). In the rotational fission model, the initial separation between the two bodies is very small. In some cases, especially for nonplanar cases, we might expect that a series approximation to the potential could cause erroneous values for both force and torque in the initial stages of the simulation, when the bounding spheres of the two bodies overlap and the power series diverges. Previous work on post-fissioned asteroid binary systems avoid this issue by imposing initial conditions which ensure that the bounding spheres do not intersect (Jacobson and Scheeres, 2011; Hou et al., 2017; Boldrin et al., 2016).

In a series of papers (Wold and Conway, 2021; Ho et al., 2021, 2022), we have investigated another approach to the F2BP, where the forces and torques (and mutual potential) are computed directly by integrating over the surface of one body in the gravitational field of the other (Conway, 2016). For ellipsoidal bodies, the surface integration approach by Conway (2016) yield exact values for force, torque, and mutual gravitational potential. Wold and Conway (2021) outline the surface integration and demonstrate the method in some torque-free planar cases of two spheroids and two disks. Ho et al. (2021) extend this to nonplanar cases, and also use it to study the dynamics of the 1999 KW4 system. While the surface integral method is exact for spheroids and triaxial ellipsoids, it can be somewhat computationally demanding as multiple double integrals must be evaluated at each time step. However, compared to evaluating triple integrals at each time step, it is very efficient. The surface integration method to compute the forces is exact for ellipsoidal bodies because it does not use series expansions, and it also produces exact results in cases when the bounding spheres of the two bodies overlap.

Hou et al. (2017) used their method to compare the differences between different expansion orders for ellipsoidal shapes, and found that the discrepancy in the results becomes smaller with higher orders. However, no comparisons with a mathematically exact method have yet been performed. In this paper, we utilize our surface integration method to investigate the errors in force and torque produced by methods that calculate force and torque based from a series approximation of the mutual potential. We also explore what consequences these initial errors may have on the dynamical behavior of a newly fissioned asteroid binary. For comparing with approximation-based methods, we have chosen to utilize the open source software "General Use Binary Asteroid Simulator" (GUBAS)[1] developed by Davis and Scheeres (2020). GUBAS uses the efficient algorithm based on recursive relations as described by Hou et al. (2017), and allows the user to choose the approximation order of the potential.

Section 2 presents a brief review of the methods that are compared in this manuscript, and the technical details of the comparisons. In Sect. 3 we consider various configurations and study the difference in the values of the forces and torques using second and fourth order approximations and the surface integration method. Two test simulations are presented in

---

[1] Github repository: `https://github.com/meyeralexj/gubas`

Sect. 4 to show the long-term consequences of using these two approaches on the prediction of the dynamic behavior of asteroid binaries. Sect. 5 compares the computational efficiency of the methods. A summary and discussion of our results are presented in Sect. 6.

2 Force, torque and mutual gravitational potential

2.1 Surface integration method

In the surface integration method, the force $\mathbf{F}$ and torque $\mathbf{M}$ on an extended body with surface S, surface normal $\mathbf{n}$ and density ρ, in the gravitational potential, Φ, of another extended body are expressed by the following integrals:

$$\mathbf{F}(\tilde{\mathbf{r}}) = \rho \iint\limits_S \Phi(\tilde{\mathbf{r}})\mathbf{n}dS \tag{1}$$

$$\mathbf{M}(\tilde{\mathbf{r}}) = -\rho \iint\limits_S \Phi(\tilde{\mathbf{r}})\mathbf{n} \times \tilde{\mathbf{r}}dS. \tag{2}$$

The mutual potential energy U between the two bodies is also expressed via a surface integral

$$U = \frac{\rho}{3} \iint\limits_S \left[\tilde{\mathbf{r}}\Phi(\tilde{\mathbf{r}}) - \frac{1}{2}|\tilde{\mathbf{r}}|^2\mathbf{g}(\tilde{\mathbf{r}})\right] \cdot \mathbf{n}dS, \tag{3}$$

where $\mathbf{g}(\tilde{\mathbf{r}}) = \nabla\Phi$ is the gravitational field acting on the integrated body at a point described by the position vector $\tilde{\mathbf{r}}$. The position vector $\tilde{\mathbf{r}}$ is measured in the body-fixed frame of the body exerting the gravitational field (see Wold and Conway, 2021; Ho et al., 2021, for details).

In this work, we assume that both bodies have uniform densities, and are triaxial ellipsoids. For a triaxial ellipsoid, Φ can be expressed analytically, hence Eqs. (1)–(3) above give solutions to the force, torque, and gravitational potential that are exact and not affected by truncation errors or other inaccuracies arising from using approximations. For the gravitational potential of a triaxial ellipsoid we use the expression derived by (MacMillan, 1930).

2.2 Mutual gravitational potential expressed as power series

Whereas in the surface integration method, the force and torque between two rigid bodies is calculated by integrating Φ over a surface, most other methods derive force and torque by first expanding U in a series, and then differentiate U. We have chosen to compare with the output from the software GUBAS (Davis and Scheeres, 2020) where the mutual potential U is expanded as

$$U = -G\sum_{n=0}^{N} \frac{1}{r^{n+1}}\tilde{U}_n, \tag{4}$$

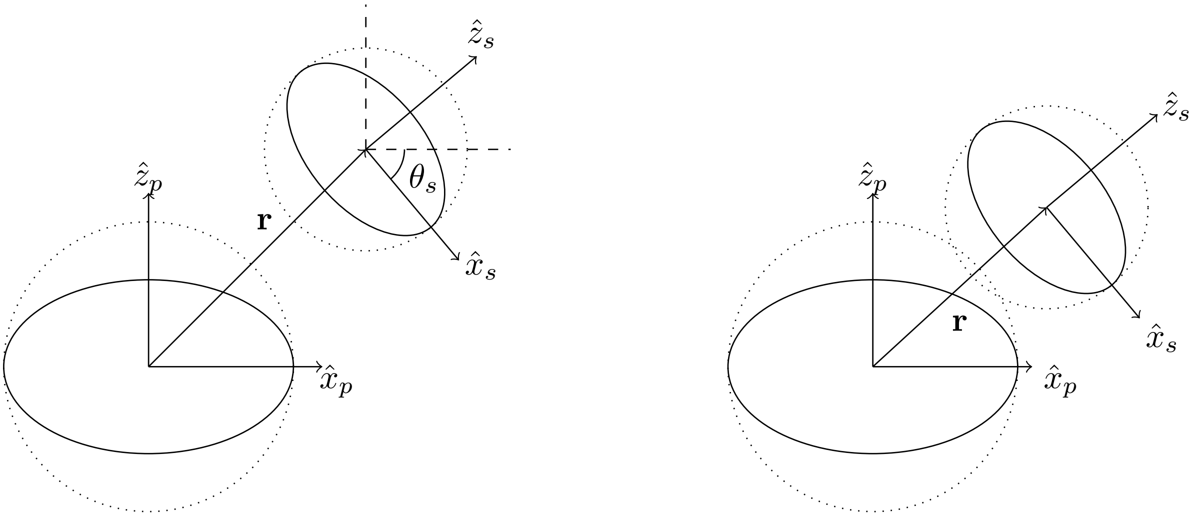

Convergent

Divergent

Figure 1: Illustration of where the series expansion given by Eq. (4) converges (*left*) and diverges (*right*) between two extended bodies. The dotted lines correspond to the bounding spheres around each respective body. In the figure, the secondary is rotated an angle θ_s around the $\hat{y}_s$-axis. The hat variables denote body-fixed coordinates.

where r is the separation between the mass centers of the two bodies, G the gravitational constant, N the truncation order of the potential, and $\tilde{U}$ contains the inertia integrals that are expanded with Legendre polynomials (Hou et al., 2017). The force is computed as

$$F_* = \frac{\partial U}{\partial (*)}, \text{ for } * = x, y, z \tag{5}$$

and the torques as (Maciejewski, 1995)

$$\mathbf{M}'_s = -\alpha_i \times \frac{\partial U}{\partial \alpha_i} - \beta_i \times \frac{\partial U}{\partial \beta_i} - \gamma_i \times \frac{\partial U}{\partial \gamma_i} \tag{6}$$

$$\mathbf{M}_p = \mathbf{r} \times \frac{\partial U}{\partial \mathbf{r}} - \mathbf{M}'_s, \tag{7}$$

where $\alpha_i, \beta_i, \gamma_i$ are the coordinate vectors of the secondary expressed in the body-fixed frame of the primary. The prime notation denotes the vector expressed in the body-fixed frame of the primary (Hou et al., 2017).

The inertia integrals make use of Legendre polynomials to describe the mass distribution of the bodies, and therefore plays the same role as the spherical harmonics coefficients (Tricarico, 2008). Similar to spherical harmonics, the power series described by Eq. (4) converges in a certain region. Tricarico (2008) showed that the mutual potential, using this formulation, converges at every point outside the bounding spheres as long as the bounding spheres do not share any common points (see Fig. 1 for an illustration).

When using the mutual potential in Eq. (4), higher order terms with order $> N$ have been neglected, which leads to truncation errors. In summary, whereas obtaining force and torque from the truncated potential is computationally efficient, the disadvantages are a divergent potential for some configurations where the bodies are in close proximity, and truncation errors. The surface integral method does not encounter these disadvantages, but might be computationally more expensive, at least compared to lower-order potentials. This is because the computational efficiency decreases with a higher number of integral dimensions. Furthermore, the only integrals required to calculate Eq. (4) are the inertia integrals, which are only solved once and can be reused throughout the simulation (Hou et al., 2017).

The surface integration method allows us to fully solve the two-body problem, for two triaxial ellipsoids, in any nonoverlapping configurations, without being affected by truncation errors in the mutual potential. This puts us in the position to investigate how truncation errors, and errors caused by divergence in the series approximation of U might affect the ensuing dynamics of the binary system.

3 Comparisons between the two methods

Thus there are two things we wish to investigate, truncation errors and errors related to overlapping bounding spheres. The first one we address by investigating the difference in force and torque between the two bodies for different positions of the secondary in the equatorial plane of the primary (for configurations where the bounding spheres do not overlap). The second one we address by investigating the difference in force and torque on the two bodies when the two bounding spheres overlap. Finally, we run some longer simulations where the equations of motion are solved in order to investigate how any errors in force and torque made at the initial stages propagate in the ensuing dynamics.

In order to extract values of the forces and torques from GUBAS, we made a slight modification to the software so that the computed forces and torques at the first time step are written to an external file. The forces and torques are also converted to standard SI units (m, s, and kg).

Whereas GUBAS uses relative coordinates for the position of the secondary relative to the primary, we use inertial frame coordinates for the positions of both bodies. Furthermore, in the formulation by Hou et al. (2017), the torque on the secondary is calculated in the body-fixed frame of the primary, while in our method the torque on the secondary is computed in its own body-fixed frame. In order to compare the torque on the secondary calculated in the two approaches, we therefore convert $\mathbf{M}'_s$ computed by GUBAS to the body-fixed frame of the secondary by the transformation

$$\mathbf{M}_s = \mathcal{R}_s^T \mathcal{R}_p \mathbf{M}'_s, \tag{8}$$

where $\mathcal{R}_p$ and $\mathcal{R}_s$ are the rotation matrices of the primary and secondary, respectively, and superscript T denotes the transpose.

Moreover, in order to compare velocities and positions from our method with that from GUBAS, we convert our positions and velocities to the body-fixed frame of the primary. The angular velocities from our code and from GUBAS are both expressed in the body-fixed frame of each respective body, hence there is no need for transformations of these.

Throughout the manuscript, whenever we compute the relative difference between two vectors $\mathbf{v_i}$ and $\mathbf{v_j}$ (can be force, torque, angular velocity, or translational velocity) from model i and j, respectively, we evaluate this as:

$$\delta v = \frac{|\mathbf{v}_i - \mathbf{v}_j|}{|\mathbf{v}_j|}, \tag{9}$$

where $|\,|$ denotes the norm.

For consistency, when we later (in Sect. 4) solve the equations of motion, we use the same Runge-Kutta method with equal time steps, in both the surface integral method and in GUBAS. Any differences between the simulations should therefore not be affected by the choice of integration scheme.

The surface integration itself in our method is performed with the QAG[2] adaptive integration algorithm from the QUADPACK implementation in the GNU scientific library (Galassi et al., 2002). The integration order can be selected from one to six, and using higher orders increases the accuracy while reducing the computational efficiency. Unless otherwise specified, we use the sixth-order QAG integrator[3].

3.1 Effect of truncation errors in mutual potential on the force and torque

For the first experiment, we assume that the binary consists of a primary with semiaxes $(a_p, b_p, c_p) = (400\text{ m}, 390\text{ m}, 350\text{ m})$ and a secondary with $(a_s, b_s, c_s) = (100\text{ m}, 90\text{ m}, 80\text{ m})$, and both have densities of $\rho = 2000\text{ kg m}^{-3}$, corresponding to a mass ratio of $q = m_s/m_p = 0.013$. A number of observed binaries have estimated mass ratios close to this value (Pravec et al., 2016; Naidu et al., 2020).

The secondary is first rotated an angle $\theta_s = 45°$ about its y-axis (see Fig. 1), and then placed with its centroid in the equatorial plane (xy-plane) of the primary (see Fig. 2). In this manner, the configuration is made nonplanar. The secondary is thereafter placed at a number of different positions in the xy-plane of the primary, so that the distance between them varies from a minimum value up to a maximum value of five primary radii (we take a_p to be the primary radius). Asteroid binary observations by Pravec et al. (2016) show that the orbits of the secondaries have semimajor axes between three to seven times the primary radius, hence our chosen range corresponds to common distances found in nature. The minimum distance at which we place the secondary corresponds to the distance when the two bounding spheres of the bodies start to intersect. This is to ensure that the mutual potential described by Eq. (4) converges.

For each position of the secondary in the equatorial plane of the primary, we compute the forces and the torques on both the primary and the secondary using the surface integral method, and using a second and fourth order mutual potential with GUBAS. In this manner, can can study how the errors in the force and torques change with increasing separation between the bodies and with the order of the potential. In our calculations, we have rounded force and torque components with magnitudes smaller than 10^{-16} off to zero.

---

[2] The QAG algorithm is the "simple adaptive integrator" in the QUADPACK library.

[3] Using an order four QAG integrator can reduce the computation time by a factor of two.

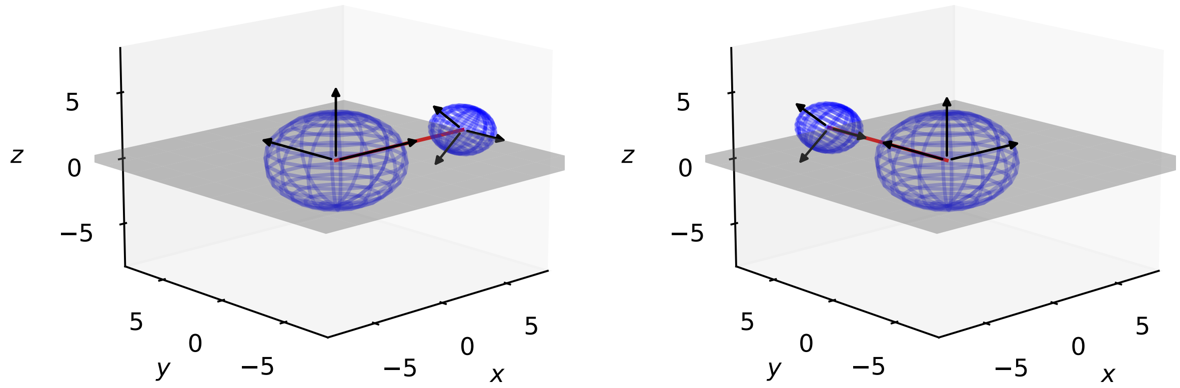

Figure 2: Illustration of how the secondary is placed in the xy-plane of the primary. The red line corresponds to the separation vector $\mathbf{r}$ between the centroids. In the *left panel*, $\mathbf{r}$ is parallel to one of the principal axes of the primary, whereas in the *right panel*, it is parallel to a principal axis of both bodies. The axes are given in dimensionless quantities.

We first study how the mutual potential differ at various separations between the methods, which is shown in Fig. 3. The errors in the mutual potential are smaller than 0.09% and 0.006% for the second and and fourth order potentials, respectively. The largest error, for this particular scenario, does not occur at the minimum separation, but takes place at approximately 1.25 primary radii. Our results are similar to the results of Chanut et al. (2015), who compared their method with the polyhedron approach by Tsoulis (2012), where they found that the largest discrepancy in the gravitational potential occurred near the edges of the asteroid in which the distance to the body's center of mass is the largest.

The results of the calculations of the forces and torques are shown in Fig. 4 where the relative difference between the surface integration method and the two expansion approaches is shown as a color scale in the xy-plane of the primary. The panels to the left show the relative difference in force, while the middle and right panels show the relative difference in the torque on the primary and secondary, respectively.

In the left-most panels it can be seen that the relative errors in the force are largest when the bodies are close: $\sim 0.4\%$ for the second order approximation, and roughly an order of magnitude smaller for the fourth order approximation. As the separation becomes larger, the errors decrease, and become negligible ($< 0.001\%$), consistent with what is to be expected. For the fourth order approximation, the error in the force has already dropped to 0.001% when the distance between the bodies is 2-3a_p. Overall, we see that the relative error in force from the fourth order potential is roughly an order of magnitude smaller than that from the second order potential, as a fourth order expansion is closer to the exact solution with smaller truncation errors.

We now consider the relative error in the torque on the primary as shown in the middle panels. When the secondary's centroid is placed either on the x- or y-axis of the primary, the

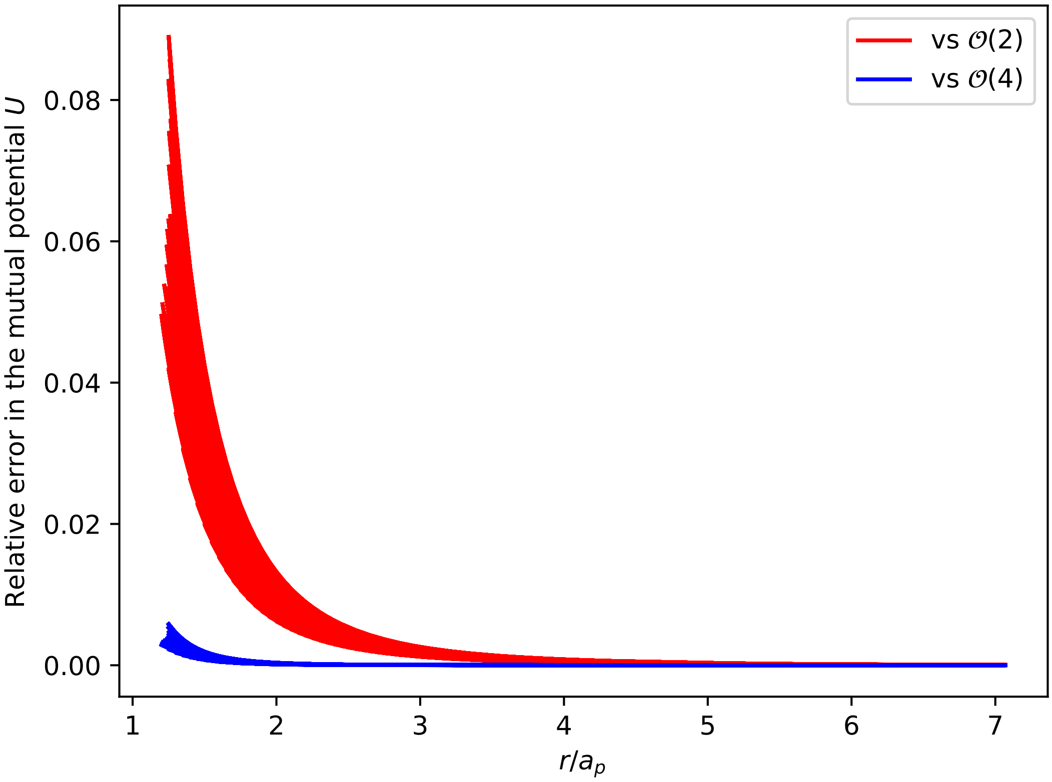

Figure 3: Relative error (in percentage) in the mutual potential U from the second (red line) and fourth order (blue line) potentials compared to the surface integration method, as functions of the separation in primary radii a_p.

error in the torque on the primary, δM_p, is 100% for the second order potential, regardless of the separation between the two bodies. This happens because in this configuration the vector between the centroids of the two bodies, $\mathbf{r}$, is parallel with the principal axes of the primary. In these configurations, the second order approximation yields a vanishing torque on the primary (Kane et al., 1983; Poursina and Anderson, 2012). The zero torque from the second order approximation is however unrealistic in this case, as the torque calculation from both the surface integration method and fourth order potential indicates that nonzero torques are experienced by the primary.

For the torque on the secondary, as is shown in the right-most panels in Fig. 4, the 100% error, from the second order approximation, occurs only when it is placed with its centroid on the y-axis of the primary. Similar to the torque on the primary, this happens because $\mathbf{r}$ is parallel with a principal axis (in this case, the intermediate-axis) of the secondary (see right panel of Fig. 2). At other regions in the xy-plane where $\mathbf{r}$ is not parallel with any one of the principal axes, the errors in $\mathbf{M_p}$, when using the second order potential, range between $\sim 2\%$ and $\sim 10\%$ when the bodies are close, and drops to $\sim 1\%$ at larger distances. The error in $\mathbf{M_s}$, on the other hand, is ~ 10 % at the smallest separation and $\sim 3\%$ at the largest distances. Furthermore, similar to the force, the relative errors in $\mathbf{M_p}$ and $\mathbf{M_s}$ using

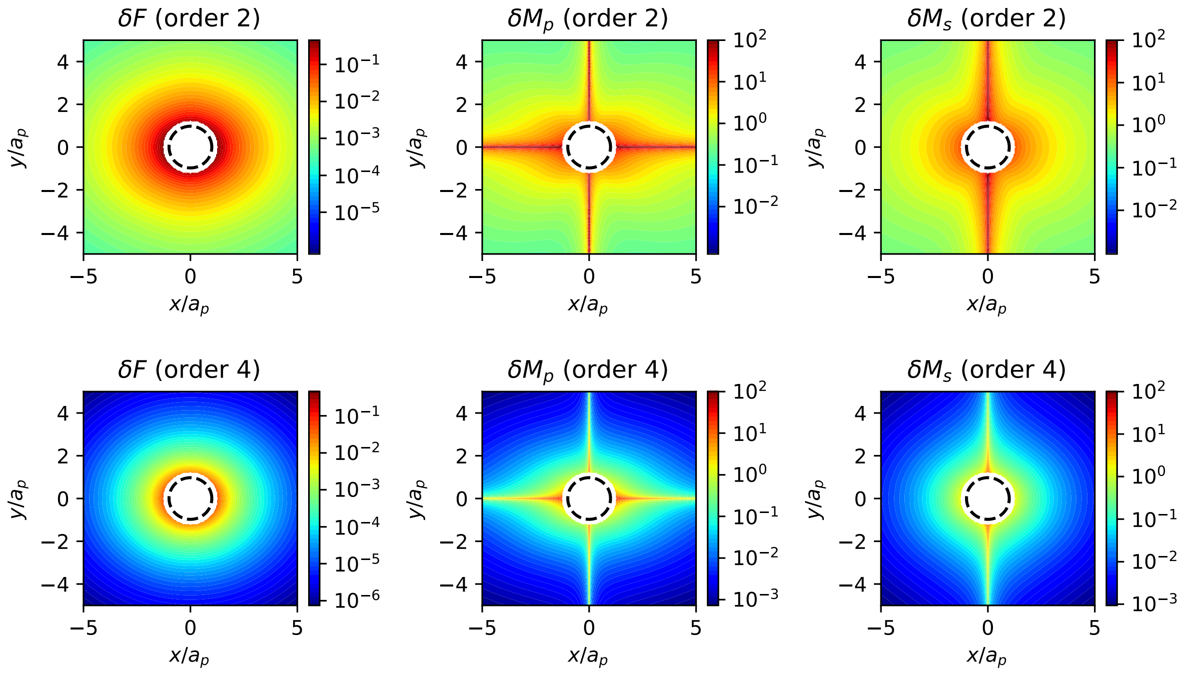

Figure 4: Relative error (in percentage) in force and torques arising from using second (*top*) and fourth order (*bottom*) mutual potentials. The two *left-most panels* show the force, and the *middle* and *right-most panels* show the torque on the primary and secondary, respectively. Each position in the xy-plane corresponds to the position of the secondary in the xy-plane of the primary. The units of the axes are units of primary radius a_p. The black dashed circles indicate the circumference of the primary, and the white region in the center corresponds to the region where the bounding spheres intersect. The color scaling is logarithmic and the color bars show numbers in percentage. The pair-wise comparisons between second and fourth order potentials share the same color scaling.

the fourth order potential are roughly an order of magnitude smaller than when using the second order potential.

It is clear from Fig. 4 and from the discussion above that the relative error in the torques is larger than in the force. This is also seen in other work that involves expansions to study electrostatic forces (Poursina and Anderson, 2012; Poursina and Butcher, 2020). We therefore argue that using approximations to the mutual potential may have a larger effect on the rotational motion of the bodies than on the translational motion.

We briefly investigate how the mass ratio of the system may affect the differences in the computed forces and torques. The semiaxes of the secondary are changed to $(a_s, b_s, c_s) = (250 \text{ m}, 240 \text{ m}, 230 \text{ m})$, while keeping the semiaxes of the primary and the densities of the bodies the same, which corresponds to a mass ratio of $q = 0.25$. The resulting errors in forces and torques are slightly lower, but similar, to that of Fig. 4. However, the decrease in the errors are less than one percent. This suggests that the mass ratio of the system should not significantly affect the computed forces and torques, provided that the bodies are sufficiently far apart.

3.2 Primary and secondary with overlapping bounding spheres

In this section, we investigate situations where the bounding spheres of the bodies overlap and the mutual potential described by Eq. (4) no longer converges (Tricarico, 2008). This happens when the surface of the secondary is allowed to almost touch the surface of the primary. This type of configuration is particularly relevant for newly fissioned asteroid systems, as the bodies are initially very close.

Figure 5 shows two examples from two different viewing angles of the configurations we investigate in this section. The position of the secondary is such that the separation between the ellipsoids is the shortest while ensuring that the surfaces of the bodies do not overlap. The bodies nearly touch, that is, there is no normal force involved in our calculations. We choose a number of different positions of the secondary such that the point P is distributed over the entire upper half of the surface of the primary (because of symmetry, we only consider surface connection points on the upper half of the primary). Contrary to what was done in the previous section, we now keep all three axes of each of the body-fixed coordinate systems parallel.

We compute force and torques as in the previous section, but for three different shapes of the primary. The long semiaxis of the primary is fixed at $a_p = 400$ m, and three values of the axis ratios a_p/b_p and a_p/c_p are chosen. The three different shape models of the primary are listed in Table 1, one is a spheroid (Model 1) and two of them are rather elongated (Models 2 and 3). The secondary is kept at the same size and shape as in the previous section.

The results of the comparison between the output from GUBAS and the output from the surface integration method are shown in Fig. 6 and Fig. 7, again as colored contour plots. All panels in the figures show the surface of the primary ellipsoid viewed from above, along the z-axis, and each point in the xy-plane represents the connection point P on the surface of the primary as illustrated in Fig. 5.

Figure 6 shows the relative error in the force that arises when using second or fourth order

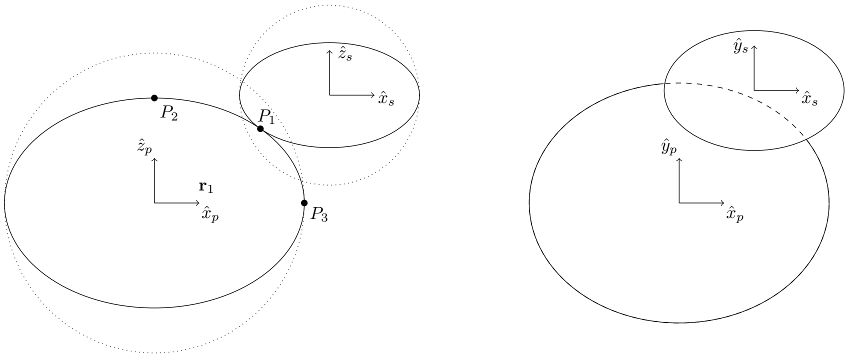

Figure 5: Example configurations where the surfaces of the ellipsoids are almost touching. The *left panel* shows a view of the xz-plane, where the bodies are almost touching at point P_1. The bounding spheres around each body are marked with dotted lines, and are seen to overlap. Point P_2 is at the pole of the primary, and P_3 at the equator. Each connection point P_i corresponds to a position vector $\mathbf{r}_i$ between the centroids of the bodies. The *right panel* shows a view from above of the xy-plane.

Model	a_p/b_p	a_p/c_p	q
Model 1	1.000	1.067	0.012
Model 2	1.231	2.000	0.028
Model 3	1.455	4.000	0.065

Table 1: Parameters used for the three models chosen for the tests in Sect. 3.2. The second and third columns show the axis ratios of the primary, while the fourth column shows the mass ratio, $q = m_s/m_p$, of the system. Model 1 is a spheroid, and Models 2 and 3 are elongated ellipsoids. The long semiaxis of the primary is fixed at $a_p = 400$ m.

potentials. The error increases as the secondary is moved closer to the pole of the primary (point P_2 in the left panel of Fig. 5). At this location the distance between the centroids is at the minimum, and the error in the force is the largest. For the spheroidal primary (Model 1), the error is rather small for both the second and fourth order approximations ($< 0.5\%$), whereas for the elongated models it ranges from $\sim 50\%$ to above 1000%.

For the more elongated model (Model 3), the errors from the fourth order approximation become larger than that from the second order. As the separation between the mass centers r becomes smaller, the bounding spheres will overlap more, causing a larger error in the mutual potential when it is expanded through power series. Furthermore, the forces between two extended bodies, obtained from expanding inertia integrals up to order N, scale as $(a_p/r)^N$ (Kane et al., 1983). For nearly all configurations we have considered here, we have that $r < a_p$. The higher order gravity terms will therefore result in values larger than the lower order terms, thus inflating the values of the computed forces. The forces from the expansion method therefore become greater than the values obtained with the surface integration method.

The error in the torque on the primary arising from using second and fourth order potentials is shown in the first and second rows of Fig. 7. Similar to the force calculations,

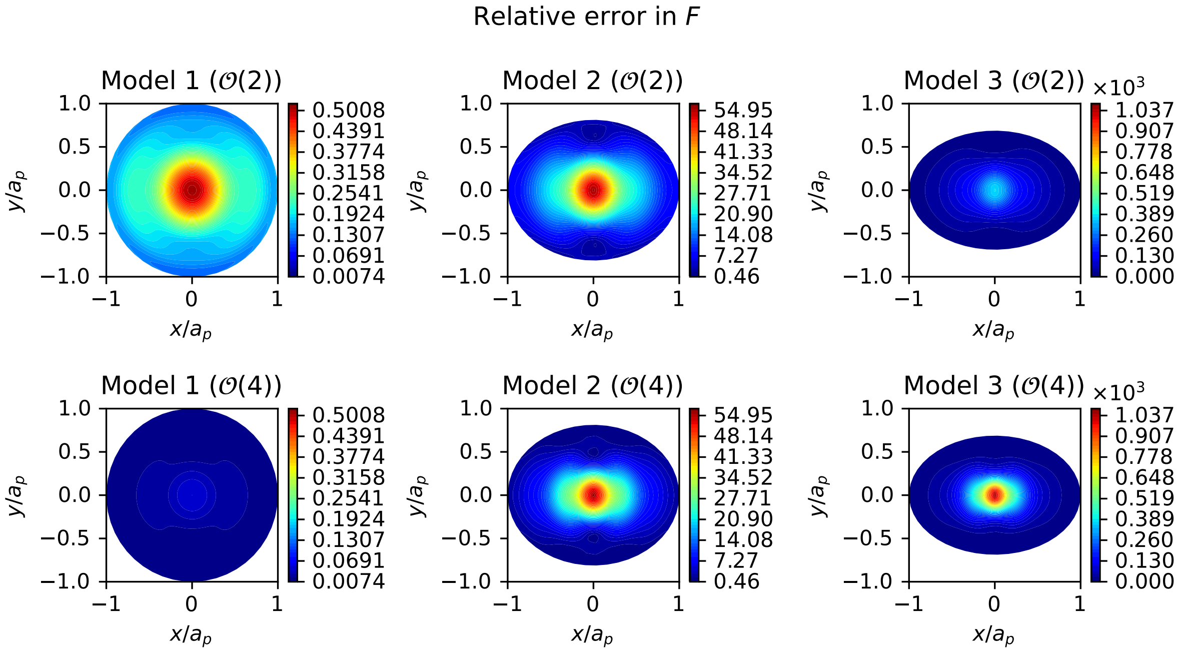

Figure 6: Percentage difference between force F from `gubas` using second and fourth order potentials, relative to force from surface integration method. The xy-plane shows the surface of the primary viewed from the top, along the z-axis. Each point in the plane corresponds to a surface connection point on the primary, i.e. a new position of the secondary. The *top* and *bottom panels* are for second and fourth order approximations, respectively, and the panels show results for three different models of the primary, see Table 1. The pair-wise comparisons between second and fourth order potentials share the same color scaling.

the error is larger for the most elongated primary, particularly near the pole, regardless of whether the expansion order is two or four. As for the force calculations, when the primary becomes more elongated, the relative error using the fourth order approximation becomes greater than when using the second order approximation. This is again because the separation r becomes smaller, and higher order gravity terms inflate the computed torques.

There are five surface connection points on the primary where the torque is zero. These are located at $(x = \pm a_p, y = 0)$ and at $(x = 0, y = \pm b_p)$ (along the equator) and at $(x = 0, y = 0)$ (the pole). Only the point in the pole is included in Fig. 7 (white region). Away from the region around the pole of the primary, Model 1 yields relative errors in M_p up to 16% with the second order approximation, while the error from using fourth order approximations is smaller by one magnitude. Hence for a spheroidal primary, both the fourth and the second order method give relatively good approximations of the torque, despite the bounding spheres overlapping.

The results for the torque on the secondary are shown in the third and fourth rows of Fig. 7. The relative error behaves in much the same way as for the primary, but is significantly larger in magnitude for model 3, as the errors can reach as high as 10^4% for the fourth order approximation.

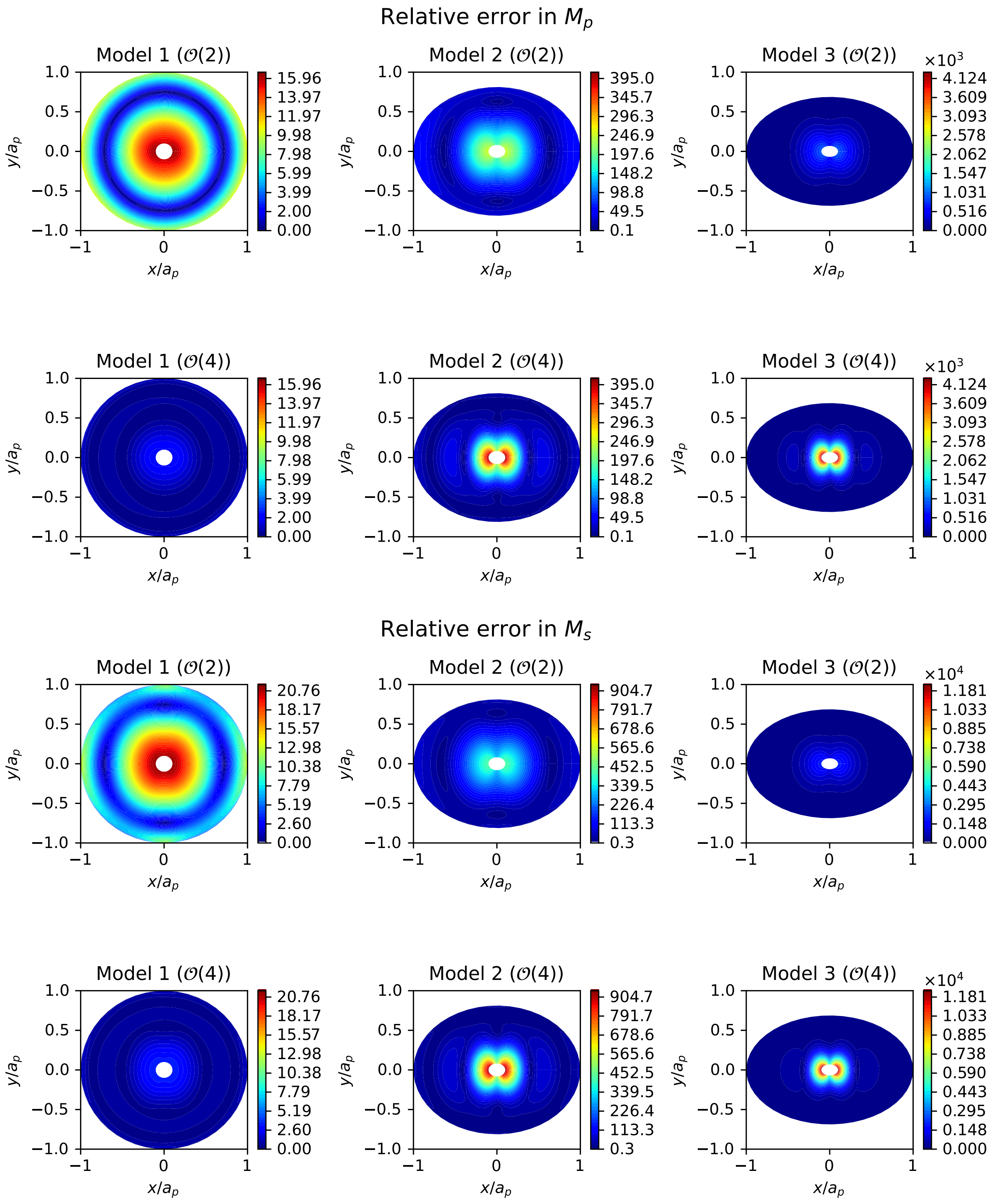

Figure 7: Same as Fig. 6, but now showing the error in the computed torques on both bodies. The *first* and *second rows* show the relative differences in the torque on the primary M_p, while the *third* and *fourth rows* show the difference in the torque on the secondary M_s. Within the white region, the torques acted on the bodies are zero, and we have chosen to exclude this region from the plot as it is difficult to show relative error in M when M is close to zero.

4 Dynamical simulations of binaries

We run two different simulations in this section, in the first one the two asteroids are spaced relatively far apart, and in the other they resemble a contact binary that just separated into two components via rotational fission. For solving the equations of motion, we use the standard fourth order Runge-Kutta method. For the surface integration method, the rotational motion is described using Euler parameters (quaternions), and the equations of motion of the bodies are described in Ho et al. (2021).

4.1 Scenario 1: A binary with moderate separation

In the first simulation, the asteroids orbit each other at a distance of three to four times the primary radius, thus resembling some observed binaries (Pravec et al., 2016). The semiaxes and densities of the two bodies are the same as in Sect. 3.1. We place the secondary initially at the position $\mathbf{r} = [1800, 0, 5]$ m relative to the primary, and give it an initial velocity $\mathbf{v} = [0, 0.12, 0]$ m s^{-1}. The primary has an initial angular velocity of $\boldsymbol{\omega}_p = [0, 0, 10^{-4}]$ rad s^{-1}, whereas the secondary has zero initial angular velocity. The bodies are also placed initially such that their body-fixed axes are parallel. The integration time is 100 days, with a fixed time step of five minutes.

Figure 8 shows the difference between the output from GUBAS and the surface integration method for the x, y and z-components of the position of the secondary. In the second order approximation, the x and y position of the secondary fails by approximately ± 50 m at the most ($\sim 3\%$ of the distance between the primary and secondary), and for the z-component with ± 0.25 m at the most. The position calculated with the fourth order approximation in GUBAS is indeed a very good approximation, as shown by the blue line in Fig. 8, where the differences are smaller than ~ 1 m for all three components. This agrees with the findings in Sect. 3.1, where the errors from the fourth order potential is an order magnitude smaller than the second order approximation.

Hou et al. (2017) compare how the x-position of the secondary deviates between different orders of the potential, with an initial separation of 3.6 times the primary radius. The deviation of the x-position, between the second and fourth order potential, surpassed over 1000 m after ~ 130 hours. In our simulations, after 130 hours, the deviation in the x-position is ~ 1.4 m and $\sim 10^{-3}$ m for the second and fourth order approximations, respectively. Our comparison between the surface integration scheme and the second order potential is similar to the order ten and order eight comparison performed by Hou et al. (2017), where the x-position deviated by ~ 5 m after 130 hours. The system considered by Hou et al. (2017) has a mass ratio of $q = 0.512$. However, as discussed in Sect. 3.1, the mass ratio of system should not significantly alter the differences in the computed forces, as long as the bodies are sufficiently far apart.

In Fig. 9 we plot the differences in the components of the angular velocities of both the primary and secondary throughout the simulation. The discrepancies between the second order approximation and the surface integration method are of order 10^{-10} rad/s and 10^{-6} rad/s for the primary and secondary, respectively, and the difference is reduced by a factor of ten when the fourth order potential is used.

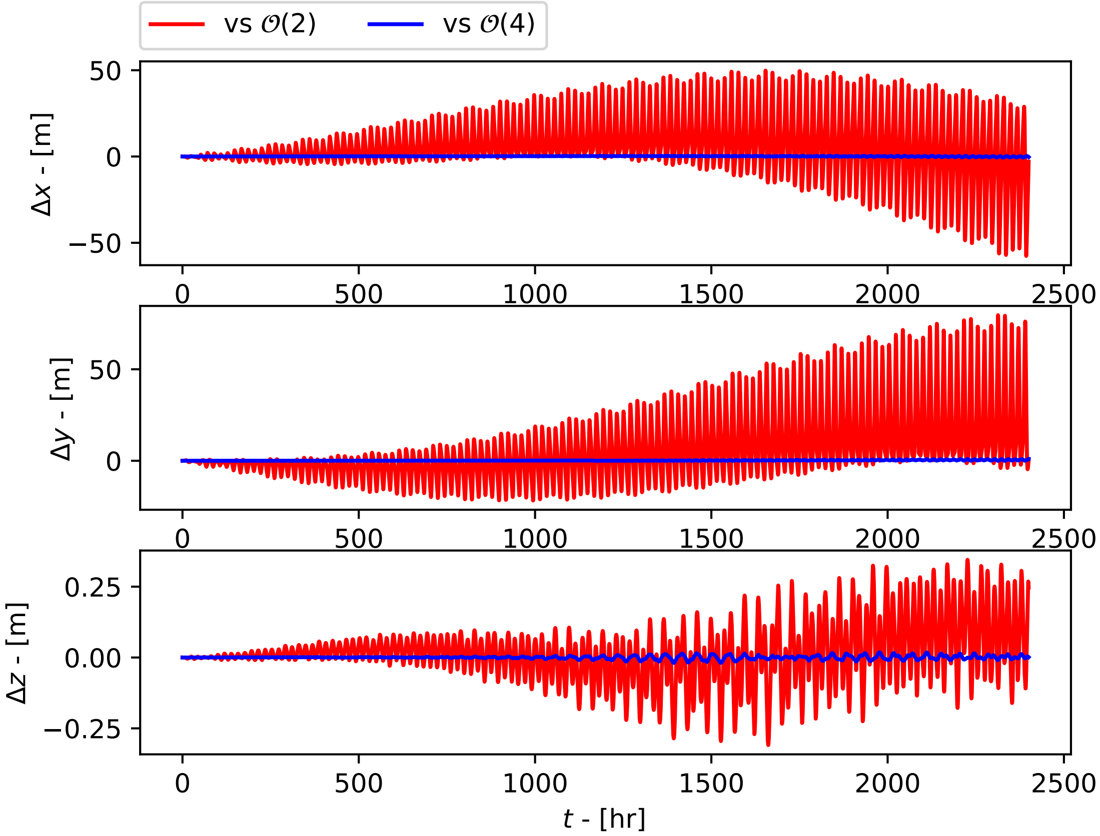

Figure 8: For scenario 1: The difference between between `gubas` and our method for the position of the secondary relative to the primary. The *top*, *middle* and *bottom* shows the difference in the x, y and z components respectively. The red line is the difference between `gubas` second order approximation and the surface integration method, whereas the blue line shows the difference between `gubas` fourth order approximation and the surface integration method.

As the results from Sect. 3 indicate that the choice of approximation order for the potential affects the rotational motion more significantly than the translational motion, we wish to compare differences in translational and rotational velocity. This is shown in Fig. 10 where we have plotted the difference in the velocity and the angular velocity of the secondary, as calculated from both the second and fourth order potential relative to the surface integration method. For the second order potential, the relative difference in the translational velocity is under $\sim 3\%$, while the relative difference in the angular velocity averages at $\sim 70\%$. The error in the rotation period of the secondary, computed as $T_s = 2\pi/|\boldsymbol{\omega}_s|$, also averages at roughly 70%. This showcases that using the surface integration scheme to determine the motion of asteroids, in which the results are exact for ellipsoidal shapes, is more important to correctly predict rotational motion.

The Double Asteroid Redirection Test (DART) is a NASA mission that aims to demon-

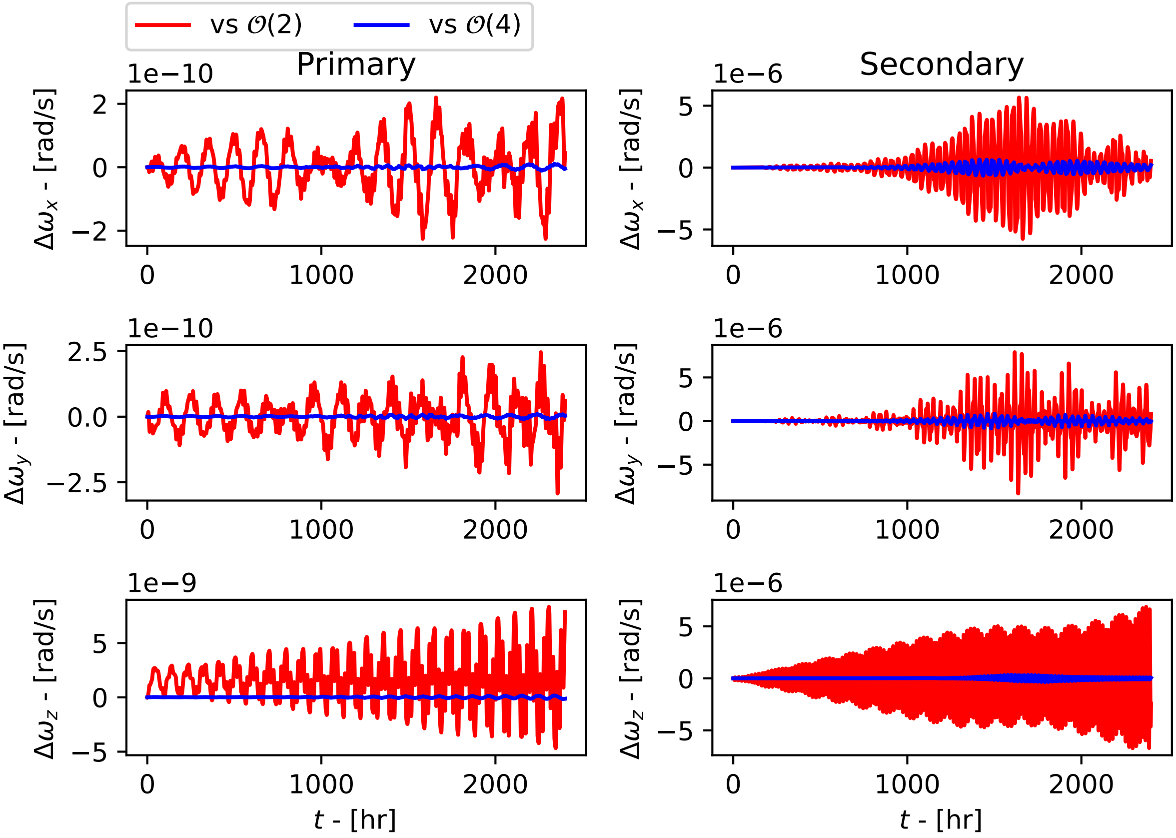

Figure 9: Same as Fig. 8, but for the components of the angular velocity. The *left panels* show the components for the primary, and the *right panels* show the components for the secondary.

strate how a kinetic impactor can be used to redirect the orbits of objects that may potentially collide with Earth (Cheng et al., 2018; Rivkin et al., 2021). One of the observable quantities after the impact is the orbital period of the secondary, and may fluctuate over time scales from days to months depending on the shape of the target body and the momentum transfer enhancement factor (Richardson et al., 2022). It is therefore interesting to briefly check whether the approximation order of the potential significantly influences the period of the secondary in a binary system. In doing this, we find (for the assumed binary in this section) a relative error of $< 0.1\%$ in the period from using the second order potential, and for the fourth order potential a relative error in the period of $< 0.001\%$. The former corresponds to a difference in ~ 3.6 seconds in the orbital period, while the latter a difference of ~ 0.4 seconds.

In summary, for the assumed binary in this section, a variation of $\sim \pm 10$ m in the position of the secondary, $\pm 10^{-6}$ rad/s in the angular velocities, and $< 0.1\%$ in the seconday's orbital period are small enough to be negligible for the overall orbit. Hence, provided the components are far enough apart, using the fourth order potential is sufficient to describe

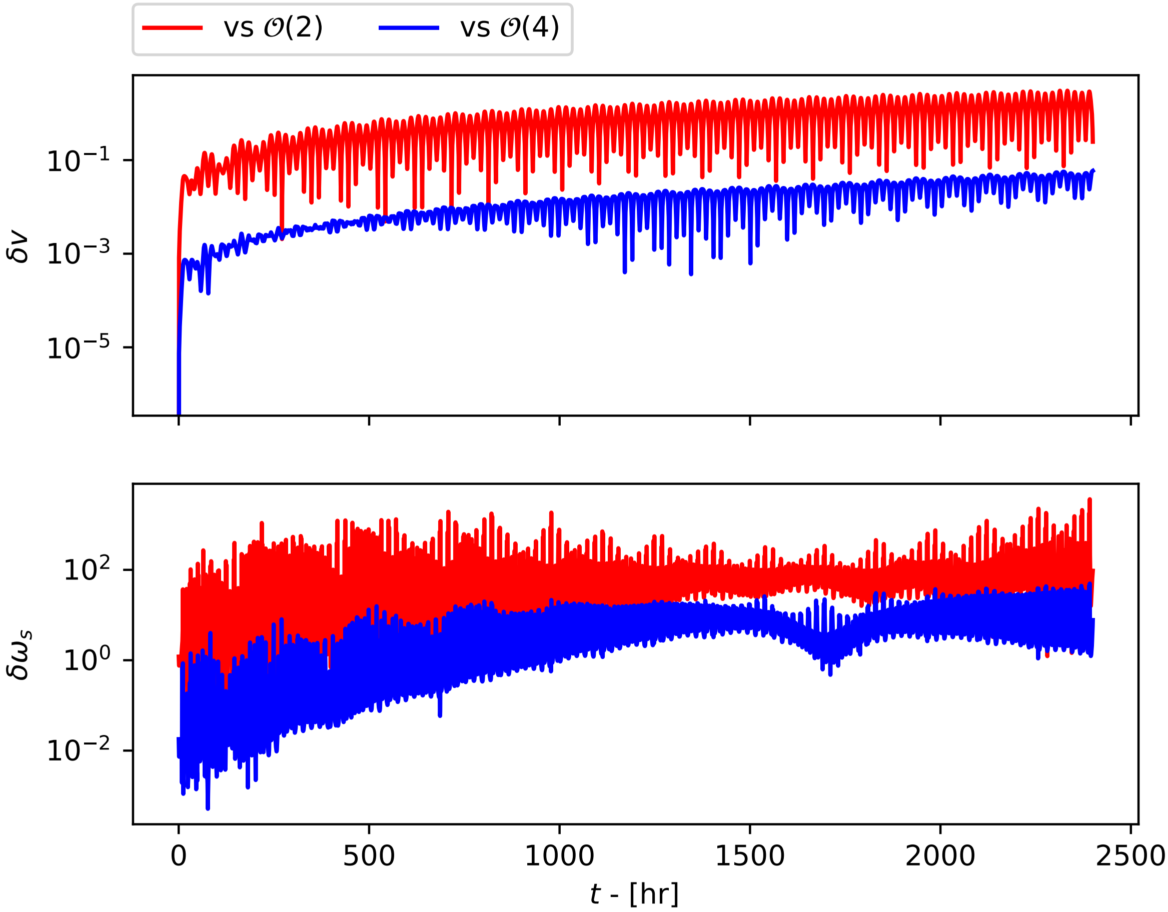

Figure 10: Relative difference (in percentage) between the models for the speed (*top*) and the angular speed (*bottom*) of the secondary. The red line shows the second order potential approximation relative to the surface integral method, and the blue line the fourth order method relative to the surface integration method.

the dynamics of asteroid systems, such as the Didymos binary system (see also Agrusa et al., 2020). However, these results are based on asteroids with perfect ellipsoidal shapes, while real asteroids are better described with, for example, polyhedral shapes.

4.2 Scenario 2: A fissioned contact binary

In this section, we simulate an asteroid binary after a contact binary has separated into two components due to rotational fission. The bodies in this system are initially very close so that their bounding spheres overlap in the initial stages of the simulation. We compare the output from simulations using the approximative method from GUBAS with that from our surface integration method.

The initial conditions are the same as those of Ho et al. (2022), where the secondary is initially rotated by an angle $\theta_s = 5°$ about its body-fixed y-axis and the surface-to-

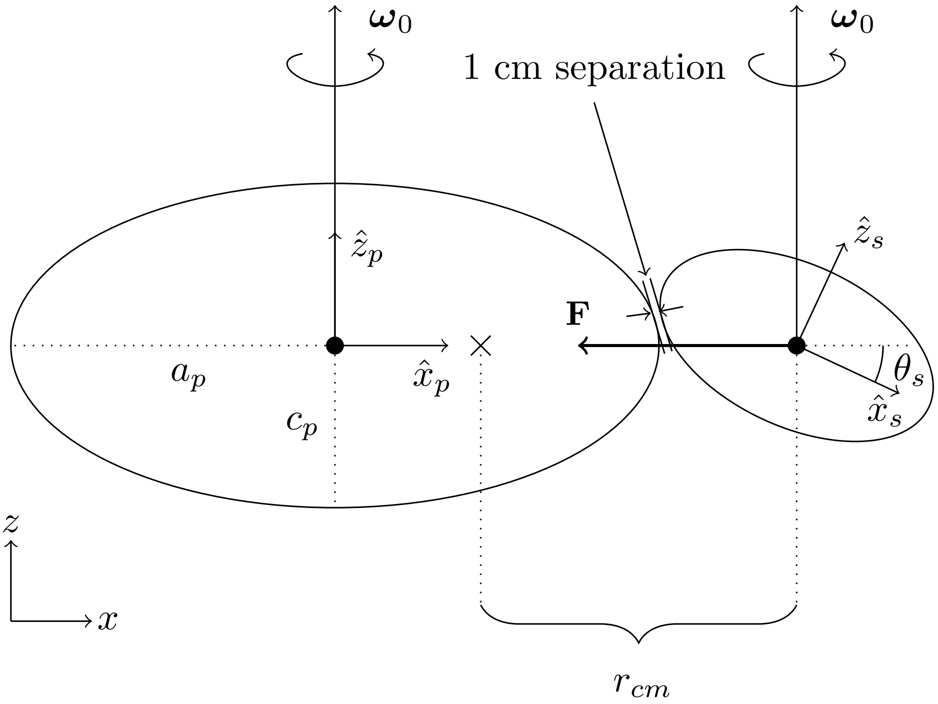

Figure 11: Illustration of the initial configuration for the rotational fission scenario described in Sect. 4.2.

surface distance between the primary and secondary is 1 cm (see Fig. 11). The semiaxes of the primary are $(a_p, b_p, c_p) = (1000, 700, 650)$ m, and for the secondary $(a_s, b_s, c_s) = (699, 469, 435)$ m, chosen so that the mass ratio is $q = 0.3$. This mass ratio is large enough to yield a negative total energy for the system so that the components do not undergo mutual escape. The integration time is one year with time steps of five minutes.

Given the selected semiaxes of the two bodies and the required surface-to-surface distance of 1 cm, the initial position of the secondary becomes $(x, y, x) = (1667.2, 0, 0)$ m, while the primary is located at the origin. By equating the centrifugal force with the gravitational attraction in this configuration, we find the initial angular velocity ω_0 that the system must have in order to undergo rotational fission (for details see Ho et al., 2022)

$$\omega_0 = \beta\sqrt{\frac{F}{m_s r_{cm}}}, \tag{10}$$

where F is the magnitude of the gravitational force, m_s the mass of the secondary, r_{cm} the distance between centroid of the secondary and the center of mass of the system (see Fig. 5) and β a cohesion factor. Following Ho et al. (2022), we use $\beta = 1.01$. The gravitational forces used to determine ω_0 are obtained by measuring $\mathbf{F}$ for the given initial configuration for all three models (similarly to what is done in Sect. 3). For the chosen configuration we get a numerical value of $\omega_0 = 2.99 \cdot 10^{-4}$ rad/s (spin period of 5.84 hr) from the surface integration method. For the second and fourth order approximation methods, we find $\omega_0 = 2.92 \cdot 10^{-4}$ rad/s and $2.97 \cdot 10^{-4}$ rad/s, respectively (corresponding to spin periods

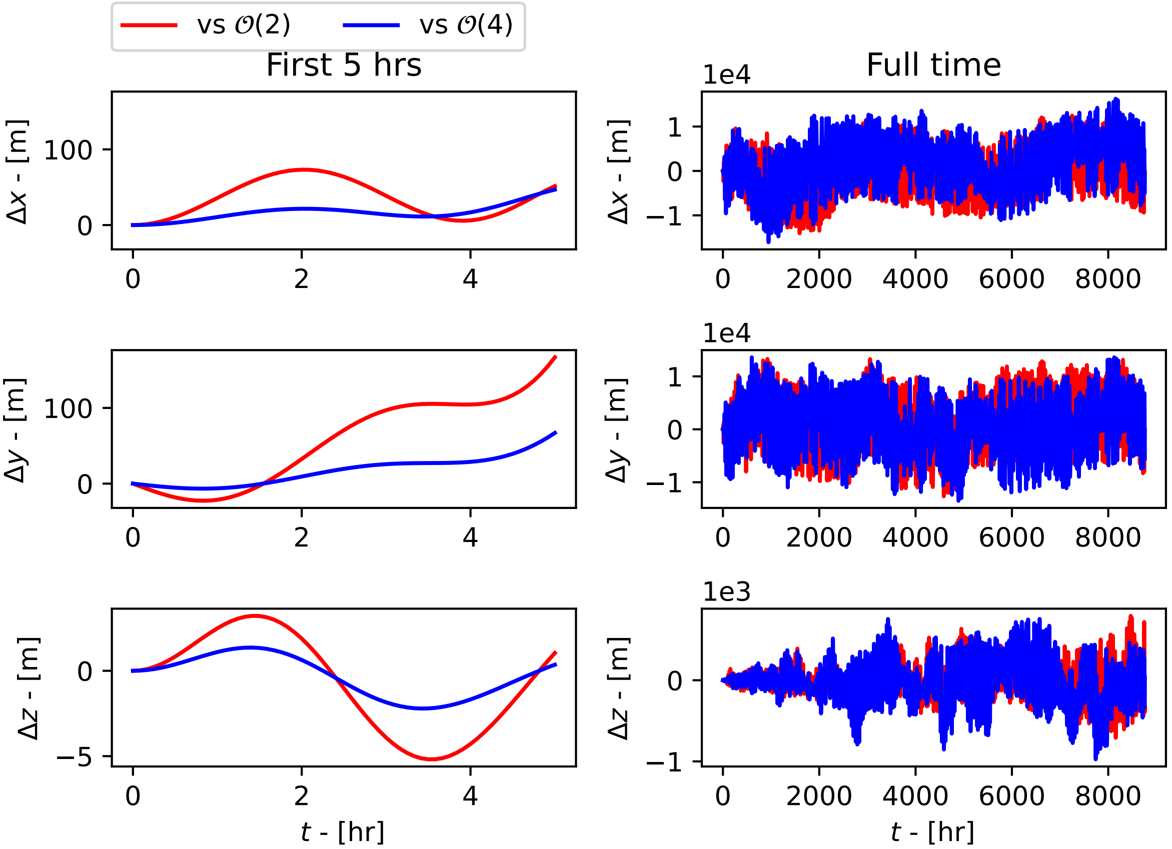

Figure 12: For scenario 2: The difference in the x-, y- and z-coordinates of the position of the secondary relative to the primary. The red and blue lines correspond to the difference between the surface integration method and the order two and four approximations by `gubas`, respectively. The *left column* shows the difference during the first five hours, while the *right column* shows the difference over the whole simulation time span.

of 5.98 hrs and 5.88 hrs). Conservation of angular momentum thereafter gives the initial translational velocities of the components (for details, see Ho et al., 2022). Thus the fission limit ω_0 is slightly different in the three cases because it ultimately depends on the mutual gravitational potential.

With these initial conditions, we compute again the difference in x-, y- and z-coordinates of the secondary as a function of integration time, and plot the result in Fig. 12, where the first five hours are plotted separately in the left-hand panels. After the first five hours, the coordinates already deviate by more than 50 m along the x and y-directions. As time passes, the difference increases, and Δx and Δy can become larger than 10 km, and Δz larger than 1 km. It also appears that the magnitude of the difference is the same regardless of whether the second order or the fourth order approximation is used.

In order to check if the large differences could be caused by slightly different initial angular velocities, we started some simulations with the same initial angular velocity of

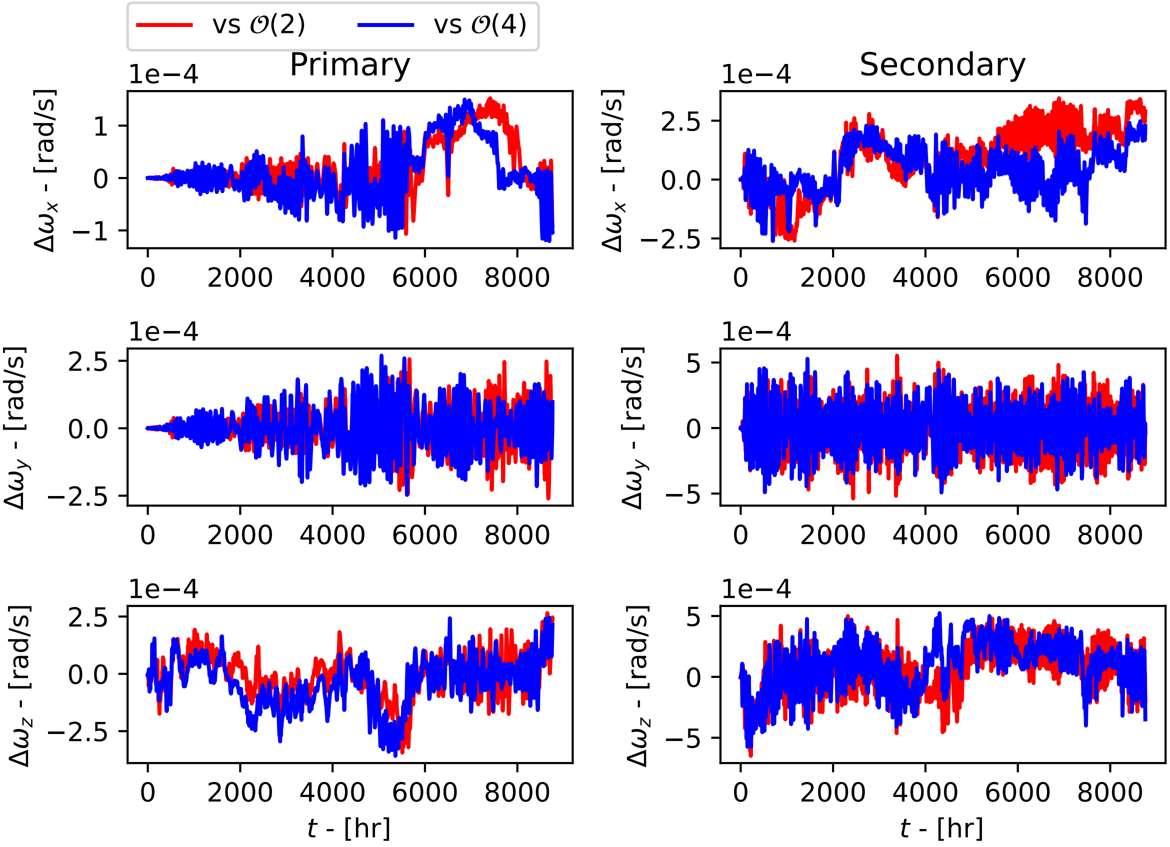

Figure 13: Difference in angular velocity components for the primary (*left*) and secondary (*right*). The red and blue lines correspond to the difference between the surface integration method, and the order two and four approximations by `gubas`, respectively.

$\omega_0 = 2.99 \cdot 10^{-4}$ rad/s (the value computed from the surface integration method) for all three models, but found that Δx-, Δy- and Δz reach the same order of magnitude as that shown in Fig. 12. Using $\omega_0 = 2.92 \cdot 10^{-4}$ rad/s as the initial angular velocity (the value from the second order potential) results in the bodies colliding for both the surface integration method and the fourth order approximation, already after the first time step.

The secondary orbits closer to the primary with the second order approximation, and the separation between the primary and the secondary is ~ 4.5 primary radii on average, and never exceeds eight primary radii. For the fourth order approximation and the surface integration method, the separation is on average ~ 5.4 and ~ 5.5 primary radii, respectively, and can reach up to ten primary radii. This is a consequence of the different initial conditions, as the second order potential yields a lower initial velocity compared to the other two methods. On the other hand, if the same initial conditions are used, the average separation is approximately 5.4 primary radii for all three models.

The differences in the angular velocity components are also larger compared to scenario 1, with a magnitude of $\Delta\omega$ of the order 10^{-4} rad/s for both bodies and for both approxi-

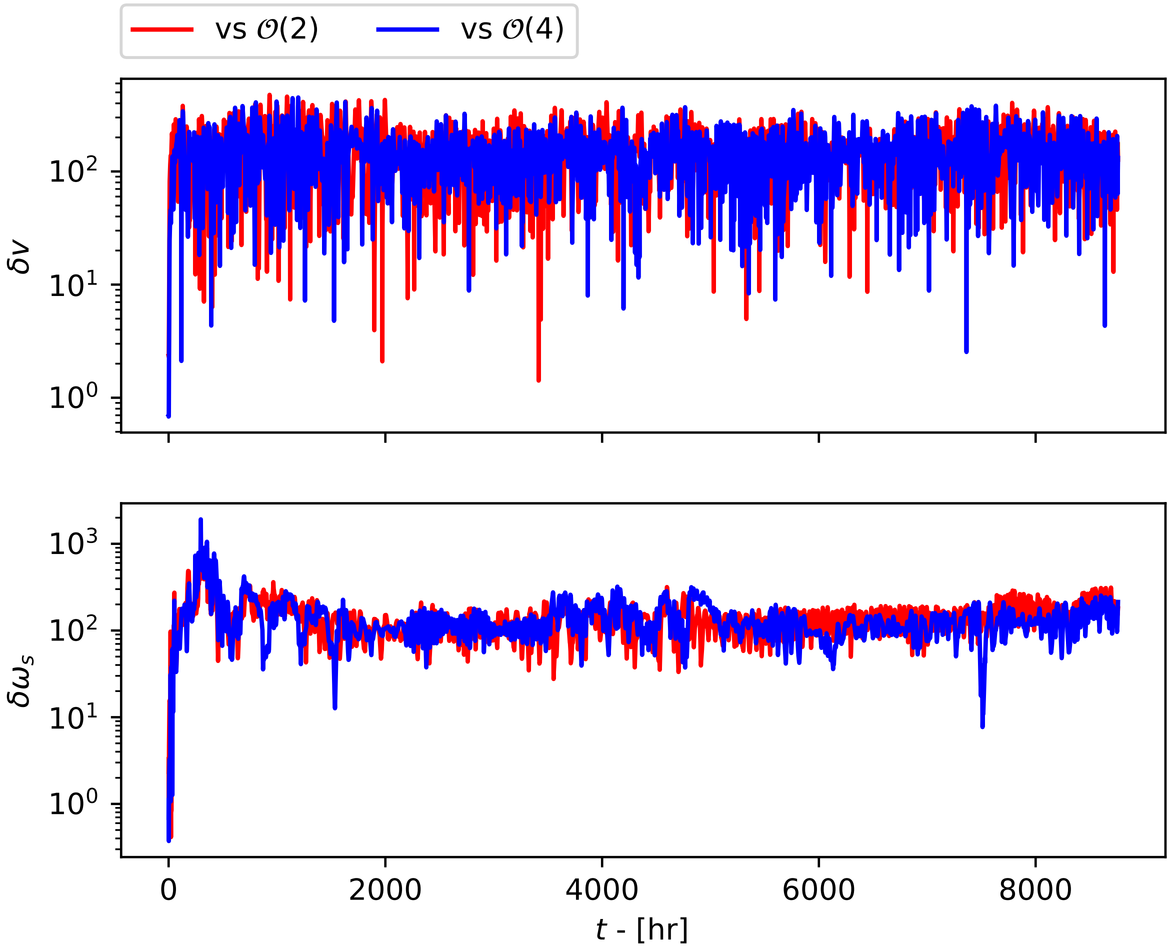

Figure 14: Same as Fig. 10, but now for scenario 2.

mations, shown in Fig. 13. This difference also occurs when the same initial conditions are used.

Contrary to the simulation in the previous subsection, where the bodies are further apart, both the second and the fourth order approximation produce equally erroneous velocities and angular velocities, as seen in Fig. 14. The relative differences are greater than 130% on average, regardless of expansion order. Provided that the bodies are modeled as ellipsoids, using an exact method therefore becomes more important for the outcome of both the translational and rotational motion of the bodies if that they are initially very close.

The relatively large differences in the evolution of the binary between the surface integration scheme and the two other methods are likely due to the proximity of the bodies during the first few hours of the simulation. After about ten hours, the average separation between the bodies is sufficiently large that the difference in the mutual potential between the surface integration approach and the other two methods is relatively small, but as the bodies have evolved very differently up till then, they continue to evolve differently.

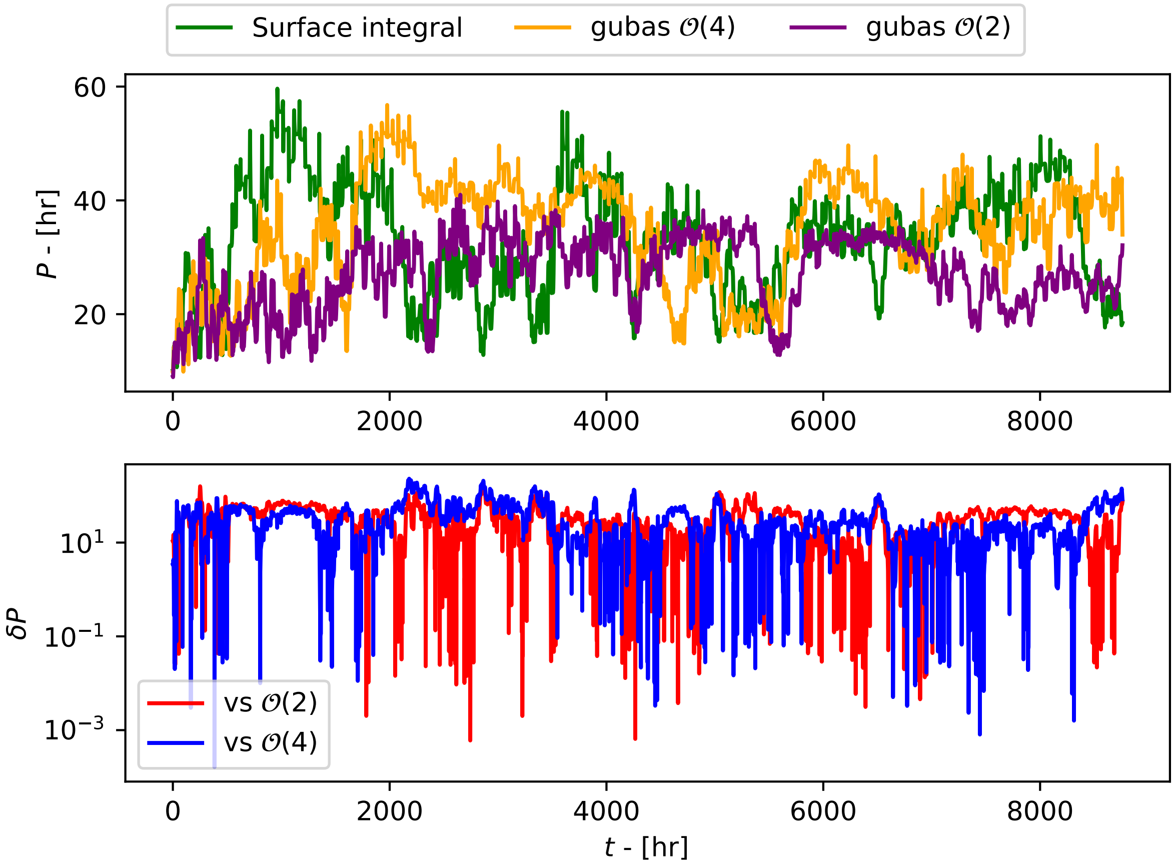

Figure 15: For scenario 2: *Top*: The orbital period of the secondary from the three models as functions of time. *Bottom*: The relative difference (in percentage) in the orbital period between the expansion methods and the surface integration method.

In Fig. 15 we show how the orbital period of the secondary changes over time with the three different methods. By using the second order potential, the orbital period is generally shorter compared to using either the fourth order potential or the surface integration method method, consistent with the secondary orbiting closer to the primary in the former case. The error in the orbital period can exceed 10% for both the second and fourth order potentials.

Hou et al. (2017) find that higher order terms become important to determine the trajectories of post-fissioned binaries if the bodies are more elongated. In order to check whether changing the shape of the primary to a more spherical shape has large effects on the outcome, we changed the semiaxes of the primary to $(a_p, b_p, c_p) = (1000, 900, 850)$ m (which also results in different semiaxes and positions of the secondary, and different values of ω_0), the discrepancy of the positions and angular velocities, between the surface integration method and the output of GUBAS, are of the same order of magnitude as in Figs. 12 and 13. Therefore, the use of a more accurate method is also important for the dynamics of newly fissioned contact binaries, even if the bodies have low elongations.

4.3 Energy differences - Formation of asteroid pairs and stable binaries

After a contact binary has separated into two components by rotational fission, the secondary may end up in a stable orbit around the primary, or escape (reimpact with the primary is also possible). This depends on the total energy of the system, if the total energy is negative, the system may become a stable binary, whereas if the total energy is positive, and there is no loss of energy, the components may undergo mutual escape. Therefore, if we assume that there is no exchange of energy with the surroundings and that the bodies are rigid, the initial total energy of the system determines whether the contact binary becomes an asteroid pair or a binary (Pravec et al., 2010; Jacobson and Scheeres, 2011; Boldrin et al., 2016; Ho et al., 2022).

In the rotational fission model, the initial energy of the contact binary depends on the mutual gravitational potential, and hence affects predictions of which systems may form binaries and which may form asteroid pairs. In order to address the influence that the choice of approximation order has on the ability to form stable binaries we compute the total energy for a number of different configurations with the three methods.

We assume a contact binary where the two components have equal shapes (as defined by their axis ratios), and vary the mass ratio from 0.01 to 0.3 as this is the region around zero total energy. For each assumed value of q, we choose several different orientation angles θ_s of the secondary, from 0° to 90° (see Fig. 11). The initial conditions are the same as described in Sect. 4.2 (see also Ho et al., 2022).

The results are displayed in Fig. 16 in the form of a line in the q-θ_s plane marking the separation between positive and negative system energies. As the mass ratio increases, the total energy of the system starts to become negative but can remain positive if θ_s is large enough. The separation between positive and negative energies varies between the methods but generally ranges between $q \sim 0.21$ and $q \sim 0.26$. The fourth order approximation is seen to produce results that are fairly close to that from the surface integration method.

The difference between the methods is larger for lower values of θ_s, but is still quite small, that is, for a given θ_s the zero energy line occurs over a span in q that is always less than 0.02. As seen in the figure, the fourth order and the surface integral method is quite similar, whereas the second order potential yields a zero energy line more shifted toward lower mass ratios. For instance, if the mass ratio is $q \approx 0.23$, the second order method predicts that the contact binary becomes a pair if $\theta_s \gtrsim 40^\circ$. But with the fourth order method, the contact binary can still form a stable binary as long as θ_s does not exceed $\sim 20^\circ$. Simulations that use the surface integral method for determining the mutual potential will therefore predict formation of asteroid pairs at slightly higher mass ratios compared to methods that use expansions of the mutual potential.

As θ_s approaches 90 degrees, the separation vector $\mathbf{r}$ becomes smaller in order to maintain the 1 cm surface-to-surface separation. As a consequence, the bounding spheres between the bodies will intersect more when θ_s increases, and we expect the mutual potential to differ more between the methods. However, as seen in Fig. 16, this is not the case, since the gap between the separation lines becomes smaller. Upon further inspection, the discrepancy in both the force and mutual potential energy become smaller when the system

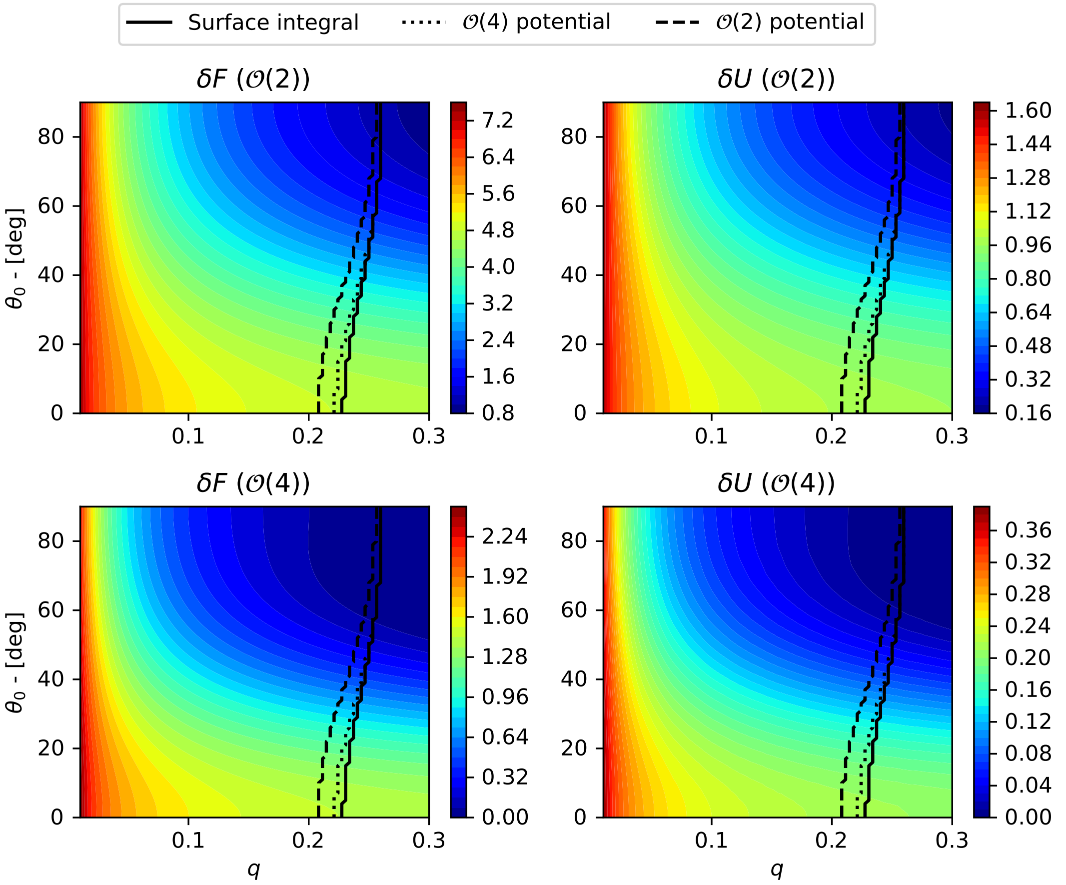

Figure 16: Relative error (in per cent) in force and mutual potential energy in the *left* and *right* columns, respectively. The *top* and *bottom* rows correspond to the relative difference of the order two and order four potentials. The black lines indicate the separation between positive and negative total energies. Regions to the left and right of the respective lines correspond to positive and negative system energies.

approaches higher mass ratios ($q \approx 0.3$) with $\theta_s = 90^\circ$, illustrated by the colored contours in Fig. 16. The largest differences are found at low mass ratios and when θ_s is small, where the errors in the force can reach 7% when $q = 0.01$ for the second order potential, while error reduces to roughly 2% when the potential is truncated to order four.

5 Computational efficiency

While the surface integration method is exact for bodies of ellipsoidal shapes, it is also more time-consuming to compute as multiple double integrals must be solved and transcendental functions need to be evaluated. In this section, we compare the CPU times required to compute the forces and torques. We also compare the CPU times of the full dynamical simulations to complete. The comparisons are performed using the same single-core

Method	Force computations Average CPU time [seconds]	Scenario 1 CPU time [seconds]	Scenario 2 CPU time [seconds]
Surface integral method	0.055	1369	6435
GUBAS ($\mathcal{O}(2)$ expansion)	$6.723 \cdot 10^{-4}$	96	375
GUBAS ($\mathcal{O}(4)$ expansion)	0.014	1555	6120
GUBAS ($\mathcal{O}(8)$ expansion)	0.877	119474	

Table 2: Comparison of CPU times for the methods. The second column shows the average CPU time required to compute the forces and torques. Scenario 1 and 2 correspond to the simulations presented in Sect. 4, where the first one is for a binary with larger separation, and the second one is for a newly fissioned contact binary.

computer.

We first investigate the efficiency in the force and torque calculations. The evaluation times are measured in the code segments where the forces and torques are calculated, which excludes the time required to initialize the program and to solve the equations of motion. The second column of Table 2 shows the CPU time required to evaluate the forces and the torques of both bodies, averaged over 37182 different configurations. The second and fourth order potentials are approximately 82 times and four times faster than the surface integration method, respectively, while the potential truncated to order eight is roughly 16 times slower than the surface integration scheme.

The third and fourth columns of Table 2 shows the CPU times of the simulations described in Sect. 4. Here, the CPU times are measured from the moment the respective programs initiate until they terminate. This includes the time required to initialize the program, solve the equations of motion, and saving the results. The output is saved at each time step both for our method and with GUBAS in order to facilitate the comparison, although this can be changed for GUBAS to reduce the CPU time. The second order potential used by GUBAS is very efficient compared to the surface integration method. However, if the potential is truncated to order four, the CPU times for the simulations are comparable to the surface integration scheme. This is due to the differences in how the equations of motions are solved, and how they are optimized, for each software. Finally, for higher orders of the potential it seems that the surface integral method would be preferable, as an approximation order of eight with GUBAS takes approximately 33 hours compared to 1369 seconds with the surface integral method.

6 Summary and discussion

By utilizing the surface integral method that we have developed and described in some recent publications (Wold and Conway, 2021; Ho et al., 2021, 2022), we are able to accurately describe, without approximations, the gravitational interaction between two triaxial ellipsoids. This makes us able to address errors in force and torque calculations between two ellipsoids using methods based on series approximations, such as the inertia integral method, where the mutual gravitational potential is truncated at a certain order. A publicly available implementation of this is GUBAS (Davis and Scheeres, 2020), which we use in this work to compute interactions between two ellipsoids based on potentials truncated at second and fourth order. Previous work have compared approximative methods to each other for ellipsoidal (Hou et al., 2017) and polyhedral shapes (Agrusa et al., 2020). In this manuscript, we have compared the surface integration method with a method that expands the mutual potential truncated up to order four.

For a typical binary asteroid, where the secondary orbits the primary in the equatorial plane, both the second and fourth order potentials give similar values of the force compared to the surface integration method. The errors become insignificant at distances of 3–5 primary radii, and less than one percent even when the secondary is close to the primary.

For the torque, however, the errors become more significant, especially if the bodies are displaced such that the separation vector between the mass centers, $\mathbf{r}$, is parallel with one of the principal axes of the body for which the torque is being calculated. In this case the second order approximation fails by 100%. This is due to a mathematical limitation inherent in the second order approximation (Kane et al., 1983; Poursina and Anderson, 2012). Fourth order potentials can correct somewhat for this, but generally if the other body lies in the neighborhood of one of the principal axis of the body for which the torque is evaluated, the errors in the torque are notably larger than elsewhere. Consequently, approximative methods affect rotational motion more than translational motion, and using a more accurate method therefore becomes more important to correctly describe the rotational motion. The percentage errors in the torques are approximately an order of magnitude larger than the errors in the force. However, as long as the separation between the two components of the binary is sufficiently large (a few primary radii), simulations using the surface integration method and the expansion approaches show negligible differences in the torques.

The most notable differences and largest errors occur in situations where the two bodies are close with their centroids not in the same plane. These configurations are particularly relevant for contact binaries that separate due to rotational fission when a certain spin limit is reached. The two bounding spheres of the bodies intersect, and the series approximation of the mutual potential described by Eq. (4) no longer converges (Tricarico, 2008). The surface integration approach, on the other hand, is still valid, and we find that for a secondary placed close to the surface of the primary (insignificant surface-to-surface distance of 1 cm), errors are largest when the secondary is placed closed to the pole of the primary. The errors from the second order approximation are generally larger than from the fourth order, but if the primary is elongated enough in this configuration, the errors from the fourth order approximation may dominate. This is because the forces obtained by inertia integrals scale as $(a_p/r)^N$ for an order N expansion. When $r < a_p$ (as is the case for overlapping bounding spheres), the contribution from higher order gravity terms may inflate the calculated force, and lead to large errors.

Using a more accurate method to determine the forces and torques in the initial stages becomes more important if the bodies are initially close and the bounding spheres overlap. In these cases, the difference in the computed forces between the methods result in significantly different angular and translational velocities in the initial stages of the simulation. This leads to, for a binary with $q = 0.3$, deviations in the position of the secondary relative to the primary of more than 10 km, while the angular velocity components differ by $\sim 10^{-4}$ rad/s. The latter corresponds to relative differences in the angular velocity (and rotation period) that exceed 100%. We also find that these initial differences can lead to differences in the orbital period of the secondary of more than 10%. These discrepancies in the simulations are also seen even when the initial conditions are equal, which indicates that the use of a more accurate method to determine the mutual potential is particularly important the first hours of a post-fissioned asteroid system, in which the bodies are still relatively close.

With the surface integration method we calculate higher system energies for contact binary systems, compared to second and fourth order methods. Assuming that there is no loss of energy, our calculations therefore predict formation of asteroid pairs (total energy positive) at slightly higher mass ratios. These calculations were done for a few configurations where the secondary lies in the equatorial plane of the primary, but the separation between positive and negative system energies also changes with the shape of the bodies and their densities (Ho et al., 2022). Furthermore, the outcome of the system, for example, whether the two components collide or how long the secondary remains in orbit before escaping, may also be affected by how the mutual potential is computed. A future study comparing these outcomes may further demonstrate the importance of using a more accurate method to determine the mutual potential in order to study dynamics of post-fissioned asteroid systems.

The mass ratio of the system does not significantly alter the differences in the computed forces or torques between the methods, provided that the bodies are sufficiently far apart. However, if the bodies are close, the use of a more realistic method becomes more important to the mutual potential for systems with lower mass ratios. For a post-fissioned asteroid system, the error in the force, from a second order potential, can reach $\sim 7\%$ when $q = 0.01$, and reduces to $\sim 4\%$ when $q = 0.30$. When the potential is truncated to order four, the errors in the force are reduced to $\sim 2\%$ and $\sim 1\%$ for mass ratios 0.01 and 0.30, respectively.

We benchmark the methods by comparing the CPU times required to compute the forces and torques, and to complete the long-term simulations. Due to the nature of double integrals, the forces computed by the surface integration scheme is slower than that of GUBAS. However, for the full simulations, the time required for the simulations to finish from the surface integration method is comparable to the ones from GUBAS when an order four potential is used.

In this manuscript, we have only considered bodies of ellipsoidal shapes. However, modeling an asteroid as a polyhedron provides a more realistic representation of its shape. It may be of interest to compare the surface integration method with other expansion methods, applied to polyhedral shapes in the future.

The authors would like to thank Sverre Lunøe-Nielsen for helpful discussions on numerical issues. We would also like to thank the anonymous referee for their feedback that improved the manuscript.

A Open-source software

The software that uses makes use the surface integration method, as outlined by Conway (2016) and Ho et al. (2021), to solve the F2BP is available on GitHub[4].

References

H. F. Agrusa et al. A benchmarking and sensitivity study of the full two-body gravitational dynamics of the DART mission target, binary asteroid 65803 Didymos. *Icarus*, 349: 113849, October 2020. doi: 10.1016/j.icarus.2020.113849.

S. Aljbaae et al. The dynamical environment of asteroid 21 Lutetia according to different internal models. *Monthly Notices of the Royal Astronomical Society*, 464(3):3552–3560, January 2017. doi: 10.1093/mnras/stw2619.

S. Aljbaae, A. F. B. A. Prado, D. M. Sanchez, and H. Hussmann. Analysis of the orbital stability close to the binary asteroid (90) Antiope. *Monthly Notices of the Royal Astronomical Society*, 496(2):1645–1654, August 2020. doi: 10.1093/mnras/staa1634.

S. Aljbaae et al. First approximation for spacecraft motion relative to (99942) Apophis. *Romanian Astronomical Journal*, 31(3):241–264, November 2021.

L. A. G. Boldrin, D. J. Scheeres, and O. C. Winter. Dynamics of rotationally fissioned asteroids: non-planar case. *Monthly Notices of the Royal Astronomical Society*, 461(4): 3982–3992, October 2016. doi: 10.1093/mnras/stw1607.

T. G. G. Chanut, S. Aljbaae, and V. Carruba. Mascon gravitation model using a shaped polyhedral source. *Monthly Notices of the Royal Astronomical Society*, 450(4):3742–3749, July 2015. doi: 10.1093/mnras/stv845.

A. F. Cheng et al. AIDA DART asteroid deflection test: Planetary defense and science objectives. *Planetary and Space Science*, 157:104–115, August 2018. doi: 10.1016/j.pss.2018.02.015.

J. T. Conway. Vector potentials for the gravitational interaction of extended bodies and laminas with analytical solutions for two disks. *Celestial Mechanics and Dynamical Astronomy*, 125:161–194, June 2016. doi: 10.1007/s10569-016-9679-y.

J. T. Conway. Analytical solution from vector potentials for the gravitational field of a general polyhedron. *Celestial Mechanics and Dynamical Astronomy*, 121(1):17–38, Jan 2015. doi: 10.1007/s10569-014-9588-x.

A. B. Davis and D. J. Scheeres. High-fidelity Modeling of Rotationally Fissioned Asteroids. *The Planetary Science Journal*, 1(1):25, June 2020. doi: 10.3847/PSJ/ab9a39.

---

[4] Github repository `https://github.com/alexhosians/SIANS`

A. B. Davis and D. J. Scheeres. Doubly synchronous binary asteroid mass parameter observability. *Icarus*, 341:113439, 2020. ISSN 0019-1035. doi: https://doi.org/10.1016/j.icarus.2019.113439.

E. G. Fahnestock and D. J. Scheeres. Simulation of the full two rigid body problem using polyhedral mutual potential and potential derivatives approach. *Celestial Mechanics and Dynamical Astronomy*, 96(3-4):317–339, November 2006. doi: 10.1007/s10569-006-9045-6.

E. G. Fahnestock and D. J. Scheeres. Simulation and analysis of the dynamics of binary near-Earth Asteroid (66391) 1999 KW4. *Icarus*, 194(2):410–435, April 2008. doi: 10.1016/j.icarus.2007.11.007.

J. Feng and X. Hou. Dynamics of Equilibrium Points in a Uniformly Rotating Second-Order and Degree Gravitational Field. *The Astronomical Journal*, 154(1):21, July 2017. doi: 10.3847/1538-3881/aa75d0.

M. Galassi et al. *GNU scientific library*. Network Theory Limited, 2002.

P. Geissler et al. Erosion and Ejecta Reaccretion on 243 Ida and Its Moon. *ICARUS*, 120 (1):140–157, Mar 1996. doi: 10.1006/icar.1996.0042.

A. Ho, M. Wold, J. T. Conway, and M. Poursina. Extended two-body problem for rotating rigid bodies. *Celestial Mechanics and Dynamical Astronomy*, 133(8):35, August 2021. doi: 10.1007/s10569-021-10034-8.

A. Ho, M. Wold, M. Poursina, and J. T. Conway. Dynamics of asteroid systems post-rotational fission. *Astronomy & Astrophysics*, 665:A43, September 2022. doi: 10.1051/0004-6361/202243706.

X. Hou, D. J. Scheeres, and X. Xin. Mutual potential between two rigid bodies with arbitrary shapes and mass distributions. *Celestial Mechanics and Dynamical Astronomy*, 127(3):369–395, March 2017. doi: 10.1007/s10569-016-9731-y.

W. Hu and D. J. Scheeres. Spacecraft Motion About Slowly Rotating Asteroids. *Journal of Guidance Control Dynamics*, 25(4):765–775, July 2002. doi: 10.2514/2.4944.

S. A. Jacobson and D. J. Scheeres. Dynamics of rotationally fissioned asteroids: Source of observed small asteroid systems. *Icarus*, 214(1):161–178, July 2011. doi: 10.1016/j.icarus.2011.04.009.

T. Kane, P. Likins, and D. Levinson. *Spacecraft Dynamics*. McGraw-Hill series in aeronautical and aerospace engineering. McGraw-Hill Book Company, 1983. ISBN 9780070378438.

A. J. Maciejewski. Reduction, Relative Equilibria and Potential in the Two Rigid Bodies Problem. *Celestial Mechanics and Dynamical Astronomy*, 63(1):1–28, March 1995. doi: 10.1007/BF00691912.

W. MacMillan. *The Theory of the Potential.* (MacMillan: Theoretical Mechanics). McGraw-Hill Book Company, Incorporated, 1930.

J. L. Margot et al. Binary Asteroids in the Near-Earth Object Population. *Science*, 296 (5572):1445–1448, May 2002. doi: 10.1126/science.1072094.

H. Moritz. *Advanced Physical Geodesy.* Sammlung Wichmann : Neue Folge : Buchreihe. Wichmann, 1980. ISBN 9780856261954.

P. M. Muller and W. L. Sjogren. Mascons: Lunar Mass Concentrations. *Science*, 161(3842): 680–684, August 1968. doi: 10.1126/science.161.3842.680.

P. M. Muller and W. L. Sjogren. Consistency of lunar orbiter residuals with trajectory and local gravity effects. *Journal of Spacecraft and Rockets*, 6:849–850, 1969.

S. P. Naidu et al. Radar observations and a physical model of binary near-Earth asteroid 65803 Didymos, target of the DART mission. *Icarus*, 348:113777, September 2020. doi: 10.1016/j.icarus.2020.113777.

M. K. Paul. An Expansion in Power Series of Mutual Potential for Gravitating Bodies with Finite Sizes. *Celestial Mechanics*, 44(1-2):49–59, March 1988. doi: 10.1007/BF01230706.

M. Poursina and K. S. Anderson. Long-range force and moment calculations in multiresolution simulations of molecular systems. *Journal of Computational Physics*, 231(21): 7237–7254, August 2012. doi: 10.1016/j.jcp.2012.06.041.

M. Poursina and E. A. Butcher. Electrostatic force and moment approximations of coulomb charged spacecraft based on center of charge. *The Journal of the Astronautical Sciences*, 67(3):829–862, 2020.

P. Pravec and A. W. Harris. Binary asteroid population. 1. Angular momentum content. *Icarus*, 190(1):250–259, September 2007. doi: 10.1016/j.icarus.2007.02.023.

P. Pravec et al. Formation of asteroid pairs by rotational fission. *Nature*, 466(7310):1085–1088, August 2010. doi: 10.1038/nature09315.

P. Pravec et al. Binary asteroid population. 3. Secondary rotations and elongations. *Icarus*, 267:267–295, March 2016. doi: 10.1016/j.icarus.2015.12.019.

D. C. Richardson et al. Predictions for the Dynamical States of the Didymos System before and after the Planned DART Impact. *The Planetary Science Journal*, 3(7):157, July 2022. doi: 10.3847/PSJ/ac76c9.

A. S. Rivkin et al. The Double Asteroid Redirection Test (DART): Planetary Defense Investigations and Requirements. *The Planetary Science Journal*, 2(5):173, October 2021. doi: 10.3847/PSJ/ac063e.

D. J. Scheeres. Stability of the planar full 2-body problem. *Celestial Mechanics and Dynamical Astronomy*, 104(1-2):103–128, June 2009. doi: 10.1007/s10569-009-9184-7.

D. J. Scheeres et al. Dynamical Configuration of Binary Near-Earth Asteroid (66391) 1999 KW4. *Science*, 314(5803):1280–1283, November 2006. doi: 10.1126/science.1133599.

D. Scheeres, S. Ostro, R. Hudson, and R. Werner. Orbits close to asteroid 4769 castalia. *Icarus*, 121(1):67 – 87, 1996. ISSN 0019-1035. doi: https://doi.org/10.1006/icar.1996.0072.

P. Tricarico. Figure figure interaction between bodies having arbitrary shapes and mass distributions: a power series expansion approach. *Celestial Mechanics and Dynamical Astronomy*, 100(4):319–330, April 2008. doi: 10.1007/s10569-008-9128-7.

D. Tsoulis. Analytical computation of the full gravity tensor of a homogeneous arbitrarily shaped polyhedral source using line integrals. *Geophysics*, 77(2):F1, January 2012. doi: 10.1190/geo2010-0334.1.

D. Tsoulis and S. Petrović. On the singularities of the gravity field of a homogeneous polyhedral body. *Geophysics*, 66(2):535, January 2001. doi: 10.1190/1.1444944.

S. J. Weidenschilling. Hektor: Nature and origin of a binary asteroid. *Icarus*, 44(3):807–809, December 1980. doi: 10.1016/0019-1035(80)90147-5.

R. A. Werner. Spherical harmonic coefficients for the potential of a constant-density polyhedron. *Computers and Geosciences*, 23(10):1071–1077, December 1997. doi: 10.1016/S0098-3004(97)00110-6.

R. A. Werner and D. J. Scheeres. Exterior Gravitation of a Polyhedron Derived and Compared with Harmonic and Mascon Gravitation Representations of Asteroid 4769 Castalia. *Celestial Mechanics and Dynamical Astronomy*, 65(3):313–344, Jan 1997.

R. A. Werner and D. J. Scheeres. Mutual Potential of Homogeneous Polyhedra. *Celestial Mechanics and Dynamical Astronomy*, 91(3-4):337–349, March 2005. doi: 10.1007/s10569-004-4621-0.

M. Wold and J. T. Conway. The planar two-body problem for spheroids and disks. *Celestial Mechanics and Dynamical Astronomy*, 133(6):27, June 2021. doi: 10.1007/s10569-021-10023-x.